



Second United States Microgravity Laboratory: One Year Report, Volume 2

M. Vlasse, Editor

Marshall Space Flight Center, Marshall Space Flight Center, Alabama

D. McCauley, Editor

University of Alabama in Huntsville, Huntsville, Alabama

C. Walker, Editor

Universities Space Research Association, Huntsville, Alabama

The NASA STI Program Office...in Profile

Since its founding, NASA has been dedicated to the advancement of aeronautics and space science. The NASA Scientific and Technical Information (STI) Program Office plays a key part in helping NASA maintain this important role.

The NASA STI Program Office is operated by Langley Research Center, the lead center for NASA's scientific and technical information. The NASA STI Program Office provides access to the NASA STI Database, the largest collection of aeronautical and space science STI in the world. The Program Office is also NASA's institutional mechanism for disseminating the results of its research and development activities. These results are published by NASA in the NASA STI Report Series, which includes the following report types:

- **TECHNICAL PUBLICATION.** Reports of completed research or a major significant phase of research that present the results of NASA programs and include extensive data or theoretical analysis. Includes compilations of significant scientific and technical data and information deemed to be of continuing reference value. NASA's counterpart of peer-reviewed formal professional papers but has less stringent limitations on manuscript length and extent of graphic presentations.
- **TECHNICAL MEMORANDUM.** Scientific and technical findings that are preliminary or of specialized interest, e.g., quick release reports, working papers, and bibliographies that contain minimal annotation. Does not contain extensive analysis.
- **CONTRACTOR REPORT.** Scientific and technical findings by NASA-sponsored contractors and grantees.

- **CONFERENCE PUBLICATION.** Collected papers from scientific and technical conferences, symposia, seminars, or other meetings sponsored or cosponsored by NASA.
- **SPECIAL PUBLICATION.** Scientific, technical, or historical information from NASA programs, projects, and mission, often concerned with subjects having substantial public interest.
- **TECHNICAL TRANSLATION.** English-language translations of foreign scientific and technical material pertinent to NASA's mission.

Specialized services that complement the STI Program Office's diverse offerings include creating custom thesauri, building customized databases, organizing and publishing research results...even providing videos.

For more information about the NASA STI Program Office, see the following:

- Access the NASA STI Program Home Page at <http://www.sti.nasa.gov>
- E-mail your question via the Internet to help@sti.nasa.gov
- Fax your question to the NASA Access Help Desk at (301) 621-0134
- Telephone the NASA Access Help Desk at (301) 621-0390
- Write to:
NASA Access Help Desk
NASA Center for AeroSpace Information
800 Elkridge Landing Road
Linthicum Heights, MD 21090-2934



Second United States Microgravity Laboratory: One Year Report, Volume 2

M. Vlasse, Editor

Marshall Space Flight Center, Marshall Space Flight Center, Alabama

D. McCauley, Editor

University of Alabama in Huntsville, Huntsville, Alabama

C. Walker, Editor

Universities Space Research Association, Huntsville, Alabama

National Aeronautics and
Space Administration

Marshall Space Flight Center

Acknowledgments

The untiring efforts and dedication of the STS-73 payload and orbiter crews, mission and program managers, and mission operations personnel were critical to the completion of the mission's objectives and are sincerely appreciated. The editors wish to thank the Office of Life and Microgravity Science and Applications (OLMSA) and the Microgravity Research Division (MRD) at NASA Headquarters for their support and encouragement. The editors also wish to thank the NASA Marshall Space Flight Center's Public Affairs Office for their help in publicizing the results of the USML-2 mission, as well as all of the investigators for contributing to this document.

Marcus Vlasse
NASA Marshall Space Flight Center
USML-2 Mission Scientist

Mark Lee
NASA Headquarters
USML-2 Program Scientist

Compilers and editors—

Dannah McCauley, University of Alabama in Huntsville/NASA MSFC
Charles Walker, Universities Space Research Association/NASA MSFC

Available from:

NASA Center for AeroSpace Information
800 Elkridge Landing Road
Linthicum Heights, MD 21090-2934
(301) 621-0390

National Technical Information Service
5285 Port Royal Road
Springfield, VA 22161
(703) 487-4650

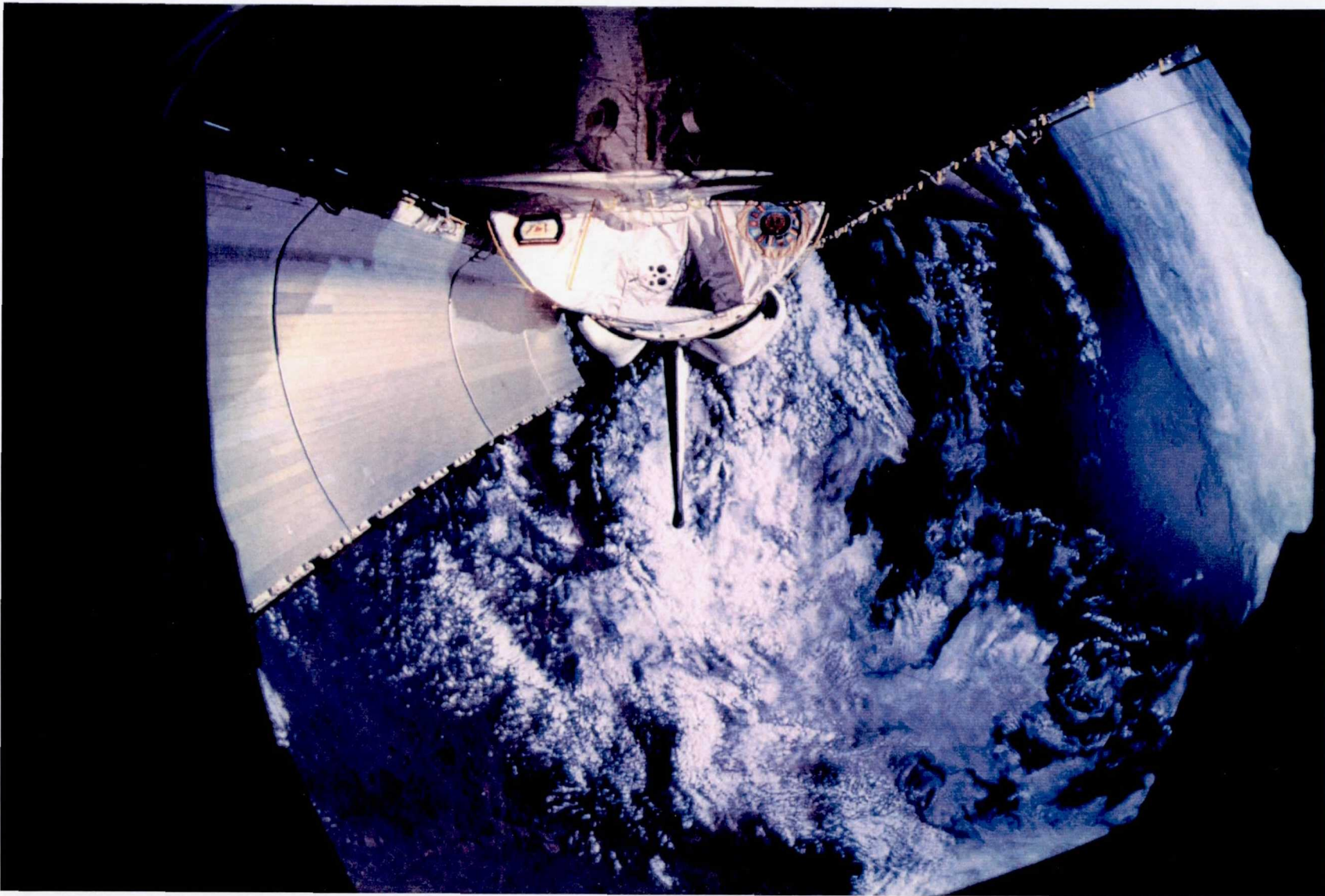


Figure 1. USML-2 payload bay view from Shuttle window.



Figure 2. USML-2 payload crewmembers; red team: Albert Sacco and Kathryn Thornton, blue team: Catherine Coleman and Fred Leslie.

TABLE OF CONTENTS

TABLE OF CONTENTS	v
LIST OF FIGURES	vii
LIST OF TABLES	xix
AUTHORS INDEX	xxi
ACRONYMS	xxv
KEY WORD INDEX	xxix
MISSION INFORMATION	xxxvii
INTRODUCTION	xxxviii
USML-2 EXPERIMENTS	
EXPERIMENT XV: Protein Crystal Growth: Light-driven Charge Translocation Through Bacteriorhodopsin ... Gottfried Wagner	15-369
EXPERIMENT XVI: Partial Improvement of Crystal Quality for Microgravity-Grown Apocrustacyanin C ₁ Naomi E. Chayen	16-379
EXPERIMENT XVII: Crystallization of the Visual Pigment Rhodopsin..... Willem J. de Grip	17-397
EXPERIMENT XVIII: Crystal Structure Analysis of the Bacteriophage Lambda Lysozyme	18-401
Jean-Paul Declercq	
EXPERIMENT XIX: Crystallization of Monoclinic and Triclinic Lysozyme (APCF Facility)	19-405
Arnaud Ducruix	
EXPERIMENT XX: Crystallization of RNA Molecules Under Microgravity Conditions	20-415
Volker A. Erdmann	
EXPERIMENT XXI: Comparative Assessment of Microgravity- and Earth-Grown Crystals Thaumatin and Aspartyl-tRNA Synthetase	21-421
Richard Giegé	
EXPERIMENT XXII: Crystallization in Space of Designed and Natural (α/β)-Barrel Structures	22-431
Joseph A. Martial	

EXPERIMENT XXIII: Comparative Analysis of Thaumatin Crystals Grown on Earth and in Microgravity	23-439
Richard Giegé	
EXPERIMENT XXIV: Crystallization of Photosystem I Protein Complex	24-455
Wolfram Saenger	
EXPERIMENT XXV: Crystallization of Glutathione S-Transferase in Microgravity	25-459
Lennart Sjölin	
EXPERIMENT XXVI: Crystallization of the Epidermal Growth Factor (EGF) Receptor	26-465
Wolfgang Weber	
EXPERIMENT XXVII: Crystallization in a Microgravity Environment of CcdB, A Protein Involved in the Control of Cell Death.....	27-469
Lode Wyns	
EXPERIMENT XXVIII: Crystallization of Ribosomal Particles in Space	28-475
Ada Yonath	
EXPERIMENT XXIX: Space Crystallization of a Binary Complex of <i>Sulfolobus Solfataricus</i> Alcohol Dehydrogenase on the United States Microgravity Laboratory (USML-2) Mission	29-479
Adriana Zagari	
EXPERIMENT XXX: Results from the USML-2 Interface Configuration Experiment	30-487
Paul Concus	
EXPERIMENT XXXI: Oscillatory Thermocapillary Flow Experiment-2 (OTFE-2).....	31-507
Yasuhiro Kamotani	
EXPERIMENT XXXII: Fiber-Supported Droplet Combustion	32-523
Forman A. Williams	
EXPERIMENT XXXIII: Crystallization of Hard Sphere Colloids in Microgravity: Results of the Colloidal Disorder-Order Transition, CDOT on USML-2	33-537
Paul M. Chaikin	
EXPERIMENT XXXIV: Dendritic Growth of Hard Sphere Crystals	34-549
William B. Russel	
EXPERIMENT XXXV: Catastrophic Collapse of Particulate Clouds: Implications From Aggregation Experiments in the USML-1 and USML-2 Glovebox	35-577
John Marshall	
EXPERIMENT XXXVI: One Year Report for SAMS and OARE on STS-73/USML-2	36-593
Roshanak Hakimzadeh	
EXPERIMENT XXXVII: 3-DMA Acceleration Measurement on USML-2/STS-73	37-613
Jan A. Bijvoet	
EXPERIMENT XXXVIII: Suppression of Transient Events by Levitation (STABLE)—Results From the USML-2 Mission	38-649
Gerald S. Nurre	

LIST OF FIGURES

Figure	Title	Page
Figure 1.	USML-2 payload bay view from Shuttle window.	iii
Figure 2.	USML-2 payload crewmembers; red team: Albert Sacco and Kathryn Thornton, blue team: Catherine Coleman and Fred Leslie.	iv
EXPERIMENT XV:		
Figure 1.	Micelle radius formed by the detergent N-octyl β -D-glucopyranoside (OG) in the experiment protocol and change in micelle size through the additives Europium (Eu), Polyethylene glycol (PEG), Benzamidine (B), and their combinations as shown in the abscissa in the absence and presence of Bacteriorhodopsin (BR). The micelle size is indicated in absolute values with standard deviations (-♦-) and in relative units (histogram) from different series of experiments. The relative units given in the histogram are normalized to the micelle radius of OG in the experiment protocol. <i>Left side</i> : both experimental set-ups (-♦-; histogram) used in the DLS analysis, showed a rise in value after the addition of Eu to OG and a steady decline with the smallest value measured for the cocktail of OG + B + PEG. <i>Right side</i> : Upon dissolution of BR, the level of micelle radius in absolute values as a function of the additives used increased more than ten times (data not shown). The pattern of the histogram, however, remained essentially the same (compare left to right side).	15-374
Figure 2.	USML-2 Flight Experiment: Bacteriorhodopsin (BR) crystal in needle habit of about 500 μ m in length. Here, the molecular rods of BR are closely packed together to form a crystal of compact morphology which resulted in sharp edges and smooth surfaces.	15-375
Figure 3.	USML-2 Flight Experiment: Bacteriorhodopsin (BR) crystal in cubic shape with axes of 150 μ m in length.	15-376
Figure 4.	USML-2 Flight Experiment: Multicrystalline needle cluster of Bacteriorhodopsin (BR) with a diameter of 300 μ m. The cluster seems to consist of single needles which fall apart easily. The individual needles show similar sharp edges and smooth surfaces as shown in figure 2.	15-377
Figure 5.	Oscillation diffraction pattern recorded at the synchrotron beam line X11; EMBL-outstation, Hamburg. The diffraction pattern of balk-shaped Bacteriorhodopsin (BR) crystal shows resolution up to a limit of 3.8 \AA in the direction perpendicular to the purple membrane plane.	15-377

EXPERIMENT XVI:

Figure 1. Dimensions of apocrustacyanin C₁ crystals used for data collection (not to scale). The relationship of the crystal habit and the unit-cell parameters is also shown. 16-388

Figure 2. Rocking curves for the (4 19 1) reflection (4 Å resolution), as a representative example, at three Ψ settings (left to right), for each of the five crystals, microgravity 1 (first row), microgravity 2 (second row), microgravity 3 (third row), Earth 1 (fourth row), and Earth 2 (fifth row). The three curves for microgravity 1 (first row) were measured in single-bunch mode; i.e., where the circulating current is approximately 1/10th of the current available for all the other curves. 16-389

Figure 3. Rocking curves for the (11 22 43) reflection (1.85 Å resolution), as a representative example, laid out in the same format as in figure 2. This reflection, being at high resolution, was measured near the start of the run for each crystal [unlike the (4 19 1) reflection which was measured near the end of the sequence of reflections, being at low resolution]. This essentially avoids any impact of radiation damage. 16-390

Figure 4. Histogram of the mosaicity for (a) the three microgravity and (b) two earth-grown apocrustacyanin C₁ crystals. 16-391

Figure 5. Plot of the mosaicity versus peak/background for the three microgravity-grown and two earth-grown control crystals of apocrustacyanin C₁. 16-392

Figure 6. Plot of the “mosaicity (rocking) volume” for (a) Earth 1 apocrustacyanin, (b) microgravity 3 apocrustacyanin, (c) earth-grown lysozyme, and (d) microgravity-grown lysozyme [Snell et al. (1995) for (c) and (d)]. All plots are on the same scale with the mosaicities given in degrees. 16-393

Figure 7. Unit-cell dimensions of apocrustacyanin C₁ and lysozyme (in Å). 16-394

Figure 8. Plot of the rocking volume projected onto the *hk* and *hl* planes for (a) earth 1 apocrustacyanin, (b) μg 3 apocrustacyanin, (c) earth-grown lysozyme, and (d) microgravity-grown lysozyme. 16-395

EXPERIMENT XVIII:

Figure 1. Very thin, needle-like crystals of bacteriophage lambda lysozyme were grown in two reactors on USML-2. 18-404

EXPERIMENT XIX:

Figure 1. Crystals of triclinic lysozymes (a) and monoclinic lysozyme (b). 19-414

EXPERIMENT XX:

Figure 1. Crystals obtained from *Thermus flavus* engineered 5S rRNA molecules grown under microgravity conditions (a) and in a laboratory control experiment (b). 20-419

EXPERIMENT XXI:

Figure 1. Comparison of thaumatin crystals grown on Earth (a-c) to those grown in microgravity (d-f). Only the protein containing chambers of the reactors are shown, and those seen here represent what is typically observed in the 188- μ l volume APCF dialysis reactors with low concentrations of thaumatin (6 mg/ml). Numerous and extremely small crystals are observed in the ground controls compared to only a few larger crystals in space. The average longest dimensions measured for crystals grown on Earth and in space were 0.1 mm and 0.5 mm, respectively. All images are at the same magnification. 21-428

Figure 2. Earth-grown thaumatin crystals (a) compared to space-grown crystals (b) in 67- μ l volume APCF dialysis reactor. The images show the protein chambers containing crystals grown at high concentrations of thaumatin (20 mg/ml). Crystals grown on Earth ranged in size from 0.1 mm to 1.2 mm in the longest dimensions, and most of the crystals are seen to have sedimented to the bottom membrane. Space-grown crystals, on the other hand, grew with a size range of 0.5 mm to 1.7 mm from apex to apex. Fewer and larger crystals were observed in this space reactor than for the corresponding Earth-control reactor. 21-429

Figure 3. Graph of the intensity (I) versus estimated error (σ) ratio as a function of resolution [$1/d^2 \text{ \AA}^{-2}$] for thaumatin Earth- and space-grown crystals. 21-430

EXPERIMENT XXII:

Figure 1. Needle-shaped micro-crystals of octarellin II obtained in space. 22-437

Figure 2. Regular shaped crystals of *thermotoga maritima* TIM obtained in space. 22-438

EXPERIMENT XXIII:

Figure 1. Comparison of thaumatin crystals grown on Earth (a-c) to those grown in microgravity [d-f (corresponding to reactors, 2, 5, and 4 respectively as listed in table 2)]. Only the protein containing chambers of the reactors are shown and those seen here represent what is typically observed in the 188- μ m volume APCF dialysis reactors with low concentrations of thaumatin (6 mg/ml). Numerous and extremely small crystals are observed in the ground controls compared to only a few larger crystals in space. The average longest dimensions measured for crystals grown on Earth and in space were 0.1 mm and 0.5 mm, respectively. All images are at the same magnification. 23-450

Figure 2. Earth-grown thaumatin crystals (a) compared to space-grown crystals (b) in a 66- μ l volume APCF dialysis reactor (table 2, reactor 1). The images show the protein chambers containing crystals grown at high concentrations of thaumatin (20 mg/ml). Crystals grown on Earth ranged in size from 0.1 mm to 1.2 mm in the longest dimension, and most of the crystals are seen to have sedimented to the bottom membrane. Space-grown crystals, on the other hand, grew with a size range of 0.5 mm to 1.7 mm from apex to apex. Fewer and larger crystals were observed in this space reactor than for the corresponding Earth-control reactor. 23-451

Figure 3. Thaumatin microgravity-grown crystals obtained at three different protein concentrations (a, 35 mg/ml; b, 17 mg/ml; c, 7 mg/ml) by free interface diffusion (table 1, reactors 8-10). Each image is at the same magnification. The largest crystals measured to be more than 2 mm in the longest direction and were the crystals used for x-ray data collection. 23-451

Figure 4. A graph of the intensity (I) versus estimated error (σ) ratio as a function of resolution ($\sin^2\theta/\lambda^2$) for thaumatin Earth- and space-grown crystals. The graph is presented as a modified Wilson Plot^{29,30} where the value of I/σ is the effective "signal-to-noise" for the diffraction pattern at the resolution corresponding to the respective ($\sin^2\theta/\lambda^2$) value. For the entire resolution range, space-grown crystals yield nearly 30 percent more diffraction intensities ($> 3\sigma$) than the best crystals grown on Earth. 23-452

Figure 5. Profiles of three representative reflections at 4 \AA were reach evaluated from an Earth- (A) and space-grown thaumatin crystal (B) studied for LMS. Reflections were obtained in the vertical diffraction plane such that the rotation axis was horizontal and perpendicular to the x-ray beam. Each set of reflection profiles for space- and Earth-grown crystals were averaged and Gaussian fits of the sets of profiles were calculated (solid lines). The full width at half maximum (FWHM) of a Gaussian fit for each profile was measured and its value is indicated by a short horizontal line. The space-grown crystal profiles have FWHM values that are about 2.5 times less than that of the Earth-grown crystal. The intensities shown are normalized and the actual peak intensities measured to 250,000 counts per 0.1 seconds for the space crystal. To the contrary, the spot intensities corresponding to the same reflections for the Earth crystal were approximately two times less. Panel C shows a relative comparison of the averaged mosaicity profiles from an Earth- to a space-grown crystal for the same reflections. 23-453

EXPERIMENT XXX:

Figure 1. Wedge container. 30-499

Figure 2. Proboscis container section showing three members of the continuum of extremal arcs. 30-499

Figure 3.	Three superimposed double proboscis container sections. From outermost to innermost, the pair of values of γ_0 for the left and right proboscides of each section are $20^\circ/26^\circ$, $30^\circ/34^\circ$, and $38^\circ/44^\circ$	30-500
Figure 4.	Computed equilibrium interface for the $30^\circ/34^\circ$ (upper-half) double proboscis section for contact angles 60° , 50° , 40° , and 35° . $\gamma_0 = 34^\circ$	30-501
Figure 5.	$20^\circ/26^\circ$ proboscis vessel (flight unit).	30-502
Figure 6a–b.	Static interface shapes for ICE–P1 ($20^\circ/26^\circ$) vessel. 6a (left)—after completion of fill; 6b (right)—after disturbances by payload specialist.	30-502
Figure 7a–d.	Static interface shapes for ICE–P2 ($30^\circ/34^\circ$) vessel. 7a (upper left)—after completion of fill; 7b (upper right). 7c (lower left), and 7d (lower right)—after successive disturbances by payload specialist.	30-503
Figure 8a–d.	Static interface shapes for ICE–P3 ($38^\circ/44^\circ$) vessel. 8a (upper left)—after completion of fill; 8b (upper right), 8c (lower left), and 8d (lower right)—after successive disturbances by payload specialist.	30-504
Figure 9.	Static interface shape for ICE–P3 ($38^\circ/44^\circ$) vessel 1 week after that shown in figure 8d.....	30-505
Figure 10.	ICE wedge vessel near critical angle.	30-505
EXPERIMENT XXXI:		
Figure 1.	Photographs of OTFE–2 test module.	31-515
Figure 2.	Cross-sectional view of test module.	31-516
Figure 3.	Temperature variations in Test 1 ($D = 1.2$ cm and $Ar = 0.5$).	31-516
Figure 4.	Temperature variations in Test 2 ($D = 1.2$ cm and $Ar = 2$).	31-517
Figure 5.	Temperature variations in Test 3 ($D = 2$ cm and $Ar = 0.5$).	31-517
Figure 6.	Temperature variations in Test 4 ($D = 2$ cm and $Ar = 2$).	31-518
Figure 7.	Thermocouple outputs in Test 2 ($D = 1.2$ cm and $Ar = 2$).	31-519
Figure 8.	Critical temperature differences measured in OTFE–2 and STDCE–2.	31-520
Figure 9.	Critical S-parameters in OTFE–2 and STDCE–2.	31-520

Figure 10. Oscillation frequencies 31-521

Figure 11. Dimensionless frequencies 31-521

EXPERIMENT XXXII:

Figure 1. Photograph of the experimental apparatus 32-534

Figure 2. Dependence of the droplet diameter at extinction on the initial droplet diameter for initially pure methanol droplets; the inset is an illustration of the shape of the droplet on the fiber 32-535

Figure 3. The square of the droplet diameter D as a function of time, for an initial droplet diameter $D_0 = 3$ mm, for initially pure methanol and methanol-water mixtures having an initial water mass fraction of 10 percent 32-535

Figure 4. The square of the droplet diameter as a function of time for two heptane-hexadecane droplets with initial heptane mass fraction $Y = 0.6$ 32-536

Figure 5. The square of the droplet diameter D as a function of time and the ratio of the upstream H_1 , to downstream H_3 flame radius as a function of time, for a methanol droplet of initial diameter $D_0 = 3.1$ mm, in an experiment in which the forced-flow velocity is increased slowly from zero to 50 mm/sec. 32-536

EXPERIMENT XXXIII:

Figure 1. (a) Photo of a sample of 508-nm PMMA spheres in index matching suspension at volume fraction $\phi = 0.504$, in the coexistence region of the phase diagram. In this preflight ground-based photo, the sample is phase separated with 0.1-mm crystallites in the bottom half of the tube. (b) The same sample after recrystallization on the Shuttle in microgravity. Millimeter-size crystals are dispersed in the liquid phase. The insert shows the dendritic arms on several of the crystallites grown in microgravity 33-544

Figure 2. (a) Bragg scattering geometry. Laser beam incident on a cylindrical sample scatters onto a cylindrical screen. (b) Bragg scattering from a $d = 518$ -nm sample with $\phi = 0.537$. Note the dominance of streaks rather than spots, indicating Bragg rods and a 2-dimensional structure as might be expected for a random hexagonal close-packed structure. (c) Computer-generated scattering pattern for FCC. (d) RHCP structures 33-545

Figure 3. Scattering intensity as a function of the angle obtained by averaging many scattering images as in figure 2b for a sample with $\phi = 0.537$. The peak in ground-based experiments at 80° is the (2 0 0) FCC Bragg peak and shows that samples grown in 1g have some fraction of FCC structure. Note the complete absence of any such FCC structure in the microgravity data. 33-546

Figure 4.	This sample, with $\phi=0.619$ (deep in the “glass” phase) completely crystallized in microgravity after failing to crystallize in 1g. The sample remained crystalline on return to ground. After 6 months the bottom part of the sample was remelted using the stirbar seen suspended in the glassy region. Two months later the bottom part of the sample remained glassy with neither nucleation nor growth in 1g.	33-547
EXPERIMENT XXXIV:		
Figure 1.	A 35-mm photograph 12 days after mixing of a 10-mm diameter sample cell containing PMMA spheres with $2a = 508$ nm at $\phi = 0.504$ in index matching mixture of decalin and tetralin illustrating large dendritic crystallites surrounded by disordered fluid, which form within 5 days under microgravity in the Space Shuttle. ¹⁹ The figure 1 insert is a closeup of the dendritic crystallites demonstrating the detailed structure, which persisted for the duration of the flight. [Reproduced with permission from Zhu, et al. <i>Nature</i> , to appear, 1997.]	34-572
Figure 2.	Digital photograph of a dendritic crystallite in a 10-mm diameter sample cell containing PMMA spheres with $2a = 518$ nm at $\phi = 0.512$ in index matching mixture of decalin and tetralin in the Space Shuttle after 5 days (subsequent to mixing) under microgravity.	32-573
Figure 3.	(a) Volume fraction profiles within a growing crystallite ($\rho < X$) and the surrounding metastable fluid ($\rho > X$) for (left) slow, diffusion limited growth with $\phi_0 = 0.514$ and $X=20$ and (right) rapid growth with $\phi_0 = 0.575$ and $X=25$. (b) Volume fractions on the fluid, ϕ_{fi} , and solid, ϕ_{si} , sides of the interface as functions of the crystallite size X for diffusion limited growth at $\phi_0 = 0.499, 0.504, 0.509, 0.514$. (c) variations in the volume fractions at the interface as functions of x for four different ϕ_0	34-574
Figure 4.	Rates of diffusion limited growth as a function of (a) the crystallite size X for $\phi_0 = 0.499, 0.504, 0.509, 0.514$, and (b) the overall volume fraction ϕ_0 for $X = 2$ (....), 4 (---), 8 (· · ·), 12 (—), 16 (-----), and (c) rapid growth for $X \gg 1$ as a function of ϕ_0 compared with the interfacial velocity from the Wilson-Frenkel law.	34-575
Figure 5.	Cross sections of perturbed crystallites with $j = 1, 2, 3, 4$ for $\varepsilon = 0, 0.2, 0.4, 0.6, 0.8$, and 1.0.	34-576
Figure 6.	Growth exponent for the three lowest unstable modes normalized by the fractional supersaturation Δ as functions of the crystallite size X	34-576

EXPERIMENT XXXV:

Figure 1. Experimental apparatus flown in USML-1. Pump base unit and the eight modular experiment chambers are shown. For scale, the windows of the modules are 5 by 5 cm. Each self-contained module is plugged into the base to provide a pulse of compressed air that disperses the grains inside the experiment volume. The volume is not pressurized by this action because the air escapes (without the grains) through chamber-wall screens. The compressed air (~12 psig) is held in a small reservoir in the pump and is derived by operation of the crank handle at right which actuates a small compressor piston. Pressure is released into the chambers by an externally operated shutter mechanism built into the base of each module. Magnified ($\times 4$) video images were obtained of all the experiments; grains were imaged as silhouettes against a diffuse backlight panel placed behind the rear window of each module. 35-590

Figure 2. Two views of aggregates formed from a dense dispersion of 0.4-mm quartz grains. The various aggregate shapes are essentially all expressions of the basic filamentary "building block" aggregate structure. Note also the complex network-like structure formed by the filaments. These aggregate populations were formed within the first 30–60 seconds of the experiment and experienced virtually no subsequent changes with time. Field of view in both cases is approximately 2.5 cm across. 35-591

Figure 3. Length of aggregates versus time for 0.4-mm quartz grains (USML-1 data). Note the rapid rise in length from the monodispersed state to "full aggregation" within the first few tens of seconds (corresponding to the period of turbulent damping). The data points represent average aggregate lengths determined from 100–200 aggregates for each still frame taken from the video. The number of grains per aggregate takes into account the foreshortening effect of the 3-dimensional structures as seen on 2-dimensional video images. 35-592

Figure 4. Giant "clod-like" aggregate formed in microgravity during manipulation of experiment chamber by the astronaut. Note filamentary, tentacle-like growths from surface. The aggregate is composed of several thousand 0.4-mm quartz grains. All of the remaining free grains within the field of view are being drawn towards the aggregate at speeds up to 1 cm/sec as a result of the strong electrostatic field produced by the aggregate itself. Field of view \approx 3 cm across. 35-592

EXPERIMENT XXXVI:

Figure 1. Orbiter body coordinate system. 36-600

Figure 2. Orbiter structural coordinate system. 36-600

Figure 3. USML-2 major attitudes. 36-601

Figure 4.	Trimmean filter OARE data for entire STS-73 mission.	36-602
Figure 5.	Trimmean filter OARE data for period when <i>Columbia</i> was in the solar inertial attitude for tire warming.	36-603
Figure 6.	Trimmean filter OARE data for period when <i>Columbia</i> was in the CGF attitude in support of one CGF experiment.	36-604
Figure 7.	Trimmean filter OARE data for period when <i>Columbia</i> was in the GG attitude.	36-605
Figure 8.	Trimmean filter OARE data for period when <i>Columbia</i> was in the GFFC attitude.	36-606
Figure 9.	SAMS TSH A data for crew quiet period. (a) Time history; (b) PSD.	36-607
Figure 10.	SAMS TSH B data vector magnitude for 5-hour period. PRCS and VRCS jet firings are indicated across top of plot.	36-608
Figure 11.	SAMS TSH A data during payload bay door opening motion. (a) Time history; (b) PSD.	36-609
Figure 12.	SAMS TSH C data during Glovebox fan operations. (a) Time history; (b) PSD.	36-610
Figure 13.	Trimmean filter OARE data showing the effects of two water dump operations.	36-611

EXPERIMENT XXXVII:

Figure 1a.	3-DMA electrical/CDMS interfaces.	37-625
Figure 1b.	3-DMA hardware.	37-626
Figure 2.	STS-73 Commander Kenneth Bowersox performs a "Monitor" operation on the Central Unit of 3-DMA.	37-627
Figure 3.	3-DMA, RU-1 in rack 8, STS-73 Spacelab.	36-627
Figure 4	3-DMA, RU-2 in rack 5, STS-73, Spacelab.	37-628
Figure 5.	3-DMA, RU-3 on subfloor, STS-73, Spacelab.	37-628
Figure 6.	STS-73 mission, 3-DMA panoramic data display.	37-629
Figure 7.	Nominal STS-73 disturbance levels.	37-629
Figure 8.	Nominal STS-73 disturbance levels.	37-630

Figure 9.	Nominal STS-73 disturbance levels.....	37-630
Figure 10.	Nominal STS-73 disturbance levels.....	37-631
Figure 11.	Nominal STS-73 disturbance levels.....	37-631
Figure 12.	Nominal STS-73 disturbance levels.....	37-632
Figure 13.	Nominal STS-73 disturbance levels.....	37-632
Figure 14.	Nominal STS-73 disturbance levels.....	37-633
Figure 15.	Nominal STS-73 disturbance levels.....	37-633
Figure 16.	Glovebox nominal.	37-634
Figure 17.	Glovebox nominal.	37-634
Figure 18.	Glovebox nominal.	37-635
Figure 19.	Glovebox nominal.	37-635
Figure 20.	Glovebox nominal.	37-636
Figure 21.	Glovebox nominal.	37-636
Figure 22.	Glovebox nominal.	37-637
Figure 23.	Glovebox nominal.	37-637
Figure 24.	Glovebox nominal.	37-638
Figure 25.	Glovebox fan turned off in two steps.	37-638
Figure 26.	Glovebox fans turned off in two steps.	37-639
Figure 27.	Glovebox fan turning off: frequencies around 12.5 Hz subtracted.	37-639
Figure 28.	Worst case RMS Glovebox disturbance.	37-640
Figure 29.	Other Glovebox fan activity.	37-640
Figure 30.	Other Glovebox fan activity.	37-641
Figure 31.	Other Glovebox fan activity.	37-641

Figure 32.	Other Glovebox fan activity.	37-642
Figure 33.	Payload bay door opening.	37-642
Figure 34.	Payload bay door opening (0-5 Hz spectrum).	37-643
Figure 35.	Payload bay door opening.	37-643
Figure 36.	Payload bay door opening.	37-644
Figure 37.	Payload bay door opening.	37-644
Figure 38.	Payload bay door opening.	37-645
Figure 39.	Payload bay door opening.	37-645
Figure 40.	Payload bay door opening.	37-646
Figure 41.	Payload bay door opening.	37-646
Figure 42.	Payload bay door opening.	37-647
Figure 43.	Disturbance of unknown origin.	37-647

EXPERIMENT XXXVIII:

Figure 1.	Astronaut Fred Leslie operating STABLE on USML-2/STS-73.	38-660
Figure 2.	The isolated platform and its experiment payload float above the non-isolated base.	38-661
Figure 3.	The SMIDEX locker for STABLE on USML-2. Inside can be seen the webbed isolated platform before installation of the science experiment CHUCK.	38-661
Figure 4.	Comparison of acceleration time histories off and on the isolated platform.	38-662
Figure 5.	A comparison of acceleration probability densities (histograms) illustrates the frequencies of occurrence of different acceleration levels.	38-662
Figure 6.	Comparison of probabilities of exceedence.	38-663
Figure 7.	Color spectrograms for the three orthogonal accelerations measured on the locker backplate over a 3-hour period.	38-664

Figure 8.	Color spectrograms for the three vertical accelerations measured on the platform over a 3-hour period.	38-665
Figure 9.	Color spectrogram for the vertical acceleration measured on the locker backplate over a 22-minute period.	38-666
Figure 10.	Color spectrogram for a vertical acceleration measured on the isolated platform over a 22-minute period.	38-667
Figure 11.	Representative power spectral density plot.	38-668
Figure 12.	Comparison with <i>ISS</i> requirements and theoretical noise levels.	38-669
Figure 13.	Degree of coherence between vertical acceleration measurements off and on the platform.	38-670
Figure 14.	Preliminary estimate of attenuation.	38-670
Figure 15.	Better estimate of attenuation, using only well-correlated data.	38-671
Figure 16.	Typical time history of the platform displacement.	38-672
Figure 17.	Typical time history of displacement and rotation at center of mass.	38-673

LIST OF TABLES

Table	Title	Page
EXPERIMENT XVI:		
Table 1.	Analysis of η values ($^{\circ}$) for the apocrustacyanin C ₁ crystals measured.	16-385
Table 2.	Mosaicity volume ellipsoid parameters for both apocrustacyanin C ₁ and lysozyme crystals.	16-385
EXPERIMENT XIX:		
Table 1.	Hen egg white lysozyme (<i>Gallus Gallus</i>).	19-409
Table 2.	List of international laboratories involved in crystallographic lysozyme studies.	19-410
Table 3.	Crystallization conditions (T for triclinic and M for monoclinic).	19-410
EXPERIMENT XXI:		
Table 1.	Number and size of space- and Earth-grown crystals in APCF dialysis reactors.	21-425
Table 2.	Crystal mosaicities estimated from Laue spot sizes.	21-426
EXPERIMENT XXIII:		
Table 1.	Content of APCF reactors.	23-442
Table 2.	Number and size of space- and Earth-grown crystals in APCF dialysis reactors.	23-445
Table 3.	Mosaicity characteristic of ground- and space-grown thaumatin crystals.	23-447
EXPERIMENT XXVII:		
Table 1.	An experimental overview.	27-472
EXPERIMENT XXXIV:		
Table 1.	Data on CDOT samples (het.xtal \geq heterogeneously crystallized).	34-554

EXPERIMENT XXXV:

Table 1.	Grain type, size, and quantity in USML experiments.	35-582
----------	--	--------

EXPERIMENT XXXVI:

Table 1.	SAMS configuration for USML-2.	36-596
----------	-------------------------------------	--------

EXPERIMENT XXXVII:

Table 1.	Channel characteristics.	37-618
----------	-------------------------------	--------

Table 2.	Nominal RMS acceleration values, medium channel (all values in g).	37-622
----------	---	--------

Table 3.	Glovebox fans, RMS values acceleration, medium channel (all values in g).	37-623
----------	--	--------

Table 4.	Payload bay door movement, highest peak-to-peak acceleration levels, medium channel (all values in g).	37-624
----------	---	--------

AUTHOR INDEX

Betzel, C. 15-371

Bijvoet, J.A. 37-615

Boggon, T.J. 16-381

Broutin, I. 19-407

Carotenuto, L. 29-481

Cassetta, A. 16-381

Chaikin, P.M. 33-539,34-551

Chayen, N.E. 16-381

Concus, P. 30-489

Day, J. 23-441

de Grip, W.J. 17-399

Declercq, J.-P. 18-403

Dietrich, D.L. 32-525

Dryer, F.L. 32-525

Ducruix, A.F. 19-407

Edberg, D.L. 38-651

Erdmann, V.A. 20-417

Evrard, C. 18-403

Finn, R. 30-489

Freund, F. 35-579

Freund, M. 35-579

Fromme, P. 24-457

Gallagher, D.T.	25-461
Giegé, R.	21-423,23-441
Gilliland, G.	25-461
Gordon, E.J.	16-381
Greenwood, A.	23-441
Haggard, J.B.	32-525
Hakimzadeh, R.	36-595
Hansen, H.A.S.	28-477
Helliwell, J.R.	16-381
Hölzer, K.	16-381
Kamotani, Y.X.	31-509
Koszelak, S.N.	23-441
Li, M.	33-539
Lorber, B.	21-423,23-441
Maes, D.	27-471
Mainfroid, V.	22-433
Marino, M.	29-481
Marshall, J.R.	35-579
Martial, J.A.	22-433
Mazzarella, L.	29-481
McPherson, A.	23-441
Meyer, W.V.	33-539,34-551
Nayagam, M.V.	32.525
Nerren, P.D.	37-615
Ng, J.D.	21-423,23-441

Nurre, G.S.	38-651
Ostrach, S.X.	31-509
Ottewill, R.H.	33-539
Perbandt, M.	15-371
Pline, A.D.	31-509
Raia, C.A.	29-481
Riès-Kautt, M.	19-407
Rogers, R.	33-539,34-551
Rossi, M.	29-481
Rothärmel, T.	15-371
Russel, W.B.	33-539,34-551
Saenger, W.	24-457
Sauke, T.B.	35-579
Schroer, K.	16-381
Shaw, B.D.	32-525
Sica, F.	29-48
Sjölin, L.	25-461
Snell, E.H.	16-381
Sorrentino, G.	29-481
Thi, M.H.D.	27-471
Tordova, M.	25-461
Vasques, G.	25-461
Wagner, G.	15-371
Weber, W.	26-467
Weckert, E.	16-381

Weislogel, M.M.	30-489
Williams, F.A.	32-525
Wyns, L.	27-471
Yonath, A.	28-477
Zagalsky, P.F.	16-381
Zagari, A.	29-481
Zhu, J.	33-539

ACRONYMS

3-DMA	3-Dimensional Microgravity Accelerometer
APCF	Advanced Protein Crystallization Facility
ARC	NASA Ames Research Center [Moffett Field, CA]
ASC	Astroculture
BNL	Brookhaven National Laboratory [Brookhaven, NY]
BSA	Bovine Serum Albumin
CARB	Center for Advanced Research in Biotechnology [Rockville, MD]
CCD	Charge-Coupled Device
CDOT	Colloidal Disorder-Order Transition
CENG	Centre d'Etudes Nuclaires National de Grenoble [Grenoble, France]
CFD	Computational Fluid Dynamics
CGBA	Commercial Generic Bioprocessing Apparatus
CGF	Crystal Growth Furnace
CMC	Center for Macromolecular Crystallography [UAB]
CMDS	Consortium for Materials Development in Space [UAH]
CMMR	Center for Microgravity and Materials Research [UAH]
CNES	Centre Nationale d'Études Spatiales [“National Center for Space Studies,” French Space Agency]
CNRS	Centre National de la Recherche Scientifique [France]
CPCG	Commercial Protein Crystal Growth
CRIM	Commercial Refrigerator/Incubator Module
CSC	Center for Space Commercialization
CSPD	Cross Power Spectral Density
CuK α_1	Copper K α_1 radiation
CVT	Chemical Vapor Transport
DARA	Deutsche Agentur für Raumfahrtangelegenheiten [“German Agency for Space Affairs,” German Space Agency]
DCRC	Double Crystal Rocking Curve
DDM	Drop Dynamics Module

DESY	Deutsches Elektronen-Synchrotron [Hamburg, Germany]
DLR	Deutsche Forshungs-und Versuchsanstait für Luft-und Raumfahrt [German Aerospace Research Establishment, used to be “DFVLR”]
DLS	Dynamic Light Scattering
DPM	Drop Physics Module
EDX	Energy Dispersive X-ray Analysis
EMBL	European Molecular Biology Laboratory [DESY, Hamburg, Germany]
EPD	Etch Pit Density
ESA	European Space Agency
ESTEC	European Space Research and Techology Center
FCC	Fluidized Catalytic Cracking
FO	Functional Objective
FPA	Fluids Processing Apparatus
FSDC	Fiber-Supported Droplet Combustion
FTIR	Fourier Transform Infra-Red
FWHM	Full-Width Half-Maximum
GBX	Glovebox
GBX-ZCG	Zeolite Glovebox Experiment
GCEL	Ground Control Experiments Laboratory [NASA MSFC]
Ge	Germanium
GFFC	Geophysical Fluid Flow Cell
HgCdTe	Mercury Cadmium Telluride
HgI ₂	Mercuric Iodide
HI-PAC	High Packed Digital Television
ICE	Interface Configuration Experiment
IML-1	First International Microgravity Laboratory [STS-42 Shuttle mission, launched in January 1992]
IML-2	Second International Microgravity Laboratory [STS-65 Shuttle mission, launched in July 1994]
IR	Infra Red
ISOVPE	Isothermal Vapor Phase Epitaxy
JPL	Jet Propulsion Laboratory [Pasadena, CA, managed by the California Institute of Technology]

JSC	NASA Johnson Space Center [Houston, TX]
KSC	NASA Kennedy Space Center [Cape Canaveral, FL]
LaRC	NASA Langley Research Center [Hampton, VA]
LeRC	NASA Lewis Research Center [Cleveland, OH]
LMS	Life and Microgravity Spacelab [STS-78 Shuttle mission, launched in June 1996]
LPE	Liquid-Phase Epitaxy
MAWS	Microgravity Acceleration Workstation
MBE	Molecular Beam Epitaxy
MET	Mission Elapsed Time
MOCVD	Molecular Chemical Vapor Disposition
MPESS	Mission Peculiar Experiment Support Structure [Shuttle]
MSAD	Microgravity Science and Applications Division [NASA MSFC; also used to be the acronym for an OLMSA division at NASA Headquarters before name was changed to "Microgravity Research Division" (still Code UG)]
MSD	Microgravity Science Division [NASA LeRC]
MSFC	NASA Marshall Space Flight Center [Huntsville, AL]
NASA	National Aeronautics and Space Administration
NIST	National Institute for Standards and Technology [Boulder, CO]
NSLS	National Synchrotron Light Source
NRC	National Research Council
OARE	Orbital Acceleration Research Experiment
OTFE	Oscillatory Thermocapillary Flow Experiment
PCF	Protein Crystallization Facility
PCGG	Protein Crystal Growth Glovebox
PDE	Particle Dispersion Experiment
PI	Principal Investigator
PIMS	Principal Investigator Microgravity Services [NASA LeRC]
PLP	Precision Lattice Parameter
POCC	Payload Operations and Control Center [NASA MSFC]
PR	Photoreflectance
PSD	Particle Size Distribution
PSD	Power Spectral Density

RPI	Rensselaer Polytechnic Institute [Troy, NY]
SACA	Sample/Ampoule Cartridge Assembly
SAMS	Space Acceleration Measurement System
SEM	Scanning Electron Microscope
SMBT	Synchrotron Monochromatic Beam Topography
SPCG	Single-locker Protein Crystal Growth
STABLE	Suppression of Transient Acceleration By Levitation Evaluation
STDCE	Surface Tension Driven Convection Experiment
STES	Single-locker Thermal Enclosure System
STS	Space Transportation System [Shuttle/external tank/solid rocket booster system, also a Shuttle mission designation]
SWBT	Synchrotron White Beam Topography
TBE	Teledyne Brown Engineering
TCS	Triple Crystal Spectroscopy
TEA	Triethanolamine
TEM	Transmission Electron Microscope
UAB	University of Alabama at Birmingham
UAH	University of Alabama in Huntsville
USML-1	First United States Microgravity Laboratory [STS-50 Shuttle mission, launched in June 1992]
USML-2	Second United States Microgravity Laboratory [STS-73 Shuttle mission, launched in October 1995]
VDA	Vapor Diffusion Apparatus
WPI	Worcester Polytechnic Institute [Worcester, MA]
XPD	X-ray Power Diffraction
ZCGG	Zeolite Crystal Growth Glovebox
Zn:CdTe	Zinc Alloyed Cadmium Telluride

KEY WORD INDEX

A

a/b-barrel fold	433
a/b-barrel protein	433
absolute acceleration.....	617
acceleration environment.....	595
Acceleration Power Spectral Densities (PSDs)	655
accelerometer systems	595
accretionary processes	580
Ackerson and Schatzel theory	553
active vibration isolation system	651
Advanced Protein Crystallization Facility.....	441
aeolian activity	579
aerodynamic drag	596
agarose gel	483
aggregate population appears instantly	584
aggregated "volcanic hail"	586
Aggregates	583
aggregation	579
Alcohol Dehydrogenase	479, 481
amphiphilic photochromic retinal protein	371
aqueous ethanol solution, 50 percent by volume	494
artificial proteins	433
aspartyl-tRNA synthetase	423
aspect ratio	509, 511
atmospheric dust pall	580
atomic force microscopy	448
attenuation of the ambient environmental vibration	652
Attitude Control	597
attraction and cohesion mechanisms	584

B

bacteriophage lambda lysozyme	403
bacteriorhodopsin	371
balk-shaped crystals	371
batch	442
Benzamidine	372
Bragg peaks	540
Bragg spots	541
Bragg streaks	541

C

canonical proboscis.....	489
Canonical Proboscis Container.....	491
catastrophic gravitational collapse.....	579
CcdB	471
cellular proteins	417
chemical potential	556, 564
chicken egg white lysozyme	407
Classical hard spheres	539
coexistence region of the phase diagram	555
collapse of particulate clouds	587
collapsing nebulae	580
colloidal crystals	539, 552
Colloidal Disorder-Order Transition	553
colloidal hard spheres	551
combustion of fuel droplets	531
complete-mixing analysis	527
Configuration Experiment	489
configurational entropy for spheres	551
contact angle	489, 496
contact angle hysteresis	496
container aspect (depth/radius) ratio	509
container geometry	496
container shape	489
convective flows	482
convective mixing	447
convective turbulence	372
Coulombic effects	580
Coulombic mechanisms	585
Crew Activity	597
crew exercise	652
critical contact angle	489
critical nucleus size	557
critical value of contact angle	490
Crystal close packing	541
crystal size	441
cyanobacteria	457

D

decalin	553
dendrites	540
dendritic arms	540
dendritic crystallites	551, 553, 555
dendritic crystals	554
dendritic growth	540

depletion zone	552
depletion zones	447
dialysis	441, 442
dialysis liquid diffusion reactors	423
diffraction resolution limit	441
diffusion	447
diffusion coefficient	528
diffusion limited	557
diffusion-limited growth	552
dipole-dipole interactions	579
discontinuous and nearly discontinuous behavior	497
discrete defects	447
dislocations	447
disorder-order transition	551
disruption	529
dissolution of the cell walls	403
DNA-topoisomerase II complexes	471
Double Proboscis Container	492
Downlink in true real time of acceleration data	617
Droplet Combustion	525, 526
droplet-combustion theory	526
dynamic light scattering	371

E

effect of aspect ratio	509
electrical conductor (copper grains)	582
electrostatic aggregation	579, 586, 587
Electrostatic charges	580
electrostatic charging	580
enzymes	461
Epidermal Growth Factor (EGF) Receptor	467
extinction of the burning	527

F

face-centered cubic	539
face-centered-cubic structure	552
filamentary aggregates	579
Filamentary Structures	583
filaments	585
fluid management	490
forced convection	530
Forced flow	527
“fractal” surface morphologies	585
free interface diffusion	442
free surface deformation	511

Frossling-type of formula	530
Full widths at half maxima	446

G

Giant “clod-like” aggregate	592
giant clod-like structures	585
Giant Self-Sustaining Aggregates	584
Glovebox Fan Disturbances	623
Glovebox Fan Operations	598
Glutathione S-Transferase (GST)	461
gradient diffusion coefficient	556
gradients in volume fraction	552
grain-to-grain attraction	583
gravitational length	555
gravitational stresses	540
gravity	540
gravity gradient (GG) effects	596
growth	557

H

hanging droplet reactors	424
hard sphere colloidal crystals	541
hard sphere crystals	552
hard-sphere	551
heptane-hexadecane mixtures	525, 529
heterogeneous nonconductor (pyroclastics)	582
Hexagonal Close Packed	541
hexagonal close packing	552
hexagonal close-packed planes	539
hexagonal symmetry	552
higher frequency data	598
homogeneous, nonconducting material (quartz)	582
hydrodynamics	556
hydrophilic interactions	371
Hysteresis	496, 497

I

I/σ ratio	446, 448
index of refraction	540
input disturbances	496
interfacial tension	565
interfacial velocity	566
interstellar dust nebulae	580
intrinsic crystal order	444
intrinsic growth rate	565
invertable accelerometers	615

Invertible Accelerometer System	617
ion-spray spectroscopy	407
K	
Kirkwood-Alder transition	551
L	
Laue diffraction patterns	424
length of time	496
Lewis numbers	528
light scattering	553
limit of resolution	446
linear stability	553
Linear Stability Analysis	560
liquid phase mixing	527
liquid-liquid diffusion	441
long-range defect structure	448
low diffusivity	447
Lysozyme	407
M	
macromolecules	417
Marangoni instability	527
Marangoni number	511
mechanical equilibrium	556
membrane protein	467
membrane proteins	399
metastable state	494
meteorite impact	579
Methanol	525, 527
methanol-dodecanol mixtures	525, 529
methanol-water mixtures	525, 528
micelles	372
microdialysis	417
microgravity environment	447
mix-melting	541
molecular crystal	551
molecular dynamics calculations	551
monoclinic form	411
monomeric enzyme of 129 amino acids	408
monomeric protein	444
Mosaic spread	407, 448
mosaicitics	444
mosaicity	407, 412, 441
mosaicity profiles	446
mosaicity studies	426

multiparametric aspect	407
N	
N-Octyl β -D-Glucopyranoside	372
Nominal Disturbance Levels	622
nonequilibrium crystal growth	542
nonlinear growth	556
normal routines	652
nucleophilic addition	461
O	
octarellins	433
onset of oscillations	511
Orbital Acceleration Research Experiment	595
Orbiter Attitude	596
orbiter body coordinate system	596
oscillation frequencies (f)	513
oscillation ranges	444
oscillations	509
oscillatory flow	509
Oscillatory thermocapillary flow	509
P	
Particle Dispersion Experiment	579
Payload Bay Door Motion	598
Payload Bay Door Movements	623
payload-bay door opening	652
Peclet number	541, 555
photoelectric and thermionic effects	580
photosystem I and II	457
planetary ring systems	580
polarization effects	584
Polyethylene glycol	372
polymer (methyl methacrylate)	552
Polymorphic crystal forms	412
Prandtl number	511
Probabilities of Exceedence for Acceleration Levels	654
Probability Densities (Histograms)	654
prokaryotic ribosomes	477
protein	471
protoplanetary dust disks	579
pseudosteady	557
pseudosteady growth	559
pure RHCP crystals	541

Q

quasi-stationary disturbances	615
quasi-steady microgravity environment	596

R

radiant energy loss	528
Random Hexagonal Close Packed	541
random stacking of hexagonal planes	555
Rapid Growth	559
Real-time microgravity data	624
real-time quasi-steady acceleration measurements	598
relative heater size	511
resolution	407
resolution limit	448
Ribonucleic acids (RNA's)	417
ribosomal 5S RNA's	417
Ribosomal Particles	477
ribosome	477
RMS acceleration environment	658
rocking widths	444
rod photoreceptor cell	399
rotational motion	596

S

S-parameter	511
sedimentation	372, 482, 540, 541
shear modulus measurements	553
silicon-carbide fiber	526
six-degrees-of-freedom isolation by "floating"	651
sleep	652
Slow Growth	558
sooty flames	530
Space Acceleration Measurements System	595
spherical crystallites	556
stability analysis	562
staged combustion	529
standard protein	407
"static" configuration	494
static light scattering	540
static shear modulus	555
Stokes settling velocity	541
Stokes-Einstein diffusion coefficient	541
supersaturation	447, 552
Suppression of Transient Events by Levitation	651
surface-plus-gravitational mechanical energy	490

synchrotron	407
T	
Telemetry in real time	621
tetralin	553
thaumatin	423, 441
thermal diffusivity	528
thermal motion	540
thermocapillary flow	511
thermodynamic and transport coefficients	556
thermophilic cyanobacterium	457
Three-Dimensional Microgravity Accelerometer	615
thruster firings	652
transient and vibratory components	596
Triclinic and monoclinic crystals of lysozyme	407
triclinic crystals	411
triosephosphate isomerasers	433
true real-time downlink	615
twinning	483
twinning phenomenon	483
twinning problem	483
two-dimensional ordered sheets	541
tyrosine kinase receptors	467
V	
van der Waals forces	553
vapor diffusion	442, 477
visual pigment rhodopsin	399
volcanic eruption plumes	579
volcanism	579
volume fraction	540
W	
Water Dump Operations	598
water dumps	652
water-rich layer	527
Wedge Container	491
Wilson-Frenkel law	557
Wilson-Frenkel model	552
X	
x-ray crystallography	417
Y	
Young-Laplace-Gauss (Y-L-G) formulation	490

MISSION INFORMATION

Mission Designation: STS-73 (72nd Shuttle mission)
Orbiter: *Columbia* (18th flight for this Shuttle)
Orbit Inclination: 39.0 degrees
Orbit Altitude: 150 nautical miles (172 statute miles)
Number of Orbits: 255 (6.6 million miles)
Major Payload: USML-2
Launch: October 20, 1995 @ 9:53 a.m. EDT
Landing: November 5, 1995 @ 6:45 a.m. EST at KSC
Mission Duration: 15 days, 21 hours, 53 minutes, 16 seconds (15/21:53:16)

Crew:
Commander: Commander Kenneth D. Bowersox, U.S. Navy
Pilot: Commander Kent V. Rominger, U.S. Navy
Payload Commander: Kathryn C. Thornton, Ph.D.
Mission Specialist: Major Catherine G. Coleman, Ph.D., U.S. Air Force
Mission Specialist: Commander Michael E. Lopez-Alegria, U.S. Navy
Payload Specialist: Fred W. Leslie, Ph.D., NASA Marshall Space Flight Center
Payload Specialist: Albert Sacco, Jr., Ph.D., Worcester Polytechnic Institute
Alt. Payload Specialist: David H. Matthiesen, Ph.D., Case Western Reserve University
Alt. Payload Specialist: R. Glynn Holt, Ph.D., Yale University

1. INTRODUCTION

1.1 Overview

The Second United States Microgravity Laboratory (USML-2) Space Shuttle mission was launched October 20, 1995, and landed November 5, 1995. The mission lasted 15 days and the Shuttle crew performed extensive microgravity science research during that time. The principal investigators for the mission submitted science reports of their research findings to the mission scientist for USML-2, and those reports were compiled into the USML-2 One Year Report. The purpose of the USML-2 One Year Report is to inform the microgravity science community and the public of the results of the experiments flown on the Shuttle mission.

The USML-2 One Year Report represents the culmination of many years of sustained effort on the part of the investigators, mission management, and support personnel, and is intended not only for the scientific community, but also for general public awareness and education. This mission gave the microgravity science community outstanding research opportunities not only to report and verify results obtained in previous flights, but to perform new experiments which contributed substantially and uniquely to the technological and commercial knowledge of the United States and its international partners. The results obtained and the lessons learned from this and future missions will lead us into a new era of microgravity research, to the Space Station and beyond.

The launch of the Space Shuttle *Columbia* with the USML-2 payload continued the legacy of one of NASA's most successful scientific mission series. Using the knowledge gained from the USML-1 mission, scientists were able to prepare and improve their investigations and experiments by enhancing procedures, refining operations, modifying hardware, and expanding methods for gathering data. The seven-member Shuttle crew performed the USML-2 experiments around the clock in order to maximize the science on orbit and interacted with scientists on the ground for a perfect example of interactive science in a unique laboratory environment.

The USML-2 mission was dedicated entirely to microgravity research and included 37 investigations in materials science, fluid dynamics, combustion, biotechnology, and technology demonstrations supported by 11 facilities and 3 acceleration measurement systems. Along with investigations that previously flew on USML-1, several new experiment facilities flew on USML-2. The Advanced Protein Crystallization Facility (APCF) was the first facility to use three methods of protein crystal growth: liquid-liquid diffusion, dialysis, and vapor diffusion. The High Packed Digital Television (HI-PAC) Technical Demonstration gave scientists on Earth the ability to view multiple channels of real-time video and to monitor and change experiment parameters as needed. This improved the quality and quantity of downlinked data, thus enhancing science returns. Ground-to-Air Television was first used on the USML-2 mission and allowed the scientists on the ground and the Shuttle crew to talk with and see each other as they discussed science operations. The Geophysical Fluid Flow Cell (GFFC) experiment, which studied how fluids move

in microgravity, first flew on Spacelab-3 in 1985 and was extensively refurbished for this mission. The facilities that measured the microgravity environment added to the success of the mission by providing a complete picture of the Shuttle's acceleration environment and disturbances. The Orbital Acceleration Research Experiment (OARE) provided real-time acceleration data to the science teams. The Microgravity Acceleration Workstation (MAWS) operated closely with OARE, comparing the environment models produced by MAWS with the actual data gathered by OARE. Two other instruments, the Space Acceleration Measurement System (SAMS) and the Three-Dimensional Microgravity Accelerometer (3DMA), collected data throughout the mission. The data were then provided to the experimenters.

The Spacelab Glovebox (GBX) provided by the European Space Agency (ESA) offered investigators the capability to carry out experiments, test science procedures, and develop new technologies in microgravity. It enabled crew members to handle, transfer, and otherwise manipulate experiment hardware and materials in ways that would be impractical in the open Spacelab. In addition, the facility allowed a visual record of experiment operations by means of video and photographic systems. Many investigations benefited from increased crew involvement and video downlink. There were seven separate USML-2 investigations carried out in the Glovebox facility: two of these were in the materials science discipline, two were solution crystal growth investigations, two studied fluid dynamics, and one was a combustion investigation. Details on each are to be found elsewhere in this publication.

The investigations performed on USML-2 brought together a large number of researchers from government, academia, and private industry. Combining the strengths of these communities allowed for more extensive ground-based research, advanced research techniques, improved microgravity experimentation, and a wider distribution of the knowledge gained in the process.

Among the mission highlights and successes:

- The processing of cadmium zinc telluride in the Crystal Growth Furnace (CGF) demonstrated that crystals grown in space without touching the walls of their containers are of markedly higher quality than Earth-grown crystals. This is expected to promote the use of these crystals in critical electronic applications such as radiation detectors, sensors, etc.
- The GFFC experiment sought to better understand the flows in the oceans and atmospheres of planets and stars. The study showed "banded" rotational patterns of flows like those seen in the atmosphere of Jupiter. These observations are expected to be of great importance in understanding weather patterns and climatic conditions on Earth.
- The protein crystal growth experiment was successful in obtaining antithrombin crystals. This protein, which controls blood coagulation in human plasma, is very difficult to grow in Earth-based laboratories. Its successful growth in space made it possible to further define its molecular model and understand how it works in the human body. This has important implications for medicine.
- In the Drop Physics Module (DPM), the influence of surfactants was examined. It was found that surfactants can change the hydrodynamics of droplets. The findings will lead to new and improved technologies in manufacturing cosmetics and synthetic drugs, in the recovery of oil, and in environmental clean-ups. The behavior of liquid drops was also studied in this facility. It was found that

drops subjected to sound waves showed unusual rotation and oscillation patterns. Findings from this study promise improved technologies in the paint, pharmaceutical, and chemical processing industries and a better understanding of rain formation and weather patterns.

KEY USML-2 PERSONNEL

USML-2 Program Scientist: Mark Lee (NASA Headquarters)
USML-2 Mission Scientist: Marcus Vlasse (NASA Marshall Space Flight Center)
USML-2 Mission Manager: Paul Gilbert (NASA Marshall Space Flight Center)
USML-2 Payload Operations Director: Bob Little (NASA Marshall Space Flight Center)
USML-2 Project Scientist for APCF: Gottfried Wagner (University of Giessen, Germany)
USML-2 Project Scientist for CGBA: Louis Stodieck (University of Colorado at Boulder)
USML-2 Project Scientist for CGF: Martin Volz (NASA Marshall Space Flight Center)
USML-2 Project Scientist for CPCG: Karen Moore (University of Alabama at Birmingham)
USML-2 Project Scientist for DPM: Arvid Croonquist (Jet Propulsion Laboratory)
USML-2 Project Scientist for GBX: Don Reiss (NASA Marshall Space Flight Center)
USML-2 Project Scientist for GFFC: Fred Leslie (NASA Marshall Space Flight Center)
USML-2 Project Scientist for PIMS: Roshanak Hakimzadeh (NASA Lewis Research Center)
USML-2 Project Scientist for STDCE: Alex Pline (NASA Lewis Research Center)

EXPERIMENT XV.

**PROTEIN CRYSTAL GROWTH: LIGHT-DRIVEN CHARGE TRANSLOCATION
THROUGH BACTERIORHODOPSIN**

ACKNOWLEDGMENTS

Flight opportunities provided through DLR/DARA and ESA/ESTEC, and financial support of the experiments in the laboratory through DARA (FKZ 50 WB 91635; 50 WB 9414), are thankfully acknowledged. Michael Degenhardt is given special thanks for his support in the DLS measurements.

PROTEIN CRYSTAL GROWTH: LIGHT-DRIVEN CHARGE TRANSLOCATION THROUGH BACTERIORHODOPSIN

Torsten Rothärmel

Gottfried Wagner

Justus-Liebig-University

Department of Biology

Senckenbergstrasse 17

35390 Giessen, Germany

Phone: +49-641-99-35140 /35142

FAX: +49-641-99-35119

E-mail: Torsten.Rothaermel@bio.uni-giessen.de; Gottfried.Wagner@bio.uni-giessen.de

Christian Betzel

Markus Perbandt

Institut für Physiologische Chemie

c/o DESY; Geb. 22a

Notkestrasse 85

22603 Hamburg, Germany

Phone: +49-40-8998-4744 /4745

FAX: +49-40-8998-4747

E-mail: Betzel@EMBL-Hamburg.de; Markus@unisgi1.desy.de

ABSTRACT

The bacteriorhodopsin (BR) crystal growth experiment in the Second United States Microgravity Laboratory was done in order to stabilize the weak hydrophilic interactions, which are critical for the single BR filaments to pack together and form crystals close to the micellar consolution boundary.

In diagnostic analysis of growth conditions relevant to microgravity, micelles of three typical sizes were determined on Earth through dynamic light scattering as a function of the detergent cocktails used. Consistently, the BR crystal growth experiments have resulted in three different habits of BR crystals, namely 1) needle-shaped, 2) cubic-shaped, and 3) balk-shaped crystals of excellent morphology, large size (up to 1.35 mm in length) and improved diffraction power (resolution limit of up to 3.8 Å).

1. INTRODUCTION

BR, a small amphiphilic photochromic retinal protein, has small surface protrusions emerging out of the cell membrane of *Halobacterium halobium*.¹ After membrane solubilization through detergent, BR will be embedded in micelles.^{2,3} Detergent-solubilized BR molecules tend to form filamentous crystals like micelles do in the hexagonal phase.⁴ The contacts that cause the BR filaments to pack together are

hydrophilic interactions between the loop regions of protruding BR molecules in aligned filaments. The hydrophilic interactions are weak and easily disturbed, resulting in considerable disorder in the BR crystalline array in the presence of convective turbulence and sedimentation.⁵

Dynamic light scattering enables determination of the size of occurring micelles. Particles in a liquid show Brownian molecular movement because of the thermodynamic movement of the liquid molecules. Thus monochromatic light is scattered by the particles and the shift of the frequency relative to the primary optical frequency can be measured. The three different micelle sizes received in detergent solutions after BR solubilization are compatible with the three different habits of BR crystals, grown in the microgravity of the USML-2 experiment and as ground control.

2. RESULTS

BR forms typical micelles in detergent solution with a substantial part of the interaction defined by the detergent coat as if the micelle would be protein-free (mixed micelle). Micelle radii were determined through dynamic light scattering⁶ using the DLS-system of Dierks & Partner, Systemtechnik (Hamburg, Germany) and Protein Solutions (Charlottesville, VA, U.S.A.) respectively, and plotted in figure 1 as a function of detergent and additives in absence and presence of BR.

Micelle radii prior to solubilization of BR range from 20 nm for micelles of N-Octyl β -D-Glucopyranoside (OG) to 6 nm for the cocktail of OG, Benzamidine (B) plus Polyethylene glycol (PEG). The mixed micelle radii, after BR solubilization, extended more than 10 times. Disregarding this large increase in mixed-micelle radius upon dissolution of BR, the tendency of the radius as a function of the detergent cocktail used remained unchanged. The radius of the micelles with OG was reduced by the addition of PEG or Benzamidine, and enlarged by the addition of Europium (Eu).

Conditions favorable for the growth of cubic crystals showed the largest micelles measured. Needles occur if the protocol conditions show smaller micelle radii, and the micelle radii of the cocktail favorable for the growth of balk-shaped crystals are the smallest.

Consistent with the different micelle sizes observed through dynamic light scattering in the presence and absence of the additives Benzamidine, PEG, and Eu, respectively, three different habits of BR crystal growth were observed, namely needle-, cubic-, and balk-shaped crystals.

In the USML-2 microgravity experiment, the molecular rods of BR were tightly packed, as reported before,^{4,5} and the crystal morphology exhibited smooth surfaces and sharp edges of up to 1 mm in length. The needle-shaped crystals (fig. 2) increased under microgravity by the factor of 1.5 in length, compared to the ground control.

Upon variation of the crystallization protocol in microgravity, the experiment leads to the growth of cubic crystals (fig. 3), while the ground control produced crystals of the needle habit. Hypothetically, under microgravity conditions the altered crystal growth protocol of enlarged micelle size stimulated the transition of BR mixed micelles from columnar hexagonal needles to the cubic habit, and the cubic habit was stabilized. Multicrystalline needle clusters (fig. 4) and single needles were produced both on Earth and in microgravity upon slightly altering the protocol conditions in salt-, additive-, and/or protein-conditions.

Cross-reactive agents, such as Gly-Gly free base,⁷ tended to favor the conditions for growth of cubic crystals on Earth, but did not have a clear impact on cubic crystal formation under microgravity.

The experiments performed under microgravity and as ground control led to a new experiment protocol. We were able to crystallize a new type of BR crystal with the habit of balks and an extended growth perpendicular to the longitudinal balk axis. Single crystals grew up to a length of 1.35 mm and width of 120 μm . The good quality BR crystals, combined with excellent synchrotron facilities,⁸ allowed partial data collection to a resolution limit of up to 3.8 \AA (fig. 5).

CONCLUSIONS

Polyethylene glycol is described as having a long-term effect at relatively high salt concentrations by decreasing the net rate of misincorporation of protein molecules into the crystalline lattice, either directly, because the protein in solution is solvated in a different way, or indirectly, by facilitating the reorientation or dissolution of misincorporated molecules. It also might keep supersaturation at a point where formation of additional nuclei is relatively improbable and eliminates unwanted protein-protein interactions and so prevents premature termination of growth or excessive showering of small crystals, or both.⁹

Polyethylene glycol, combined with chosen BR mixed-micelle size and suppression of gravity-driven convection and sedimentation of BR in the process of crystallization, enabled the growth of tightly packed crystals with smooth surfaces and sharp edges of different habits.

The resolution limit of 3.8 \AA reached so far for the new balk-shaped BR crystals is unmatched for the triclinic space group of this protein. The progress encourages the future use of microgravity as a favourable environment of improved crystallogenesis of difficult membrane proteins such as BR.

REFERENCES

1. Oesterhelt, D.; Bräuchle, C.; and Hampp, N.: *Quart. Revs. Biophysics*, 24, 425–478, 1991.
2. Boden, N.: *Micellar liquid crystals*. M.W. Gelbart et al. (eds.): *Micelles, Membranes, Microemulsions and Monolayers*, Springer New York-Heidelberg-Berlin, 1994.
3. Tan, E.H.L.; and Birge, R.R.: *Biophys. J.*, 70, 2385–2395, 1996.
4. Wagner, G.: *ESA-Proc. Space Station Utilization*, SP-385, 235–238, Dec. 1996.
5. Wagner, G.: *ESA J.*, 18, 25–32, 1994.
6. Schmitz, K.S.: *Dynamic Light Scattering by Macromolecules*, Academic Press, Inc., 1990.
7. Cudney, B.; Patel, S.; Weisgraber, K.; Newhouse, Y.; and McPherson, A.: *Acta Cryst.*, D50, 414–423, 1994.
8. Wagner, G.; Rothärmel, T.; Perbandt, M.; and Ch. Betzel: *DESY Yearbook*, in press, 1996.
9. Ray, W.J., Jr.: *Proteins: Structure, Function, and Genetics*, 14, 300–308, 1992.

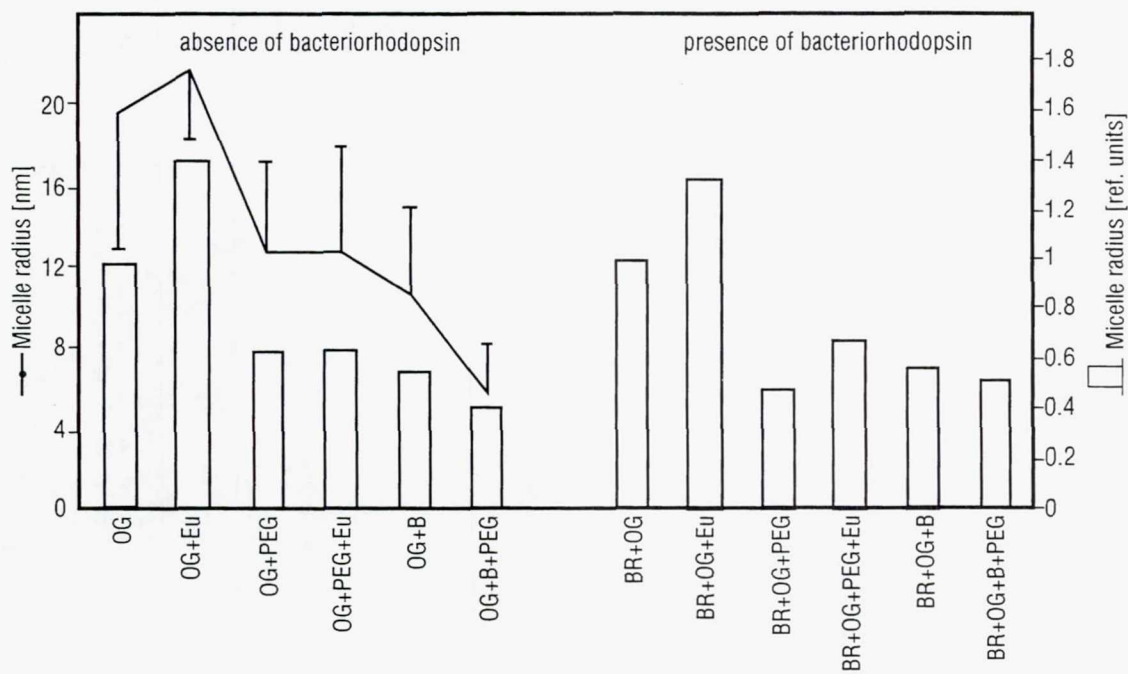


Figure 1. Micelle radius formed by the detergent N-octyl β -D-glucopyranoside (OG) in the experiment protocol and change in micelle size through the additives Europium (Eu), Polyethylene glycol (PEG), Benzamidine (B), and their combinations as shown in the abscissa in the absence and presence of bacteriorhodopsin (BR). The micelle size is indicated in absolute values with standard deviations (-♦-) and in relative units (histogram) from different series of experiments. The relative units given in the histogram are normalized to the micelle radius of OG in the experiment protocol. *Left side:* Both experimental set-ups (-♦-; histogram) used in the DLS analysis, showed a rise in value after the addition of Eu to OG and a steady decline with the smallest value measured for the cocktail of OG + B + PEG. *Right side:* Upon dissolution of BR, the level of micelle radius in absolute values as a function of the additives used increased more than ten times (data not shown). The pattern of the histogram, however, remained essentially the same (compare left to right side).



Figure 2. USML-2 Flight Experiment: Bacteriorhodopsin (BR) crystal in needle habit of about 500 μm in length. Here, the molecular rods of BR are closely packed together to form a crystal of compact morphology which resulted in sharp edges and smooth surfaces.



Figure 3. USML-2 Flight Experiment: Bacteriorhodopsin (BR) crystal in cubic shape with axes of 150 μm in length.

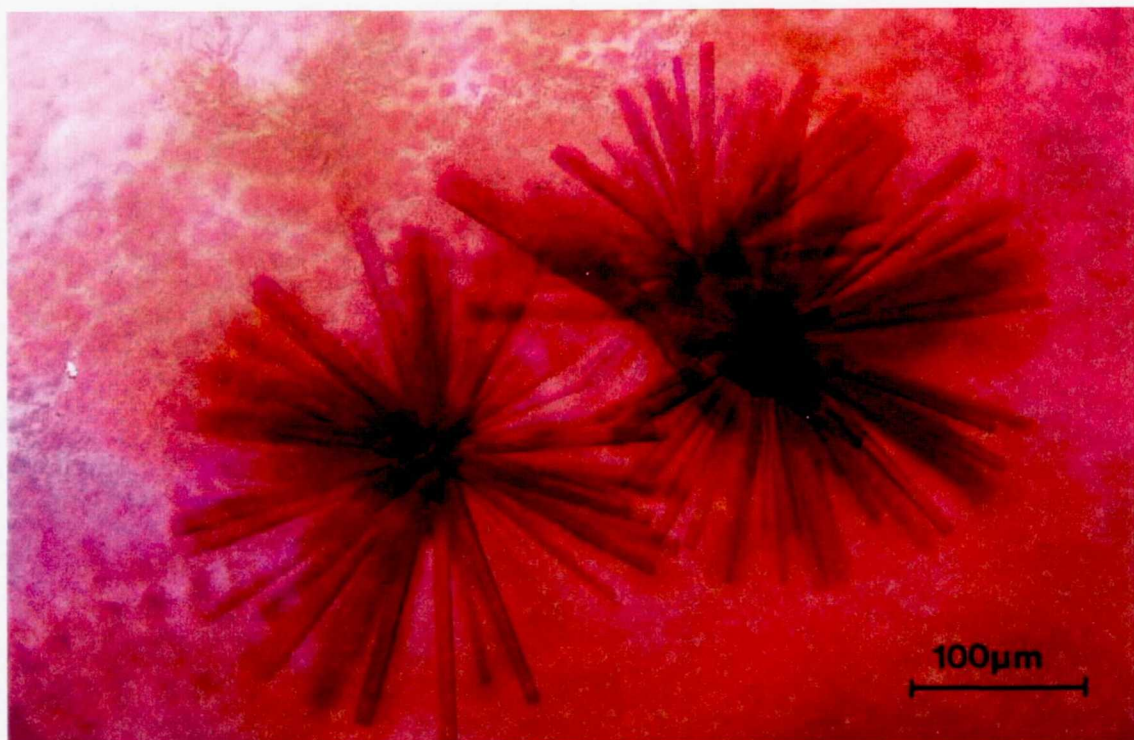


Figure 4. USML-2 Flight Experiment: Multicrystalline needle cluster of bacteriorhodopsin (BR) with a diameter of 300 μm . The cluster seems to consist of single needles which fall apart easily. The individual needles show similar sharp edges and smooth surfaces as shown in figure 2.

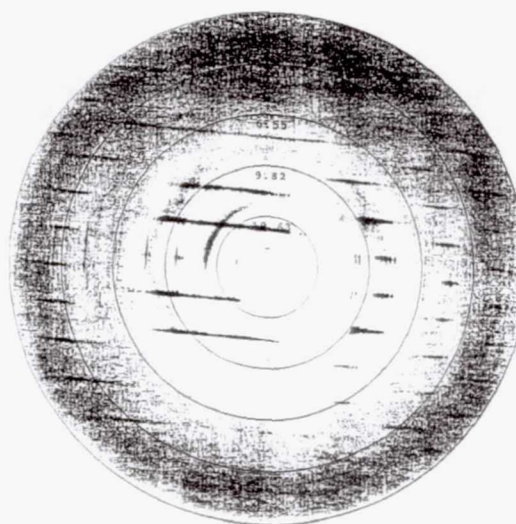


Figure 5. Oscillation diffraction pattern recorded at the synchrotron beam line X11; EMBL-outstation, Hamburg. The diffraction pattern of balk-shaped bacteriorhodopsin (BR) crystal shows resolution up to a limit of 3.8 \AA in the direction perpendicular to the purple membrane plane.

Page intentionally left blank

EXPERIMENT XVI.

**PARTIAL IMPROVEMENT OF CRYSTAL QUALITY FOR MICROGRAVITY-GROWN
APOCRUSTACYANIN C₁**

ACKNOWLEDGMENT

We would like to express our thanks to the Swiss-Norwegian CRG at the ESRF, Grenoble, for providing access to their beamline facilities, and in particular to Dr. Phil Pattison and his colleagues for their help. We are extremely grateful to ESA for flight opportunities and, in this particular study, for financing the beamtime at ESRF. Drs. H.U. Walter, H. Martinides, K. Fuhrmann, and O. Minster are thanked for their regular help and support. The Dornier and ESA staff are thanked for all their work in the development, support, and discussions with respect to APCF and PCDF apparatus. E.H. Snell and T.J. Boggon are grateful to the EPSRC and the University of Manchester, respectively, for studentship support. P.F. Zagalsky acknowledges support from the EEC commission (grant ERBSCI-CI 920813). A. Cassetta was an EU Host Institute Fellow in Manchester on leave from the CNR in Italy.

**PARTIAL IMPROVEMENT OF CRYSTAL QUALITY FOR MICROGRAVITY-GROWN
APOCRUSTACYANIN C₁***

E.H. Snell

A. Cassetta

J.R. Helliwell

T.J. Boggon

Chemistry Department

University of Manchester

M13 9PL, England

E-mail: john.helliwell@man.ac.uk

N.E. Chayen

Biophysics Section, The Blackett Laboratory

Imperial College of Science, Technology and Medicine

London SW7 2BZ, England

E. Weckert

K. Hölzer

K. Schroer

Institut für Kristallographie

University of Karlsruhe (TH)

Kaiserstrasse 12, Postfach 6980

D-76128 Karlsruhe, Germany

E.J. Gordon

Institut de Biologie Structurale

Laboratoire de Cristallographie Macromoleculaire

41 avenue des Martyrs

F-38027 Grenoble CEDEX, France

P.F. Zagalsky

Biochemistry Department, Royal Holloway

University of London, Egham

Surrey TW20 0EX, England

ABSTRACT

The protein apocrustacyanin C₁ has been crystallized by vapor diffusion in both microgravity (The Second United States Microgravity Laboratory (USML-2) mission) and on the ground. Rocking width measurements were made on the crystals at the ESRF Swiss-Norwegian beamline using a high-resolution

* This paper was previously published in *Acta Cryst.*, D53, 231–239, 1997.

Ψ -circle diffractometer from the University of Karlsruhe. Crystal perfection was then evaluated from comparison of the reflection rocking curves from a total of five crystals (three grown in microgravity and two Earth controls) and by plotting mosaicity versus reflection signal/noise. Comparison was then made with previous measurements of almost "perfect" lysozyme crystals grown aboard IML-2 and Spacehab-1 and reported by Snell et al.¹ Overall, the best diffraction-quality apocrustacyanin C₁ crystal was microgravity-grown, but one Earth-grown crystal was as good as one of the other microgravity-grown crystals. The remaining two crystals (one from microgravity and one from Earth) were poorer than the other three and of fairly equal quality. Crystal movement during growth in microgravity, resulting from the use of vapor-diffusion geometry, may be the cause of not realizing the "theoretical" limit of perfect protein crystal quality.

1. INTRODUCTION

Microgravity has been used as a crystallization environment for improving protein crystal quality through reduced sedimentation and convection effects. Growth in microgravity has been shown to reduce the mosaicity of lysozyme crystals with a resulting increase in the signal-to-noise ratio of reflection intensity data, thereby facilitating measurement of weaker high-resolution data.^{1,2} The mosaic spread, unlike resolution limit, is a crystal parameter which can be independent of the incident x-ray beam and detector setup and gives a direct indication of the geometric perfection of a crystal. It does, however, require a finely collimated beam and high-resolution diffractometer to avoid the beam effects smearing out the rocking width so as to analyze the reflection in detail.³

In the event of a reduction in mosaicity in the crystal, this should manifest in an enhancement of the signal-to-noise ratio of the reflection intensity measured, provided extinction is absent, and is particularly valuable for considering the optimization of the measurement of weak high-resolution protein diffraction data. In our previous report,¹ this was strongly manifest in favor of microgravity-grown crystals of lysozyme over Earth-grown controls on two separate missions measured by two different methods. Moreover, the microgravity-grown crystals were the most perfect protein crystals ever reported to date, very close to the theoretical limit, and thereby setting bounds on the size of diffraction apparatus that might usefully be considered (e.g., several meters for the crystal-to-detector distance, which in turn defines a maximum useful detector size for a given x-ray wavelength). In Snell et al.,¹ it was readily possible to find reflections at 1.2 Å by use of a 0.0002° angular step scan, with an instrument resolution function of 0.00195° on the ESRF Swiss-Norwegian bending magnet beamline. In contrast, with a 1° scan, Vaney, Maignan, Riès-Kautt, and Ducruix⁴ at the LURE synchrotron obtained a resolution limit of 1.4 Å for a microgravity-grown lysozyme crystal.

The purpose of this paper is to extend the comparisons of protein crystal quality to other protein cases. We report here the mosaicity measurements on apocrustacyanin C₁.

2. EXPERIMENTAL

2.1 Crystallization

The crystallization of the protein apocrustacyanin C₁, a subunit of the α -crustacyanin protein responsible for the blue coloration of the carapace of the lobster *Homarus gammoros*, has been described elsewhere.⁵ Apocrustacyanin C₁, molecular weight 20 kDa, crystallizes in space group *P*2₁2₁2₁, *a*=42.1, *b*=81.0, *c*=110.7 Å and $\alpha=\beta=\gamma=90^\circ$ with two subunits per asymmetric unit. For the experiment reported here, the protein solution (20 mg•ml⁻¹ in 0.1 *M* Tris-HCl, 1 mM EDTA pH 7.0) was mixed 1/1(*v/v*) with a reservoir solution (5 percent (*v/v*) 2-methyl-2,4-pentanediol (MPD), 1 mM EDTA, 0.1 *M* Tris-HCl pH 9.0 and 1.9 *M* ammonium sulfate) to form 50-μl drops.

The microgravity equipment for crystallization was the European Space Agency (ESA) Advanced Protein Crystallization Facility (APCF).^{6,7} The APCF is a modular system containing 48 reactors each allowing one of three modes of crystallization, namely dialysis, liquid-liquid (free interface), and vapor diffusion. The vapor-diffusion reactor used in this case consists of a reservoir formed by two porous, ultra-high molecular weight, polythene blocks (each holding 0.35 ml of solution) and protein solution held in a glass cylindrical tube which can be raised to activate crystallization. The APCF was flown on board the USML-2, STS-73, NASA Space Shuttle mission. Crystallization took place over a period of 14 days, 11 hours, 17 minutes (347 hours, 17 minutes) of microgravity time at a temperature of 273 ± 0.1 K. Ground controls were grown simultaneously with identical materials in identical apparatuses with temperature control also to ± 0.1 K.

2.2 Data Collection

Measurement of the rocking widths by monochromatic methods requires a synchrotron x-ray beam with very low divergence and small $\delta\lambda/\lambda$. This has to be combined with a small angular step-size diffractometer to fully probe the rocking width in detail. Data collection took place on station A of the joint Swiss-Norwegian beamline at the ESRF. The Swiss-Norwegian beamline has a Huber ψ -circle diffractometer. The primary role of this diffractometer is the direct determination of triplet phases.^{8,9} The instrument contains two circles (θ, ν) for the detector with axes perpendicular to each other and four circles for the crystal motion. The first crystal axis is parallel to the first detector axis ($\omega-2\theta$ relation). Perpendicular to the ω -axis, a second axis for the ψ rotation is installed. This ψ -axis bears an Eulerian cradle with motions χ and ϕ . Thus, an arbitrary scattering vector \mathbf{h} can be aligned with the ψ -axis and a ψ -scan (i.e., rotation around a reciprocal lattice vector for any hkl) performed by moving only one circle (with a consequent improvement in accuracy).

A total of three microgravity-grown crystals and two Earth-grown crystals (fig. 1) were mounted in glass capillaries of 1.0 mm diameter for data collection. The three microgravity crystals were of approximate volume 0.108, 0.06, and 0.03 mm³ (labeled microgravity 1, 2, and 3 respectively). No artificial mother liquor was used, but plugs of stabilizing solution (2.0 *M* ammonium sulfate) were placed at either end of the capillaries before sealing with wax. Unfortunately, the largest microgravity crystal, microgravity 1, showed a crack across it halfway down its length. The two ground control crystals were of approximate volume 0.11 and 0.01 mm³ (labeled Earth 1 and 2, respectively) and were also mounted in 1.0-mm glass

capillaries. For each crystal the same set of 60 different reflections (over a resolution range of 12.39 to 1.44 Å) were measured at three ψ angles of -45° , 0° , and 45° . There was no appreciable difference in the incident intensity between the start and end of the reflection scans. Figure 2 shows, as examples, the rocking curves for the (4 19 1) reflection for three ψ settings for each of the five crystals and, likewise, figure 3 shows the curves for the (11 22 43) reflection.

The instrument resolution function (IRF)¹⁰ was calculated at 0.00195° excluding the reflection-dependent $(\Delta\lambda/\lambda)\tan\theta$ component, which was dealt with on a per-reflection basis (i.e., according to the appropriate θ angle). The source-to-instrument distance was 45 m with a double crystal Si(111) monochromator providing a 1 Å wavelength beam. The vertical beam source size was, at full width at half maximum (FWHM), 200 μm and the wavelength bandpass, $\delta\lambda/\lambda$, equal to 2×10^{-4} .

2.3 Data Processing

The boundary of the reflection was determined by the Lehmann-Larsen¹¹ method. This allows determination of the reflection background boundary as a minimum in $\sigma(I)/I$ over the range of each reflection profile. This was used because some of the reflections were quite weak. The scattering angle, θ , was then evaluated and also the FWHM, φ_R , of the reflection measured. The crystal sample mosaicity, η , can be determined by deconvoluting out these geometric and spectral parameters from the measured φ_R by use of:

$$\eta = (\varphi_R^2 - \text{IRF}^2)^{1/2} ,$$

where IRF is the reflection-dependent instrument resolution function.¹⁰

3. RESULTS AND DISCUSSION

Table 1 illustrates the maximum, minimum, and standard deviation of the mosaicity values obtained from the crystals. Crystal microgravity 1, which displayed a crack (as referred to above), displayed the second highest average mosaicity as well as the worst maximum and minimum values. Because of the crack, this crystal must, unfortunately, be discounted for the purposes of comparison (other than its volume). None of the minimum values reach the quality of the lysozyme mosaicity results obtained previously.¹ On the basis of the number of unit cells in each direction of the crystal habit (and the respective unit-cell size in each direction), we can calculate minimum mosaicity values³ (e.g., for Earth 1, of $0.00021^\circ \times 0.0019^\circ \times 0.0016^\circ$). Hence, the theoretical limit isn't approached either. On the basis of table 1, there is no clear distinction in favor of microgravity versus Earth-grown crystals, microgravity 2 being marginally the best (η) and with the lowest maximum η , but Earth 1 and microgravity 3 have the best minimum η . A population analysis of the mosaicity values for the crystals is shown in figure 4. If any discrimination is to be found between the crystals grown by the two different routes, we need a more sensitive measurement than the mosaicity provides in this case. Towards that end, a plot of mosaicity versus peak/background was investigated and is shown in figure 5. It can be seen clearly (also in the raw data in figures 2 and 3) that microgravity 2 produces much higher peak-to-background ratio (i.e., better signal-to-noise ratio) than the other crystals for the same set of reflections. One other microgravity crystal and an Earth crystal are of comparable, very good quality (microgravity 3 and Earth 1). The poorest quality crystals are microgravity 1 and Earth 2, the former's low quality was probably a result of crystal splitting. The poor quality of microgravity 1 and Earth 2 is clearly seen in figure 3, the high-resolution reflection (11 22 43) is well measured for microgravity 2, microgravity 3 and Earth 1 only.

Table 1. Analysis of η values ($^{\circ}$) for the apocrustacyanin C_1 crystals measured.

Crystal	Max η	Min η	$\langle \eta \rangle$	$\sigma(\eta)$	Reflections
microgravity 1	0.2160	0.0167	0.0393	0.0328	148
microgravity 2	0.0648	0.0143	0.0303	0.0118	168
microgravity 3	0.0708	0.0131	0.0378	0.0118	164
Earth 1	0.0840	0.0118	0.0344	0.0110	165
Earth 2	0.0780	0.0131	0.0501	0.0164	44

We suspect that a large range of values within the crystals (table 2) strongly suggests an anisotropic mosaicity for the crystals. To investigate the possible anisotropy in the mosaicity, a "mosaicity volume" plot can be made (i.e., plotting the unit diffraction vector of a reflection along with its magnitude as the mosaicity (a mosaicity vector). Figures 6(a) and 6(b) show this for the apocrustacyanin (Earth-grown and microgravity-grown reflections, respectively) and figures 6(c) and 6(d), for comparison, show values from our previous work with lysozyme (Earth-grown and microgravity-grown, IML-2 mission, respectively)¹ using the same scale. This demonstrates pictorially the level of improvement that can be made towards producing perfect crystals (in the ideal case of an infinitely large perfect crystal the rocking volume would be a point). Figure 7 illustrates the relative dimensions of the unit cells in the same orientation of the mosaicity volume plot with figure 1 showing the crystal habit of apocrustacyanin C_1 . Figure 8 shows the 2-dimensional projection of the "mosaicity volume" onto the hk and hl planes. The "mosaicity volume" is evaluated as the volume of an ellipsoid having values of principal half axes as maximum mosaicity magnitude in x , y , and z real-space directions (for space group $P2_12_12_1$, coaxial with h , k , and l directions). Table 2 gives these ellipsoid parameters for the apocrustacyanin C_1 and comparison values for lysozyme. In the case of apocrustacyanin C_1 the consistently smallest mosaicity occurs along the h axis, correlated with the theoretical mosaicity along a . This is demonstrated in table 2 with the exception of the cracked microgravity 1 crystal. With lysozyme, by comparison, the mosaicity is isotropic.

Table 2. Mosaicity volume ellipsoid parameters for both apocrustacyanin C_1 and lysozyme crystals.

Crystal	η_x	η_y	η_z	η volume
microgravity 1	0.1624	0.1777	0.1446	0.01748
microgravity 2	0.0298	0.0641	0.0459	0.00037
microgravity 3	0.0364	0.0496	0.0592	0.00045
Earth 1	0.0397	0.0681	0.0754	0.00085
Earth 2	0.0258	0.0743	0.0543	0.00044
Earth lysozyme	0.0254	0.0254	0.0341	0.00009
microgravity lysozyme	0.0069	0.0100	0.0069	0.000002

The parameters η_x , η_y , and η_z being the maximum mosaicity vector, in the x , y , and z directions, respectively (values in $^{\circ}$).

4. CONCLUDING REMARKS

The plot of mosaicity versus signal/noise is very sensitive to crystal quality. In the case of apocrustacyanin, the main noticeable improvement in crystal quality through microgravity growth is indeed as measured by this plot and manifest really only for one crystal. This is in contrast to the clear improvement for all the lysozyme crystals in our previous study.¹ How can this be explained? CCD observation of the vapor-diffusion crystallization of apocrustacyanin C₁ in microgravity has shown a rapid motion of crystals within the drop.¹² CCD observation of other microgravity crystallizations based on different methods (e.g., dialysis crystallization of lysozyme¹³ and free interface crystallization of α -crustacyanin on board an unmanned space platform¹⁴ has shown a little and no motion, respectively). In the vapor-diffusion case for the apocrustacyanin C₁, this motion, probably resulting from Marangoni convection,^{15,16} may well be the limiting factor on the quality of the crystals that can be produced. In comparison with the microgravity-grown lysozyme crystal case, there is room for improvement for the apocrustacyanin C₁, at least as evidenced by the mosaicity volume plots and the CCD video monitor. Hence, a repeat experiment of apocrustacyanin C₁ crystal growth in microgravity but using dialysis or liquid-liquid diffusion (rather than vapor diffusion) suggests itself, whereby the crystals would remain stationary during the growth process. Moreover, with lysozyme, instead of dialysis,² vapor diffusion might be used, inducing crystal movement even in microgravity, so as to reduce the crystal perfection from that obtained previously.¹ Finally, in the Protein Crystallization Diagnostic Facility (PCDF) being planned by ESA [Stapelmann et al., unpublished work], a detailed history of a particular crystal growth process will be established via laser light scattering (nucleation step), interferometry (growth stage), and CCD video monitoring (to track crystal movement and growth), all prior to harvesting and full x-ray diffraction characterization and data collection for protein structure analysis.

REFERENCES

1. Snell, E.H.; Weisgerber, S.; Helliwell, J.R.; Weckert, E.; Hölzer, K.; and Schroer, K.: *Acta Cryst.*, D51, 1099–1102, 1995.
2. Helliwell, J.R.; Snell, E.H.; and Weisgerber, S.: *Proceedings of 1995 Berlin Microgravity Conference*, L. Ratke, H. Walter, and B. Feuerbacher, eds., Berlin, Springer-Verlag, 155–170, 1995.
3. Helliwell, J.R.: *J. Cryst. Growth*, 90, 59–272, 1988.
4. Vaney, M.C.; Maignan, S.; Riès-Kautt, M.; and Ducruix, A.: *Acta Cryst.*, D52, 505–517, 1996.
5. Chayen, N.E.; Gordon, E.J.; and Zagalsky, P.F.: *Acta Cryst.*, D52, 156–159, 1996.
6. Snyder, R.S.; Fuhrmann, K.; and Walter, H.U.: *J. Cryst. Growth*, 110, 333–338, 1991.
7. Bosch, R.; Lautenschlager, P.; Potthast, L.; and Stapelmann, J.: *J. Cryst. Growth*, 122, 310–316, 1992.
8. Hümmer, K.; Weckert, E.; and Bondza, H.: *Acta Cryst.*, A45, 182–187, 1989.
9. Weckert, E.; Schwegle, W.; and Hümmer, K.: *Proc. R. Soc. London Ser. A*, 442, 33–46, 1993.
10. Colapietro, M.; Cappuccio, G.; Marciante, C.; Pifferi, A.; Spagna, R.; and Helliwell, J.R.: *J. Appl. Cryst.*, 25, 192–194, 1992.
11. Lehmann, M.S.; and Larsen, F.K.: *Acta Cryst.*, A30, 580–584, 1974.
12. Chayen, N.E.; Snell, E.H.; Helliwell, J.R.; and Zagalsky, P.F.: *J. Cryst. Growth*, in press, 1997.
13. Snell, E.H.; Boggon, T.J.; Helliwell, J.R.; Moskowitz, M.E.; and Nadarajah, A.: *Acta Cryst.*, D53, submitted, 1997.
14. Boggon, T.J.; Chayen, N.E.; Zagalsky, P.F.; Snell, E.H.; and Helliwell, J.R.: *Biophys. J.*, submitted, 1997.
15. Molenkamp, T.; Janssen, L.P.B.M.; and Drenth, J.: *Final Reports of Sounding Rockets in Fluid Science and Material Science, TEXUS 28 to 30, MAUSER 5 & MAXUS*, ESA SP-1132, 4, 22–43, 1994.
16. Savino, R.; and Monti, R.: *J. Cryst. Growth*, 165, 308–318, 1996.

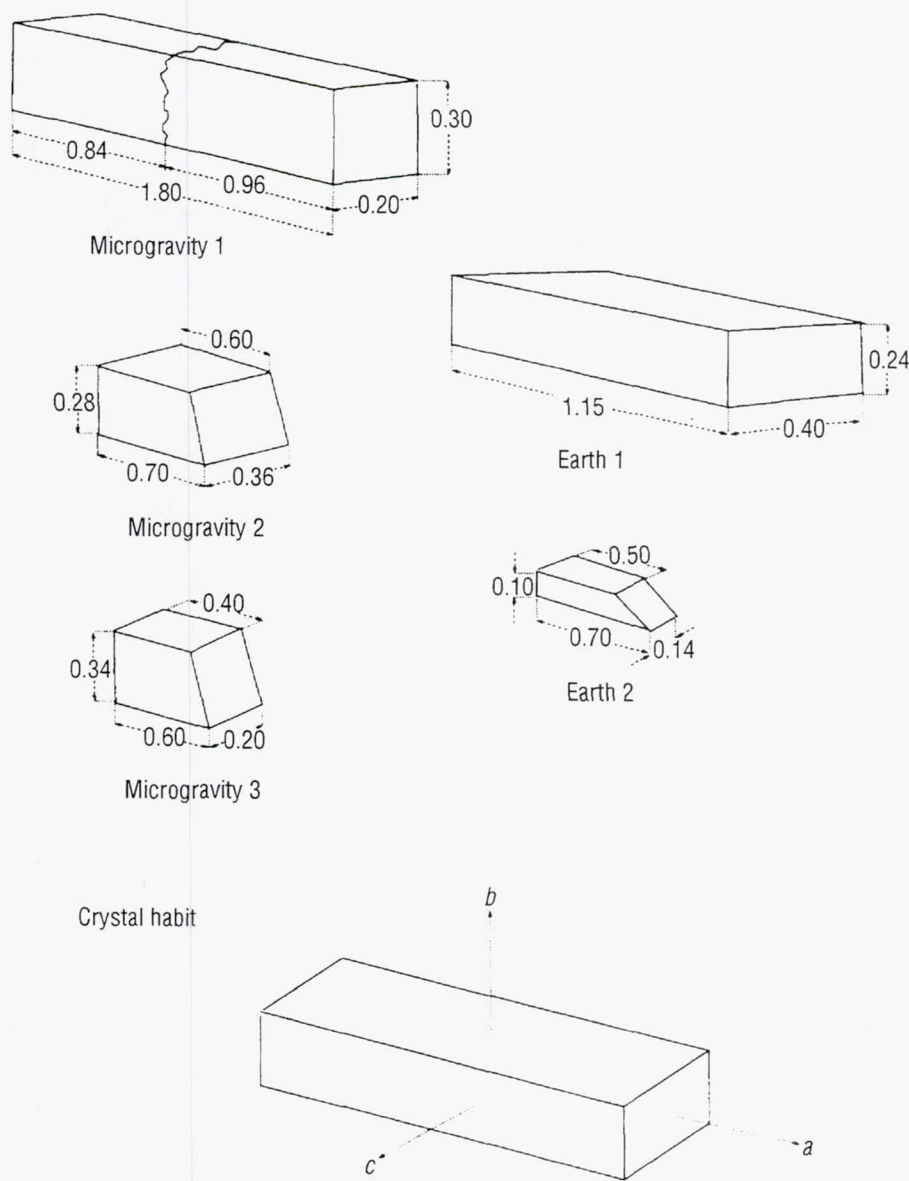


Figure 1. Dimensions of apocrustacyanin C_1 crystals used for data collection (not to scale). The relationship of the crystal habit and the unit-cell parameters is also shown.

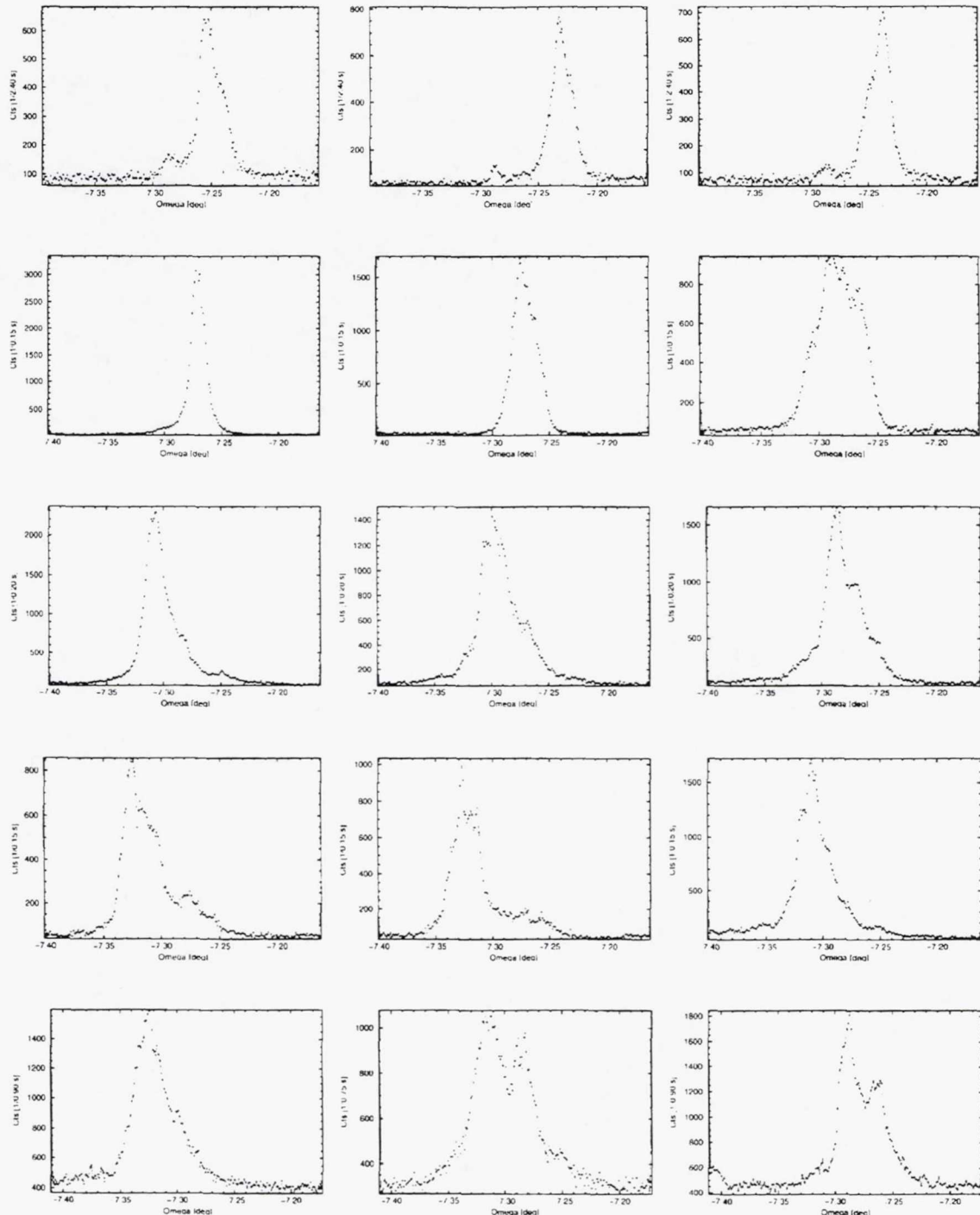


Figure 2. Rocking curves for the (4 19 1) reflection (4 Å resolution), as a representative example, at three Ψ settings (left to right), for each of the five crystals, microgravity 1 (first row), microgravity 2 (second row), microgravity 3 (third row), Earth 1 (fourth row), and Earth 2 (fifth row). The three curves for microgravity 1 (first row) were measured in single-bunch mode; i.e., where the circulating current is approximately 1/10th of the current available for all the other curves.

Microgravity-grown apocrustacyanin C₁

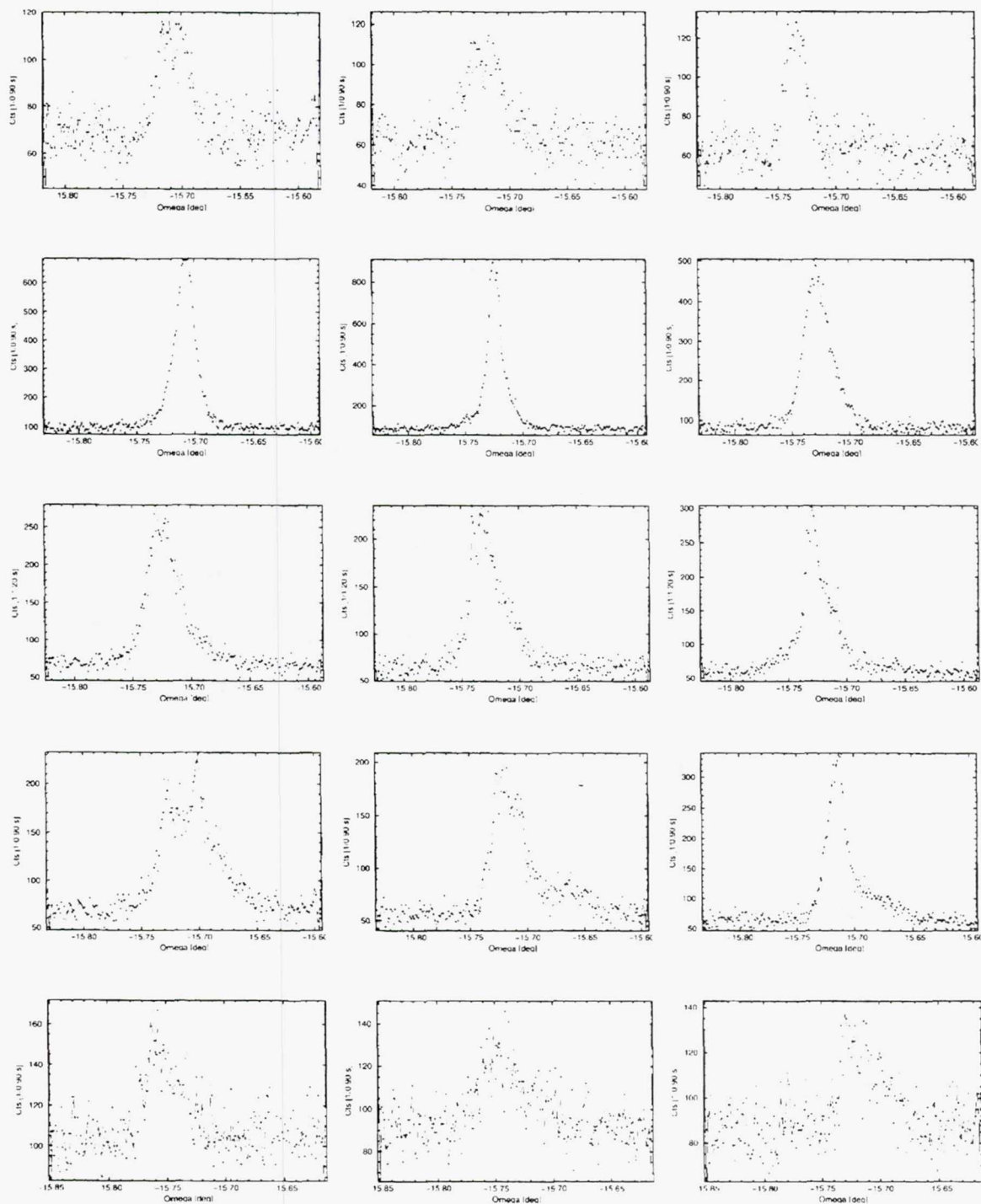


Figure 3. Rocking curves for the (11 22 43) reflection (1.85 Å resolution), as a representative example, laid out in the same format as in figure 2. This reflection, being at high resolution, was measured near the start of the run for each crystal [unlike the (4 19 1) reflection which was measured near the end of the sequence of reflections, being at low resolution]. This essentially avoids any impact of radiation damage.

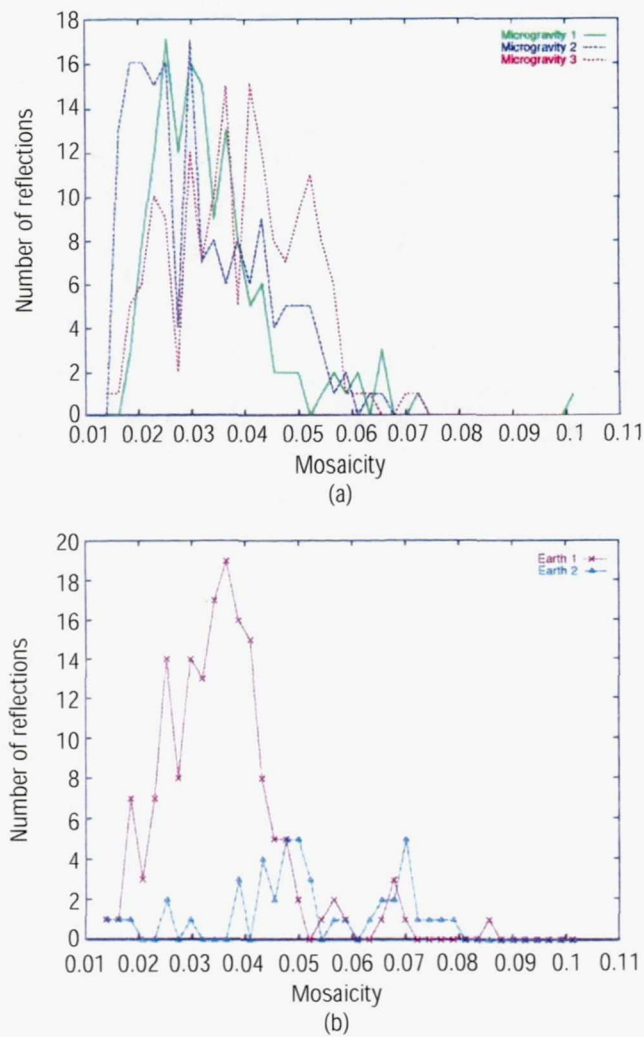


Figure 4. Histogram of the mosaicity for (a) the three microgravity and (b) two Earth-grown apocrustacyanin C_1 crystals.

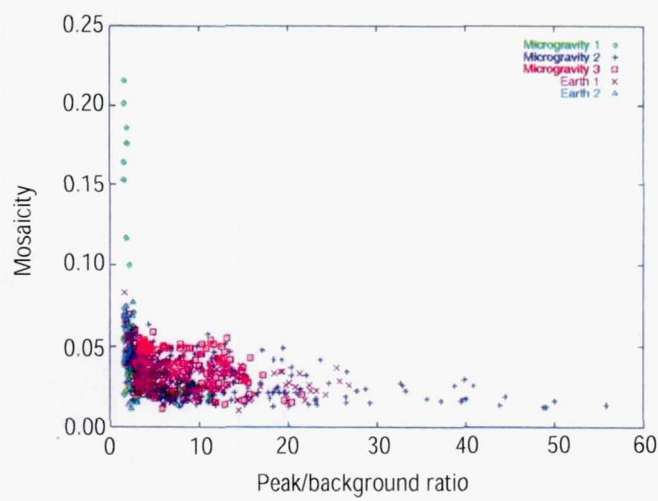


Figure 5. Plot of the mosaicity versus peak/background for the three microgravity-grown and two Earth-grown control crystals of apocrustacyanin C₁.

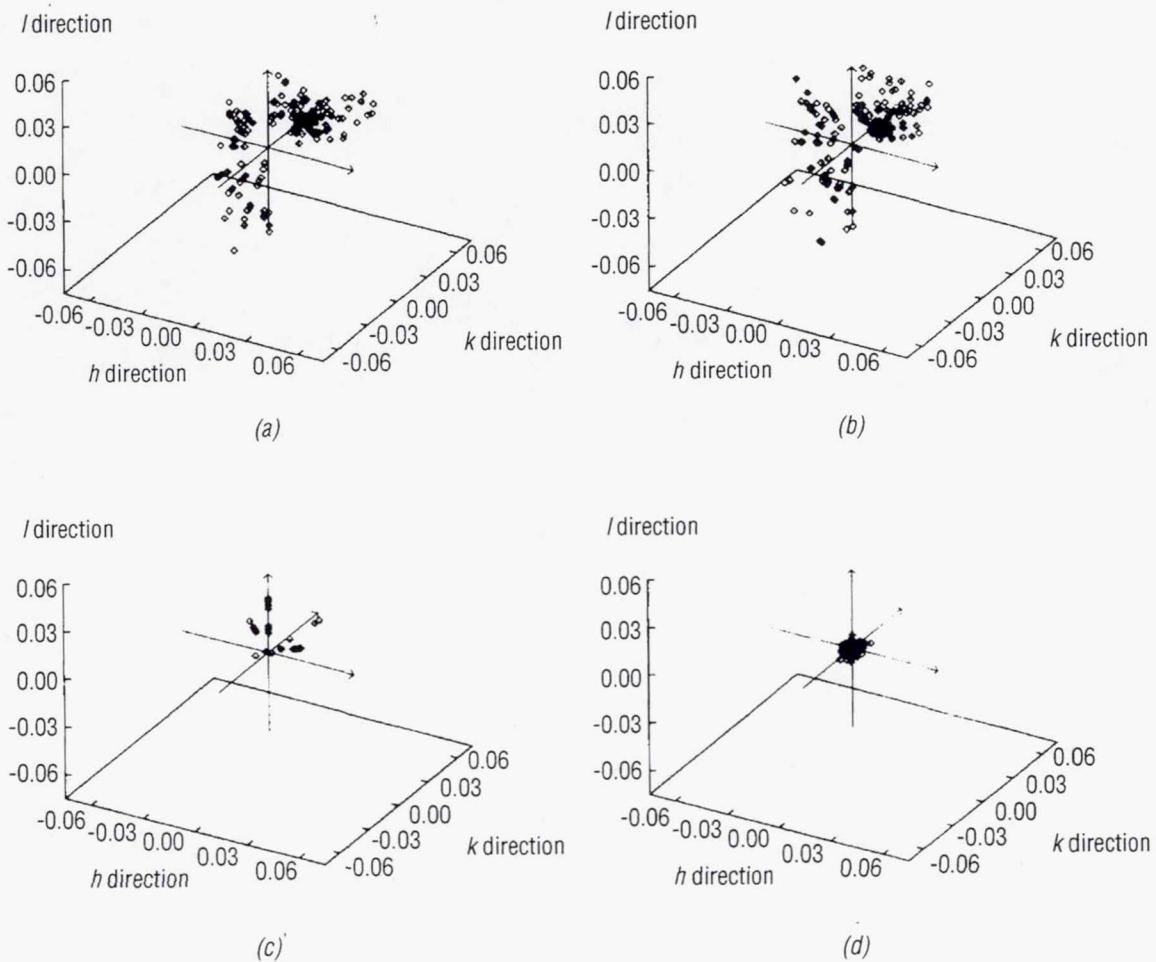


Figure 6. Plot of the “mosaicty (rocking) volume” for (a) Earth 1 apocrustacyanin, (b) microgravity 3 apocrustacyanin, (c) Earth-grown lysozyme, and (d) microgravity-grown lysozyme [Snell et al. (1995) for (c) and (d)]. All plots are on the same scale with the mosaicties given in degrees.

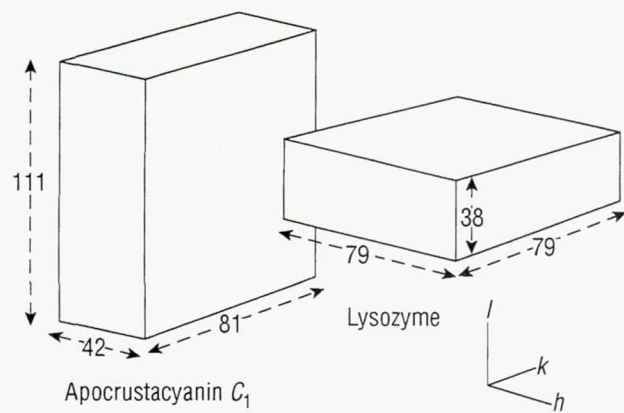


Figure 7. Unit-cell dimensions of apocrustacyanin C_1 and lysozyme (in Å).

Microgravity-grown apocrustacyanin C₁

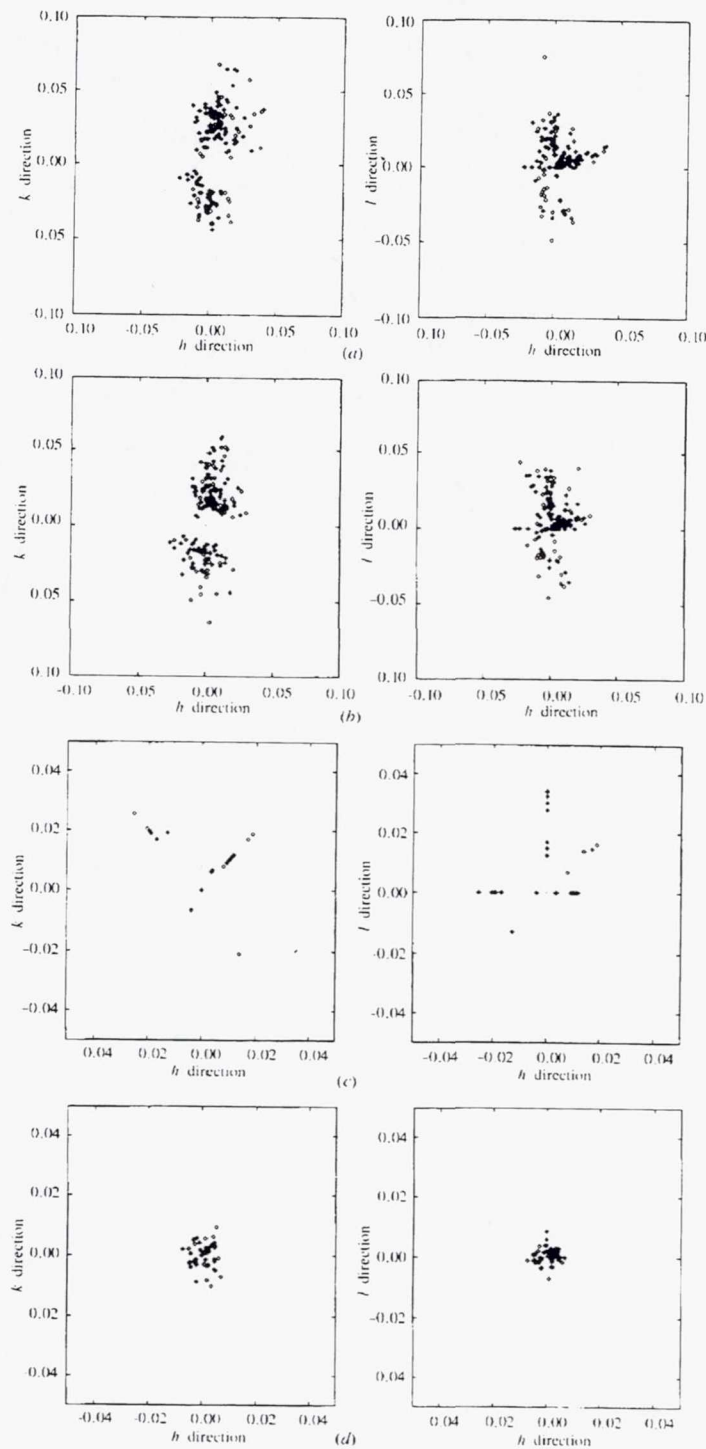


Figure 8. Plot of the rocking volume projected onto the *hk* and *hl* planes for (a) earth 1 apocrustacyanin, (b) μ g 3 apocrustacyanin, (c) earth-grown lysozyme, and (d) microgravity-grown lysozyme.

Page intentionally left blank

EXPERIMENT XVII.

CRYSTALLIZATION OF THE VISUAL PIGMENT RHODOPSIN

Page intentionally left blank

CRYSTALLIZATION OF THE VISUAL PIGMENT RHODOPSIN

Dr. W.J. de Grip

University of Nijmegen

6500 HB Nijmegen

The Netherlands

Phone: 011-31-24-3614263

Fax: 011-31-24-3540525

E-mail: wdegrif@baserv.uci.kun.nl

ABSTRACT

This experiment addressed the potential of microgravity for crystallization of the visual pigment rhodopsin. The high-resolution structure of this protein is unknown, which seriously hampers studies of the signal transduction mechanism on a molecular level. Better insight will increase our basic knowledge of this protein and may have medical and pharmacological applications. Hardware problems were encountered in four of the six reactors. Of the remaining two reactors, one had some small crystalline objects and the other one showed an abundance of small needles, including some clusters. All objects were shown to contain rhodopsin but were too small (<80 μ m in the largest dimension) for diffraction analysis.

1. INTRODUCTION

Rhodopsin is the light-sensitive protein (visual pigment) of the rod photoreceptor cell in the vertebrate retina. It is a member of the large family of G-protein coupled receptors. To understand receptor properties and signal-transduction mechanism of this membrane protein family on a molecular level, detailed knowledge of the three-dimensional structure is essential. Since these proteins are too large (40 to 70 kD) to allow structural analysis by NMR techniques, crystallization with high-resolution analysis by x-ray diffraction is the only feasible approach. This requires relatively large amounts of purified protein, and bovine rhodopsin is the only representative of this receptor family that can be isolated and purified from its native source in sufficient quantities for this purpose. The amino acid sequence of bovine rhodopsin was elucidated a decade ago, and very recently a low-resolution projection structure obtained from 2-dimensional crystals was reported. However, a detailed three-dimensional structure is still not available.

We have obtained crystals of rhodopsin (40 kD) in our laboratory using the sitting-drop vapor diffusion technique, but so far they were too small or disordered to provide any diffraction information. A major problem with crystallization of membrane proteins is their amphipathic character, requiring detergents and detergent phase-shift modifiers, and their relatively low polar surface area prohibits extensive strong protein-protein interactions. We have investigated many parameters to produce optimal conditions (protein concentration, type and concentration of detergents, type and concentration of precipitant, buffer, pH, temperature, lipids, and stabilizing or micelle-modifying additives).

Evidence is accumulating that microgravity not only could be beneficial to protein crystallization in that larger size or better ordered crystals can be obtained than at 1g, but also that diffractable crystals are generated from proteins that on Earth only give low-order or microcrystals. The latter condition prevails for rhodopsin.

2. RESULTS

Six different crystallization conditions that generated small crystals of various shapes on Earth were tested in hanging-drop Advanced Protein Crystallization Facility (APCF) reactors. The APCF reactors were fitted with long-pass filters (690 nm cut-off) to ensure that rhodopsin was not exposed to any light (to which it is very sensitive (280–650 nm)) during handling of the reactors.

Screening for crystal formation was done microscopically in red light (Schott long-pass filter RG645) using shape and birefringence as criteria to identify crystals. Mother liquor and crystalline structures were screened for the presence and quantity of intact protein by immunoblot analyzing using specific antibodies.

Unfortunately, we seem to have had some hardware problems. Two of the six reactors had partially or completely lost their hanging drop and two other reactors had not (well) equilibrated (almost no reduction in volume of protein solution). Of the remaining two reactors one had some small crystalline objects and the other one showed an abundance of small needles, including some clusters. All objects were too small (maximally 80 μm in only one dimension) to attempt x-ray diffraction analysis (this would require a minimal size of 50 to 100 μm in all dimensions).

Electroimmunoblotting analysis showed that the needle-shaped objects contain rhodopsin. This could not be unequivocally demonstrated for the other shape, possibly since the amount of protein was below the detection level. As far as we could determine, there was no sign of spectral deterioration of the samples, indicating that the precautions taken to prevent light damage had worked properly.

These results are less positive than those obtained with earlier flights. The hardware problems so far are unexplained but do not appear to depend on the type of detergent used. Although crystal sizes are usually smaller in the ground controls, laboratory-grown crystals tend to grow larger upon prolonged incubation (4 to 12 weeks). This would suggest performing crystallization experiments with rhodopsin under microgravity for more prolonged time periods (1 to 3 months).

3. CONCLUSIONS

Earlier experiments indicated that microgravity seems to have a positive effect on the rhodopsin crystallization process. One option to explore further is to try more extended crystallization time periods (>1 month). Another option to explore further is based on the recent observation that the optimal crystallization conditions in microgravity might slightly differ from those on Earth. This would prompt crystallization trials in microgravity using a range of conditions close to the optimal ones found at 1g.

EXPERIMENT XVIII.

CRYSTAL STRUCTURE ANALYSIS OF THE BACTERIOPHAGE LAMBDA LYSOZYME

Page intentionally left blank

CRYSTAL STRUCTURE ANALYSIS OF THE BACTERIOPHAGE LAMBDA LYSOZYME

Prof. Jean-Paul Declercq

C. Evrard

Unité CPMC

Lab. de Chimie Physique et de Cristallographie

Université Catholique de Louvain

1, Place Louis Pasteur

B-1348 Louvain-la-Neuve

BELGIQUE (BELGIUM)

Phone: 011-32-10-472924

Fax: 011-32-10-472836

E-mail: declercq@cpmc.ucl.ac.be

1. PURPOSE

The bacteriophage lambda lysozyme is a small protein of 158 amino acids. Like other known lysozymes, it is involved in the dissolution of the cell walls of bacteria. This enzyme is remarkable in that its mechanism of action is different from the classical lysozyme's mechanism; moreover, from the point of view of protein evolution, it shows features of lysozymes from different classes. After many years of efforts toward crystallization of the native enzyme, no suitable crystals could be obtained. Before this mission, different mutants also were tested, and it appears that the best results were obtained after replacement of the tryptophane residues by aza-tryptophanes, using the hanging drop technique. Investigators were able to grow only very small crystals of this mutant, even after seeding experiments. These crystals were too small for complete structure analysis but allowed determination of preliminary crystallographic data. The aim of this investigation was to produce well-ordered crystals suitable for high-resolution x-ray structure determination and analysis.

2. METHOD

The crystallization experiment of the bacteriophage lambda lysozyme was achieved using the vapor diffusion method. Five 8-ml handgun drop reactors were available for the experiment. Crystallization occurred at 20 °C in the same conditions used for the laboratory-grown crystals.

3. RESULTS

Crystallization of the protein occurred in two of the allocated reactors. Several very thin needles (fig. 1) were picked out but appeared to be smaller than the crystals grown on the ground and were, therefore, unusable for high-resolution x-ray structure determination and analysis. Precipitates were found in the other reactors.

4. PRELIMINARY CONCLUSIONS

It was concluded that the crystallization conditions of the bacteriophage lambda lysozyme seem to have changed during the microgravity experiment on USML-2. It can be assumed that it will be possible to optimize the microgravity crystallization parameters to obtain crystals of suitable size for x-ray analysis.

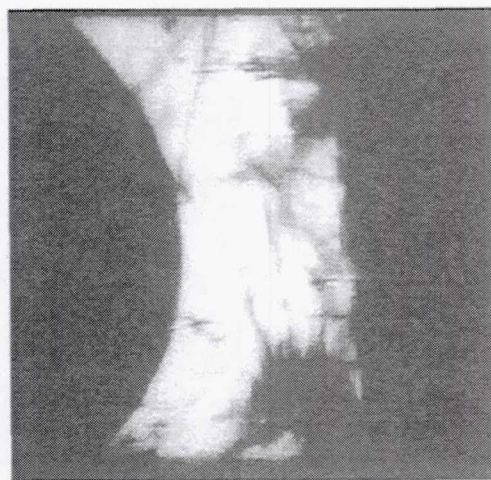


Figure 1. Very thin, needle-like crystals of bacteriophage lambda lysozyme were grown in two reactors on USML-2.

EXPERIMENT XIX.

CRYSTALLIZATION OF MONOCLINIC AND TRICLINIC LYSOZYME (APCF FACILITY)

ACKNOWLEDGMENTS

Isabelle Broutin was supported by the Centre National d'Etudes Spatiales (CNES). We thank CNES and the Centre National de la Recherche Scientifique Française (CNRS) for financial support of this project. We are indebted to the European Space Agency (ESA) for its assistance throughout the project. We are grateful to R. Fourme and J.P. Benoit for the development of the W32 station.

CRYSTALLIZATION OF MONOCLINIC AND TRICLINIC LYSOZYME (APCF FACILITY)

I. Broutin

M. Riès-Kautt

A. Ducruix

Laboratoire d'Enzymologie et Biochimie Structurales—CNRS
Bât. 34, 91198 Gif sur Yvette cedex, France

ABSTRACT

Lysozyme has been widely used as a standard protein for protein crystal growth. Lysozyme crystals are extremely polymorphic. Triclinic and monoclinic crystals of lysozyme were grown under a microgravity environment using an APCF instrument during the USML-2 mission. Proper ground controls were performed using different techniques (solution or gel growth) as well as different chemical compositions of a crystallizing agent. Space-grown crystals and ground controls were analyzed using synchrotron radiation to assess their diffraction limits. Ground- and microgravity-grown crystals are isomorphous. The best resolution for ground- and microgravity-grown crystals is the same (1.45 Å) for both crystal forms. Triclinic crystals were only partially recorded for a statistical analysis because ground crystals diffracting to 0.99 Å were already recorded by another group. As for the monoclinic form, because the highest resolution of chicken egg white lysozyme deposited at the PDB is 1.72 Å resolution, it was decided to collect a full data set with microgravity-grown crystals. The structure is under refinement.

1. INTRODUCTION

Due to the multiparametric aspect of protein crystallization,¹ it is somewhat difficult to quantify the influence of one particular parameter on protein crystal growth and crystal perfection. Important biophysical parameters such as pH and temperature can be analyzed by measuring their effectiveness on protein solubility.² Purity of lysozyme can be assessed by many means including ion-spray spectroscopy.³ One must find a way to quantify the influence of microgravity on crystal quality. Two parameters are good candidates: mosaicity and resolution. In both cases, the use of synchrotron radiation appears to be crucial but results are quite dependent on experimental set-up. Mosaic spread, describing crystal perfection, is experimentally measured by rocking curves.^{4,5} Resolution gives the crystal diffraction limit. However, the operational definition of resolution limit varies depending on authors. It is sometimes related to the ratio $\langle I \rangle / \langle \sigma(I) \rangle$ as a function of resolution shells or on values of R_{sym} (the relative disagreement between intensities of symmetry equivalent reflections) as a function of the resolution S . In order to perform appropriate comparison between space- and ground-grown crystals, one may either compare the space-grown crystals to the best ever ground crystal or use rigorously the same experimental conditions such as protein concentration, pH, temperature, volume or transportation conditions, time of storage, etc. In the present work, we have used both approaches.

We initially planned to use APCF reactors to study the influence of microgravity for two proteins, Grb2 and chicken egg white lysozyme, which have been studied in our group.

Grb2 is an "adaptor" protein which on one side binds to the phosphotyrosine of a receptor, and on another side to a proline-rich domain of Sos, a guanine nucleotide exchange factor of Ras. Crystals do not diffract better than 3.1 Å, and we expected a better resolution from space-grown crystals. Unfortunately, the Grb2 samples proved to be unstable a few weeks before launch, and there was no time for another purification process. Therefore, the corresponding APCF reactors (six) were returned to ESA, and we focused on lysozyme crystals.

Lysozyme (14306 Da molecular weight) is a monomeric enzyme of 129 amino acids (pI 11.1) which has been used systematically as a model by protein crystal growers over the last decade. The protein is not glycosylated, and there is no free cysteine. There are three disulfide bridges. Its physical-chemistry properties⁶ and 3-dimensional structure^{7, 8, 9, 10} have been thoroughly described. For the sake of clarity, we have summarized all the space group data concerning chicken egg white lysozyme from the Brookhaven Protein Data Bank (PDB)¹¹ (table 1). Four space groups are currently explored by several laboratories (table 2). In SpaceHab-01, a previous flight in 1993, we studied the tetragonal form. Although results were better than any previous ones (crystals diffracted to 1.3 Å), there is no significant difference between ground control and space experiments.^{10,12} During the USML-2 mission, we aimed at producing large crystals of triclinic and monoclinic chicken egg white lysozyme under a microgravity environment using an APCF instrument for mosaicity, rocking curve and topography studies.

Table 1. Hen egg white lysozyme (*Gallus Gallus*).

PDB code	space group	solvent Nb Wat	reso (Å)	comments	references
193L	P4 ₃ 2 ₁ 2	142	1.33	SpaceHab-01 ground control	(Vaney et al., 1996)
194L	P4 ₃ 2 ₁ 2	138	1.40	SpaceHab-01 space experiment	(Vaney et al., 1996)
1LZB	P4 ₃ 2 ₁ 2	97	1.50	+ tri-N-acetylchitotriose	(Maenaka et al., 1995)
1LZA	P4 ₃ 2 ₁ 2	104	1.60		(Maenaka et al., 1995)
1HEL	P4 ₃ 2 ₁ 2	185	1.70	recombinant form	(Wilson et al., 1992)
1LSA	P4 ₃ 2 ₁ 2	127	1.70	120 K	(Kurinov et al., 1995)
1LSB	P4 ₃ 2 ₁ 2	122	1.70	180 K	(Kurinov et al., 1995)
1LSC	P4 ₃ 2 ₁ 2	105	1.70	250 K	(Kurinov et al., 1995)
1LSD	P4 ₃ 2 ₁ 2	96	1.70	280 K	(Kurinov et al., 1995)
1LSE	P4 ₃ 2 ₁ 2	99	1.70	295 K	(Kurinov et al., 1995)
1LSF	P4 ₃ 2 ₁ 2	119	1.70	95 K	(Kurinov et al., 1995)
1LSM	P4 ₃ 2 ₁ 2	170	1.70	mutant (I55L, S91T, D101S)	(Shih et al., 1995)
1HEW	P4 ₃ 2 ₁ 2	103	1.75	+ tri-N-acetylchitotriose	(Cheetham et al., 1992)
1HEM	P4 ₃ 2 ₁ 2	185	1.80	mutant (S91T)	(Wilson et al., 1992)
1HEN	P4 ₃ 2 ₁ 2	185	1.80	mutant (I55V, S91T)	(Wilson et al., 1992)
1HEO	P4 ₃ 2 ₁ 2	185	1.80	mutant (I55V)	(Wilson et al., 1992)
1HEP	P4 ₃ 2 ₁ 2	185	1.80	mutant (T40S, I55V, S91T)	(Wilson et al., 1992)
1HEQ	P4 ₃ 2 ₁ 2	185	1.80	mutant (T40S, S91T)	(Wilson et al., 1992)
1HER	P4 ₃ 2 ₁ 2	185	1.80	mutant (T40S)	(Wilson et al., 1992)
1LZC	P4 ₃ 2 ₁ 2	109	1.80	+ tetra-N-acetylchitotetraose	(Maenaka et al., 1995)
1LZD	P4 ₃ 2 ₁ 2	79	1.80	mutant (W62Y)	(Maenaka et al., 1995)
1LZE	P4 ₃ 2 ₁ 2	106	1.80	mutant (W62Y) + tri-N-acetylchitotriose	(Maenaka et al., 1995)
1LZG	P4 ₃ 2 ₁ 2	85	1.80	mutant (W62F) + tri-N-acetylchitotriose	(Maenaka et al., 1995)
5LYT	P4 ₃ 2 ₁ 2	237	1.90	100K	(Young et al., 1994)
6LYT	P4 ₃ 2 ₁ 2	100	1.90	298K	(Young et al., 1994)
1LSY	P4 ₃ 2 ₁ 2	139	1.90	mutant (D52S)	(Hadfield et al., 1994)
1LSN	P4 ₃ 2 ₁ 2	177	1.90	mutant (I55L, S91T, D101S)	(Shih et al., 1995)
1LSZ	P4 ₃ 2 ₁ 2	126	2.00	mutant (D52S) + product GlcNAc4	(Hadfield et al., 1994)
2LYM	P4 ₃ 2 ₁ 2	151	2.00	1 atm - 1.4 M NaCl	(Kundrot et al., 1987)
3LYM	P4 ₃ 2 ₁ 2	163	2.00	1000 atm - 1.4 M NaCl	(Kundrot et al., 1987)
1LYZ	P4 ₃ 2 ₁ 2	97	2.00	set W2	(Diamond, 1974)
2LYZ	P4 ₃ 2 ₁ 2	97	2.00	set RS5D - different refinement	(Diamond, 1974)
3LYZ	P4 ₃ 2 ₁ 2	97	2.00	set RS6A - different refinement	(Diamond, 1974)
4LYZ	P4 ₃ 2 ₁ 2	97	2.00	set RS9A - different refinement	(Diamond, 1974)
5LYZ	P4 ₃ 2 ₁ 2	97	2.00	set RS12A - different refinement	(Diamond, 1974)
6LYZ	P4 ₃ 2 ₁ 2	97	2.00	set RS16 - different refinement	(Diamond, 1974)
4LYM	P4 ₃ 2 ₁ 2	157	2.10	low humidity form	(Kodandapani et al., 1990)
8LYZ	P4 ₃ 2 ₁ 2	0	2.50	iodine-inactivated	(Beddell et al., 1975)
9LYZ	P4 ₃ 2 ₁ 2	0	2.50	nam-nag-nam substrate only	(Kelly et al., 1979)
132L	P2 ₁ 2 ₁ 2 ₁	78	1.80	reductively-methylated lysines	(Rypniewski et al., 1993)
1RCM	P2 ₁ 2 ₁ 2 ₁	133	1.90	partially reduced, carboxymethylated	(Hill et al., 1993)
2LZH	P2 ₁ 2 ₁ 2 ₁	0	6.00	carbon alpha atoms only	(Artymiuk et al., 1982)
1LYS	P2 ₁	215	1.72	313K	(Harata, 1994)
1LMA	P2 ₁	148	1.75	low humidity form - 2 nitrates	(Madhusudan et al., 1993)
3LYT	P2 ₁	406	1.90	100K	(Young et al., 1993)
4LYT	P2 ₁	191	1.90	298K	(Young et al., 1993)
1LYM	P2 ₁	0	2.50		(Rao et al., 1983)
1LZH	P2 ₁	0	6.00	carbon alpha atoms only	(Artymiuk et al., 1982)
1UCO	P2 ₁	266	2.00		(Nagendra et al., 1996)
5LYM	P2 ₁	111	1.80	6 nitrates	(Rao et al., 1996)
1LZT	P1	220	1.97		(Hodson et al., 1990)
2LZT	P1	249	1.97	5 nitrates	(Ramanadham et al., 1990)
7LYZ	P1	97	2.50		(Herzberg et al., 1976)
1HWA	NMR			NMR, minimized average	(Smith et al., 1993)

Table 2. List of international laboratories involved in crystallographic lysozyme studies.

Space group	Resolution	Mosaicity
Triclinic	Gif, Hamburg	Gif, Paris
Monoclinic	Gif,	Gif, Paris
Orthorhombic	Gif, Daresbury	Gif, Paris
Tetragonal	Gif, Daresbury	Gif, Paris, ESRF, Huntsville, Granada
Gif: Paris: ESRF: Daresbury Granada Huntsville	LEBS CNRS (France) LMCP CNRS (France) Grenoble (France) Chemistry Dept., Manchester (UK) IACT CSIC (Spain) CMMR and NASA, Huntsville (USA)	

2. RESULTS

2.1 Crystallization

A set of five FID reactors each containing 450- μ l lysozyme solutions were used for dialysis technique. The reactors were filled in Strasbourg (France) on September 19, 1995, according to table 3.

Table 3. Crystallization conditions (T for triclinic and M for monoclinic).

		T1	T2	M3	M4	M5
Nominal final concentration of NaNO_3 (mM)		158	158	295	295	295
Protein (450 μ l)	lyso/Tp NaNO_3 /Tp	10 γ 450 mM	10 γ 450 mM	12 γ 0	10 γ 0	8 γ 0
Piston (235 μ l)	NaNO_3 /Tp	0	0	340 mM	340 mM	340 mM
Reservoir (598 μ l)	NaNO_3 /Tp	0	0	500 mM	500 mM	500 mM

2.2 Mission

Ground controls were run in parallel in our laboratory using spare reactors. A temperature of 4 °C was selected for transportation of the flight reactors to KSC. All reactors were activated on October 20 after several launch delays. The protein is extremely stable, and this property has been very useful in the present case of repeated launch delays. The active crystallization experiments were performed at 18 °C. The microgravity experiments flew during the 16-day USML-2 mission of the Shuttle *Columbia* which landed on November 5. Two days after landing, the reactors were recovered and analyzed in France. Temperature was continuously recorded in the APCF unit and in the transport containers from the time of reactor filling to that of crystal recovery in Europe.

2.3 Analysis

Crystals of both monoclinic and triclinic lysozyme were immediately mounted in glass capillaries and were submitted to x-ray radiation for diffraction limits. First of all, it should be noted that using synchrotron radiation instead of a rotating anode is generally a major parameter improving resolution. This is true for lysozyme and most proteins. All the crystals were analyzed at 4 °C on the wiggler beam line DW32¹² at LURE (Synchrotron, Orsay, France) using a wavelength of 0.981 Å and a Mar-Research image plate system (diameter of the plate is 300 mm). Crystal to detector distance was 100 mm. Because synchrotron beam time allowance was limited, it was not possible to record full data sets for all crystals, and we verified that for partial data sets the quantity of data recorded in reciprocal space was large enough to give a number of unique reflections and a completeness statistically significant. For each crystal a partial data set was recorded in order to analyze statistically the difference of diffraction quality between them. As lysozyme crystals proved to be homogenous in function of the analyzed orientation, a continuous range (rotation of 20°) of reciprocal space was recorded for all crystals. Data treatment convinced us that it is better to perform a continuous rotation rather than sampling with small rotations in different zones of reciprocal space.

2.4 APCF performance

The postflight controls revealed the following:

- The reactors did not leak, as final salt concentrations were nominal;
- Temperature recorded data was nominal (18 °C);
- pH was close to nominal for the five reactors; and
- Crystals grew in all reactors (flight and ground controls).

Therefore, the APCF device proved to work successfully as concerning activation, deactivation, equilibration of protein/reservoir solution, leaking, and thermal regulation. As concerning video recording, a technical problem prevented recording and therefore analysis.

2.5 Crystal quality

Unit cell is $a=34.2$, $b=31.8$, $c=27.1$ Å, $\alpha=111.6$, $\beta=108.3$, $\gamma=88.8^\circ$ for the triclinic crystals belonging to the space group P1 with one molecule in the asymmetric unit. For the P2₁ monoclinic form, crystals (fig. 1) belong to space group P2₁ with $a=27.96$, $b=60.61$, $c=62.94$ Å, $\beta=90.82^\circ$ and two molecules in the asymmetric unit. Ground- and microgravity-grown crystals are isomorphous.

It is to be noted that visual inspection of digitized images of diffracted intensities gives a fairly close approximation of resolution limit.

The best resolution is 1.45 Å for both monoclinic and triclinic microgravity and ground crystals which is better than any published values. Because the highest resolution of monoclinic HEW lysozyme deposited at the PDB is 1.72 Å resolution (table 1), it was decided to collect a full data set with a microgravity-grown crystal and refine the structure. As far as the triclinic crystals are concerned, the highest resolution deposited at the PDB is 1.97 Å, but it was known (Keith Wilson, private communication) that ground crystals diffracting up to 0.99 Å resolution were analyzed at the EMBL out-station in Hamburg. Therefore, only partial data were collected but proved to be difficult to process.

2.6 Mosaicity

Ground crystals of monoclinic and triclinic lysozyme crystals were analyzed using the quasi-planar wave produced by a four-reflection monolithic Si crystal on the standing wave station¹³ D25B at LURE-DCI (France). Ground crystals of both monoclinic and especially triclinic crystals displayed a surprisingly large mosaicity of the order of a tenth of a degree.

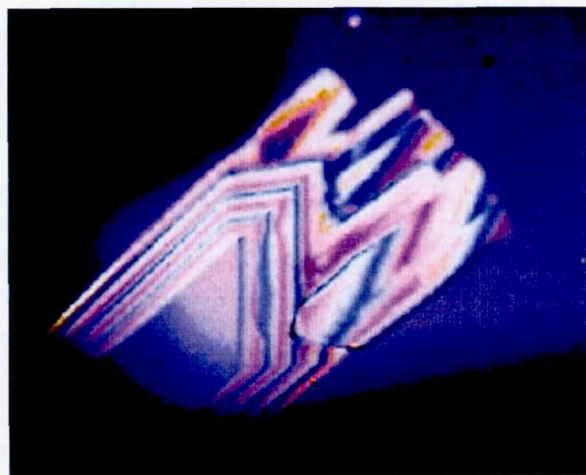
Unfortunately, beam time was not available when we mounted microgravity-grown crystals. The experiment should be repeated with freshly grown crystals.

3. CONCLUSION

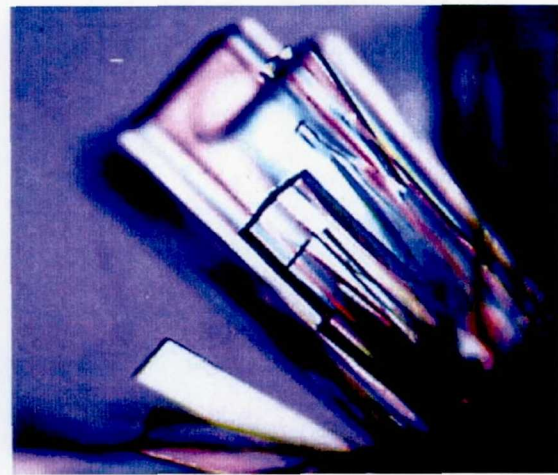
Lysozyme proved to be a good candidate for the understanding of the influence of microgravity for protein crystal growth. Polymorphic crystal forms display a variety of behavior for resolution and mosaicity and this should help to answer the question of a putative correlation between these two parameters. Furthermore, because the different space groups observed for lysozyme crystals are generally correlated to the chemical nature of the crystallizing agent, we intend to uncouple the influence of microgravity from the chemical one.

REFERENCES

1. Giegé, R.; Lorber, B.; and Théobald-Dietrich, A.: *Acta Cryst.*, D50, 339, 1994.
2. Riès-Kautt, M.; and Ducruix, A.: *Crystallization of Protein and Nucleic Acids: A Practical Approach*, Ed. A. Ducruix and R. Giegé, IRL/Oxford Press, 195, 1992.
3. Riès-Kautt, M.; Ducruix, A.; and Van Dorsselaer, A.: *Acta Cryst.*, D50, 366–369, 1994.
4. Helliwell, J.R.: *J. Cryst. Growth*, 90, 259, 1988.
5. Fourme, R.; Ducruix, A.; Riès-Kautt, M.; and Capelle, B.: *J. Synchrotron Rad.*, 2, 1, 1995.
6. Fredericks, W.; Hammonds, M.; Howard, S.; and Rosenberger, F.: *J. Cryst. Growth*, 141, 183, 1994.
7. Blake, C.C.F.; Koenig, D.F.; Mair, G.A.; North, A.C.T.; Phillips, D.C.; and Sarma, V.: *Nature*, London, 206, 757, 1965.
8. Diamond, R.: *J. Mol. Biol.*, 82, 371, 1974.
9. Wilson, K.P.; Malcolm, B.A.; and Matthews, B.W.: *J. Biol. Chem.*, 267, 10842, 1992.
10. Vaney, M.C.; Maignan, S.; Riès-Kautt, M.; and Ducruix, A.: *Acta Cryst.*, D52, 505, 1996.
11. Abola, E.E.; Bernstein, F.C.; Bryant, S.H.; Koetzle, T.F.; and Weng, J.: *Crystallographic Databases—Information Content, Software Systems, Scientific Applications*, Vol. edited by F.H. Allen, G.B., R. Sievers, pp. 107–132, 1987. Bonn/Cambridge/Chester: Data commission of the international union of crystallography.
12. Fourme, R.; Dhez, P.; Benoit, J.-P.; Kahn, R.; Dubuisson, J.-M.; Besson, P.; and Frouin, J.: *Rev. Sci. Instrum.*, 63, 982, 1992.
13. Fourme, R.; Riès-Kautt, M.; Ducruix, A.; and Capelle, B.: *J. Synchr. Rad.*, 2, 136, 1995.



(a)



(b)

Figure 1. Crystals of triclinic lysozyme (a) and monoclinic lysozyme (b).

EXPERIMENT XX.

CRYSTALLIZATION OF RNA MOLECULES UNDER MICROGRAVITY CONDITIONS

Page intentionally left blank

CRYSTALLIZATION OF RNA MOLECULES UNDER MICROGRAVITY CONDITIONS

Dr. Volker A. Erdmann

Fachbereich Chemie
Institut für Biochemie
Freie Universität Berlin
Thielallee 63
D-14195 Berlin, Germany
Phone: 011-49-30-838-6002
Fax: 011-49-30-838-6403

1. PURPOSE

Ribonucleic acids (RNA's) are essential macromolecules in living cells because they can assume not only structural functions (in the ribosomes) but also enzymatic functions (ribozymes) and can act as carriers of genetic information. This diversity has led to a new research field, called RNA-technologies, in which the structural and functional potentials of RNA are used in the areas of molecular biology, biotechnology, and medical diagnostics and therapy. To develop the RNA-technologies, it is essential that the structures of RNA molecules be determined at atomic resolution. The large size of RNA molecules limits structural determination to x-ray crystallography. One problem with the x-ray method is that it requires crystals of suitable size and quality for successful analysis. It is known that more than 20 different parameters influence the crystallization of biological molecules. Gravity is one of these influencing factors.

The goal of this APCF project was to analyze the influence of gravity on the crystallization of RNA molecules. The RNA molecules chosen for this study are ribosomal 5S RNA's (5S rRNA's) from *Thermus flavus*. The 5S rRNA molecules are essential components of the ribosomes, which are large RNA-protein complexes responsible for the synthesis of all cellular proteins. Since the 5S rRNA crystals obtained so far have exhibited a resolution of only 8 Å, which is not enough for x-ray analysis, the USML-2 experiment was designed to improve the quality of these crystals and to determine whether this improvement can be achieved under microgravity conditions.

2. METHOD

The crystallization experiments performed during the USML-2 mission consisted of *Thermus flavus* 5S rRNA species, which had been engineered at their 3'- and 5'-ends in such a way that their structures were more stable than the wild-type molecule. It was anticipated that the structurally stabilized 5S rRNA variants would be better suited for the crystallization and x-ray analysis.

The crystallization experiments were performed in five APCF reactor chambers (15-µl volume). The crystallization method used was microdialysis.

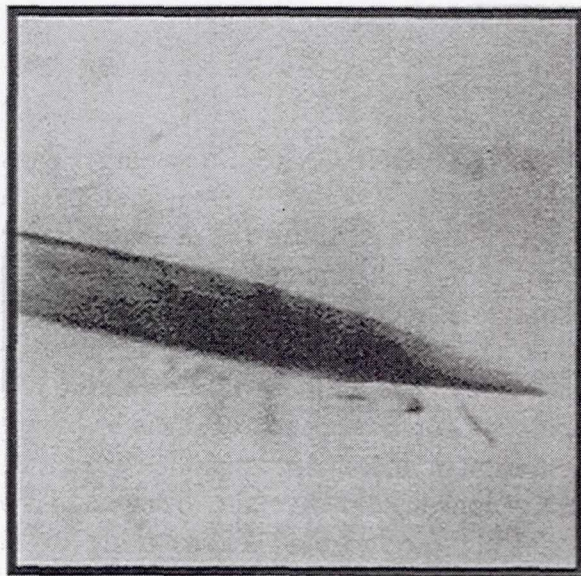
3. RESULTS

Of the five crystallization experiments performed, three yielded crystals. The crystals obtained were larger in size and more numerous than those obtained in simultaneous ground-control experiments. The largest space-grown crystals exhibited a length of 0.7 mm. In the ground-control experiments, only two chambers yielded crystals. These were smaller in size and less numerous than those grown in space. The largest crystal had a length of 0.45 mm. Figure 1 shows samples of the ground- and space-grown crystals.

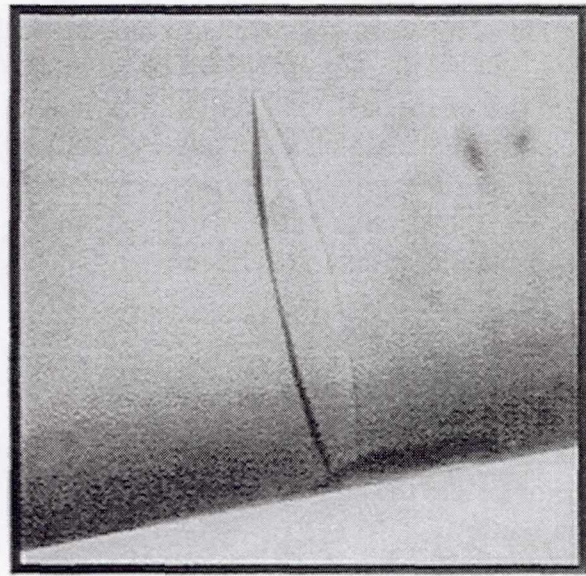
All crystals were analyzed by synchrotron radiation at the DESY facility in Hamburg, Germany, 6 days after landing. Both space and ground-control crystals exhibited a resolution of 13 Å.

4. PRELIMINARY CONCLUSIONS

The results show that the crystallizations performed in space yielded more and larger crystals than those in the ground experiments. The fact that the space crystals did not exhibit a better resolution by x-ray analysis may be connected to the last launch delay. During the 7-day delay, the RNA samples were stored at 20 °C. Ground-control studies have shown that an 11-day storage period at 20 °C caused a yield in only two of five crystal growth chambers. Storage at that temperature for 4 days has shown crystal growth in four of five chambers. The results, therefore, imply that an extended storage of the RNA molecules at 20 °C will have a negative effect upon the crystallization process. Better results are anticipated in future missions in which the nominal period of storage (4 days) is not exceeded.



(a)



(b)

Figure 1. Crystals obtained from *Thermus flavus* engineered 5S rRNA molecules grown under microgravity conditions (a) and in a laboratory control experiment (b).

Page intentionally left blank

EXPERIMENT XXI.

**COMPARATIVE ASSESSMENT OF MICROGRAVITY- AND EARTH-GROWN CRYSTALS
THAUMATIN AND ASPARTYL-tRNA SYNTHETASE**

ACKNOWLEDGMENTS

This research was supported by the Centre National d'Etudes Spatiales (CNES), and the Centre National de la Recherche Scientifique (CNRS). We acknowledge the help of Philippe Dumas, A. Théobald-Dietrich, and C. Sauter at various steps of this project in Strasbourg. We thank J.R. Helliwell for discussions on mosaicity. We are grateful to R. Bosch and P. Lautenschlager at Dornier GmbH for their technical support. We thank DESY at Hamburg for the provision of synchrotron facilities. Our appreciation also extends out to the European Space Agency (ESA) and NASA for flight opportunities in Europe on the Space Shuttle. Final thanks go to K. Fuhrmann and O. Minster of ESA for their administrative support.

COMPARATIVE ASSESSMENT OF MICROGRAVITY- AND EARTH-GROWN CRYSTALS THAUMATIN AND ASPARTYL-tRNA SYNTHETASE

Joseph D. Ng
Bernard Lorber
Richard Giegé
UPR 9002 IBMC du CNRS
15 rue Descartes
F-67084 Strasbourg Cedex, France

The plant sweetening protein, thaumatin, from *Thaumatococcus daniellii* (molecular weight of 25 kD)¹ and the thermophilic aspartyl-tRNA synthetase (ttAspRS) from *Thermus thermophilus* (molecular weight of 120 kD)² were studied here as model proteins for crystallization under microgravity aboard the U.S. Space Shuttle mission USML-2 (STS-73). Following retrieval of the samples, postflight microscopy and x-ray analyses were carried out on the crystals grown in microgravity and on ground controls prepared in parallel. We have evaluated and compared the quality of space- and Earth-grown thaumatin crystals for x-ray diffraction studies characterized by size, relative plots of I/sigma versus resolution, and mosaicity.

1. CRYSTALLIZATION APPARATUS AND CONDITIONS USED

We have utilized dialysis liquid diffusion reactors (DIA) for crystallization within the Advanced Protein Crystallization Facility (APCF) developed by Dornier Deutsch Aerospace^{3, 4} aboard the Space Shuttle. The dialysis reactor consists of two quartz glass blocks separated by a dialysis membrane. The upper block contains the protein solution (67 μ l or 188 μ l), the lower block, the salt solution. A cylindrical quartz glass plug containing a buffer solution separates the salt and buffer chambers. Upon rotation of the glass plug, all chambers become open and all volumes then come into contact. Likewise, the plug is rotated back during deactivation before returning to Earth. Reactors for space and ground controls were prepared in exactly the same manner and underwent the exact same transport and prelaunch conditions (including any delay in launch time). The DIA ground control reactors were also activated for the same period of time as the ones that were launched in space in parallel with the time of flight.

1.1 Thaumatin

Thaumatin was purchased from Sigma (St. Louis, MO). A single batch (Cat. No. T-7638, lot 108F0299) of dry protein powder was used. The protein was dissolved in a buffer prepared with 0.1M N-[2-acetamido]-2 iminodiacetic acid (ADA) (Cat. No. A-98883, lot 92H5635, Sigma) adjusted at pH with NaOH to a protein concentration between 6-20 mg/ml. For crystallization, the precipitant stock solution was 1.6M sodium DL t-tartaric acid (Cat. No. T-5259, lot 101H0695, Sigma) in 0.1M ADA titrated with NaOH to pH 6.5. All solutions were prepared with ultrapure sterile water (Fresenius, Louviers, France) and sterilized by filtration through 0.22- μ m pore size membranes (Millex, Millipore). A concentrated stock solution of thaumatin was freshly prepared by adding 1 ml of ADA buffer pH 6.5 to 100 mg protein

powder. After dissolution, the solution was centrifuged for 20 min at 15,000 g. The supernatant was filtered through 0.22- μ m Ultrafree low binding membranes (Cat. No. UFC# 0GV 00, Millipore). The protein concentration was calculated from the UV absorbance of a 1/250 dilution using a molar extinction coefficient of 28,270 (based on the tryptophan and tyrosine content).

Five APCF dialysis (DIA) reactors were used to investigate crystal growth under microgravity conditions. These include four 188- μ l DIA reactors, each one containing thaumatin solutions in the protein, buffer, piston T-type, and salt chambers. A 67- μ l DIA reactor with the same chamber components also was used, but it included different protein concentrations. Ground controls for all DIA reactors were prepared in exactly the same manner as the microgravity experiments and underwent the exact same transport and prelaunch conditions, including the launch delay time.

1.2 Aspartyl-tRNA Synthetase

Thermophilic AspRS has been cloned and overexpressed in *E. coli*. The protein was purified in a three-step procedure, including a flocculation at 70 °C and two chromatographies on DEAE-cellulose and hydroxyapatite columns. Starting with 50 g of overexpressing *E. coli* cells yields about 50 mg of pure enzyme. As estimated by activity assays, gel electrophoresis, and dynamic light scattering, the enzyme is pure and conformationally homogeneous.

AspRS was prepared in three 67- μ l dialysis and two 80- μ l hanging droplet reactors. The dialysis reactors were prepared as described above. The protein chamber contained 10 mg/ml in 5-percent saturated sodium formate in 25 mM Tris-HCl pH 7.5, 1 mM MgCl₂, and 0.1 mM EDTA. The buffer volume contained the same reagent as the protein chamber without the enzyme. The piston and salt chambers contained 30-percent, 35-percent, and 40-percent saturated sodium formate in 25 mM Tris-HCl pH 7.5, 1 mM MgCl₂, and 0.1 mM EDTA in each respective reactor. In the hanging droplet reactors, 10 mg/ml of AspRS in 12.5-percent and 15-percent saturated sodium formate mixed with 25 mM Tris-HCl pH 7.5, 1 mM MgCl₂, and 0.1 mM EDTA were set to equilibrate to 25-percent and 30-percent saturated sodium formate respectively in the two separate hanging drop reactors.

2. X-RAY INTENSITY MEASUREMENTS

Three-dimensional x-ray data were collected at the EMBL Outstation DESY, Hamburg, Germany, on beam line X11 using a MAR Research image plate. Complete data sets of space thaumatin crystals and their corresponding Earth controls were obtained using crystals of same size and volume. Data were collected at 20 °C with a crystal-to-detector distance of 250 mm. Oscillation angles of 0.5° were used with an x-ray wavelength of approximately 0.91 Å with exposure time varying from 20 to 30 sec. Data collection was evaluated on line with the programs DENZO and SCALEPACK⁵ at the DESY synchrotron station. Both Earth- and microgravity-grown crystals were collected to 1.6 Å with R_{sym} ranging from 0.025 to 0.115 to the limits of resolution of the data set for reflections having an I/σ greater than 3.

Laue diffraction patterns have been recorded with synchrotron radiation at the same facility as previously described above for two microgravity- and two Earth-grown crystals. The Laue geometry is particularly sensitive to mosaic spread and a relationship between mosaic spread and Laue spot extension was deduced. The reflection profile was used to make deductions about the mosaic spread and its uniformity. Medium intensity diffraction spots were collected in all cases to avoid any flaring of spots.

3. RESULTS AND DISCUSSION

3.1 Thaumatin

3.1.1 Visual and Microscopic Observations

The number and sizes of crystals were assessed with an optical microscope and are summarized in table 1. Each of the flight reactors contained 30 to 250 crystals having a size range of 0.4 mm to 1.8 mm. The corresponding ground control reactors contained approximately 550 to more than 1,000 crystals having a size of 0.1 mm to 0.9 mm. Figures 1 and 2 contain representative photographs of the microgravity-grown crystals compared to corresponding Earth-grown crystals. The average length or volume of protein crystals grown under microgravity was approximately 5 times larger with about 100 times less nucleation than to their corresponding Earth control crystals.

Table 1. Number and size of space- and Earth-grown crystals in APCF dialysis reactors.

Reactor	Space		Corresponding Earth Controls	
	No. of Crystals	Average Size (mm) (longest dimensions)	No. of Crystals	Average Size (mm) (longest dimensions)
(Protein chamber size)				
1 (67 μ l)	30	1.5	550	0.8
2 (188 μ l)	150	0.6	1,000+	0.1
3 (188 μ l)	50	0.6	1,000+	0.1
4 (188 μ l)	275	0.5	1,000+	0.1
5 (188 μ l)	150	0.5	1,000+	0.1

Reactors containing more than 1,000 crystals are noted as 1,000+. The number of crystals exceeding over 1,000 could not be measured with high accuracy; therefore, a more precise number was not indicated in these reactors.

Visually, the quality of the crystals, particularly those growing free of any surfaces and including the largest, was very high. They appeared virtually flawless, with no observable imperfections, striations, or habit anomalies. Crystals attached to the cell walls (and which presumably nucleated there) did show defects near the sites of growth initiation but became flawless as growth proceeded into the bulk solution.

3.1.2 X-ray Intensity Measurements

Thaumatin crystals obtained on Earth and in space are tetragonal having space group $P4_12_12$ with unit cell dimensions of $a = b = 58.6 \text{ \AA}$, $c = 151.8 \text{ \AA}$, $\alpha = \beta = \gamma = 90^\circ$. A complete data set from a crystal grown in microgravity was analyzed by comparing the average intensities divided by their estimated error (I/σ) as a function of resolution along with comparable data from the Earth-grown control (fig. 2). The amount of data greater than 3σ (the average I/σ in all resolution ranges) was better by a considerable extent for the microgravity crystal than for that grown on Earth. Both Earth and space crystals diffract easily beyond 1.6 \AA with the inclination of the space-grown crystal to extend to higher resolution. The true limit of

resolution for microgravity crystals was never measured in this analysis because technical constraints prevented collection of data beyond 1.6 Å resolution. These results are similar in most cases to other protein crystals grown in microgravity.^{6,7}

We have performed mosaicity studies on the thaumatin crystals grown in space in comparison to those obtained on Earth to see if there is any direct association between improved I/σ values for weak reflections with the mosaic properties in the crystals. Representative samples of reflections at various Bragg angles were scanned, and the full widths at half maximum intensity were quantified (table 2). Crystals grown in space have lower mosaicity than those grown in laboratories on the ground. These measurements were made on a synchrotron beam line assumed to have an almost parallel beam, such that the angular width of the diffraction profile would be dominated by the mosaicity of the crystal rather than the x-ray beam divergence or spectral spread.

Table 2. Crystal mosaicities estimated from Laue spot sizes.

	EARTH 1	EARTH 2	SPACE 1	SPACE 2
η dev. spots	0.0081	0.0075	0.0049	0.0035
	0.0003	0.0005	0.0006	0.0007
	10	9	12	11

Reflection spot sizes were converted to mosaic spread values, η according to the formula (Andrews, Hails, Harding & Cruichshank, 1987) $\Delta_{\text{radial}} = 2\eta D/\cos^2\theta$ where Δ_{radial} is the spot size, with the direct beam size at the detector subtracted out, D is the crystal-to-detector distance and the θ Bragg angle of a Laue spot.

3.2 Thermophilic Aspartyl-tRNA Synthetase

None of the reactors that contained AspRS contained any crystals of diffractable size. Most of the reactors contained slight precipitation, and in one of the dialysis reactors, very small crystals were observed. These small crystals had an estimated size of less than 0.050 mm. We have speculated that the activity of this particular enzyme did not withstand the flight delay of this mission. Even though AspRS is known to retain its activity longer than most enzymes, the observation of precipitation suggests that the protein had denatured during the extended delay. This was also observed in the ground-control reactors where the preactivation and activation conditions were treated as identically as possible. Earlier ground-control tests did produce crystals under the same crystallization conditions, where the duration of the preactivation step was not as long.

4. CONCLUSION

The improvement of mosaicity in space-grown crystals over Earth-grown is certainly linked to the improved I/σ values for all reflections. The most striking observation is that the increase in peak count is more than expected from the consideration of crystal volume. Overall, our observations here with thaumatin indicate that its crystal growth is more favorable in a gravity-free environment. In a practical sense, these studies contribute to the understanding and improvement of measuring weak reflections such as that occurring at high diffraction resolution for structure determination.

Apart from lysozyme, no other protein has been used to investigate the direct mosaicity differences between Earth-grown and space-grown crystals. We show here the mosaicity values of microgravity-grown thaumatin are improved by about a factor of two over the Earth-grown control values. This is comparable to what has been observed for tetragonal lysozyme where space-grown crystals were improved by a factor of three over its corresponding Earth control.^{8, 9, 10} It is evident that the decrease in mosaicity values observed in the thaumatin space-grown crystals is accompanied by a reduction in the number of mosaic blocks in a crystal. Further investigations with thaumatin and other proteins are needed to determine whether crystals grown under nonconvective flow environment (e.g., microgravity, gels) can be consistently correlated to their smaller mosaic spread.

The general conclusion for thaumatin crystal growth is that microgravity provides better looking and higher crystallographic quality crystals as judged by their intensity of diffraction and mosaicity.

The data reported here have contributed to a formal publication¹¹.

REFERENCES

1. De Vos, A.M.; Hatada, M.; Van der Wel, H.; Krabbendam, H.; Peerdeman, A.F.; and Kim, S.H.: *Proc. Natl. Acad. Sci. USA*, 82, 1406–1409, 1985.
2. Delarue, M.; Potersman, A.; Nikonov, S.; Garber, M.; Moras, D.; and Thierry, J.-C.: *EMBO*, 13, 3219–3229, 1994.
3. Snyder, R.; Fuhrmann, K.; and Walter, H.U.: *J. Cryst. Growth*, 110, 333–338, 1991.
4. Bosch, R.; Lautenschlager, P.; Potthast, L.; and Stapelmann, J.: *J. Cryst. Growth*, 122, 310–316, 1992.
5. Otwinowski, Z.; and Minor, W.: *Methods in Enzymology*, 276, C.W. Carter, Jr., and R.M. Sweet, Eds., Academic Press, 1996.
6. DeLucas, L.J.; Suddath, F.L.; Snyder, R.; Naumann, R.; Broom, M.B.; Pusey, M.; Yost, V.; Herren, B.; Carter, D.; Nelson, B.; Meehan, E.J.; McPherson, A.; and Bugg, C.E.: *J. Cryst. Growth*, 76, 681–693, 1986.
7. McPherson, A.; Greenwood, A.; and Day, J.: *Adv. Space Res.*, 7, 343–356, 1991.
8. Helliwell, J.R.: *J. Cryst. Growth*, 90, 259–272, 1988.
9. Ferrer, J.-L.; Hirschler, J.; Roth, M.; and Fontecilla-Camps, J.C.: *ESRF Experiments Reports*, 27–29, 1996.
10. Snell, E.H.; Weisgerber, S.; Helliwell, J.R.; Weckert, E.; Holzer, K.; and Schroer, K.: *Acta Crystallographica D51*, 1099–1102, 1995.
11. Ng, J.D.; Lorber, B.; Giegé, R.; Koszelak, S.; Day, J.; Greenwood, A.; and McPherson, A.: *Acta Crystallographica*, in press, 1997.

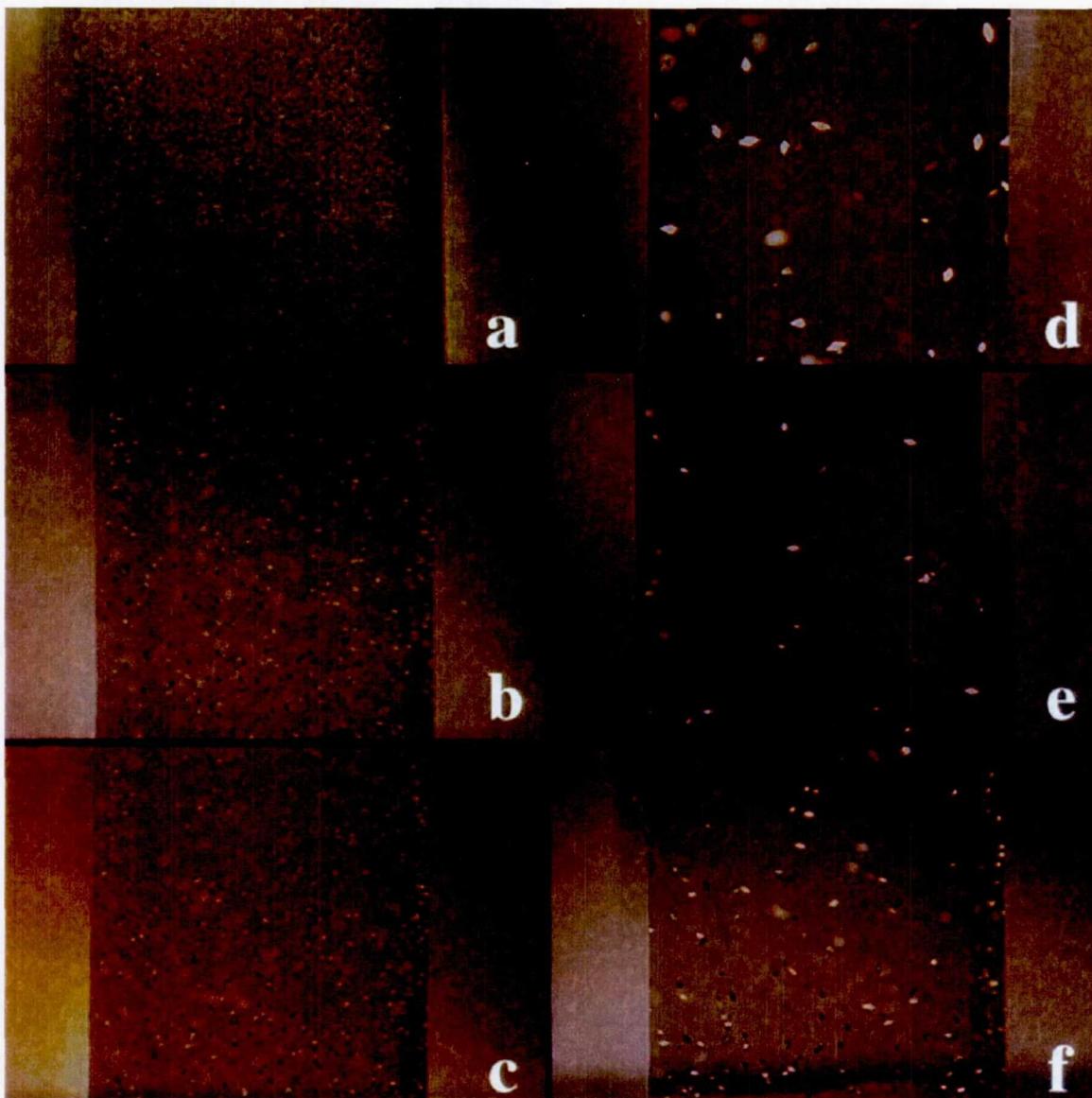


Figure 1. Comparison of thaumatin crystals grown on Earth (a-c) to those grown in microgravity (d-f). Only the protein containing chambers of the reactors are shown, and those seen here represent what is typically observed in the 188- μ l volume APCF dialysis reactors with low concentrations of thaumatin (6 mg/ml). Numerous and extremely small crystals are observed in the ground controls compared to only a few larger crystals in space. The average longest dimensions measured for crystals grown on Earth and in space were 0.1 mm and 0.5 mm, respectively. All images are at the same magnification.



Figure 2. Earth-grown thaumatin crystals (a) compared to space-grown crystals (b) in a 67- μ l volume APCF dialysis reactor. The images show the protein chambers containing crystals grown at high concentrations of thaumatin (20 mg/ml). Crystals grown on Earth ranged in size from 0.1 mm to 1.2 mm in the longest dimensions, and most of the crystals are seen to have sedimented to the bottom membrane. Space-grown crystals, on the other hand, grew with a size range of 0.5 mm to 1.7 mm from apex to apex. Fewer and larger crystals were observed in this space reactor than for the corresponding Earth-control reactor.

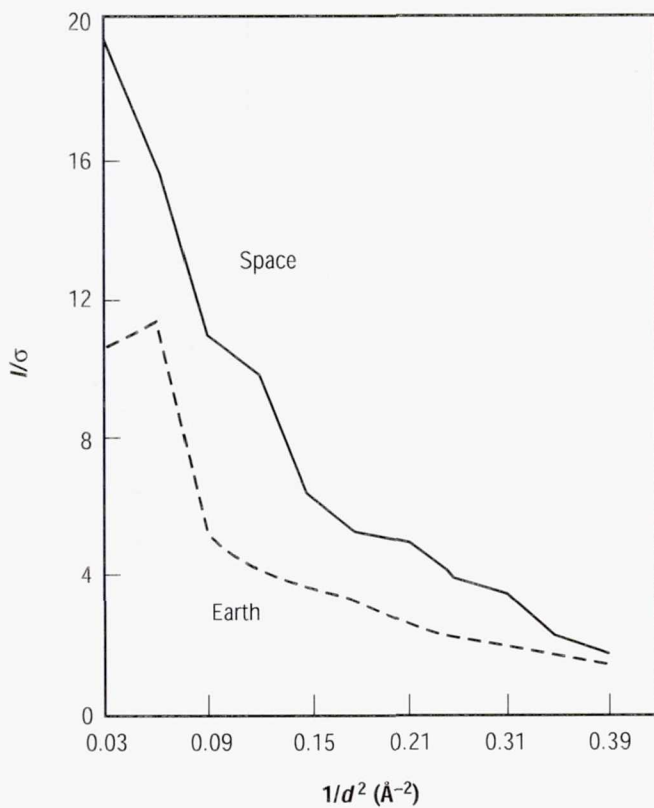


Figure 3. Graph of the intensity (I) versus estimated error (σ) ratio as a function of resolution [$1/d^2 (\text{\AA}^{-2})$] for thaumatin Earth- and space-grown crystals.

EXPERIMENT XXII.

**CRYSTALLIZATION IN SPACE OF DESIGNED AND NATURAL
(α/β)-BARREL STRUCTURES**

Page intentionally left blank

CRYSTALLIZATION IN SPACE OF DESIGNED AND NATURAL (α/β)-BARREL STRUCTURES

Prof. Joseph A. Martial

Dr. Véronique Mainfroid

University of Liège

Laboratory of Molecular Biology and Genetic Engineering

Institute of Chemistry, B6

B-4000 SART TILMAN BELGIUM

Phone: 32-4-366.33.71

Fax: 32-4-366.29.68

E-mail address: jmartial@ulg.ac.be

1. INTRODUCTION

The *de novo* design of proteins is an original and promising approach to elucidate the forces stabilizing well-defined protein tertiary structures. Determination of *de novo* structures using x-ray crystallography provides the most critical test for the concepts and principles used to guide protein design.

To date, two generations of octarellins, artificial proteins modeled on the α/β -barrel fold, were completed in our laboratory.^{1, 2, 3} Octarellins I and II exhibit an eight-fold symmetry, since a basic motif (loop– β -strand–loop– α -helix) is repeated eight times; while in octarellin III, the β -strands exhibit a four-fold symmetry. All attempts to crystallize octarellin I, generated during the first design cycle, failed, and the low compactness of this protein was believed to be the main reason why it was so hard to crystallize. This is why the major aim when designing octarellins II and III, which belong to the second generation of artificial proteins, was to improve the proteins' compactness and solubility. Spectroscopic and biophysic characterizations revealed that both octarellins II and III are more compact and soluble than octarellin I.³ Octarellin II, which is only marginally stable, binds the hydrophobic probe ANS and exhibits no CD signal in the near-UV. On the contrary, octarellin III exhibits a high conformational stability and has a characteristic CD signal in the near-UV. Preliminary crystallization experiments were performed on octarellin II, notably during the IML-2 flight of July 1994. Very small crystals, unsuitable for data collection, were obtained and used as seeds for further crystallization experiments.

To determine the structural parameters leading to stable α/β -barrel folds, two natural proteins were also included in these crystallization experiments. Both are triosephosphate isomerases (TIM's), dimeric enzymes composed of two identical α/β -barrel monomers. The first one is a mutant of human TIM (hTIM), engineered to form a stable monomeric α/β -barrel protein.^{4, 5} The second is TIM from the hyperthermophilic bacterium *Thermotoga maritima*. Analysis of these α/β tridimensional structures (a monomeric and a thermostable TIM barrel) will contribute to the design of more stable "octarellin folds."

2. OBJECTIVE

The objective of the microgravity experiments performed during the USML-2 flight was to pursue the crystallization of both natural and *de novo* designed α/β -barrel structures. Crystallization of octarellin II was continued on the basis of the experimental conditions previously selected. Since octarellin III displays the best structural characterizations among the three artificial proteins, determination of its 3-dimensional structure appears to be of the highest interest and was initiated. Crystallization of *Thermotoga maritima* TIM and of the stable, monomeric mutant of human TIM was also initiated, to determine the structural parameters leading to a stable α/β -barrel fold. By including TIM crystallization trials, our aim was to obtain a set of data concerning a native α/β -barrel for use as a reference with which to compare the space-collected data of octarellins.

3. PROCEDURE

The production and thorough purification of large amounts of the various proteins to be studied were performed in the Liège-based laboratory. Preliminary crystallization assays were performed in Pr. Wijns' laboratory (University of Brussels, Belgium). Based on this screening, various conditions were selected for the hanging drop and FID reactors.

4. RESULTS

Reactors	Experimental conditions	Observations and results
FID 312 200 μ l	Protein chamber: Octarellin II: 10.1 OD Bottom solution: 295 μ l of 8-percent PEG 6000; 100 mM Tris/HCl, pH 8.5	Needle-shaped micro-crystals (fig. 1)
HD 107 80 μ l	Protein drop: 12 μ l of Octarellin III (5 mg/ml) in Tris/HCl 50 mM pH 8 + 68 μ l bottom solution Bottom solution: 25-percent PEG 5000; 0.01M NiZnSO ₄ ; 100 mM MES pH 6.5	No crystals obtained

HD 184	Protein drop: 40 μ l of <i>Thermotoga maritima</i> TIM (1.6 mg/ml) in Triethanolamine/HCl 100 mM pH 7.6 + 40 μ l bottom solution	Many small and very regular crystals (fig. 2)
80 μ l		
Video	Bottom solution: 2-percent PEG 400; 2M $(\text{NH}_4)_2\text{SO}_4$; 100 mM HEPES pH 7.5	
FID 305	Protein chamber: hTIM: 14.02 OD	Very small needle-shaped crystals
200 μ l		
Video	Bottom solution + salt chamber: 295 μ l of 15-percent PEG 5000; 100 mM MES pH 6.5	
FID 311	Protein chamber: monomeric hTIM mutant: 2.26 OD	Very small needle-shaped crystals
200 μ l	Bottom solution + salt chamber: 295 μ l of 15-percent PEG 5000; 100 mM MES pH 6.5	

5. CONCLUSIONS

The most significant results were obtained with octarellin II and *Thermotoga maritima* TIM.

Needle-shaped microcrystals of octarellin II were obtained in the space reactor (fig. 1) as well as in the Earth control. They were investigated at the synchrotron in Grenoble. In addition to this, three small crystals (10 microns) grown on Earth were found to diffract to below 3 \AA and were quite resistant to radiation damage. With these three crystals, 70 percent of data were collected. The results obtained through this project should be of considerable impact since no artificial protein with the size of octarellins has been crystallized to date. What's more, this project should enable us to integrate the tridimensional structural data obtained through the building of a third generation of octarellins.

Many small and very regular crystals of *Thermotoga maritima* TIM were obtained in the space reactor (fig. 2). They were used for diffraction assays at the synchrotron in Grenoble and were found to diffract to a resolution of 3 \AA . Crystals were also obtained in the ground control reactor (HD 102). We noted two different morphologies—a lot of needle-shaped crystals and some rare regular crystals bigger than those obtained in space. The latter diffracted up to 2.3 \AA . All these crystals were very sensitive to radiation damage. As a result, only a partial data set was collected.

For hTIM and the monomeric hTIM mutant, very irregular, needle-shaped crystals were obtained. They were unsuitable for data collection.

REFERENCES

1. Goraj, K.; Renard, A.; and Martial, J.A.: "Synthesis, Purification and Initial Structural Characterization of Octarellin, a *de novo* Polypeptide Modeled on the Alpha/Beta-barrel Proteins," *Protein Engng.*, 3, 259–266, 1990.
2. Beauregard, M.; Goraj, K.; Goffin, V.; Heremans, K.; Goormaghtigh, E.; Ruysschaert, J.M.; and Martial, J.A.: "Spectroscopic Investigation of Structure in Octarellin (A *de novo* Protein Designed to Adopt the Alpha/Beta-Barrel Packing)," *Protein Engng.*, 4, 745–749, 1991.
3. Houbrechts, A.; Moreau, B.; Abagyan, R.; Mainfroid, V.; Préaux, G.; Lamproye, A.; Poncin, A.; Goormaghtigh, E.; Ruysschaert, J.M.; Martial, J.A.; and Goraj, K.: "Second Generation Octarellins. Two New *de novo* ($\beta\alpha$)₈ Polypeptides Designed for Investigating the Influence of the β -Residue Packing on the α/β Barrel Structure Stability," *Protein Engng.*, 8, 249–259, 1995.
4. Mainfroid, V.; Terpstra, P.; Beauregard, M.; Goraj, K.; Frère, J.M.; Mande, S.C.; Hol, W.G.J.; and Martial, J.A.: "Three hTIM Mutants That Provide New Insights on Why TIM Is a Dimer," *J. Mol. Biol.*, 257, 441–456, 1996.
5. Mainfroid, V.; Mande, S.C.; Goraj, K.; Hol, W.G.J.; and Martial, J.A.: "Stabilization of Human Triosephosphate Isomerase by Improvement of the Stability of Individual α -Helices in Dimeric as Well as Monomeric Forms of the Protein," *Biochemistry*, 35, 4110–4117, 1996.



Figure 1. Needle-shaped micro-crystals of octarellin II obtained in space.

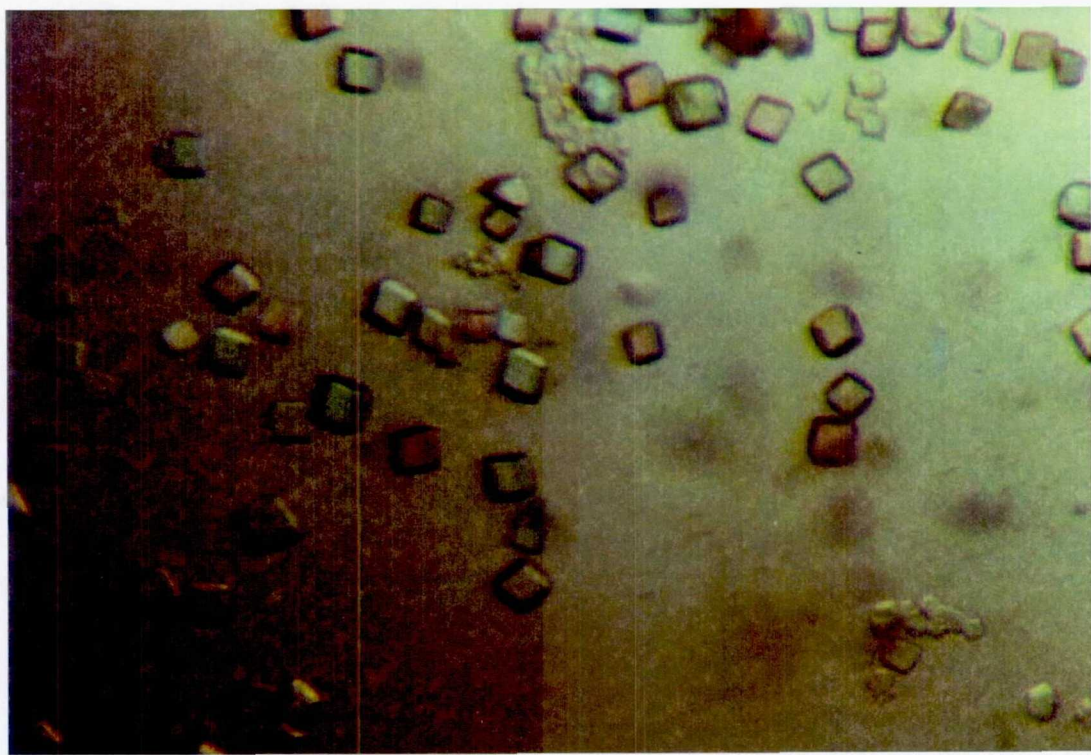


Figure 2. Regular shaped crystals of *Thermotoga maritima* TIM obtained in space.

EXPERIMENT XXIII.

**COMPARATIVE ANALYSIS OF THAUMATIN CRYSTALS GROWN ON EARTH
AND IN MICROGRAVITY**

ACKNOWLEDGMENTS

This research was supported by grants from the National Aeronautics and Space Administration (NASA), the Centre National d'Etudes Spatiales (CNES), and the Centre National de la Recherche Scientifique (CNRS). We acknowledge the help of Philippe Dumas, A. Théobald-Dietrich and C. Sauter at various steps of this project in Strasbourg. We thank J.R. Helliwell and J. Hirschler for discussions on mosaicity. We are grateful to R. Bosch and P. Lautenschlager at Dornier GmbH for their technical support. We are grateful to the ESRF at Grenoble for the provision of synchrotron facilities and M. Roth for his assistance. Our appreciation also extends out to the European Space Agency (ESA) for flight opportunities in Europe on the NASA Space Shuttle, and K. Fuhrmann and O. Minster of ESA for their administrative support. Finally, we thank CNES for a fellowship to J.D. Ng.

COMPARATIVE ANALYSIS OF THAUMATIN CRYSTALS GROWN ON EARTH AND IN MICROGRAVITY

Joseph D. Ng

Bernard Lorber

Richard Giegé (Corresponding Author)

UPR 9002, Structure des Macromolécules Biologiques et Mécanismes de Reconnaissance

Institut de Biologie Moléculaire et Cellulaire du CNRS

15 rue René Descartes

F-67084 Strasbourg Cedex, France

Stanley Koszelak

John Day

Aaron Greenwood

Alexander McPherson

University of California, Irvine

Department of Molecular Biology and Biochemistry

Irvine, California 92697-3900 USA

ABSTRACT

The protein thaumatin was studied as a model macromolecule for crystallization in microgravity environment experiments conducted on two U.S. Space Shuttle missions (second United States Microgravity Laboratory (USML-2) and Life and Microgravity Spacelab (LMS)). In this investigation we evaluated and compared the quality of space- and Earth-grown thaumatin crystals using x-ray diffraction analysis and characterized them according to crystal size, diffraction resolution limit, and mosaicity. Two different approaches for growing thaumatin crystals in the microgravity environment, dialysis and liquid-liquid diffusion, were employed as a joint experiment by our two investigative teams. Thaumatin crystals grown under a microgravity environment were generally larger in volume with fewer total crystals. They diffracted to significantly higher resolution and with improved diffraction properties as judged by relative Wilson plots. The mosaicity for space-grown crystals was significantly less than for those grown on Earth. Increasing concentrations of protein in the crystallization chambers under microgravity lead to larger crystals. The data presented here lend further support to the idea that protein crystals of improved quality can be obtained in a microgravity environment.

1. INTRODUCTION

Previous experiments have demonstrated that, in at least some cases, macromolecular crystals of improved quality can be grown in a microgravity environment as was obtained, for example, on the U.S. Space Shuttle or the Russian Space Station.^{1,2,3,4} Presently, the most extensively used facility for such experiments is the European Space Agency (ESA) designed Advanced Protein Crystallization Facility

(APCF).^{5,6} This system allows crystallization to proceed by vapor diffusion, batch, dialysis, and free interface diffusion methods and provides limited video recording of some experiments as they proceed in space.

On Space Shuttle missions USML-2, October 1995, and LMS, June 1996, joint experiments were carried out by our French (Strasbourg) and American (Riverside) groups based on the crystallization of the protein thaumatin. Using common protein, buffer, and precipitant solutions, thaumatin was crystallized at a variety of protein concentrations using two different approaches—dialysis and liquid-liquid diffusion. Following retrieval of the samples, postflight microscopy and x-ray analyses were carried out on the crystals grown in microgravity and on ground controls prepared in parallel. Of particular interest to us were 1) relevance of the choice of methodology, 2) the influence of protein concentration on crystal size, and 3) quantitative comparison of microgravity-grown crystals with those produced on Earth.

2. MATERIALS AND METHODS

2.1 Protein and Chemicals

Thaumatin was purchased from Sigma (St. Louis, MO). A single batch (Cat. No. T-7638, lot 108F0299) of dry protein powder was used. The protein was dissolved either in a buffer prepared with 0.1M N-[2-acetamido]-2 iminodiacetic acid (ADA) (Cat. No. A-9883, lot 92H5635, Sigma) adjusted at pH 6.5 with NaOH, or in water (table 1). For crystallization, the precipitant stock solution was 1.6 M sodium DL-tartrate acid (Cat. No. T-5259, lot 101H0695, Sigma) in 0.1M ADA titrated with NaOH to pH 6.5. All solutions were prepared with ultrapure sterile water (Fresenius, Louviers, France) and sterilized by filtration through 0.22- μm pore size membranes (Millex, Millipore).

Table 1. Content of APCF reactors.

Reactor No.	Flight	Type	Reactor Chambers								
			Protein			Buffer		Piston		Salt	
			Protein conc. (mg/ml)	Buffer	Volume (μl)	Buffer	Volume (μl)	Buffer	Volume (μl)	Buffer	Volume (μl)
1	USML-2	D	6	A	188	B	59	B	246	B	295
2	USML-2	D	6	A	188	B	59	B	246	B	295
3	USML-2	D	6	A	188	B	59	B	246	B	295
4	USML-2	D	6	A	188	B	59	B	246	B	295
5	USML-2	D	20	A	67	B	21	B	85	B	257
6	LMS	D	20	A	188	B	59	B	246	B	295
7	LMS	D	20	A	188	B	59	B	246	B	295
8	USML-2	FID	7	H_2O	470	N	N	A	235	A	598
9	USML-2	FID	17	H_2O	470	N	N	A	235	A	598
10	USML-2	FID	35	H_2O	470	N	N	A	235	A	598
11	LMS	FID	35	H_2O	470	N	N	A	235	A	598
12	LMS	FID	100	H_2O	470	N	N	A	235	A	598

Chambers exist for both APCF dialysis (D) and free interface diffusion reactors (FID) except for the buffer chamber which is absent in the FID cells.

Solution A: 0.1M ADA buffer and 0.20M sodium tartrate pH 6.5.

Solution B: 0.1M ADA buffer and 0.95M sodium tartrate pH 6.5.

N: None.

Ground reactors were prepared in parallel with the exact same content as those of reactors 1-7.

A concentrated stock solution of thaumatin was freshly prepared by adding 1 ml of ADA buffer pH 6.5 to 100 mg protein powder. After dissolution, the solution was centrifuged for 20 minutes at 15,000 g. The supernatant was filtered through 0.22- μ m Ultrafree low binding membranes (Cat. No. UFC3 OGV 00, Millipore). The protein concentration was calculated from the UV absorbance of a 1/250 dilution using a molar extinction coefficient of 28,270 (based on the tryptophan and tyrosine content). Solutions used by both laboratories were made in Strasbourg and divided between investigators.

2.2 Instrumentation and Crystallization Conditions

The APCF has been previously described^{5, 6} and, indeed, successful experiments with other proteins and viruses have been reported.^{3, 7, 8} An APCF unit provides for a total of 48 individual reactors maintained at constant temperature ($22^{\circ}\text{C} \pm 0.1^{\circ}$ in this case) from the time of loading, the duration of the mission, to analysis. Both dialysis and free interface diffusion cell types are activated by 90° rotation of a stopcock valve that establishes continuity between protein and precipitant chambers. For dialysis, a semi-permeable membrane separates the two chambers. In experiments conducted on USML-2 the Strasbourg group used five dialysis crystallization reactors and the Riverside group used three free interface diffusion reactors. For LMS, the Strasbourg group used two reactors of the dialysis type and the Riverside group used two reactors of the liquid-liquid diffusion type. The contents of the reactors and the crystallization conditions are described in table 1. Methodological aspects of the preflight ground experiments for optimal use of the APCF reactors during an actual space mission have been evaluated in a maiden experiment on SpaceHab-1 during the IML-2 mission in 1994.⁹

The APCF was activated on both the USML-2 and LMS missions several hours after a microgravity environment was achieved, and deactivated (the stopcocks rotated in reverse) a few hours before reentry. Duration of activation of the crystallization reactors under the microgravity environment was 14 days for the USML-2 mission and 16 days for the LMS mission. In the case of the dialysis cells, parallel experiments were carried out in Strasbourg in identical reactors during the periods of both missions. No parallel ground controls were carried out for the free interface diffusion reactors since the method functions quite differently in a 1g environment. Following the missions, the dialysis cells were returned to Strasbourg for analysis and the free interface diffusion cells to Riverside. They were, in both cases, immediately examined and photographed, and x-ray diffraction analysis was initiated.

2.3 Crystallographic Methods

At the University of California at Riverside, complete 3-dimensional x-ray diffraction data were collected at 17°C on the crystals grown on USML-2 by free interface diffusion as described previously^{10, 11, 12} from capillary-mounted crystals using a San Diego Multiwire Systems (SDMS) double multiwire detector system¹³ with crystal-to-detector distances of 900 mm and 838 mm. Frame sizes were 0.10° with 2.5 min/frame. The x-rays were generated by a Rigaku RU-200 rotating anode generator operated at 45 kV and 135 mA with a Supper monochromator to give $1.54\text{-}\text{\AA}$ wavelength radiation. Crystals were exposed for a total of 24–48 hours. Data collection procedures and experimental parameters were identical for both Earth- and space-grown crystals. Redundancy of recordings ranged from four to eight. Data correction, reduction, merging, and statistical analysis used the programs supplied by SDMS. For both Earth- and microgravity-grown crystals the R_{sym} 's varied from 0.035 to 0.06 to the limits of resolution of the data sets.

Three-dimensional x-ray data were collected from thaumatin crystals grown by the Strasbourg group on LMS using a Mars Research image plate and evaluated on line with the programs DENZO and SCALEPACK at the DESY synchrotron station, Hamburg, Germany.

The mosaicities of the thaumatin crystals, obtained under both ground and space growth conditions, were evaluated by measuring the rocking widths for selected reflections.¹⁴ Crystal mosaicity yields the angular dispersion of the crystal blocks characterizing the crystals and, in turn, reflects the intrinsic crystal order.¹⁵ Crystals of the same volumes were mounted in standard glass capillaries of 0.5-mm diameter. Space and ground control crystals with a size of 0.3 mm in the longest dimension were used for analysis. In these cases, the smallest crystals obtained from space were compared to the largest crystals obtained on the ground. Data for mosaicity measurements were recorded by using a CCD detector on beamline CRG BM2 (D2AM) at ESRF, Grenoble, France. This particular synchrotron beamline produces a highly collimated, intense radiation of very low divergence and minimal $\delta\lambda/\lambda$. The critical energy was 19.5 keV with a focused beam of 0.3-mm diameter at the sample with a maximum vertical divergence of 0.48 mrad and a maximum horizontal divergence of 9.0 mrad.¹⁶ The intensity of the full beam was about 10^{11} ph/sec at 0.98-Å wavelength with an energy resolution, $\delta\lambda/\lambda$, of approximately 10^{-4} . Direct monochromatic measurements were obtained by recording data over oscillation ranges of 0.5 degrees for indexing of reflections and subsequently an oscillation angle of 0.003 degrees with 0.2 degrees of crystal rotation at 10 sec. exposure per frame. The data for mosaicity analysis were processed with XDS and images of the intensities visually observed and quantitated with MARVIEW.

Reflections were measured in the vertical plane with respect to the direct beam so that a fully recorded reflection can be expressed as:

$$\varphi_r = \gamma + \eta + (\delta\lambda/\lambda)\tan\theta ,$$

where φ is the reflecting range, γ is the mean divergence in the plane defined by the direct and the diffracted beams, η is the crystal sample mosaicity, λ is the average wavelength of the x-ray beam, and θ is the Bragg angle of the reflection.^{7,16} The values of γ and $\delta\lambda/\lambda$ were minimized in this study by considering only reflections located in the vertical plane, including the incident beam and those at low resolution. The profiles presented here were not corrected for Lorentz broadening.

3. RESULTS AND DISCUSSION

3.1 The Protein Model

Thaumatin is a monomeric protein from the African serendipity berry (*Thaumatococcus daniellii*) valued for its intensely sweet taste and its use as a noncaloric sweetener. It has a molecular weight of 21,500, contains four disulfide bridges, and possesses a high degree of stability. It consists primarily of beta structure organized in two associated domains. The structure was first determined in an orthorhombic crystal at 1.7-Å resolution¹⁷ and later in a second orthorhombic, a monoclinic, and a tetragonal crystal form.¹⁷ The tetragonal crystal form, grown from tartrate and refined to 1.7-Å resolution,¹⁸ was the crystal form studied in these experiments. The mechanisms and kinetics of growth at the molecular level for thaumatin crystals are among the most thoroughly characterized of any protein crystal.^{19,20} Crystals can be

grown in a conventional laboratory in 12 to 48 hours at room temperature by a variety of methods. The crystals are of space group $P4_12_12$ with $a = b = 59 \text{ \AA}$ and $c = 158 \text{ \AA}$ having a single molecule as the asymmetric unit. The habit is that of a tetragonal bipyramid, often reaching linear dimensions in the conventional laboratory greater than 1 mm. The crystals, which contain about 45-percent solvent, are mechanically robust. Their growth has been studied by a variety of physical techniques including interferometry²¹ and atomic force microscopy.^{19, 20}

3.2 Visual and Microscopic Observations

For both missions, crystals were observed in all of the reactors, both dialysis and free interface diffusion, for microgravity and for ground controls. There was a clear increase in average and largest sizes of crystals grown by dialysis in microgravity compared with ground controls, as seen in table 2 and figures 1 and 2. In the best of the three free interface diffusion reactors, the largest crystals (fig. 3) were three to five times the volume of the best crystals produced in either laboratory on Earth. In both cell types some of the largest thaumatin crystals measured more than 2 mm from apex to apex of the tetragonal bipyramids.

Table 2. Number and size of space- and Earth-grown crystals in APCF dialysis reactors.

Reactor (Protein chamber size)	Space		Corresponding Earth Controls	
	No. of crystals	Average Size (mm) (longest dimensions)	No. of crystals	Average Size (mm) (longest dimensions)
1 (67 μl)	30	1.5	550	0.8
2 (188 μl)	150	0.6	1,000+	0.1
3 (188 μl)	50	0.6	1,000+	0.1
4 (188 μl)	275	0.5	1,000+	0.1
5 (188 μl)	150	0.5	1,000+	0.1
*6 (188 μl)	1,000+	0.4	1,000+	0.3
*7 (188 μl)	1,000+	0.4	1,000+	0.3

Reactors 1-5 were on USML-2 and 6*, 7* were on LMS.

Reactors containing more than 1,000 crystals are noted as 1,000+. The number of crystals exceeding over 1,000 could not be measured with high accuracy; therefore, a more precise number was not indicated in these reactors.

* Even though reactors flown on LMS contained many crystals from space as well as on the ground, it was qualitatively observed that there were less and bigger crystals grown in the space reactors than those that grew on earth.

The number and sizes of crystals from the dialysis reactors were assessed with an optical microscope and are summarized in table 2. Each of the flight reactors contained 30 to 250 crystals having a size range of 0.4 mm to 1.8 mm. The corresponding ground control reactors contained approximately 550 to more than 1,000 crystals having a size range of 0.1 mm to 0.9 mm. Figure 1 contains representative photographs of the microgravity grown crystals compared to corresponding Earth crystals.

A notable observation originating independently from both the Strasbourg group (using dialysis) and the Riverside group (using free interface diffusion) was the dependence of average and largest size on protein concentration, a primary experimental variable. Independent of approach, the largest crystals consistently grew at highest protein concentration and the smallest crystals at lowest protein concentration. This is shown in figure 3 for crystals grown at three different protein concentrations (35, 17, and 7 mg/ml) by free interface diffusion under otherwise identical conditions.

Visually, the quality of the crystals, particularly those growing free of any surfaces, and including the largest, was very high. They appeared virtually flawless, with no observable imperfections, striations, or habit anomalies. Crystals attached to the cell walls (and which presumably nucleated there) did show defects near the sites of growth initiation but became flawless as growth proceeded into the bulk solution.

3.3 X-ray Intensity Measurements

X-ray diffraction data were collected from a total of four thaumatin crystals grown in microgravity by free interface diffusion in microgravity. The data were merged to form a single data set. This microgravity set was then compared with the best data previously obtained from crystals grown in a conventional laboratory—data which were, in fact, used to solve and refine the reported structure of the tetragonal thaumatin crystals.¹⁸ This comparison is shown as a modified Wilson plot in figure 4 where average intensity divided by estimated error is presented as a function of $\sin^2\theta/\lambda^2$.

As with several previously reported investigations of macromolecular crystal growth in microgravity, two features of the comparison emerged. First, the I/σ ratio of reflections obtained for crystals grown in microgravity was higher (approximately double) than for ground-grown crystals, and over the entire resolution range analyzed. Second, the limit of resolution of the diffraction pattern was higher for microgravity-grown crystals when compared to that for crystals grown on Earth, 1.5-Å versus 1.7-Å resolution respectively. While 0.2 Å may appear only a marginal increase, it is significant in this portion of the resolution range and, combined with the improved I/σ over the entire resolution range, yields nearly 30 percent more diffraction intensities ($> 3 \sigma$) for the microgravity-grown crystals. We would like to point out that the true limit of resolution for the microgravity crystals was never measured in this analysis because technical constraints prevented collection of data beyond 1.5 Å. The continued strength of the diffraction pattern at the 1.5-Å mark suggested to us that the actual resolution limit of the microgravity grown crystals was beyond this point.

Figure 5 presents typical mosaicity profiles of three representative reflections from both space- and Earth-grown crystals obtained in the frame of the LMS experiment (broken lines). The reflection profiles lie in the vertical plane of diffraction at approximately a 4-Å resolution and were normalized for their direct comparison. The curves appear coarse, displaying numerous shoulders, particularly in the latter portions of the profiles (figs. 5A and 5B). For all reflections such irregularities were present, suggesting that the local features of the profile could be reflective of intrinsic properties of the crystal.

Each set of reflection profiles of the space- and Earth-grown crystals was averaged and Gaussian fits of the sets of profiles were calculated (solid lines). Full widths at half maxima (FWHM) of the Gaussian curves were measured, and in this case the FWHM was 48 millidegrees (0.048°) from a crystal grown on Earth (panel A) compared to 20 millidegrees (0.020°) from the space crystal (panel B).

Notably, in all the reflections of all the space-grown crystal mosaicity profiles analyzed, a principle shoulder is observed in the beginning of the profiles while the end of the profile remains very smooth and the curve diminishes sharply. We have no clear explanation for this observation. This phenomenon contributes to the nonsymmetrical fit of the Gaussian curves. In our measurements, the Gaussian plots are fitted to the principal peaks in which the FWHM's were evaluated. We have only considered the principal peak at this instant to represent the actual mosaicity profile for the space-grown crystals. Even if the shoulder

widths were included in the measurement of the FWHM, the value would still be significantly less than that of the Earth-grown crystals.

Consistently, reflections from crystals grown in microgravity from both space missions displayed narrower peaks of greater amplitude. This is likely a consequence of reduced or perhaps even virtual elimination of discrete defects and dislocations. The relative intensity and peak width differences of averaged profiles measured from reflections derived from space- and Earth-grown crystals presented in figure 5 typify the mosaicity of thaumatin crystals obtained on Earth and in space. Table 3 summarizes the mosaicity evaluations of the space- and Earth-grown crystals.

Table 3. Mosaicity characteristic of ground- and space-grown thaumatin crystals.

Crystal	Earth 1	Earth 2	Space 1	Space 2
FWHM (mdeg)	55	48	23	20
Deviation (mdeg)	5	5	3	5
Number of spots	5	3	5	3

Crystals labeled as (1) were retrieved from reactor No. 4 (USML-2) and (2) from reactor No. 7 (LMS).

4. CONCLUSIONS

The results presented here for thaumatin crystals grown in microgravity in the APCF by two different techniques are consistent. They reinforce the conclusions of other reports based on different macromolecules that a microgravity environment can provide unique advantages.²² In these experiments the best crystals grown in relatively few microgravity samples were compared with the best crystals obtained in many thousands of ground-based trials. Thus, on a purely statistical basis, the conventional laboratory results were highly favored. Yet the microgravity-grown crystals were consistently and significantly larger, and substantially more defect-free as judged by direct visual inspection. In this investigation this appears to be independent of the choice of crystallization method and the loading and handling of the APCF cells.

An interesting observation was the clear correlation between ultimate crystal size and protein concentration. We observed in both dialysis and free interface diffusion reactors that larger crystals were obtained at increasingly high protein concentrations in space. On Earth, developing protein crystals are continuously exposed to the full concentration of protein in the bulk solvent. Due to convective mixing, excessive and unfavorable supersaturation prevails throughout growth. In the absence of gravity, there is no convective mixing and thus solute transport is entirely dominated by diffusion.²³

Because of the large size of the protein molecules and their low diffusivity, concentration gradients form in the neighborhood of the growing crystal. Without convection, these gradients, or depletion zones, are quasi-stable in microgravity.²⁴ The crystals under these circumstances are exposed to nutrient solutions of reduced supersaturation. The process of macromolecular crystal growth in microgravity is in a sense self-regulating. This idea may explain the observations presented here which show both qualitatively and quantitatively that under a microgravity environment, crystal growth is improved compared to the Earth counterpart.

The results presented here suggest that in future experiments, larger crystals of greater perfection may be obtained by even further increasing macromolecule concentration over that utilized in the conventional laboratory. This is contrary to what one would do generally in the conventional laboratory where the best results are usually achieved at the lowest levels of supersaturation.

The resolution limit of the diffraction pattern, the I/σ ratio as a function of the Bragg angle, and the mosaic spread of crystals are generally agreed to reflect both the degree of internal order and the long-range defect structure and its distribution within the crystal. That is, they serve as measures of the average statistical disorder of the molecules about the lattice points, as well as the extent of local but severe disorder introduced by defects such as dislocations, stacking faults, point defects, or incorporated foreign material.²⁵ All of the data presented here, both intensity distributions and mosaic spread measurements, imply a higher degree of internal order, a lower defect density, and a reduction of severe faults for crystals grown in the absence of gravity.

While similar results, based on intensity data for microgravity-grown crystals of several proteins, have been reported previously,^{1, 2, 24} and comparable results based on mosaicity measurements have been presented for others,²⁶ this is the first experiment to produce crystals grown by multiple methods and analyzed by both approaches. Indeed, our conclusion is that they are mutually supportive and complementary, and both suggest the same conclusion—that crystals grown in microgravity can be significantly improved in their diffraction properties when compared with those grown on Earth.

Apart from lysozyme, no other protein crystal has been used to investigate mosaicity differences between Earth-grown and space-grown crystals. The data presented here indicate that the mosaic spread of reflections from microgravity-grown thaumatin are reduced by more than a factor of two over Earth-grown crystals. This is comparable to what was observed for tetragonal lysozyme where space-grown crystals were observed to be improved by a factor of three over corresponding Earth controls.^{26, 16, 7}

Thaumatin crystals grown on Earth may be comprised of multiple mosaic blocks represented by shoulders in the profiles which can be decomposed into unresolved minor peaks. Substructures of a mosaic crystal could contribute to the individual peaks and such substructural components in single crystals may be a consequence of crystal growth dislocations. The density of these dislocations is not uniform as they have the tendency to group themselves into cell (subgrain) boundaries.²⁷ This is indicated by the monochromatic x-ray topographs of hen egg white lysozyme which show fluctuating rocking width profiles corresponding to the misorientation of subgrains.²⁸ In the case of thaumatin, atomic force microscopy (AFM) studies have shown that crystals exhibit a variety of defects ranging from unoccupied lattice sites, to linear defects, and to stacking faults.²⁰ The profiles shown in figure 5 typify the mosaic spread obtained from all control crystals analyzed, and their irregular profiles may reflect the ensemble of defects characteristic of Earth-grown crystals. The Gaussian fits of representative space-grown crystal reflection profiles have average FWHM values about 2.5 times less than those of Earth-grown crystals (figure 5b). In contrast to profiles from Earth-grown crystals, those of the space-grown crystals are smoother and more intense, and display narrower peaks.

REFERENCES

1. DeLucas, L.J.; Smith, C.D.; Smith, H.W.; Senagdi, V.K.; Senadhi, S.E.; Ealick, S.E.; Bugg, C.E.; Carter, D.C.; Snyder, R.S.; Weber, P.C.; Salemme, F.R.; Ohlendorf, D.H.; Einspahr, H.M.; Clancy, L.; Navia, M.A.; McKeever, B.; Nagabhushan, T.L.; Nelson, G.; Babu, Y.S.; McPherson, A.; Koszelak, S.; Stammers, D.; Powell, K.; and Darby, G.: *Science*, 246, 651–654, 1989.
2. Day, J.; and McPherson, A.: *Protein Science*, 1, 1254–1268, 1992.
3. Koszelak, S.; Day, J.; Leja, C.; Cudney, R.; and McPherson, A.: *Biophys. J.*, 69, 13–19, 1995.
4. Long, M.M.; Bishop, J.B.; Nagabhushan, T.L.; Reichert, P.; Smith, G.D.; and DeLucas, L.J.: *J. Cryst. Growth*, 168, 233–243, 1996.
5. Snyder, R.S.; Fuhrmann, K.; and Walter, H.U.: *J. Cryst. Growth*, 110, 333–338, 1991.
6. Bosch, R.; Lautenschlager, P.; Potthast, L.; and Stapelmann, J.: *J. Cryst. Growth*, 122, 310–316, 1992.
7. Snell, E.H.; Weisgerber, S.; Helliwell, J.R.; Weckert, E.; Hölzer, K.; and Schroer, K.: *Acta Cryst.*, D51, 1099–1102, 1995.
8. Chayen, N.E.; Gordon, E.J.; and Zagalsky, P.F.: *Acta Cryst.*, D52, 156–159, 1996.
9. Riès-Kautt, M.; Broutin, I.; Ducruix, A.; Shepard, W.; Kahn, R.; Chayen, N.; Blow, D.; Paal, K.; Littke, W.; Lorber, B.; Théobald-Dietrich, A.; and Giegé, R.: *J. Cryst. Growth*, submitted 1997.
10. Ko, T.-P.; Ng, J.D.; and McPherson, A.: *Plant Physiol.*, 101, 729–744, 1993a.
11. Ko, T.-P.; Ng, J.D.; Day, J.; Greenwood, A.; and McPherson, A.: *Acta Cryst.*, D49, 478–489 1993b.
12. Larson, S.B.; Koszelak, S.; Day, J.; Greenwood, A.; Dodds, A.; and McPherson, A.: *J. Mol. Biol.*, 231, 375–391, 1993.
13. Xuong, N.-H.; Nielson, C.; Hamlin, R.; and Anderson, D.: *J. Appl. Cryst.*, 18, 342–360, 1985.
14. Helliwell, J.R.: *J. Cryst. Growth*, 90, 259–272, 1988.
15. Weisgerber, S.; and Helliwell, J.R.: Joint CCP4 & ESF-EACBM newsletter on Protein Crystallography, 29, 10–13, 1993.
16. Ferrer, J.-L.; Hirschler, J.; Roth, M.; and Fontecilla-Camps, J.C.: *ESRF Experiments Reports*, 27–28, 1996.
17. Ogata, C.M.; Gordon, P.F.; de Vos, A.M.; and Kim, S.H.: *J. Mol. Biol.*, 3, 893–908, 1992.
18. Ko, T.-P.; Day, J.; Greenwood, A.; and McPherson, A.: *Acta Cryst.*, D50, 813–825, 1994.
19. Malkin, A.J.; Kuznetsov, Yu-G.; and McPherson, A.: *J. Struct. Biol.*, 117, 124–137, 1996a.
20. Malkin, A.J.; Kuznetsov, Yu-G.; Glantz, W.; and McPherson, A.: *J. Phys. Chem.*, 100, 11736–11743, 1996b.
21. Kuznetsov, Yu-G.; Malkin, A.J.; Greenwood, A.; and McPherson, A.: *J. Struct. Biol.*, 114, 184–196, 1995.
22. Giegé, R.; Drenth, J.; Ducruix, A.; McPherson, A.; and Saenger, W.: *Prog. Cryst. Growth and Charact.*, 30, 237–281, 1995.
23. Pusey, M.; Witherow, W.K.; and Naumann, R.: *J. Cryst. Growth*, 90, 105–111, 1988.
24. Koszelak, S.; Leja, C.; and McPherson, A.: *Biotech. and Bioeng.*, 52, 449–458, 1996.
25. McPherson, A.: *Crystallography Reviews*, 6(2), 157–308, 1996.
26. Helliwell, J.R.; Snell, E.; and Weisgerber, S.: *Materials and Fluids Under Low Gravity*, Lecture Notes in Physics (L. Ratke, H. Walter and B. Feuerbacher, eds), 155–170, Springer, 1996.
27. Rosenberger, F.; Muschol, M.; Thomas, B.R.; and Vekilov, P.G.: *J. Cryst. Growth*, 168, 1–27, 1996.
28. Fourme, R.; Ducruix, A.; Riès-Kautt, M.; and Capelle, B.: *J. Synchrotron Rad.*, 2, 136–142, 1995.
29. Wilson, A.J.C.: *Acta Cryst.*, 2, 318–321, 1949.
30. Wilson, A.J.C.: Elements of X-ray intensities. Addison-Wesley, Reading, 1970.

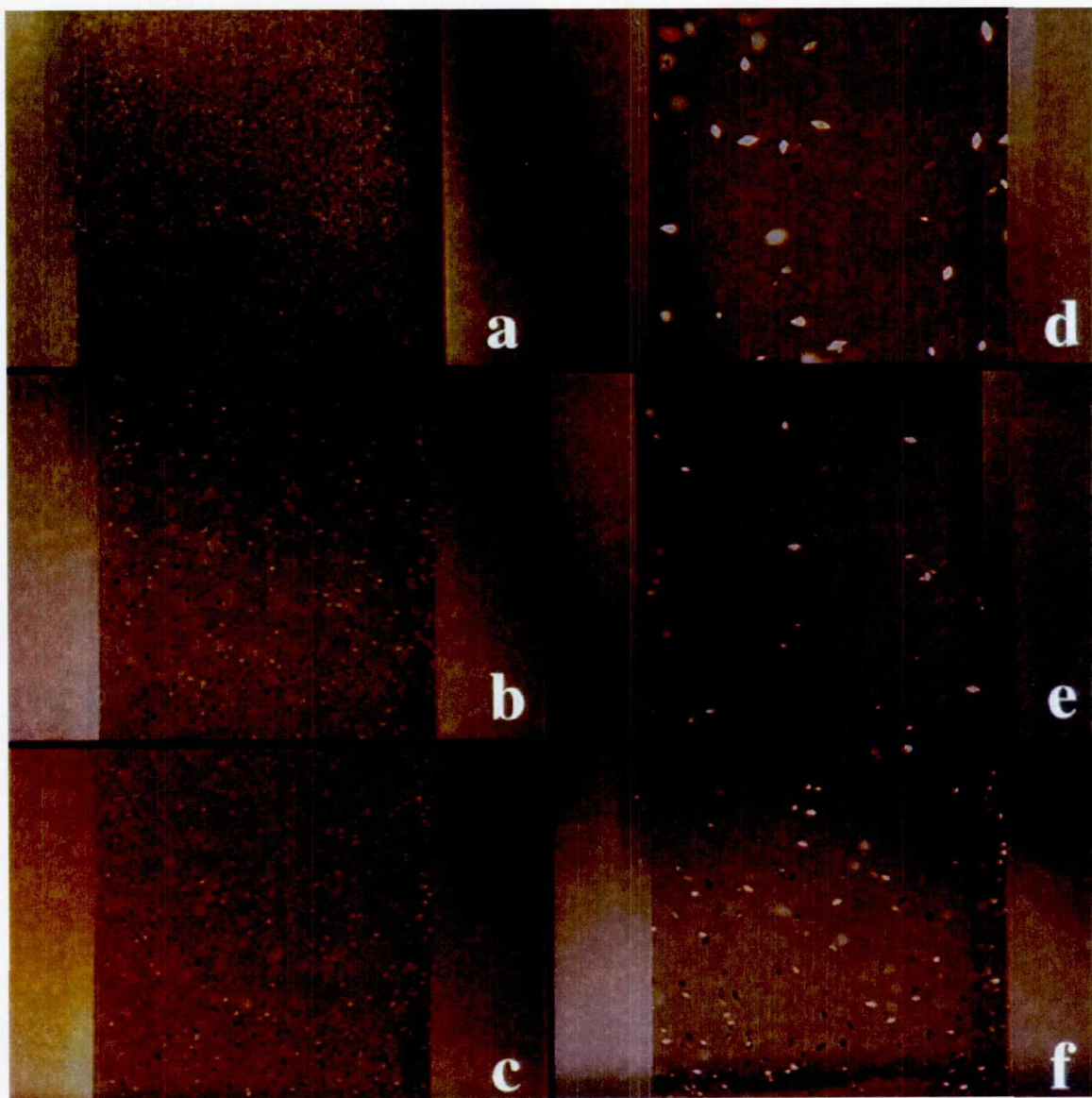


Figure 1. Comparison of thaumatin crystals grown on Earth (a-c) to those grown in microgravity [d-f (corresponding to reactors 2, 5, and 4 respectively as listed in table 2)]. Only the protein containing chambers of the reactors are shown and those seen here represent what is typically observed in the 188- μ l volume APCF dialysis reactors with low concentrations of thaumatin (6 mg/ml). Numerous and extremely small crystals are observed in the ground controls compared to only a few larger crystals in space. The average longest dimensions measured for crystals grown on Earth and in space were 0.1 mm and 0.5 mm, respectively. All images are at the same magnification.

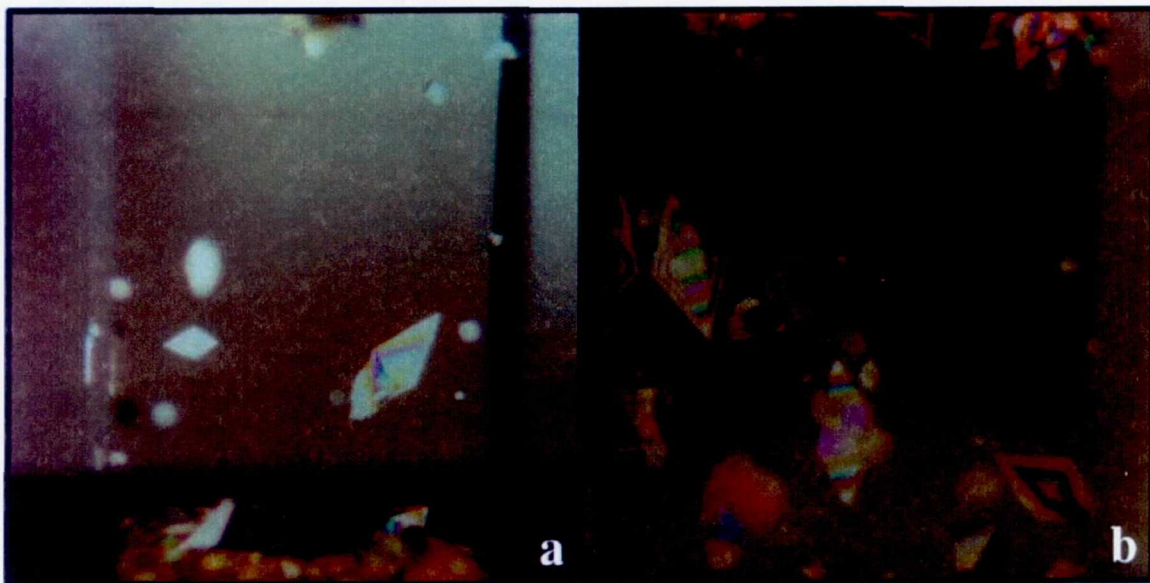


Figure 2. Earth-grown thaumatin crystals (a) compared to space-grown crystals (b) in a 67- μ l volume APCF dialysis reactor (table 2, reactor 1). The images show the protein chambers containing crystals grown at high concentrations of thaumatin (20 mg/ml). Crystals grown on Earth ranged in size from 0.1 mm to 1.2 mm in the longest dimension, and most of the crystals are seen to have sedimented to the bottom membrane. Space-grown crystals, on the other hand, grew with a size range of 0.5 mm to 1.7 mm from apex to apex. Fewer and larger crystals were observed in this space reactor than for the corresponding Earth-control reactor.

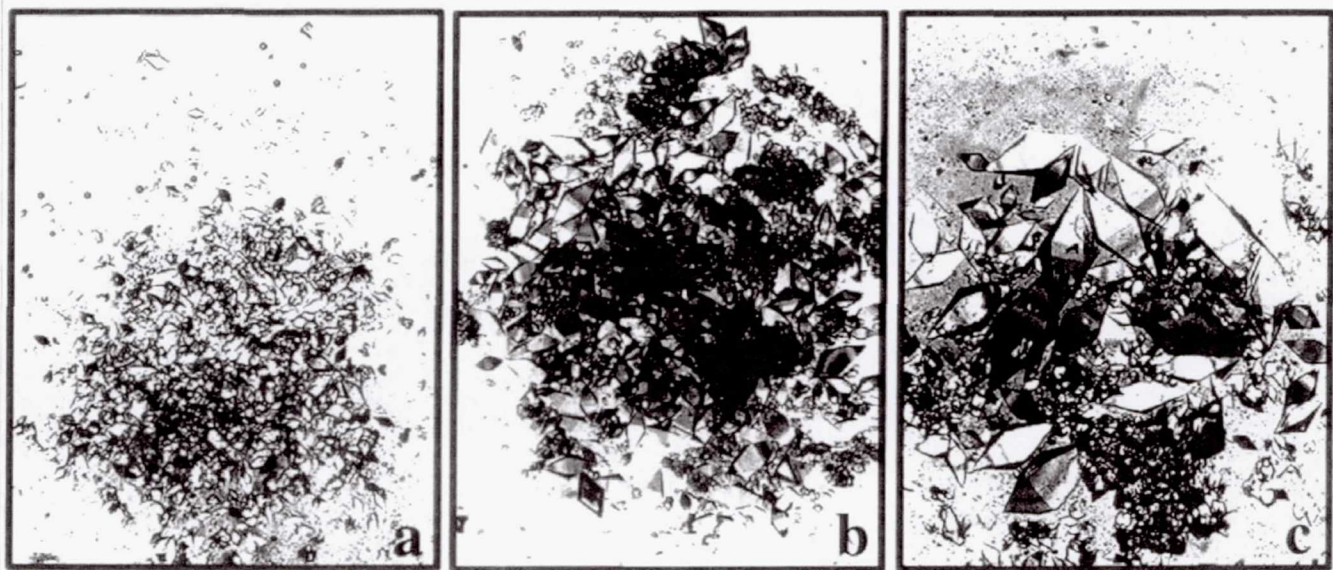


Figure 3. Thaumatin microgravity-grown crystals obtained at three different protein concentrations (a, 35 mg/ml; b, 17 mg/ml; c, 7 mg/ml) by free interface diffusion (table 1, reactors 8–10). Each image is at the same magnification. The largest crystals measured to be more than 2 mm in the longest direction and were the crystals used for x-ray data collection.

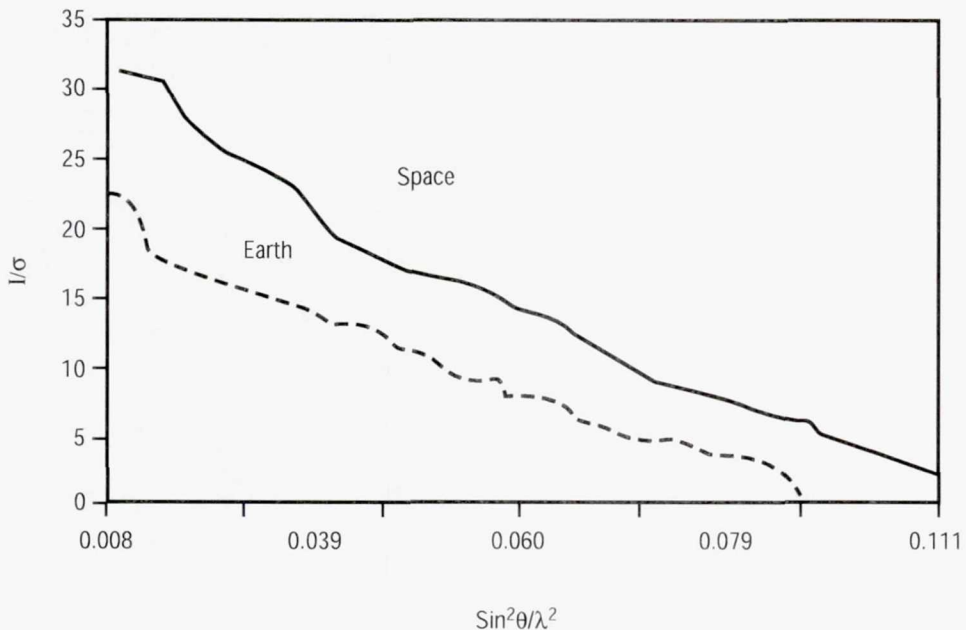


Figure 4. A graph of the intensity (I) versus estimated error (σ) ratio as a function of resolution ($\sin^2\theta/\lambda^2$) for thaumatin Earth- and space-grown crystals. The graph is presented as a modified Wilson Plot^{29,30} where the value of I/σ is the effective “signal-to-noise” for the diffraction pattern at the resolution corresponding to the respective ($\sin^2\theta/\lambda^2$) value. For the entire resolution range, space-grown crystals yield nearly 30 percent more diffraction intensities ($> 3\sigma$) than the best crystals grown on Earth.

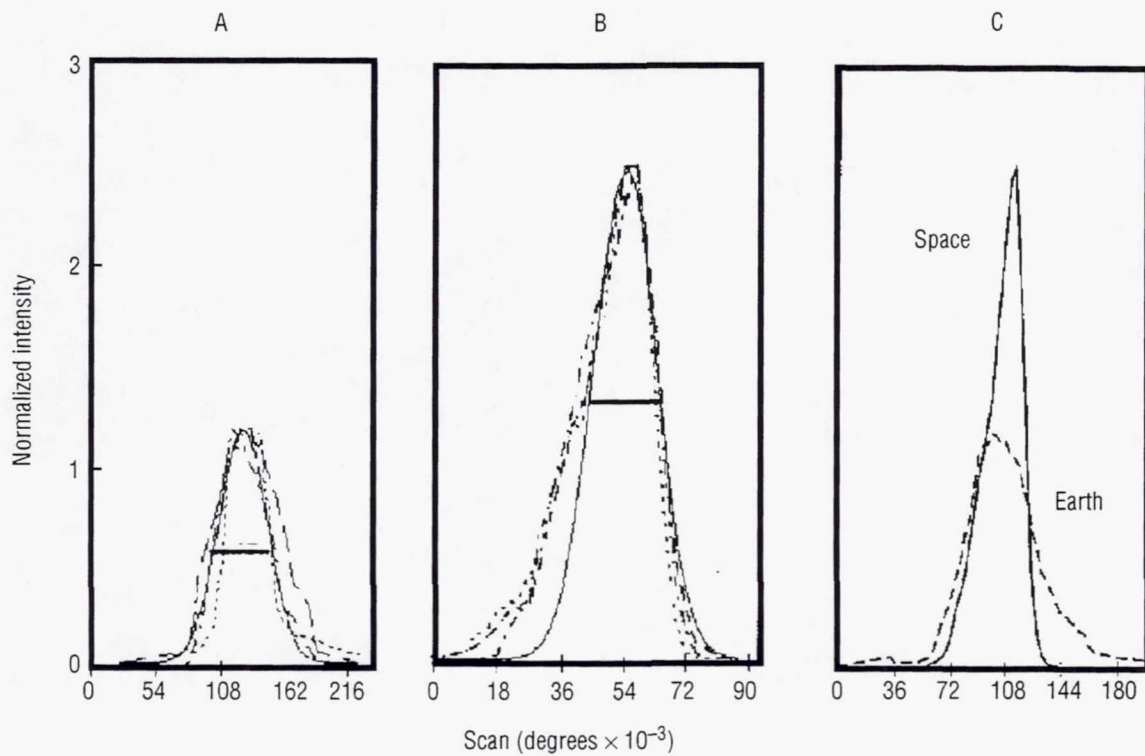


Figure 5. Profiles of three representative reflections at 4 \AA were each evaluated from an Earth- (A) and space-grown thaumatin crystal (B) studied for LMS. Reflections were obtained in the vertical diffraction plane such that the rotation axis was horizontal and perpendicular to the x-ray beam. Each set of reflection profiles for space- and Earth-grown crystals were averaged and Gaussian fits of the sets of profiles were calculated (solid lines). The full width at half maximum (FWHM) of a Gaussian fit for each profile was measured and its value is indicated by a short horizontal line. The space-grown crystal profiles have FWHM values that are about 2.5 times less than that of the Earth-grown crystal. The intensities shown are normalized and the actual peak intensities measured to 250,000 counts per 0.1 seconds for the space crystal. To the contrary, the spot intensities corresponding to the same reflections for the Earth crystal were approximately two times less. Panel C shows a relative comparison of the averaged mosaicity profiles from an Earth- to a space-grown crystal for the same reflections.

Page intentionally left blank

EXPERIMENT XXIV.

CRYSTALLIZATION OF PHOTOSYSTEM I PROTEIN COMPLEX

Page intentionally left blank

CRYSTALLIZATION OF PHOTOSYSTEM I PROTEIN COMPLEX

Dr. Wolfram Saenger

Institut für Kristallographie

Technische Universität und Freie Universität

Takustraße 6

D-14195 Berlin, Germany

Phone: 011-49-30-838-3412

Fax: 011-49-30-838-6702

E-mail: saenger@chemie.fu-berlin.de

Petra Fromme

Technische Universität und Freie Universität

D-10623 Berlin, Germany

E-mail: fromme@phosis1.chem.tu-berlin.d400.de

1. PURPOSE

In all green plants and cyanobacteria, two protein complexes are involved in photosynthesis—photosystem I and II (PSI and PSII). PSI, from the thermophilic cyanobacterium *Synechococcus elongatus*, consists of 11 polypeptide chains, about 90 chlorophyll *a* molecules, and three Fe_4S_4 clusters and occurs *in vivo* as a trimer. PSI has been crystallized, and the x-ray structure analysis has provided an electron density map at 4-Å resolution. The crystals show a large mosaic spread of $>1^\circ$. It was hypothesized that this large spread could be reduced by growing the crystals in microgravity. The USML-2 PSI crystal growth experiments were conducted in an attempt to reduce the mosaic spread, thereby increasing the resolution of the diffraction data.

2. METHOD

PSI was dissolved at a concentration of 80 mg/ml in 100mM MgSO_4 , 5 mM MES-buffer pH 6.4, 0.02-percent betadodecylmaltoside. In the APCF, this solution was dialysed against a buffer with reduced salt concentration (with an end concentration of 11mM MgSO_4) at 20 °C. Because the flight was postponed, the dialysis cells had to be filled twice to have the material as fresh as possible for the crystallization experiment.

3. RESULTS

The results of the experiment are very encouraging. On Earth, the largest of the hexagonal rod-like crystals grew on the dialysis membrane and was 2 mm long and 0.5 mm Ø (volume of 0.4 mm³). In space, the crystals grow to 4 mm long and 1.5 mm Ø (volume of 7 mm³). A temperature of 20 °C was required for

technical reasons, but the optimum temperature for growth of PSI is 4 °C. The diffraction quality of the crystals decays with time and is worse at 20 °C than at 4 °C. In spite of this, the crystals still diffracted to 3.8 Å, and the mosaic spread reduced slightly to approximately 0.7°. A data set was collected and is currently being evaluated.

4. PRELIMINARY CONCLUSIONS

The experiment was very successful, but it should be repeated at the optimum temperature of 4 °C. This should produce crystals that would have a lower mosaic spread and should permit collection of x-ray diffraction data at higher resolution than with Earth-grown and previous space-grown crystals.

EXPERIMENT XXV.

CRYSTALLIZATION OF GLUTATHIONE S-TRANSFERASE IN MICROGRAVITY

Page intentionally left blank

CRYSTALLIZATION OF GLUTATHIONE S-TRANSFERASE IN MICROGRAVITY

Lennart Sjölin

Department of Inorganic Chemistry
Chalmers University of Technology and the University of Göteborg
S-41296 Göteborg, Sweden

Gary Gilliland

Travis Gallagher

Maria Tordova

Gregory Vasques

Center for Advanced Research in Biotechnology of the Maryland Biotechnology Institute
University of Maryland, Shady Grove
9600 Gudelsky Drive
Rockville, MD 20878, USA

1. GLUTATHIONE S-TRANSFERASE (GST)

The glutathione S-transferases (GST; EC 2.5.1.18) are a family of enzymes involved in the detoxification of endogenous and xenobiotic electrophilic substances. These proteins catalyze the nucleophilic addition of glutathione (GSH) to substrates bearing electrophilic functional groups. The dimeric cytosolic enzymes which are composed of subunits with a molecular weight of 25,000 have been classified into four distinctive isoenzymic species designated alpha, mu, pi, and theta. Sequence identities between enzymes in different gene classes range between 25 to 35 percent, and between isozymes in the same gene class from 60 to 80 percent. Heterodimers may form between different isozymes from the same gene class, but inter-gene class heterodimers have not been observed.

The glutathione-binding site (G site) of all known GST's is primarily associated with the N-terminal domain at one end of the antiparallel beta-sheet with beta-strands found in a beta2 beta1 beta3 beta4 arrangement. Beta1 and beta2 are parallel, and beta3 is antiparallel to beta1 and beta4. The GSH binding site is near the C-terminal ends of beta1 and beta2. GSH binds in a similar manner in each of the structures which have been determined, but the specific details vary significantly, primarily because of the large variation in the sequence.

2. MICROGRAVITY CRYSTALLIZATION

Microgravity crystallization utilizes the HD reactors. The primary goal of the 4-4 GST studies includes increasing the size, improving the resolution, and reducing the nucleation of the crystals. Investigations involve a protocol similar to that carried out for the previous RNase S crystallization studies which

recently have been completed. It is believed that improvement of these characteristics would allow the structure determination of this important mu isozyme. Design of suitable experiments to optimize each of these parameters is necessary along with appropriate control experiments.

3. RESULTS

The reactors were inspected immediately after the flight return and small, irregular crystals were found in three of the four reactors flown. These crystals were of poorer quality than other crystals grown on Earth using regular laboratory equipment. X-ray analysis was not feasible on these crystals. Instead some effort has been spent on understanding why the crystallization experiment in space evidently gave crystals of poorer quality than similar crystallization experiments in the laboratory.

It appears that the reason we did not get good, diffraction-quality crystals is ultimately due to the reactor design. We have evidence that the protein was good. The other major problem was that the wicks were dried out, or more accurately, close to being dry, when the reactors from the Shuttle were opened. The wick problem resulted from just adding 350 μ l of precipitant to each wick instead of saturating them as we had done before.

The evidence that the protein was good and that the problem with the microgravity crystals was a result of reactor design is as follows:

1) The same protein under the same sample conditions yielded untwinned, birefringent, diffraction-quality crystals in plates of sitting drops using our regular laboratory equipment (so, the protein was good).

2) The control reactors had the same sample conditions with the exception that the wicks were saturated with precipitant instead of using only 350 μ l, and they yielded lots of twinned plates which grew on the wall of the reactor, at the interface between the Teflon™ plunger and the plastic wall of the cylinder. These crystals were thicker and less twinned than the microgravity crystals, but still not diffraction quality. Drying of the wicks in the microgravity crystals cannot fully explain the poor quality of the microgravity crystals, though the drying of the wicks seems to have caused more twinning and therefore was somewhat detrimental.

3) The microgravity crystals grew from the interface between the plunger and the cylinder wall. The reactor design results in initiation of crystallization at this interface.

4. CONCLUSION

The solutions were evidently good, so the problems were caused by something else. If the problems are from the reactor design, the major difference between the sitting drop plates and the reactors are due to the container surfaces. The sitting drop bridges used in the regular laboratory experiments are very smooth and highly polished. The reactor surfaces may be pitted along the top edge of the cylinder wall, due to its contacts when sealed, but is in contact with the drop when activated. The plastic of the reactor wall is of a different material than that of the highly polished plastic, sitting-drop bridge. The Teflon™ surface could be allowing multiple initiations of the crystals also, though the crystals are located at the interface with the cylinder, implying that initiation cannot start on the Teflon™.

The crystallization solutions were very complex (seven components in the drop and three components in the reservoir/wicks), and this might have resulted in unpredicted interactions of the solutions with the reactor plastic/Teflon™ or the wick material. A major difference between the crystallization plates and the reactors is that the coverslips are sealed with grease and the reactors have a rubber gasket, and this may result in a difference in the quality/integrity of the seals which could effect both the vapor diffusion and how quickly the wicks dry out (though one would have expected one of the other groups to notice this also). Finally, the precipitant may not be vapor-diffusing as efficiently or at the same effective concentration as the wicks compared to the well solutions of the plates.

Page intentionally left blank

EXPERIMENT XXVI.

CRYSTALLIZATION OF THE EPIDERMAL GROWTH FACTOR (EGF) RECEPTOR

Page intentionally left blank

CRYSTALLIZATION OF THE EPIDERMAL GROWTH FACTOR (EGF) RECEPTOR

Dr. Wolfgang Weber, Ph.D.

Institut für Physiologische Chemie
Universität Hamburg
Martinstraße 52
D-20246 Hamburg, Germany
Phone: 011-49-40-4717-4459
Fax: 011-49-40-4717-6818
E-mail: weber@uke.uni-hamburg.de

1. PURPOSE

The EGF receptor is the prototype of a family of tyrosine kinase receptors involved in cell growth control. Many human malignancies are characterized by its overexpression. The solution of the EGF receptor structure would pave the way for drug design and novel concepts of therapeutic treatment of tumors; however, the crystal structure of none of the growth factor receptors has been obtained thus far. The difficulty of crystallizing a membrane protein has been overcome by purifying only the hydrophilic external domain of the EGF receptor. Using this ectodomain, the co-crystallization with the ligand EGF was achieved; diffraction of these crystals had been poor, probably because of the high amount of heterogeneous carbohydrate (30 percent of molecular mass). Microgravity conditions have been found to favor crystal growth.

2. METHOD

On USML-2, various forms of EGF receptor protein were flown, differing in glycosylation and in pI values. Hanging drop reactors and dialysis reactors were used. Except for some setups with microcrystals, only one hanging-drop reactor yielded crystals suitable for x-ray analysis. It contained about 10 crystals of 0.3-mm diameter. The EGF receptor protein used in this reactor had been biosynthetically modified in its glycosylation. Compared to the wild-type receptor, the carbohydrate of this form was rich in mannose rather than in complex structures. This modification may reduce microheterogeneity and is assumed to favor crystal growth.

3. RESULTS

Diffraction data from three crystals were collected using the synchrotron beam line BW6 at the DORIS storage ring, DESY Hamburg. The storage ring operated in the main user mode with 4.5 GeV and up to 100 mA. Images were recorded on the 300-mm MAR image plate scanner at 4 °C and at room temperature. Exposure times were in the range of 3 to 5 minutes for 1.5-degree rotation using a wavelength of 0.96 Å. The crystal-to-plate distance was set to 600 mm. The diffraction of all crystals analyzed was comparable—maximum resolution was 6 Å with a remarkably high quality of spots. The space group P2₁2₁2 could be evaluated using the DENZO processing package.

4. PRELIMINARY CONCLUSIONS

These results confirmed previous data obtained on STS-47. The best Earth-grown crystals had yielded comparable results but required larger sizes and much more time to grow. EGF receptor crystallization, therefore, seems to benefit from microgravity conditions. Further modifications of receptor glycosylation are now being generated and will be tested to improve crystal quality.

EXPERIMENT XXVII.

**CRYSTALLIZATION IN A MICROGRAVITY ENVIRONMENT OF CcdB, A PROTEIN
INVOLVED IN THE CONTROL OF CELL DEATH**

Page intentionally left blank

CRYSTALLIZATION IN A MICROGRAVITY ENVIRONMENT OF CcdB, A PROTEIN INVOLVED IN THE CONTROL OF CELL DEATH

Prof. Dr. Lode Wyns

Dr. Minh Hoa Dao Thi

Dr. Dominique Maes

Department of Ultrastructure

Institute of Molecular Biology

Free University of Brussels (VUB)

Belgium

Phone: 011-32-2-359-02-82

Fax: 011-32-2-359-02-89

E-mail: ljwvns@vub.ac.be

1. INTRODUCTION

CcdB is a protein involved in the control of cell death. The CcdB-mediated cell killing involves poisoning of DNA-topoisomerase II complexes; it converts the wild-type gyrase in a DNA-damaging agent.

Poisons of eucaryotic topoisomerases are regarded as potent candidates of anti-cancer drugs. Elucidation of the structure and the mode of action of the CcdB protein may lead to the design of new antibiotics and anti-tumoral drugs.

Efforts to crystallize CcdB on Earth led to the identification of experimental conditions for the growth of several crystal forms. The objectives of the microgravity experiments were the following:

- Improvement of crystal quality and more specifically an attempt to solve a systematic twinning problem.
- The crystallization of a specific double mutant (Gly70Cys and Glu77Gln), which did not produce crystals large enough for data collection on Earth.

2. METHOD

The wild-type CcdB as well as the mutant were used, for 1 HD and 1 FID, and for 1 HD and 1 FID, respectively. The choice of conditions used in these flight APCF reactors was based on prior knowledge from previous Earth crystallization experiments.

The reactors were filled on the 10th of October and returned on the 14th of November.

Table 1. An experimental overview.

Reactors	Experimental conditions	Observations and results
HD 172 video 80 μ l	protein drop: 50 μ l CcdB mutant 4.5 mg/ml in 100 mM MOPS pH 7.0 bottom solution: 30 μ l of 30-percent MPD 100 mM Na-acetate, pH 4.6	slight precipitation few needle-shaped crystals
HD 127 80 μ l	protein drop: 30 μ l CcdB wild type 3.7 mg/ml in 100 mM MOPS pH 7.0 bottom solution: 50 μ l of 10-percent PEG 5000 100 mM Na-acetate, pH 4.6	heavy precipitation large number of twinned crystals with size 0.3 by 0.2 by 0.2 mm a few single crystals with size 0.1 by 0.05 by 0.02 mm
FID 207 video 200 μ l	protein chamber: 115 μ l CcdB mutant 4.5 mg/ml in 100 mM MOPS pH 7.0 and 85 μ l bottom solution bottom solution + salt chamber: 295 μ l of 2.0 M NaCl 0.2 M Ammonium-Acetate 100 mM Na-acetate, pH 4.6	small aggregation and precipitation salt chamber remains clear NB: post activation resulted after 1 week in several needle-shaped crystals in the salt chamber
FID 203B 200 μ l	protein chamber: 40 μ l CcdB wild type 7.4 mg/ml in 100 mM MOPS pH 7.0 and 160 μ l bottom solution bottom solution + salt chamber: 295 μ l of 10-percent PEG 5000 100 mM Na-acetate, pH 4.6	a few twinned crystals with size 0.2 by 0.1 by 0.1 mm salt chamber: 3 big twinned crystals and one single crystal size 0.02 by 0.05 by 0.02 mm

3. RESULTS

3.1 Wild-type CcdB

The ground control reactor did not provide any crystals both in HD and in FID. Until now we were not able to obtain any CcdB crystal in a FID ground setup. The major problem is the appearance of precipitation immediately after the activation of the reactor. By contrast, in microgravity we got crystals as well in FID as in HD. During investigation of the crystals at ESRF, it was shown that twinning was still present, although single crystals were obtained in the FID reactor.

3.2 Mutant CcdB

In the ground control, small needle-shaped crystals were obtained in the HD as well as in the salt chamber of the FID reactor.

In the space HD reactor the same amount of crystals were obtained but smaller in size. On the other hand, in the space FID reactor no crystals were obtained; postflight activation of this reactor resulted in a crystallization (in the salt chamber) comparable to the ground control.

The wild-type HD crystals have been analyzed with a classic rotating anode generator/imaging plate system. Crystals, like earth-grown ones, diffract in the 2.2 Å to 2.5 Å range. During the last months we made a breakthrough in the phase determination (using seleno methionine—CcdB) and are on our way towards the final solution of the CcdB structure.

BIBLIOGRAPHY

1. Bernard P. and Couturier M.: (1992) Cell-killing by the F-plasmid CcdB protein involves poisoning of DNA-topoisomerase II complexes. *J. Mol. Biol.* 226, 735-745.
2. Bernard P., Kezdy K., Van Melderen L., Steyaert J., Wyns L., Pato M., Higgins P. and Couturier M.: (1993) The F-plasmid CcdB protein induces efficient ATP-dependent DNA cleavage by Gyrase. *J. Mol. Biol.* 234, 534-541.
3. Steyaert J., Van Melderen L., Bernard P., Dao Thi M.H., Loris R., Wyns L. and Couturier M.: (1993) Purification, circular dichroism analysis, crystallization and preliminary x-ray diffraction analysis of the F-plasmid CcdB killer protein. *J. Mol. Biol.* 231, 513-515.

Page intentionally left blank

EXPERIMENT XXVIII.

CRYSTALLIZATION OF RIBOSOMAL PARTICLES IN SPACE

Page intentionally left blank

CRYSTALLIZATION OF RIBOSOMAL PARTICLES IN SPACE

Harly A.S. Hansen

Ada Yonath

Max-Planck Laboratory for Ribosomal Structure
Hamburg, Germany

1. EXPERIMENTAL OBJECTIVES

Our long-term goal is to elucidate the molecular structure of the ribosome by x-ray crystallography. Ribosomes are the universal cell organelles facilitating the translation of the genetic code into polypeptide chains. The prokaryotic ribosomes are assemblies of a total molecular weight of 2.3×10^6 daltons, containing up to 73 different proteins and three RNA chains with about 4,500 nucleotides. Crystals of intact ribosomal particles, suitable for such studies, have been grown in our laboratory. Data collection became feasible by the introduction of cryo temperature, since upon irradiation at ambient temperatures the ribosomal crystals deteriorate instantaneously.

All ribosomal particles display a marked tendency to form extremely thin crystals (2–10 microns thickness) which tend to fracture, split or crack upon handling, causing a loss of precious synchrotron radiation time and severe difficulties in data collection and evaluation. As we consistently observed that significantly better crystallographic data could be collected from occasionally grown thicker crystals, we have invested a lot of effort in increasing the thickness of the crystals. However, our experience shows that this aim is far from being trivial or routine.

We assume that the tendency of the crystals to form thin plates is influenced by the contact of their nuclei with the flat surfaces of the growth chambers. Under microgravity conditions the situation should be different since the crystals are supposed to float freely, hence their contact with flat surfaces will be eliminated or reduced, facilitating the growth of thicker crystals. Thus, we intended to use microgravity not only for extending the morphology and the size of the crystals, but also for further improvement of their internal order and mechanical properties. We expected that these crystals would yield crystallographic data of a high quality.

2. EXPERIMENTAL PROCEDURES

We used a method of vapor diffusion, attempting slow equilibration of small droplets with their reservoirs. The samples were prepared immediately before delivery to the space center, and inspected right after they were brought back. In the preparation for the mission we ran several test experiments, screening for the particular conditions which were most suitable for each of the ribosomal preparations. To mimic microgravity conditions in ground experiments, we systematically varied the geometrical parameters of the chambers used for crystal growth as well as the densities of the growth solutions. Consequently, the crystallization mixtures and reservoirs were prepared with the same compositions which have been proven to be suitable on Earth.

In crystallization experiments performed on Earth, we found that the time needed to reach equilibration within the crystallization chambers plays a crucial role in the formation of quality crystals from ribosomal particles. We also constructed crystallization solutions with densities similar to those of the crystals, and attempted crystallization in these solutions, assuming that the crystals, once formed, would float rather than sink. In parallel, we tried to grow crystals within gels. None of these attempts were successful, presumably because the composition of the modified crystallization solutions were not suitable for crystal growth.

3. EXPERIMENTAL RESULTS

The results of our space experiments showed that, despite the extreme difficulties in obtaining crystals of intact ribosomal particles, such crystals do grow in space. Almost all crystals grown in space are rather round, a property never observed on Earth. Of special importance is the morphology of the crystals. A few crystals grown in space are of somewhat better proportions than those grown on earth and have a more isotropic shape, indicating the potential of microgravity. Furthermore, most of the fragile and delicate crystals did not break on returning to Earth, and already formed crystals, sent to space as a control experiment, remained intact after the mission was completed.

EXPERIMENT XXIX.

**SPACE CRYSTALLIZATION OF A BINARY COMPLEX OF *SULFOLOBUS SOLFATARICUS*
ALCOHOL DEHYDROGENASE ON THE UNITED STATES MICROGRAVITY
LABORATORY (USML-2) MISSION**

ACKNOWLEDGMENTS

We acknowledge ESA and NASA for the flight opportunity; ICMIB: Reparto Batteri Termofili CNR for supplying the biomass; Dr. G. Wagner as Project Scientist; Drs. R. Geigé and J. Ng for their hospitality; Dr. P. Lautenschlager for assistance with reactor filling; and Dr. V. Lamzin for help with x-ray analysis at DESY. This work was financially supported by ASI and by CNR, Progetto Strategico "Biologia Strutturale." The research of Dr. Sica has been partially supported by the NATO Collaborative Research Grant No. 931439.

**SPACE CRYSTALLIZATION OF A BINARY COMPLEX OF *SULFOLOBUS SOLFATARICUS*
ALCOHOL DEHYDROGENASE ON THE UNITED STATES MICROGRAVITY
LABORATORY (USML-2) MISSION**

F. Sica

G. Sorrentino

L. Mazzarella

A. Zagari

Centro di Biocristallografia, CNR and Dipartimento di Chimica
Università di Napoli, Federico II
Naples, Italy

L. Carotenuto

Microgravity Advanced Research and Support Center
Naples, Italy

C.A. Raia

M. Marino

M. Rossi

Instituto di Biochimica delle Proteine ed Enzimologia, CNR
Naples, Italy

Dr. Filomen Sica (contact author)

Dipartimento di Chimica

Via Mezzocannone 4

80134 Napoli, Italy

Phone: 39-81-5476513

FAX: 39-81-5527771

E-mail: Sica@alpha.dichi.unina.it.

ABSTRACT

Crystallization of biological macromolecules as well as of low-molecular-weight compounds sometimes results in twin crystals. The reduction of data from twinned crystals is not straightforward and often impossible, thereby preventing crystallographic structure determination. Crystals of the binary complex of alcohol dehydrogenase from *Sulfolobus solfataricus* with its cofactor (NADH) grown on Earth in several different experimental conditions were found to undergo twinning. During the Second United States Microgravity Laboratory (USML-2) mission, in October/November 1995, crystallization experiments were carried out in space to investigate for the first time the effects of gravity on twinning.

INTRODUCTION

Several laboratories around the world have performed microgravity protein crystal growth experiments on board U.S. Space Shuttles,^{1,2} unmanned reentry capsules,³ and the Russian space station *Mir*.⁴ The improvement of the quality of ground-grown crystals was the principal aim of these space experiments. In a few cases some attempts were made to obtain crystals of proteins that do not achieve crystallization on Earth. In a field of gravity, the growing crystals come into contact with the surface of the protein solution container and/or the surface of other crystals due to sedimentation. These surface contacts hinder the uniform growth of the crystals. In addition, density-driven convective flows produce turbulence in the solution from which crystals grow and can cause dislocation and other imperfections as well as the formation of secondary nucleation sites. In the absence of gravity, the elimination of both convective flows and sedimentation of growing crystals are found to facilitate the formation of more ordered crystals.

Thus, the properties inherent in a microgravity environment prompted us to examine the role of gravity on the crystal twinning, which had not yet been analyzed. The determination of the 3-dimensional structure of proteins strictly from data of twinned crystals has been possible only in a few cases, since crystal twinning almost inevitably impedes successful structure determination. It is, therefore, worthwhile to study the influence of microgravity on the twinning.

Our laboratory is currently carrying out experimentation^{5,6} on the alcohol dehydrogenase extracted from *Sulfolobus solfataricus* (SsADH), an archaeon that thrives at high temperature (~ 90 °C) and low pH (~ 3.5).⁷ Crystallization experiments have been successfully carried out on Earth⁵ using this protein complexed with its cofactor, β-Nicotinamide Adenine Dinucleotide Reduced Form (NADH). Twinning of these crystals has been proven by a detailed analysis of the diffraction pattern of these crystals: a monoclinic reciprocal lattice ($a=131.5 \text{ \AA}$, $b=85.8 \text{ \AA}$, $c=70.8 \text{ \AA}$, $\beta=97^\circ$), with C2 space group symmetry is superimposed upon an identical reciprocal lattice related to the first by a 180° rotation around the a -axis. These ground-grown crystals, however, are not suitable for x-ray analysis, given the presence of twinning. The results of the crystallization experiments of SsADH (NADH)₂ complex under microgravity conditions are reported here.

2. MATERIALS AND METHODS

Crystallization experiments were carried out in the 8-μL vapor diffusion reactors of the Advanced Protein Crystallization Facility (APCF) manufactured by Dornier GmbH⁸ both on Earth and in space.

2.1 Preflight Experiments

Conditions for ground crystallization of SsADH(NADH)₂ complex were established in our laboratory.⁶ Using 2-methyl-2,4-pentane-diol (MPD) as precipitating agent, large ($\leq 0.8 \text{ mm}$) prismatic crystals usually grow within 2–3 weeks at 20 °C by the hanging drop method. Preflight tests were performed using three APCF reactors to optimize conditions for crystallization in space. Particular attention was devoted to the total time span of the complete crystallization process since the duration of the shuttle flight was

predicted to be 16 days. We found that a decrease in dilution ratio of the precipitant agent between the droplet and the reservoir resulted in a reduction of the time needed to grow sufficiently large (> 0.3 mm) crystals. Crystallization time was reduced to 10–14 days by using a ratio of 2:3, instead of the usual 1:2 ratio. Further attention was given to the protein solution stored in the glass tube of the reactor in the presence of precipitating agent, which can lead to prenucleation during the time lapse between filling the reactors on Earth and activating the experiments in space. To evaluate this, each setup was checked for a month, stopping the equilibration via the vapor phase.

2.2 Space and Ground Reference Experiments

Experimentation consisted of varying both the concentration of the protein from 8 to 10 mg/ml and the concentration of the precipitating agent, MPD, from 46 to 48 percent (v/v), while maintaining the pH fixed at 8.4 (TRIS-HCl buffer 50mM). Three separate experiments were carried out in duplicate both in space and on the ground to check the reproducibility of the crystallization trials. Six crystallization reactors were used for the space experiments. Protein droplet solutions and reservoir solutions were filled into the reactors in the laboratory of Prof. Geigé (Strasbourg, France). The reactors were then integrated into the APCF and transported by the European Space Agency (ESA) to the launch site (Kennedy Space Center, USA). The temperature was kept at a constant 18 °C through the transport, storage, and the crystallization experiments.

Ground experiments acting as controls consisted of filling six reactors in our laboratory, using the same reagent solutions. The experiments both on the ground and in space were activated the day after the launch and stopped the day before the Shuttle's reentry. After the mission the reactors were transported to the European Molecular Biology Laboratory (EMBL) at the Deutsches Elektronen-Synchrotron in Hamburg, Germany (DESY) and subsequently delivered to us. Crystals were mounted in thin-wall x-ray capillaries and examined using synchrotron radiation on the EMBL beam line X11 at the storage ring DORIS (DESY).

RESULTS AND DISCUSSION

Several crystallization trials have been performed on Earth dealing with the twinning problem, as reported in the references.⁶ Crystals that showed a marked decrease in twinning were eventually grown in agarose gel. Convective flows and sedimentation effects were found to be lowered in a gelled medium simulating a microgravity environment. It is known that the mechanism which produces nonordered crystals is dependent on convection effects near the growing crystal surfaces, and that twinning in crystals is a form of disorder. It followed, then, that gravity could have an important effect on the twinning phenomenon.

The APCF reactors offer a modified geometry compared with the devices normally used for the hanging drop method, which prompted us to optimize the crystallization conditions used in the preflight tests. Thus, some slight but significant differences were noted in the optimum growth conditions compared to the usual hanging drop experiment, due to the alteration in vapor mobility in the reactors caused by the different surface area of the reservoir.

In order to realistically evaluate the effect of microgravity in space, crystallization experiments were performed simultaneously on Earth. Identical conditions were assured by using the same reagent solutions, crystallization hardware, and temperature as those used in microgravity.

SsADH(NADH)₂ crystals were obtained either on Earth or in space only in two duplicates out of six reactors, where both the protein and the precipitant concentrations were highest. Average crystal size was about 100 μm , with the crystal habit showing some irregularities. Problems were encountered with crystal nucleation along the walls of the reactors, both in flight and in ground reactors, hindering the harvesting of the crystals. Crystalline particles were often found with undefined morphologies and disrupted edges, perhaps due to damage caused during harvesting or deactivation of the crystallization process. Traces of amorphous precipitate were also seen in all reactors.

A possible explanation for these results could be found in the partial denaturation of the enzyme. Although the protein is ordinarily very stable, it might undergo a slight degradation over considerable time. In fact, after filling of reactors, the launch was delayed by 23 days due to both technical and atmospheric problems. In spite of the small size, two SsADH(NADH)₂ crystals were mounted in a Lindemann capillary and exposed to the synchrotron radiation at DESY. Further analysis was excluded, however, due to the poor diffraction power.

Several (but not all) cases cited in the literature were confirmed by our experiments, i.e., that the reproducibility of crystal formation results, under the same conditions, was the same in microgravity as on Earth, at least for this protein. However, these initial experiments on crystallization of SsADH(NADH)₂ complex in a microgravity environment provided some preliminary information which prompted us to pursue further experimentation in space. In fact, we also participated in the subsequent Life and Microgravity Spacelab (LMS) Space Shuttle Mission in June/July 1996, obtaining large crystals (0.5-0.8 mm) of SsADH complex diffracting to a higher resolution than normally seen in those grown on Earth. Evaluation of the x-ray diffraction data, from both the space- and the ground-grown crystals, is still underway.

REFERENCES

1. Chayen, N.E.; Gordon, E.J.; and Zagalsky, P.F.: *Acta Cryst.*, D52, 156, 1996.
2. Day, J.; and McPherson, A.: *Protein Science*, 1, 1254, 1992.
3. Hilgenfeld, R.; Liesum, A.; Storm, R.; and Plaas-Link, A.: *J. Crystal Growth*, 122, 330, 1992.
4. Strong, R.K.; Stoddard, B.L.; Arrott, A.; and Farber, G.K.: *J. Crystal Growth*, 119, 200, 1991.
5. Pearl, L.H.; Demasi, D.; Hemmings, A.M.; Sica, F.; Mazzarella, L.; Raia, C.A.; D'Auria, S.; and Rossi, M.: *J. Mol. Biol.*, 229, 782, 1993.
6. Sica, F.; Demasi, D.; Mazzarella, L.; Zagari, A.; Capasso, S.; Pearl, L.H.; D'Auria, S.; Raia, C.A.; and Rossi, M.: *Acta Cryst.*, D50, 508, 1994.
7. Amendola, S.; Raia, C.A.; Caruso, C.; Camardella, L.; D'Auria, S.; De Rosa, M.; and Rossi, M.: *Biochemistry*, 31, 12514, 1992.
8. Bosch, R.; Lautenschlager, P.; Potthast, L.; and Stapelmann, J.: *J. Crystal Growth*, 122, 310, 1992.

Page intentionally left blank

EXPERIMENT XXX.

RESULTS FROM THE USML-2 INTERFACE CONFIGURATION EXPERIMENT

ACKNOWLEDGMENTS

We wish to thank crew members Catherine Coleman and Fred Leslie for the highly skilled manner in which they carried out the experiments. This work was supported in part by the National Aeronautics and Space Administration under Grants NCC3-329 and NAG3-1941, by the National Science Foundation under Grants DMS-9400778 and DMS-9401167, and by the Mathematical Sciences Subprogram of the Office of Energy Research, U.S. Department of Energy, under Contract Number DE-AC03-76SF00098.

RESULTS FROM THE USML-2 INTERFACE CONFIGURATION EXPERIMENT

Paul Concus

Lawrence Berkeley National Laboratory and Department of Mathematics
University of California
Berkeley, CA 94720
Phone: 510-486-5508
FAX: 510-486-5401
E-mail: concus@math.berkeley.edu

Robert Finn

Department of Mathematics
Stanford University
Stanford, CA 94305-2125
Phone: 415-723-2605
FAX: 415-725-4066
E-mail: finn@gauss.stanford.edu

Mark Weislogel

NASA Lewis Research Center
Cleveland, OH 44135
Phone: 216-433-2877
FAX: 216-433-8660
E-mail: weislog@lerc.nasa.gov

ABSTRACT

Mathematical theory predicts that small changes in container shape or in contact angle can give rise to large shifts of liquid in a microgravity environment. For studying such shifts, container shapes are described that were flown on board the Space Shuttle USML-2 mission as part of the Glovebox Interface Configuration Experiment. These containers are in the form of a circular cylinder with two diametrically opposed "canonical proboscis" protrusions. The containers were designed with the goal of having two desirable properties—that sufficient liquid would participate in the shift to permit easy observation, and that the change would be abrupt enough to allow accurate determination of critical contact angle. The observed behavior for these vessels is depicted, along with behavior for a movable wedge vessel, which also formed part of the experiment. The experimental results support the validity of the concept of macroscopic contact angle, basic to the theory, and thereby its use in predicting fluid behavior under reduced gravity. The results indicate, as well, the role of hysteresis in impeding orientation to equilibrium.

1. INTRODUCTION

When planning space-based operations, it is important to be able to predict the equilibrium locations and configurations that fluids will assume in containers under low-gravity conditions. Currently available mathematical theory applies completely, however, to only a few particular configurations, such as the partially filled right circular cylindrical container with liquid simply covering the base. For such a configuration, behavior in space is not dramatically different from what is familiar from common experience in a terrestrial environment. For more general containers, however, fluids in reduced gravity can behave in striking, unexpected ways.

The classical theory, according to the Young-Laplace-Gauss (Y-L-G) formulation, characterizes fluid locations as equilibrium configurations for the surface-plus-gravitational mechanical energy. Using this point of view in a mathematical study, we have shown that for a cylindrical container of general cross-section in zero gravity, the surface change arising from small changes in geometry or contact angle can be discontinuous or "nearly discontinuous," leading to large shifts of the liquid mass. Attempts to observe this behavior experimentally can be valuable as tests of validity of the concept of macroscopic contact angle used in the classical theory, and thereby of the theory's effectiveness in predicting fluid behavior in applications such as fluid management under microgravity.

The principal mathematical result underlying the behavior is that for particular cylindrical sections, a discontinuous kind of change can be realized as the contact angle γ crosses a critical value γ_0 intrinsic to the container. When γ is larger than γ_0 , there exists an equilibrium configuration of liquid that covers the base of the cylindrical container simply, while for contact angles smaller than γ_0 no such equilibrium configuration is possible. In the latter case liquid moves to the walls and can rise arbitrarily high along a part of the wall, uncovering a portion of the base if the container is tall enough. By simple physical observation of bulk behavior of the liquid, one can thereby determine whether the contact angle is larger than or smaller than the critical value for the container. A practical challenge in this connection is to design cross-sections for which a large enough portion of the liquid will rise up the walls for easy observation as the critical value of contact angle is crossed (without the containers being unrealistically tall) and so that the change will be abrupt enough to allow accurate determination of critical contact angle value.

By using two or more containers corresponding to appropriately chosen values of γ_0 , differing, say, by the accuracy desired for contact angle evaluation, one can determine the value of the critical contact angle to lie within a particular interval. In some cases, geometries can be "combined" into a single container for determining such an interval. For our Interface Configuration Experiment (ICE) on the Second United States Microgravity Laboratory (USML-2) Space Shuttle flight STS-73, we conjoin these two approaches.

We describe next some of the mathematical and computational results that form the basis for the USML-2 space experiment. These results are discussed in detail in reference 1; further background and historical information can be found in references 2-4; and some related work is found in references 5-7. We restrict discussion here to the case of a wetting liquid (contact angle less than $\pi/2$), which is the case for the experiment materials.

2. WEDGE CONTAINER

For a cylindrical container whose section Ω has boundary Σ consisting of a circular arc and a protruding corner of opening angle 2α , as in figure 1, the critical value of contact angle is $\gamma_0 = \frac{\pi}{2} - \alpha$. For $\frac{\pi}{2} > \gamma \geq \gamma_0$ (and for liquid volume sufficient to cover the base), the height of the free surface S can be given in closed form as a portion of a lower hemisphere meeting the walls with the prescribed contact angle γ . Thus for a given volume of liquid the height is bounded uniformly in γ throughout this range. For $0 \leq \gamma < \gamma_0$, however, the liquid will necessarily move to the corner and rise arbitrarily high at the vertex, uncovering the base regardless of liquid volume. The behavior for the wedge domain is thus discontinuous at $\gamma = \gamma_0$. Procedures for determining critical contact angle for the phenomenon can give very good accuracy for larger values of γ (closer to $\pi/2$) but may be subject to experimental inaccuracy when γ is closer to zero, as the “singular” part of the section over which the liquid accumulates when the critical angle γ_0 is crossed then becomes very small and may be difficult to observe.

3. CANONICAL PROBOSCIS CONTAINER

As a way to overcome the experimental difficulty, “canonical proboscis” sections were introduced in reference 8. These domains consist of a circular arc attached symmetrically to a (symmetric) pair of curves described by:

$$x + C = \sqrt{R_0^2 - y^2} + R_0 \sin \gamma_0 \quad \ln \frac{\sqrt{R_0^2 - y^2} \cos \gamma_0 - y \sin \gamma_0}{R_0 + y \cos \gamma_0 + \sqrt{R_0^2 - y^2} \sin \gamma_0} , \quad (1)$$

and meeting at a point P on the x -axis (fig. 2). Here R_0 , as well as the particular points of attachment, may be chosen arbitrarily. The (continuum of) circular arcs Γ_0 , of which three are depicted by the dashed curves in figure 2, are all horizontal translates of one such arc, of radius R_0 and with center on the x -axis, and the curves (1) have the property that they meet all the arcs Γ_0 in the constant angle γ_0 . The radius ρ of the circular boundary arc can be chosen in such a way that the arcs Γ_0 become extremals for a certain “subsidiary” variational problem⁹ (see also chapter 6 of references 2 and 4).

One can show that a solution of the governing equations should exist in Ω if, and only if, $\gamma > \gamma_0$. Additionally, the liquid height should rise unboundedly as γ decreases to γ_0 , precisely in the region swept out by the arcs Γ_0 (the entire proboscis region to the right of the leftmost arc Γ_0 shown in fig. 2). These conjectures were proved completely in reference 10; specifically, it was established that a unique value of ρ can be obtained for any prescribed proboscis length, that $R_0 \cos \gamma_0 < \rho < 2R_0$ holds, and that the conjectured behavior of the liquid rise is the only one possible.

In reference 11, numerical solutions of the equations determining the equilibrium free surface are depicted for some canonical proboscis-containers. Although the liquid rise in the corner is not discontinuous as occurs for a planar wedge, it can be "nearly discontinuous" in that the rise height in the proboscis is relatively modest until γ decreases to values close to γ_0 , and then becomes very rapid as γ decreases still further. Additionally, since the proboscis can be made relatively as large a portion of the section as desired, the shift can be easily observed for a broad range of γ_0 . Through proper choice of the domain parameters for the cases considered, an effective balance can be obtained between conflicting requirements of a sharp near discontinuity (for accurate measurement) and a sizable volume of liquid rise (for ease of observation).

4. DOUBLE PROBOSCIS CONTAINER

For the USML-2 experiment, double proboscis containers are used. These containers are similar to the single proboscis one of figure 2, except that there is a second proboscis diametrically opposite to the first, in effect combining two containers into one. The values of γ_0 in equation (1) differ for the left and right proboscides, whose values of γ_0 we denote by γ_L and γ_R , respectively. Similarly, we denote the values of R_0 for the left and right proboscides by R_L and R_R . There holds:¹

$$R_R \cos \gamma_R = R_L \cos \gamma_L .$$

The critical value for the container is the larger of γ_L and γ_R . For the containers considered here, we shall take $\gamma_R > \gamma_L$, so that the critical contact angle γ_0 for the container is equal to γ_R .

The sections for the experiment, superimposed on one another, are shown in figure 3. They have been scaled so that the circular portions all have radius unity. The meeting points of the vertices with the x -axis are, respectively, a distance 1.5 and 1.6 from the circle center. For the sections depicted in figure 3 the values of γ_L and γ_R are respectively 20° and 26° for the outermost section, 30° and 34° for the middle section, and 38° and 44° for the innermost section.

For these containers the explicit behavior has not yet been determined mathematically in complete detail, as it has for the single proboscis containers. However, numerical computations and the known behavior of the single proboscis solution surfaces suggest that the behavior will be as follows: for contact angles $\gamma \geq \gamma_0$, as γ decreases to γ_0 , the liquid will rise higher in the right than in the left proboscis, with the rise becoming unbounded in the right proboscis at γ_0 . For contact angles between γ_L and γ_R , the liquid will rise arbitrarily high in the right proboscis, but the height in the left will still be bounded. For smaller contact angles the liquid will rise up both proboscides arbitrarily high. By observing the liquid shift, one can then bracket the contact angle relative to the values of γ_L and γ_R . For a practical situation in which the container is of finite height with a lid on the top, the liquid will rise to the lid along one or both of the proboscides in the manner described above (provided the liquid volume is adequate); in some cases, liquid may then travel along the corner at the lid and flow into the other proboscis from the top.

The selected values of γ_L and γ_R for the three containers are based on the value of approximately 32° measured in a terrestrial environment for the contact angle between the ICE experiment liquid and the acrylic plastic material of the container. The spread of values of contact angle covered by the three containers is intended to allow observation of possible effects of contact angle hysteresis, which is not included in the classical theory.

5. COMPUTED SURFACES

The mathematical equations governing the free surface were solved numerically for the three double proboscis container sections depicted in figure 3, for a range of contact angles γ , to obtain details of the anticipated liquid behavior. It was adequate to compute solutions only for the upper-half domains, because of the reflective symmetry. The adaptive-grid finite-element software package PLTMG¹² was used.

The numerically calculated solution surface for the upper half of the 30°/34° domain is shown in figure 4 for four values of contact angle, 60°, 50°, 40°, and 35°. (The critical value for the domain is $\gamma_0 = 34^\circ$.) The 3-dimensional views of the surface are color-shaded by PLTMG to indicate contour levels, grayscale versions of which are shown in the figure. The viewpoint for each surface is the same. Generally, the computations indicate that as γ decreases toward the critical contact angle, liquid moves toward and up the two proboscis walls, with the local maximum heights, as calculated by the program, at the proboscis tips. The heights at the right are higher than the corresponding ones at the left. The surfaces for the 20°/26° and 36°/44° proboscis domains behave similarly.

One sees that the numerically computed rise height in the container is modest until γ gets close to the critical value. The computations indicate that using containers of sufficient height (five for our containers), one could distinguish between the critical value γ_0 for the container (liquid in right proboscis rises to the lid) and a contact angle value 1° greater (liquid rise height < five).

6. USML-2 ICE EXPERIMENT

In addition to the three double proboscis containers depicted in figure 3, the USML-2 ICE experiment also has a wedge container. This container is constructed to allow the interior wedge angle 2α (fig. 1) to be varied, allowing observation of the wedge phenomenon for both the advancing and receding cases.

All vessels flown were similar in construction; the 20°/26° proboscis vessel is depicted in figure 5. The primary vessel components are a two-piece acrylic-plastic (transparent) body, an aluminum piston and control dial, a stainless steel drive screw, an aluminum valve, and an aluminum base for securing the vessel to the experiment platform. O-ring seals are employed throughout. The internal surfaces of the proboscis vessels were precision milled on a numerically-controlled machine using a diamond tipped cutting tool; the coordinates were computed from equation (1). The critical surfaces were finished by an extremely light polish ("wipe") using a dry cloth. These vessels were fabricated in halves divided by the plane of symmetry, and the two halves were fused without corruption of the interior corner at the joint. Postfabrication calibration of the vessels revealed a mean tolerance of less than 76 μm for the proboscis shapes, as determined by the distance of the container wall to the measured cylinder axis. Based on the maximum container section dimension of 1.5 cm, compliance of the proboscis profiles with those determined mathematically were estimated to be within ± 0.5 percent.

The general experimental procedure for ICE during the USML-2 flight was to partially fill the selected vessels with prescribed volumes of fluid and to record with video cameras the fluid interface configurations that resulted. The crew procedures for carrying out the experiment consisted primarily of the following steps: 1) unstow equipment, 2) set up Glovebox and vessel, 3) charge vessel/activate, 4) observe stable surfaces, 5) disturb surface configuration(s) (varying wedge angle for wedge container), 6) observe resulting surfaces, 7) repeat steps 5) and 6), and 8) reverse fill procedure and stow. Approximately 50 min were required for each vessel. The Spacelab camcorder and a Glovebox full-color 1:1 video camera were utilized. Devices for the measurement of ambient Glovebox temperature and local acceleration levels (SAMS) were also used.

To begin the experiment, a crew member retrieved the Spacelab camcorder and unstowed the ICE vessel to be tested. An additional Glovebox full-color 1:1 camera was used for the wedge vessel, which required two orthogonal views. A diffuse backlight panel provided illumination for the video photography.

6.1 Proboscis Vessels

The test liquid for the proboscis vessels was an aqueous ethanol solution, 50 percent by volume. This particular concentration was selected for the specific wetting conditions desired. The longtime "equilibrium" contact angle for this liquid on acrylic plastic in the presence of ethanol saturated air was $32^\circ \pm 2^\circ$. The widest range of static contact angle hysteresis measured for the liquid on a machined, lightly-polished acrylic surface was 18° for the receding value and 43° for the advancing value. Mean values were 20° and 41° , respectively, with an equilibrium value of $\gamma_{eq} = 32^\circ$, all values producing a consistent uncertainty of $\pm 2^\circ$.

To carry out the fill procedure for the proboscis vessels, the crew member pulled open the reservoir valve and turned the control dial, displacing the entire liquid contents of the reservoir into the container. The liquid then assumed a particular "static" configuration (not necessarily an equilibrium configuration—a "static" configuration of an interface implies a possibly metastable state, common in partially wetting, contact-line-dominated situations exhibiting significant contact angle hysteresis).¹³ Time was allowed for the configuration to stabilize (up to 5 min). The crew member then disturbed the surface by tapping the side of the container with his finger, lightly at first and then subsequently with increasing force. All new surfaces that formed in the container during the tapping process were given time to stabilize and were captured on video. The tapping, which led eventually to larger scale rocking and sloshing, produced different results for each of the three containers. These results are discussed below.

6.1.1 Vessel ICE-P1

The first vessel tested was ICE-P1, the $20^\circ/26^\circ$ vessel, as depicted in figure 3. Both proboscides for this vessel are subcritical for the $\gamma_{eq}=32^\circ$ liquid. Figures 6a-b show two static interface shapes for the vessel. Figure 6a was taken shortly after the fill procedure was completed, and figure 6b was taken after significant disturbances to the vessel had been imparted by the payload specialist. Very little change in the interface can, nevertheless, be distinguished between initial and final states. This is in accord with the mathematical predictions, as the measured equilibrium contact angle $32^\circ \pm 2^\circ$ is greater than the critical angles for both proboscides. The somewhat more elevated surface in the righthand 26° proboscis relative to the lefthand one is anticipated, as the critical angle for it is closer to the value $\gamma_{eq} = 32^\circ$ (cf., fig. 4).

Imparting larger disturbances might possibly have “released” the liquid to end up with a somewhat larger height difference between the two proboscides, as, say, in the 40° case in figure 4; but, generally, the video indicated much more stable behavior for this vessel than for the subsequent ones described below.

6.1.2 Vessel ICE-P2

The left-hand/right-hand proboscides for the ICE-P2 vessel are the 30°/34° ones. Thus, the left-hand proboscis is subcritical with respect to $\gamma_{eq} = 32^\circ$, while the right-hand one is supercritical. A series of static interfaces that formed during the test sequence is shown in figures 7a-d. Figure 7a is taken shortly after completion of the fill procedure. Figures 7b, 7c, and 7d are images of static interface configurations after successive disturbances to the vessel by the payload specialist. Once the liquid fill was completed in this test, light taps on the side of the container produced small, high frequency surface waves, but did not lead to observable bulk reorientation of the liquid. However, as the disturbances were increased in magnitude, the liquid rose noticeably and somewhat equally in the proboscides (fig. 7b), instead of returning to the initial state of figure 7a (as was the case for vessel ICE-P1, figs. 6a-b). After allowing sufficient time for stabilization, the crew member repeated the disturbances to the vessel but did not increase them in magnitude. Each disturbance was imparted by a single “push” (impulse) to the top left-hand side of the vessel which acted to rock the interface with a mean amplitude of ≈ 4 mm over a 0.4-sec (2.5-Hz) interval. The interface responded to the impulse disturbance with ≈ 1.3 Hz damped oscillations that decayed within 10 sec. The interface was allowed time to stabilize between each disturbance.

As seen in figures 7c and 7d, subsequent, larger disturbances, which were imparted to explore further the initial liquid rise, led to an increased rise only in the 34° right-hand supercritical proboscis. The penetration of the liquid into the right-hand proboscis took place regardless of whether the disturbances to the cell were applied to the top right-hand or left-hand side of the vessel. This result indicates, somewhat dramatically, that the slight differences in proboscis fabrication, which were designed to produce unbounded flow up the right-hand proboscis only, do influence fluid behavior strongly, even in the presence of hysteresis. In practice, however, significant disturbances ($2.5 \times 10^{-3} g_0$, $Bo_{dyn} = 0.19$) were necessary in order to overcome contact angle hysteresis and bring about the large shifts of liquid depicted in figures 7c-d. It is astonishing that though the hysteresis range for the test liquid is $20^\circ \leq \gamma \leq 41^\circ$, the interface behaved in a manner that is in accord with the mathematical predictions based on the idealized Y-L-G theory using a value $\gamma_{eq} = 32^\circ$. It is also striking that the uncertainty of $\pm 2^\circ$ for γ_{eq} did not mask the effect of the subtle differences in the left and right proboscides designed for the 30°/34° critical angles. We watched the behavior on the downlinked video as it occurred and were indeed astonished. It would be of interest to repeat the experiment to confirm the behavior and to rule out random or other effects that may have influenced it, but until then there remains the record of the compelling results that were obtained.

6.1.3 Vessel ICE-P3

Both proboscides for the third vessel, the 38°/44° one, are supercritical for the test fluid. Therefore, the mathematical predictions are that the liquid should rise spontaneously to the lid in both left and right proboscides. Because the right proboscis is more supercritical than the left, greater/faster rise may be anticipated there. A series of images, similar to those in figures 7a-d, are presented for vessel ICE-P3 in figures 8a-d. Figure 8a shows the interface after completion of the fill procedure, and figures 8b, 8c, and 8d show interfaces after subsequent disturbances to the vessel. Again, each image displays the liquid in a

static state. Disturbances to this vessel caused large shifts of liquid up both proboscides, with more up the right-hand proboscis. The liquid continued to penetrate higher in each proboscis regardless of the direction of the impulse disturbance. These results are in accordance with the predictions, except that the liquid did not move spontaneously—significant disturbances were necessary to bring about equilibrium-type behavior within the approximately 20 min allowed for the experiment.

After completion of the ICE-P3 procedures (figs. 8a-d), the crew placed the vessel (delicately) in the aft end cone of the Spacelab, where it was allowed to remain for 7 days. During this time it was observed that the liquid continued to creep, though very slowly, toward the end state configuration of figure 9, which was photographed with a 35-mm camera at the end of the 7 days. The lighting is not as favorable here, but the liquid free surface can nevertheless be identified satisfactorily. The liquid is seen to have risen further in the left-hand proboscis (cf., fig. 8d), while the liquid in the right-hand proboscis rose to the lid, covered it, at least partially, and then started advancing down the left-hand proboscis. The G-Y-L equilibrium state requires that the base, lid, and entire length of both proboscides be wet by the liquid. (The isolated drop in the lower left quadrant of fig. 9 was present prior to the long term storage (fig. 8d).)

These findings suggest that the theory can indeed be successful in predicting fluid behavior, if sufficient time is available to establish equilibrium. The time required to reach the configuration in figure 9 may have been lessened by existing mechanical and thermal disturbances, the latter hastening migration of the liquid toward equilibrium through successive evaporation and condensation, a process (associated with Kelvin energy) not included in the Y-L-G theory. Figures 8d and 9 show that the fluid bulk remained connected and that condensate drops on the container walls, common in many partial wetting systems subject to temperature cycling on Earth, were not present. We note that liquid near the proboscis tip in the cases for which the theory predicts the liquid still should be advancing (right proboscis in fig. 7c-d, both proboscides in fig. 8c-d) resembles the convex shape computed in reference 14 for the tip of a spreading liquid drop in a wedge.

The above results provide insight into the role of container geometry, contact angle, contact angle hysteresis, input disturbances, and length of time in predicting interface configurations. What is clearly established is the role of hysteresis near critical values for which slight changes in container geometry result in large changes in interface configuration. Hysteresis is found not to prevent the predicted behavior, but only to noticeably impede it. Significant perturbations to the interface are necessary to “encourage” the fluid to behave as predicted in reasonably rapid time.

6.2 Wedge Vessel

The test liquid for the wedge vessel is an immersion liquid, a blend of hydrogenated terphenyl and an aliphatic hydrocarbon. It possesses the special property of having a refractive index matched with that of the acrylic container, thus reducing optical distortions. A coating (FC-723, manufactured by 3M) was applied to the internal surfaces of the vessel to obtain the desired wetting conditions. The liquid was lightly dyed in order to enhance visibility of the interface.

For the wedge vessel, after filling is complete, the wedge adjustment knob is turned to gradually decrease the interior angle of the wedge. As the critical angle is traversed, the liquid is anticipated to “rise” rapidly in the corner. This angle is recorded on video. The wedge angle adjustment procedure is then reversed and repeated.

In figure 10 the vessel is shown for an interior wedge angle slightly less than the critical value; the liquid, which originally resided near the black dashed lines, rose to the lid of the vessel. The half-angle α was measured to be $\approx 21.5^\circ$, which is in accord with the ground-based contact angle measurement of $\gamma_{eq}=70^\circ$ ($+5^\circ$ – 10°). This experiment was a first step in demonstrating the functionality of the movable wedge apparatus and the feasibility of observing the discontinuous liquid behavior. The experiment is continuing on the current Mir 23/NASA 4 mission, and we plan to report the results after its completion.

7. CONCLUSIONS

The USML-2 ICE experiment shows in a striking way the discontinuous and nearly discontinuous behavior at the predicted critical angles. Even though hysteresis was large and surface friction impeded reorientation of the liquid, the mathematically predicted behavior at critical contact angle was observed. This lends credence to the validity of the concept of macroscopic contact angle and its Y-L-G formulation as tools for predicting fluid behavior.

REFERENCES

1. Chen, A.; Concus, P.; Finn, R.; and Weislogel, M.: "On Cylindrical Container Sections for a Capillary Free-Surface Experiment," *Microgravity Sci. Technol.*, to appear in 1997.
2. Finn, R.: *Equilibrium Capillary Surfaces*, Springer-Verlag, New York, 1986. Russian translation (with appendix by H.C. Wente), Mir Publishers, 1988.
3. Concus, P. and Finn, R.: "On Capillary Free Surfaces in the Absence of Gravity," *Acta Math.*, 132, 177–198, 1974.
4. Concus, P.; and Finn, R.: "Dichotomous Behavior of Capillary Surfaces in Zero Gravity," *Microgravity Sci. Technol.*, 3, 87–92, 1990; Errata, 3, 230, 1991.
5. Langbein, D.: "The Shape and Stability of Liquid Menisci at Solid Edges," *J. Fluid Mech.*, 213, 251–265, 1990.
6. Langbein, D.: "Liquid Surfaces in Polyhedral Containers," in *Advances in Geometric Analysis and Continuum Mechanics*, P. Concus and K. Lancaster, eds., International Press, Boston, 175–180, 1995.
7. Langbein, D.; Grossbach, R.; and Heide, W.: "Parabolic Flight Experiments on Fluid Surfaces and Wetting," *Microgravity Sci. Technol.*, 2, 198–211, 1990.
8. Fischer, B. and Finn, R.: "Non-Existence Theorems and Measurement of Capillary Contact Angle," *Zeit. Anal. Anwend.*, 12, 405–423, 1993.
9. Finn, R.: "A Subsidiary Variational Problem and Existence Criteria for Capillary Surfaces," *J. Reine Angew Math.*, 353, 196–214, 1984.
10. Finn, R. and Leise, T.: "On the Canonical Proboscis," *Zeit. Anal. Anwend.*, 13, 443–462, 1994.
11. Concus, P.; Finn, R.; and Zabihi, F.: "On Canonical Cylinder Sections for Accurate Determination of Contact Angle in Microgravity," *Fluid Mechanics Phenomena in Microgravity*, D.A. Siginer and M.M. Weislogel, eds., AMD Vol. 154, Amer. Soc. Mech. Engineers, New York, 125–131, 1992.
12. Bank, R.E.: PLTMG: A Software Package for Solving Elliptic Partial Differential Equations, SIAM, Philadelphia, 1994; software available via Netlib (WWW: <http://www.netlib.org>, E-mail: netlib@research.att.com).
13. Kistler, S.F.: "Hydrodynamics of Wetting," in *Wettability*, J.C. Berg, ed., Surfactant Science Series, 49, Chap. 6, 1993.
14. Weislogel, M.: "Capillary Flow in an Interior Corner," doctoral dissertation, Northwestern Univ., 1996.

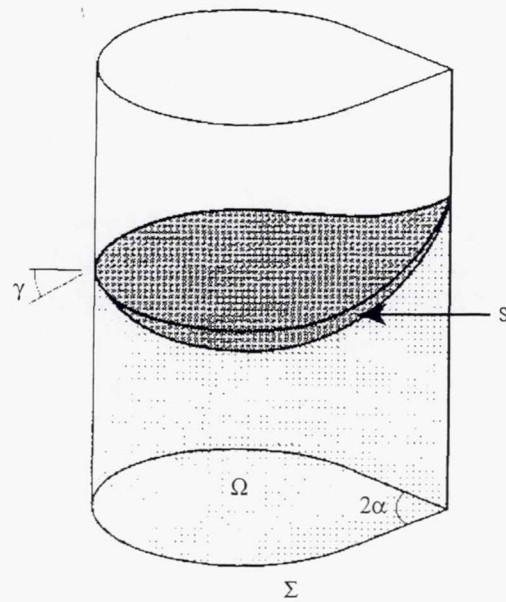


Figure 1. Wedge container.

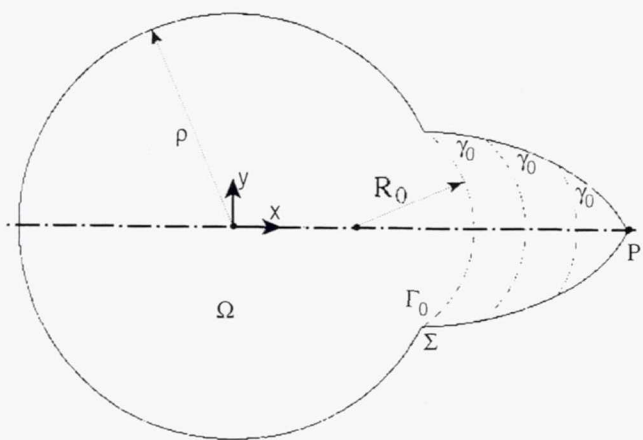


Figure 2. Proboscis container section showing three members of the continuum of extremal arcs.

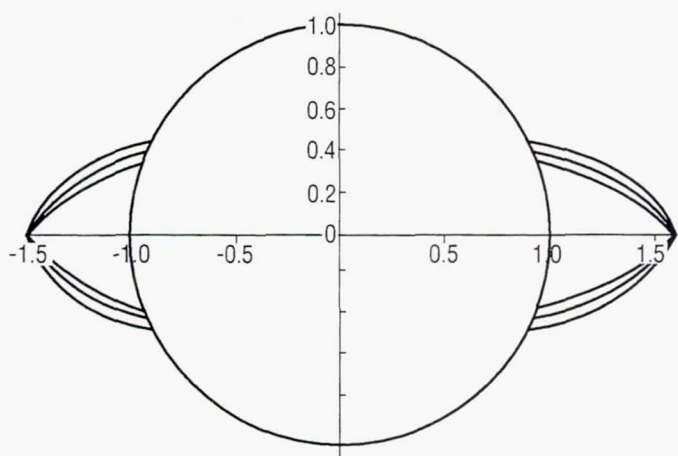


Figure 3. Three superimposed double proboscis container sections. From outermost to innermost, the pair of values of γ_0 for the left and right proboscides of each section are $20^\circ/26^\circ$, $30^\circ/34^\circ$, and $38^\circ/44^\circ$.

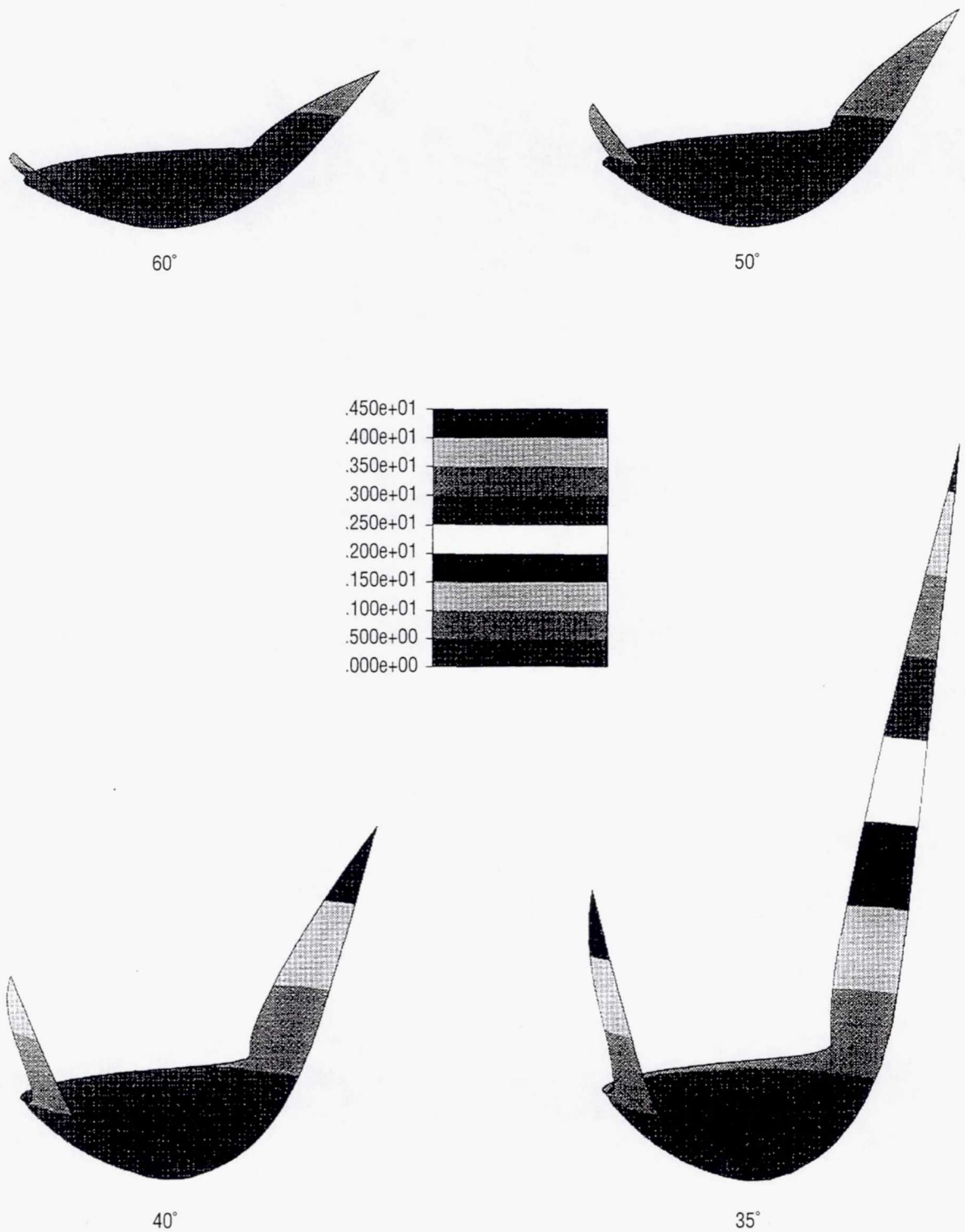


Figure 4. Computed equilibrium interface for the 30°/34° (upper-half) double proboscis section for contact angles 60°, 50°, 40°, and 35°. $\gamma_0 = 34^\circ$.

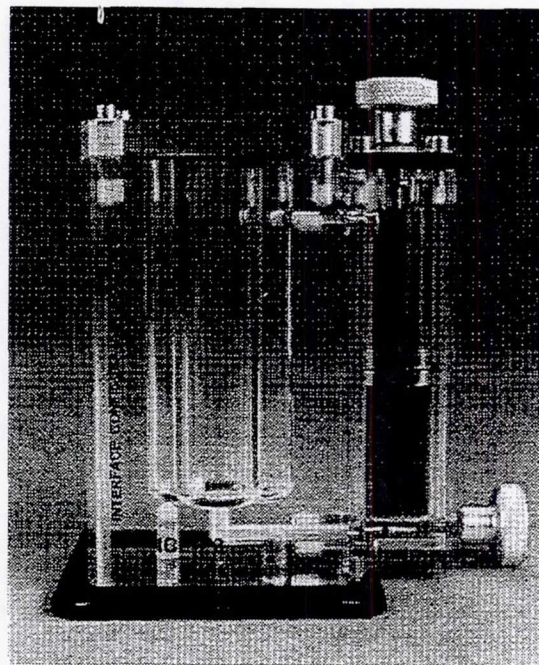
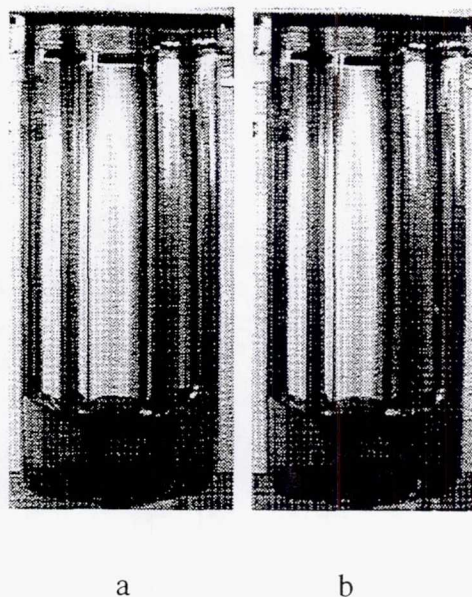
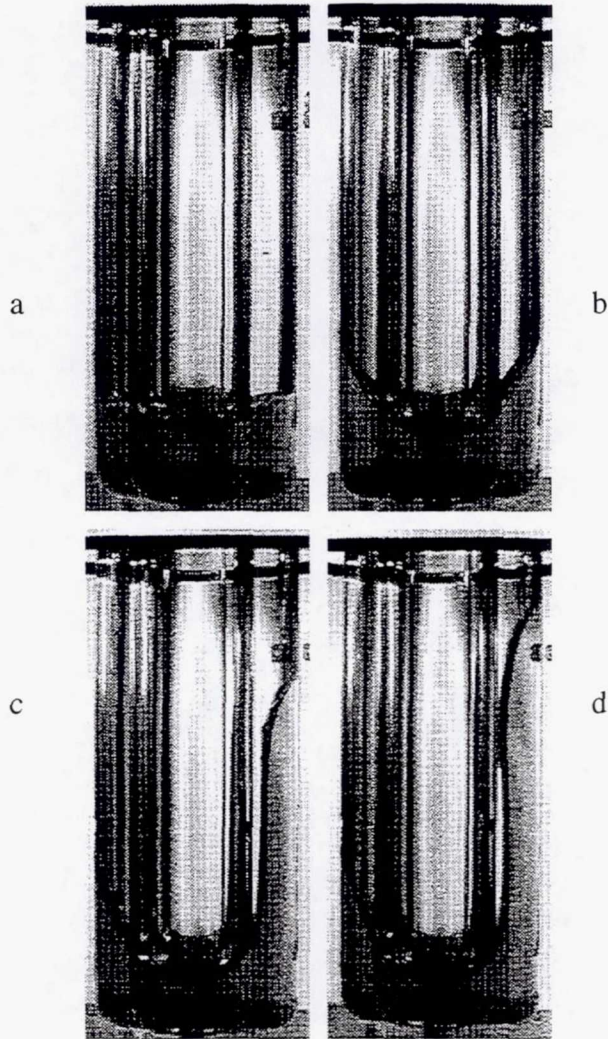


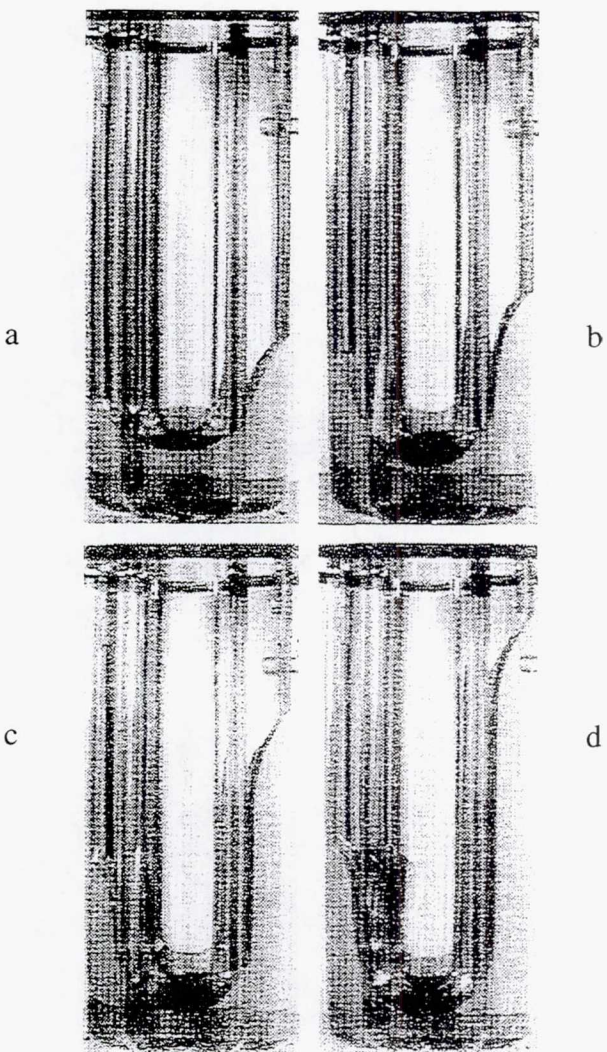
Figure 5. 20°/26° proboscis vessel (flight unit).



Figures 6a-b. Static interface shapes for ICE-P1 (20°/26°) vessel. 6a (left)—after completion of fill; 6b (right)—after disturbances by payload specialist.



Figures 7a-d. Static interface shapes for ICE-P2 (30°/34°) vessel. 7a (upper left)—after completion of fill; 7b (upper right), 7c (lower left), and 7d (lower right)—after successive disturbances by payload specialist.



Figures 8a-d. Static interface shapes for ICE-P3 ($38^\circ/44^\circ$) vessel. 8a (upper left)—after completion of fill; 8b (upper right), 8c (lower left), and 8d (lower right)—after successive disturbances by payload specialist.

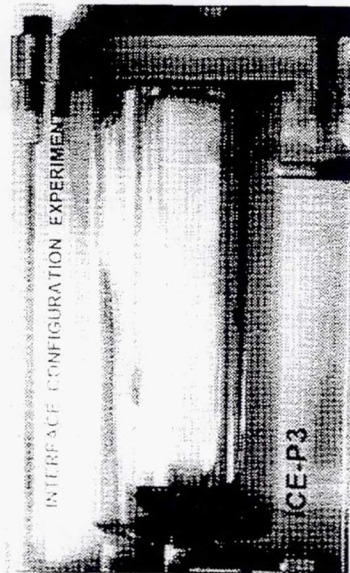


Figure 9. Static interface shape for ICE-P3 ($38^\circ/44^\circ$) vessel 1 week after that shown in figure 8d.



Figure 10. ICE wedge vessel near critical angle.

Page intentionally left blank

EXPERIMENT XXXI.

OSCILLATORY THERMOCAPILLARY FLOW EXPERIMENT-2 (OTFE-2)

ACKNOWLEDGMENTS

The authors would like to thank Dr. Fred Leslie who conducted the OTFE-2 tests expertly. We acknowledge the financial support of NASA. The authors also wish to thank Ms. Li Wang for her help in the data analysis.

OSCILLATORY THERMOCAPILLARY FLOW EXPERIMENT-2 (OTFE-2)

Yasuhiro Kamotani

Department of Mechanical and Aerospace Engineering
Case Western Reserve University
Cleveland, OH 44106

Phone: 216-368-6455
FAX: 216-368-6445
E-mail: yxk@po.cwru.edu

Simon Ostrach

Department of Mechanical and Aerospace Engineering
Case Western Reserve University
Cleveland, OH 44106

Alexander D. Pline

Code UG
NASA Headquarters
Washington, DC 20546

ABSTRACT

Oscillatory thermocapillary flow experiments were performed in the Glovebox aboard the USML-2 Spacelab which was launched on October 20, 1995. Open cylindrical containers of 1.2 and 2.0 cm in diameter were used. The ratio of container depth to radius (aspect ratio) was set at 0.5 and 2. Silicone oil of 2 centistokes kinematic viscosity was the test fluid. The fluid was heated by a cylindrical heater placed along the center axis of the container. The fluid motion was studied by flow visualization. The effect of aspect ratio on the onset of oscillations and on the oscillatory flow was investigated. It was found that the onset of oscillations was delayed when the container was made more shallow.

1. INTRODUCTION

Oscillatory Thermocapillary Flow Experiment-2 (OTFE-2) was conducted aboard the USML-2 Spacelab in conjunction with the STDCE-2. An introduction to this subject is found in the STDCE-2 report. The main objective of the OTFE-2 was to investigate the effect of container aspect (depth/radius) ratio on the oscillatory thermocapillary flow phenomenon. In the STDCE-2 the container aspect ratio was unity in most of the tests. Based on earlier studies it is known that the aspect ratio has a strong effect on the onset of oscillations. For that reason the aspect ratio of the OTFE-2 test chambers was set at 0.5 and 2 in order to supplement the STDCE-2 data. The heating mode was the constant temperature (CT) mode of the

STDCE-2, in which the fluid was heated by a cylindrical heater along the container centerline. The OTFE-2 tests were performed in the glovebox aboard USML-2. We performed similar Glovebox experiments, called the OTFE-1, aboard the USML-1 Spacelab in 1992. Although steady flow was observed in the OTFE-1, bubbles generated in the fluid disturbed the flow before it became oscillatory so that the conditions for the onset of oscillations were not determined. The container design was improved in the OTFE-2 to minimize the appearance of bubbles.

2. EXPERIMENTAL APPARATUS AND PROCEDURE

The experimental configuration of the OTFE-2 was the CT configuration of the STDCE-2 and the same test fluid (2 centistokes silicone oil) was used in both experiments. Cylindrical test chambers of 1.2-and 2-cm diameters were used (1.2-, 2-, and 3-cm test chambers in the STDCE-2). For each container diameter, two modules having the container depth/radius ratio of 0.5 and 2 were prepared. Therefore, a total of four test modules were used in the OTFE-2. Each module was configured around a base plate. Two photographs of the test module are given in figure 1, and a cross-sectional view of the module is sketched in figure 2.

The side wall of the test chamber was made of copper. Because there was no active cooling of the side wall, the mass of the copper chamber was sized appropriately for the amount of heat produced by the heater. The bottom wall was Teflon® for thermal insulation, through which the heater was inserted into the test chamber. The diameter of the heater was 10 percent of the container diameter. The current through the heater was controlled by adjusting a 10-turn potentiometer with an attached gauge to count the turns. It had been found in ground tests that air bubbles tended to appear from the gap between the heating rod and the Teflon® bottom when the heater became hot. Epoxy was used to seal the gap in the OTFE-1, but the epoxy generated vapor when it became very hot and disrupted the tests. In the OTFE-2 the epoxy was replaced by high-temperature grease which was found to be effective in reducing bubble appearance in our ground-based tests. The internal walls of the test chamber were blackened to reduce unwanted reflections. The lid to the test chamber was made of Lexan® with an anti-reflective coating. The test fluid was kept in a cylindrical reservoir with a movable piston. Tracer particles (70- μ m-diameter Pliolite®) were mixed with the fluid in the reservoir for flow visualization. A small stainless steel ball was placed in the reservoir to provide a method to mix the tracer particles uniformly in the fluid prior to operation. The fluid was delivered to the covered test cell by turning the piston handle. The displaced air from the test cell filled the space behind the piston, maintaining a closed system. The reservoir design and the method of filling were the same as those in the STDCE-2.

A thermocouple was imbedded in the heater to monitor its temperature. Another thermocouple monitored the side wall temperature near the fluid pinning edge. A thermocouple probe was placed in the fluid at the half-radius location, whose axial position was one-third of the depth away from the free surface. The size of thermocouple joint was about 0.25 mm. As in the STDCE-2 design, the thermocouple imbedded in the heater was near the heating element so the measured temperature tended to be higher than the heater outside surface temperature which was needed in computing ΔT . After the flight we measured the outside surface temperature by a fine thermocouple and determined the relationship between the internal thermocouple data and the surface temperature. The heater and thermocouple leads were routed through the base plate to a printed circuit board. The circuit board contained signal conditioning electronics and LED displays for three thermocouples and a heater power control unit. Two video cameras were used—

one to view the flow field in the chamber through the top of the Glovebox and one to view the LED displays. The flow field was illuminated by the Glovebox light source. Both video tapes were time-stamped so that they can be temporally correlated after the experiment.

The experimental procedure went generally as follows. After a desired test module was placed in the Glovebox, the test chamber was filled until the fluid free surface was judged to be flat (the fluid volume out of the reservoir was also monitored). Then the heater power was increased in a stepwise manner while watching the flow field. The heater power was adjusted by setting the dial on the externally mounted heater control pot. After oscillations were found, the flow was observed for some time. The heater power was then decreased below the onset point and then increased to check the onset point again. After that the power was increased further to investigate pronounced oscillation patterns. The video information was downlinked in real time to the ground station where we monitored the experiment so that we were able to control the experiment interactively with the astronaut experimenter.

3. PARAMETRIC RANGES

The important dimensionless parameters for steady thermocapillary flow in the present configuration are: Marangoni number (Ma) = $\sigma_T \Delta T R / \mu \alpha$, Prandtl number (Pr) = ν / α , aspect ratio (Ar) = H/R , and relative heater size (Hr) = D_H/D , where σ_T is the temperature coefficient of surface tension, ΔT the temperature difference between the heater and the side wall, H the container depth, D the container diameter, R the radius, D_H the heater diameter, ν the fluid kinematic viscosity, μ the dynamic viscosity, α the thermal diffusivity. As we found in our past studies, the onset of oscillations cannot be characterized by the above parameters alone, and we have proposed an additional parameter (S -parameter) which represents free surface deformation. In the report for the STDCE-2, the S -parameter for the CT configuration is defined as:

$$S = \left(\frac{\rho \alpha^2}{\sigma R} \right)^{1/2} Ma , \quad (1)$$

where ρ is the fluid density and σ the surface tension. As shown in the STDCE-2 report, the parameter characterizes the onset of oscillations in the STDCE-2 and in our ground-based tests in the CT configuration with $Ar = 1$. Note that the S -parameter is associated only with the onset conditions of oscillations.

In the OTFE-2, Hr was fixed at 0.1 as in the STDCE-2, and Ar was 0.5 and 2 (unity in the STDCE-2). The value of Pr varied as the fluid viscosity changed with temperature, and it ranged from 19 to 26 in the experiments, where the fluid viscosity was evaluated at the mean temperature of the heater and the side wall. The maximum value of Ma in the experiments was 2.6×10^5 . The values of S at the critical conditions will be given later.

4. RESULTS AND DISCUSSIONS

A total of four tests were conducted as originally planned. Oscillations were found in all of them. Bubbles appeared occasionally, but they were removed (except one case which is discussed below) so they did not affect the oscillation phenomenon. How the heater and side wall temperatures varied in those tests are shown in figures 3-6. As mentioned earlier, the thermocouple inside the heater did not give the correct heater surface temperature, and the reading was calibrated, after the flight, against a more accurate measurement of the surface temperature. The data shown in figures 3-6 are the corrected data.

The data in figure 3 were obtained with the 1.2-cm-diameter test chamber with $Ar = 0.5$. Since this was the first OTFE-2 test, it was not known how the potentiometer turn was related to the actual heater temperature. For that reason, the heater temperature was increased too fast and the heater became very hot. The heater power was then switched off and, after the whole system became thermally equilibrated, its power was increased again but more slowly. Nevertheless, the fast power increase gave us useful information regarding the effect of heating rate on the onset of oscillations. As seen in figure 3, the onset of oscillations was delayed when the heater temperature was increased too fast. In the second power ramp-up, we made sure that the flow field became steady at each power setting. The flow was found to become oscillatory at $\Delta T_{cr} = 45.0$ °C. The oscillatory flow was similar to that found in the STDCE-2 with $Ar = 1$: the tracer particles moved back and forth in the azimuthal direction as they circulated in the flow cell. The back-and-forth motion became clearer when, after the flight, the tape was viewed in fast-forward mode. The heater power was reduced after some time to stop the oscillations. In the third power ramp-up, the heater power was increased quickly to the level just below the critical power found in the second ramp-up. The onset occurred at $\Delta T_{cr} = 42.8$ °C. Based on our past experiments of oscillatory thermocapillary flows, we can say that for a given test setup, the value of ΔT_{cr} is reproducible within about ± 10 percent. Therefore, the above two values of ΔT_{cr} are within that range.

Figure 4 shows the data taken with the 1.2-cm-diameter container with $Ar = 2$. The power was again increased very quickly at first. The flow became oscillatory, but the value of ΔT_{cr} was large. After the onset the heater power was decreased slowly until the oscillations disappeared, which happened at $\Delta T = 19.5$ °C. The power was then increased slowly, and the oscillations were found at $\Delta T = 20.8$ °C. After some time the power was decreased, and the flow became steady at $\Delta T = 18.5$ °C. Therefore, in this test whether with increasing power or decreasing power, ΔT_{cr} did not change much. After a pause the power was increased to higher levels to study pronounced oscillations. The output from the thermocouple probe placed in the fluid is shown in figure 7, which was obtained when the flow was oscillating strongly. The thermocouple was not sensitive enough to detect oscillations near the onset.

The data taken with the 2-cm-diameter container with $Ar = 0.5$ are presented in figure 5. The heater power was increased very gradually from the beginning. In the process small bubbles appeared, apparently from the gap between the container side wall and the Teflon® bottom, but they were small (about 10 percent of container radius or smaller). It is our experience that a bubble stuck to the heater disrupts the flow most as thermocapillary flow is generated around the bubble. The bubbles in this test were moving freely and, since the flow was recirculating and the bubbles were lighter than the fluid, they eventually

went to the center of the recirculating cell and stayed there. There were two bubbles, about 30° apart in the azimuthal direction, at the onset of oscillations and they started to move back and forth in the azimuthal direction at the onset. The bubble motion was found to be a good indicator of oscillations. Interestingly, six of the bubbles eventually appeared and positioned themselves about 40° apart from each other in the azimuthal direction in the oscillatory flow. That suggested that the oscillatory flow had several secondary cells in the azimuthal direction (pie-shaped cells). At present we do not know whether the secondary flow was created by the bubbles. After the flow became oscillatory, the power was reduced gradually until the flow became steady. As seen in the figure, ΔT_{cr} to stop oscillations (25.3 °C) was smaller than that to induce oscillations (33.4 °C). In the second power ramp-up, in which six bubbles were present from the beginning (compared to two in the first ramp-up), ΔT_{cr} to induce oscillations was found to be 27.7 °C. It seems that the bubbles did affect the onset, especially when there were six bubbles.

The data for the 2-cm-diameter container with $Ar = 2$ are shown in figure 6. The power was increased gradually and, after the onset of oscillations was identified, the power was reduced. Hysteresis was seen. The power was increased again until the onset of oscillations. The difference between the value of ΔT_{cr} to induce oscillations found in the second power ramp-up (14.6 °C) and that found in the first ramp-up (16.1 °C) was within the aforementioned data reproducibility.

The values of ΔT_{cr} found in the OTFE-2 tests and in the CT flat surface tests of the STDCE-2 are shown in figure 8 as a function of Ar . Those values are the ΔT_{cr} to induce oscillations. Figure 8 shows that for a given container diameter, ΔT_{cr} decreased with increasing Ar . The trend is somewhat misleading because there was a difference in fluid viscosity in the two experiments. In the STDCE-2, the side wall was actively cooled by the Spacelab water by way of a heat exchanger, so it was maintained at about 15 °C. In the OTFE-2, the side wall was not actively cooled, and its temperature stayed in the range 25–30 °C. Consequently, the fluid viscosity was generally larger in the STDCE-2. Therefore, the critical conditions found in the two experiments should be compared in dimensionless terms.

The data in figure 8 are then replotted in terms of S (defined in Equation (1)) and Ar in figure 9. As the figure shows, the S -parameter correlates the data from two different size containers well. The effect of Ar was strong when Ar was less than one. The critical S -parameter increased sharply with decreasing Ar . When Ar was larger than one, the onset condition was a relatively weak function of Ar . Those trends are consistent with our earlier results from ground-based tests.

The oscillation frequencies (f) near the onset of oscillations are given in figure 10, together with the STDCE-2 data. For a given container diameter the frequency increases sharply with decreasing Ar (or container depth) when Ar is less than about one. For a given Ar the frequency decreases with increasing container diameter. The above trends are due to the fact that the oscillation period scales with the time of convection of the bulk flow. Based on that, we non-dimensionalize the oscillation frequency as follows, as explained in the STDCE-2 report:

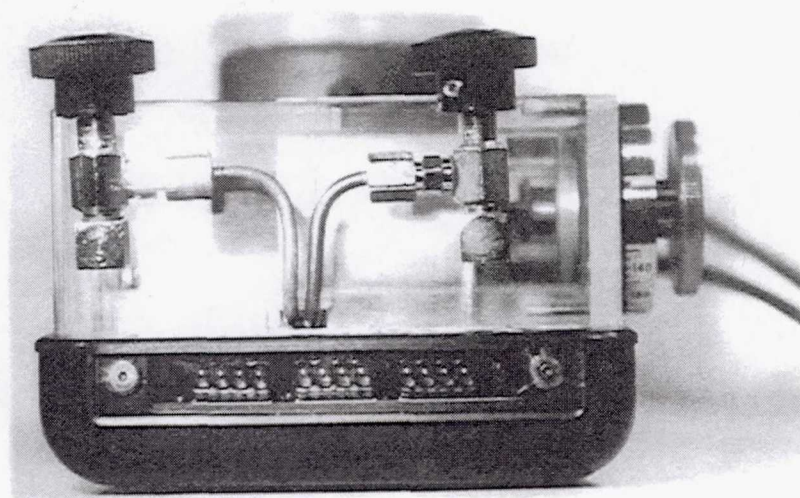
$$f^* = \frac{f}{U_b / R} = \left(\frac{fR^2}{\alpha} \right) / Ma^{4/5}, \quad (2)$$

where U_b is the bulk flow velocity scale. The dimensionless frequencies f^* are given in figure 11. As seen in the figure, Equation (2) correlates the data well and the dimensionless frequency is nearly constant (≈ 0.016) for all the tests.

CONCLUSIONS

Some conclusions obtained in the OTFE-2 are as follows.

- The oscillatory flow structure observed in the containers of $Ar = 0.5$ and 2 was qualitatively similar to that observed in the STDCE-2 with $Ar = 1$.
- The critical temperature difference, ΔT_{cr} , for $Ar = 0.5$ was much larger than that for $Ar = 2$. The S -parameter and Ar correlated the critical conditions found in the OTFE-2 and STDCE-2 well. S increased sharply with decreasing Ar when Ar was less than one.
- ΔT_{cr} to induce oscillations was larger than that to stop oscillations (hysteresis effect) in two tests, but no such hysteresis was found in one test.
- The oscillation period scales with the time of convection of the bulk flow.



Side view



Top view

Figure 1. Photographs of OTFE-2 test module.

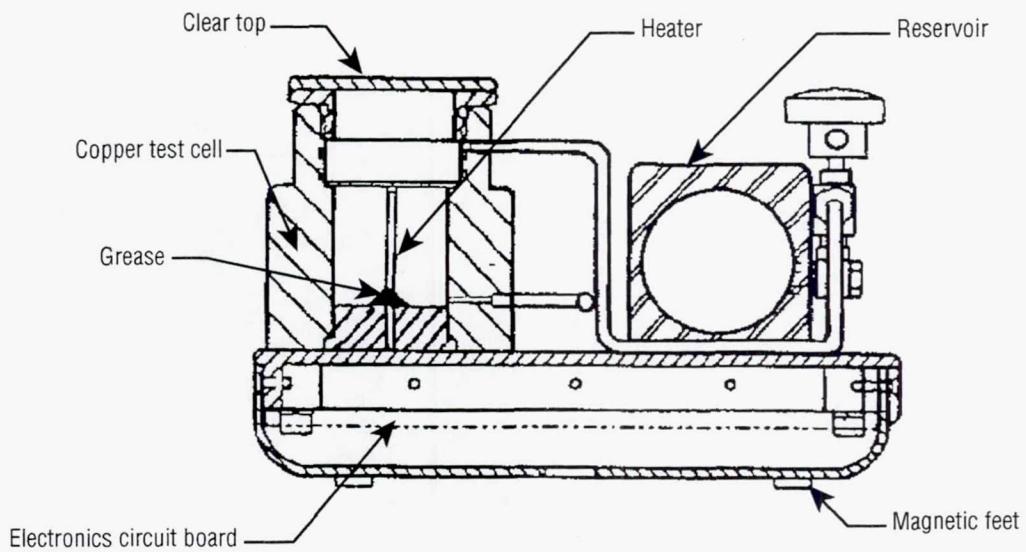


Figure 2. Cross-sectional view of test module.

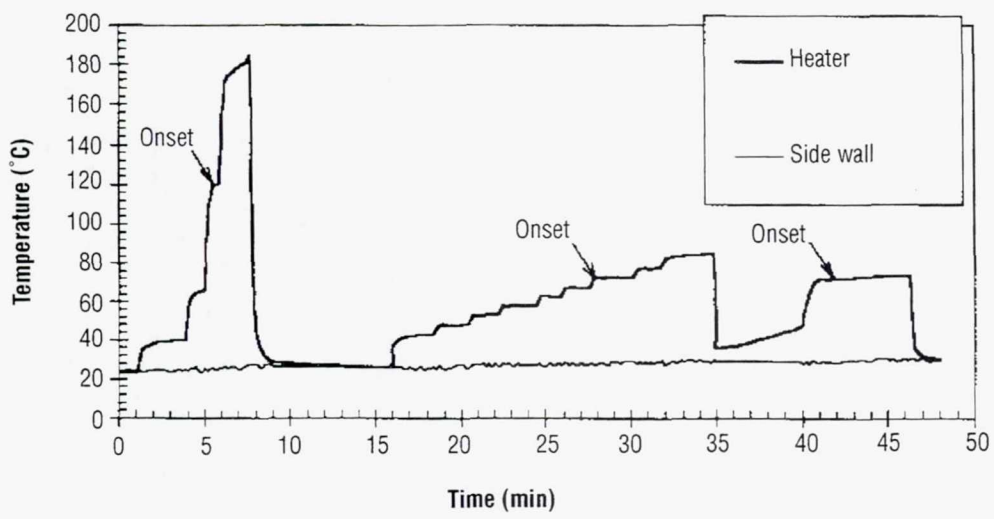


Figure 3. Temperature variations in Test 1 ($D = 1.2$ cm and $Ar = 0.5$).

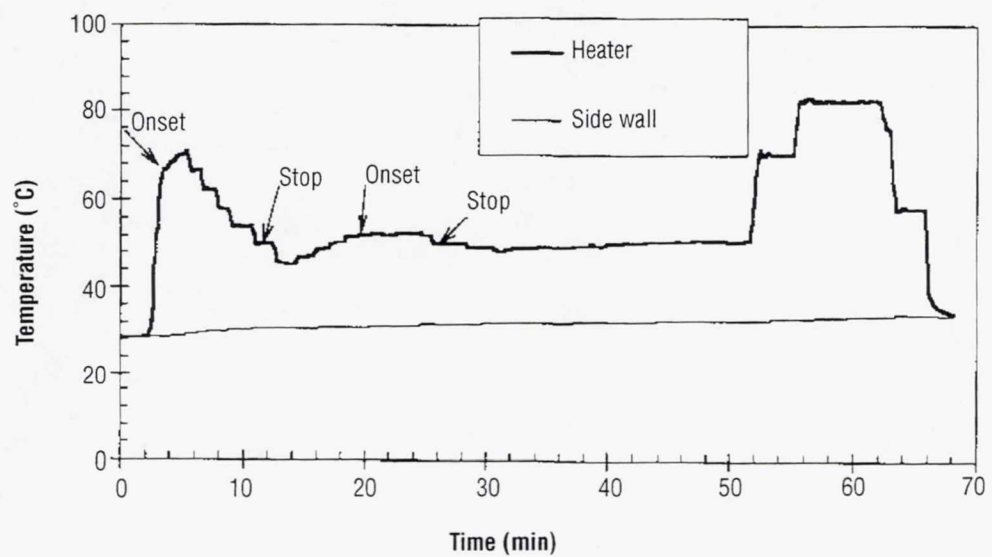


Figure 4. Temperature variations in Test 2 ($D = 1.2$ cm and $Ar = 2$).

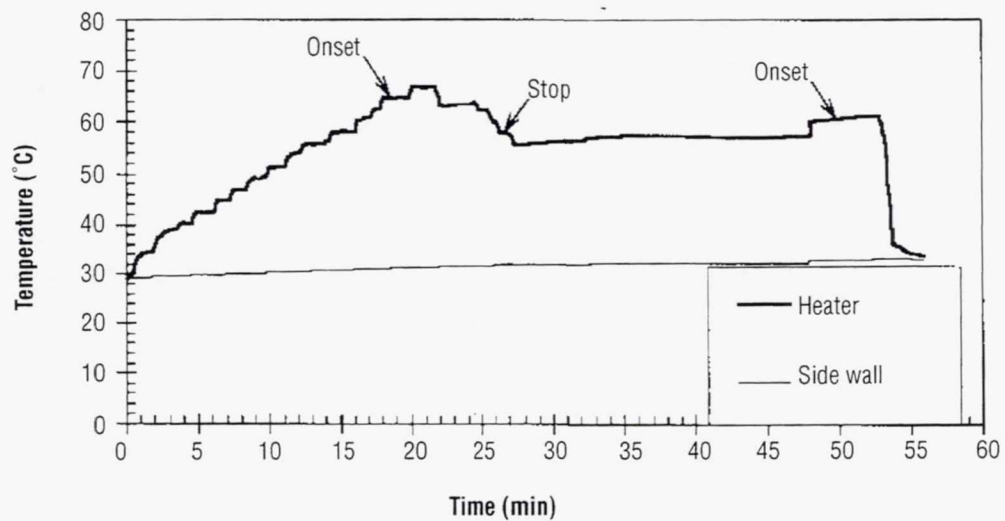


Figure 5. Temperature variations in Test 3 ($D = 2$ cm and $Ar = 0.5$).

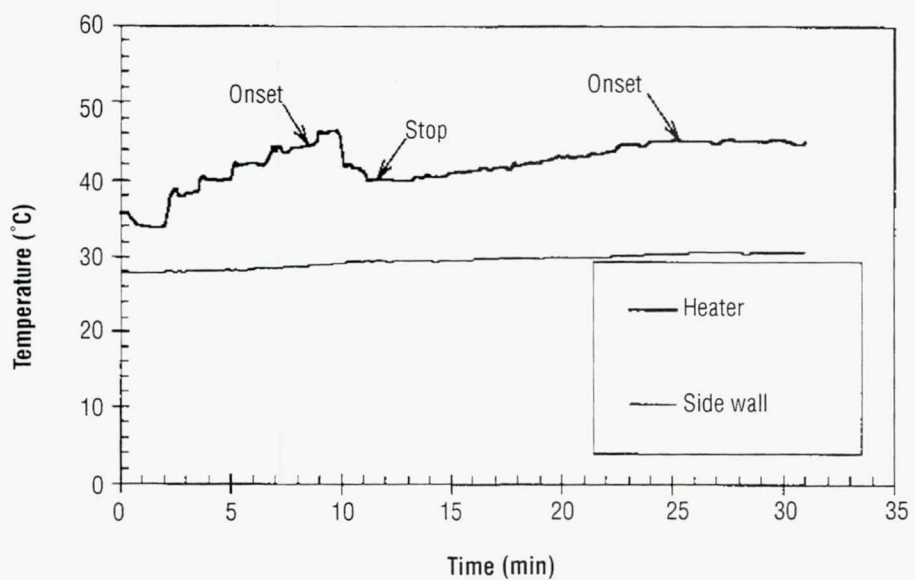
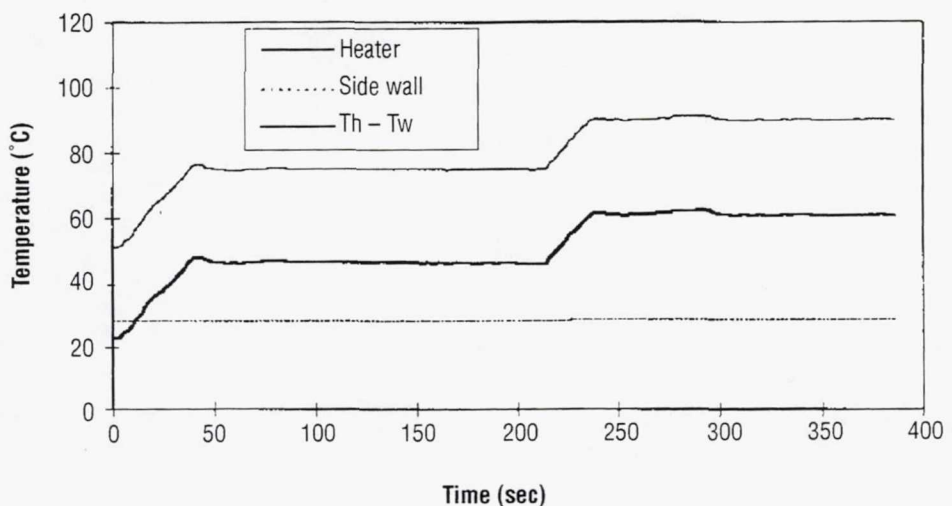
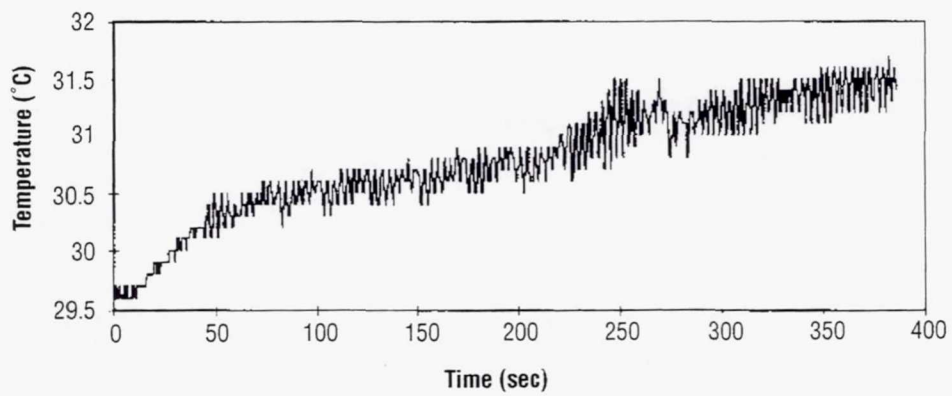


Figure 6. Temperature variations in Test 4 ($D = 2$ cm and $Ar = 2$).



(a) Variations of heater and side wall temperatures



(b) Output from thermocouple in fluid

Figure 7. Thermocouple outputs in Test 2 ($D = 1.2$ cm and $Ar = 2$).

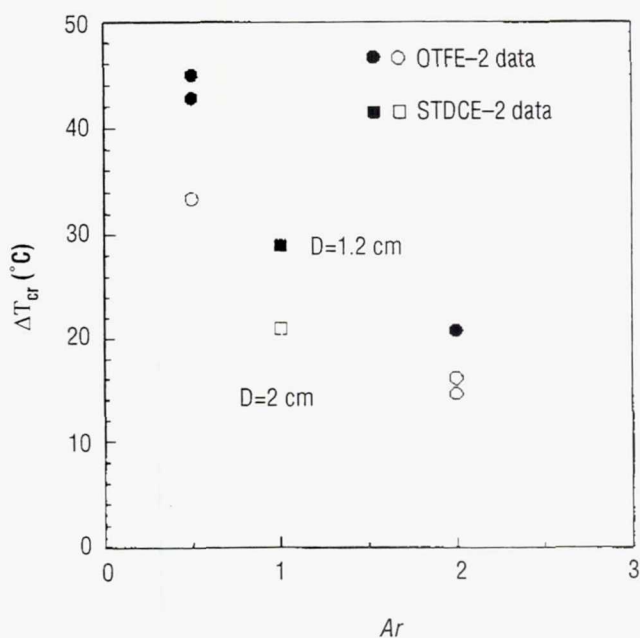


Figure 8. Critical temperature differences measured in OTFE-2 and STDCE-2.

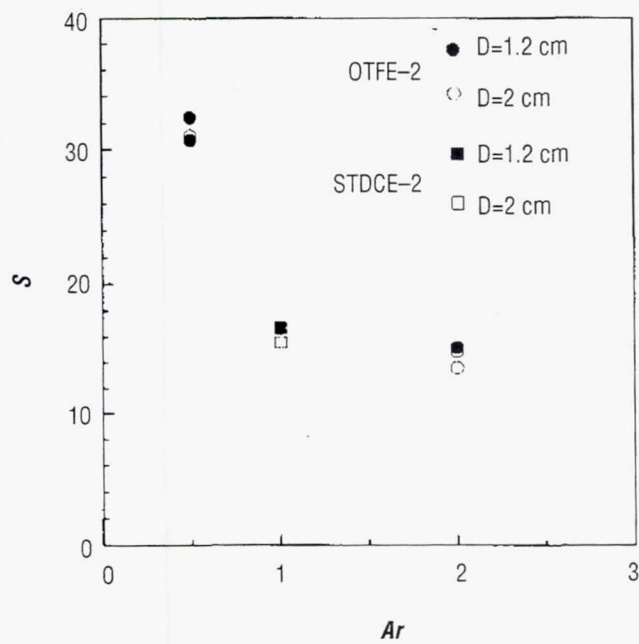


Figure 9. Critical S -parameters in OTFE-2 and STDCE-2.

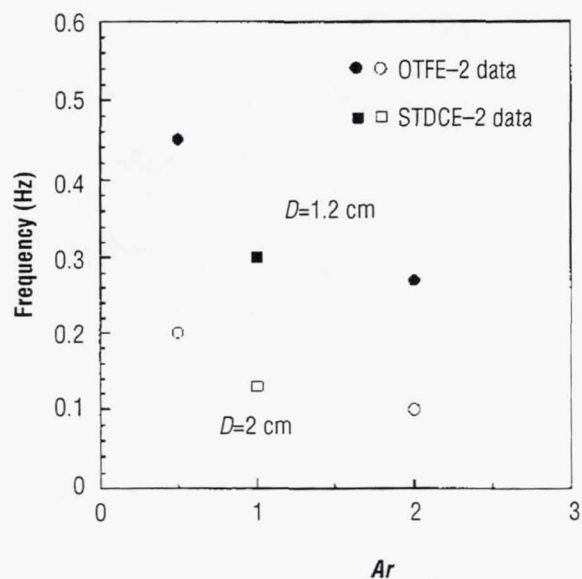


Figure 10. Oscillation frequencies.

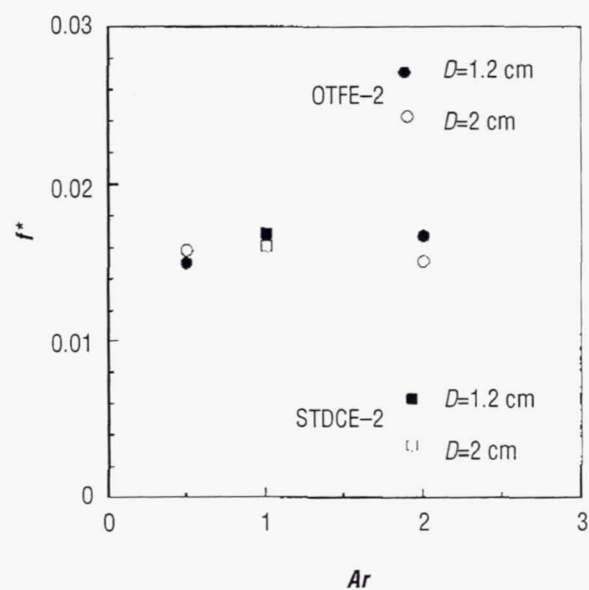


Figure 11. Dimensionless frequencies.

Page intentionally left blank

EXPERIMENT XXXII.

FIBER-SUPPORTED DROPLET COMBUSTION

ACKNOWLEDGMENT

We extend sincere thanks to John Parina and to Carl Fritz for assistance in preparing the flight hardware. We also wish to thank Anthony Marchese (Princeton) and Bai-Li Zhang (UCSD) who, as graduate students, have supported this work through data reduction and modeling efforts. This research was sponsored by the NASA microgravity combustion science program.

FIBER-SUPPORTED DROPLET COMBUSTION

Daniel L. Dietrich

John B. Haggard Jr.

Vedha Nayagam

NASA Lewis Research Center

21000 Brookpark Road

Cleveland, OH 44135

Frederick L. Dryer

Department of Mechanical and Aerospace Engineering

Princeton University

Princeton, NJ 08544

Ben D. Shaw

Department of Mechanical, Aeronautical and Materials Engineering

University of California, Davis

Davis, CA 95616

Forman A. Williams

Center for Energy and Combustion Research, 0411

University of California, San Diego

La Jolla, CA 92093

Phone: 619-534-4285

FAX: 619-534-5354

Email: faw@ames.ucsd.edu

ABSTRACT

Individual droplets with diameters ranging from about 2 mm to 5 mm were burned under microgravity conditions in air at 1 bar with an ambient temperature of 300 K. Each droplet was tethered by a silicon carbide fiber of 80 mm or 150 mm diameter to keep it in view of video recording, and, in some tests, a forced air flow was applied in a direction parallel to the fiber axis. Methanol, two methanol-water mixtures, two methanol-dodecanol mixtures and two heptane-hexadecane mixtures were the fuels. Droplet diameters were measured as functions of time and compared with existing theoretical predictions. The prediction that methanol droplets extinguish at diameters that increase with increasing initial droplet diameter is verified by these experiments. In addition, the quasi-steady burning rate constant of the heptane-hexadecane mixtures appears to decrease with increasing droplet diameter; obscuration consistent with very heavy sooting, but without the formation of soot shells, is observed for the largest of these droplets. Forced convective flow around methanol droplets was found to increase the burning rate and to produce a

ratio of downstream-to-upstream flame radius that remained constant as the droplet size decreased, a trend in agreement with earlier results obtained at higher convective velocities for smaller droplets having larger flame standoff ratios. There are a number of implications of the experimental results regarding droplet-combustion theory.

1. INTRODUCTION

The classical theory of droplet combustion in quiescent atmospheres hypothesizes spherical symmetry,^{1,2} which is destroyed by buoyancy at normal gravity for sufficiently large droplets. A motivation for investigation of large droplets is the increase in the characteristic time scales with size, in proportion to the square of the droplet diameter, according to dimensional analysis; different elementary chemical and physical processes that occur on longer time scales may be observed by studying larger droplets. Kumagai³ pioneered spherical droplet-combustion experiments by employing a drop tower that provided approximately 1 sec of microgravity, sufficient time to capture the complete combustion histories of typical fuel droplets having initial diameters on the order of 1 mm. A great deal of research on the subject has been performed in the NASA Lewis 2-sec and 5-sec drop towers.⁴ The largest Earth-bound microgravity facility available today is the 10-sec drop shaft in Hokkaido, Japan, which allows complete combustion histories to be recorded for droplets up to about 3 mm in diameter. Although aircraft flying parabolic trajectories can provide longer test times, it is difficult to achieve gravity levels even approaching 10^{-3} g in aircraft tests, whereas levels in the range of 10^{-4} g to 10^{-6} g (the latter typical of drop-tower microgravity) are needed to remove noticeable gravity influences in droplet combustion. For this reason, an experiment was designed and flown in Spacelab on the Second United States Microgravity Laboratory (USML-2) mission of the Space Shuttle *Columbia* in October 1995 (STS-73). Droplets having initial diameters up to about 5 mm were investigated, and in some cases burning times in excess of 40 sec were observed. A preliminary analysis of the results is being published.⁵

2. EXPERIMENT DESIGN

Figure 1 shows the experimental apparatus. The experiment, labeled FSDC (fiber-supported droplet combustion) because the droplet is supported on a silicon-carbide fiber, was operated by the payload crew inside the Glovebox facility, which provided power and video capabilities for the experiment. Each fuel is contained in 1 of 11 modified, air-tight, commercial syringe cartridges. Because of fuel volatility, the loaded fuel cartridges were stowed in the Shuttle only 24 hours before launch. To operate the experiment, the fuel cartridge is screwed into the base of the experiment module. A crew member turns a plunger screw, forcing fuel through two opposed hypodermic needles to the deployment site on the fiber located between the needles and perpendicular to them. Numbered needle pairs, the fiber stretched between them and fuel cartridges in back may be seen in figure 1. After the fuel coalesces into a droplet of the desired size, the needles are slowly retracted to minimize contact of the liquid with the needle surfaces. The stretched droplet is then deployed by retracting the needles rapidly into the bottom of the chamber.

Motions of the deployed droplet are allowed to damp before the ignition button is depressed. This automatically raises a replaceable igniter into place on one side of the droplet (parallel to the fiber) approximately 3.5 mm from the fiber and simultaneously provides DC electric current to the igniter. The igniter, seen on the chamber floor in figure 1, is a coiled loop of an aluminum alloy wire (resistivity 0.04 ohm.cm) with a diameter of 0.25 mm, a total length of about 35 mm, and carrying a current of

approximately 3 amps. The igniter button is released after ignition is detected visually by the crew, automatically retracting the igniter to the bottom of the test chamber.

Data are provided by two video views, one a backlit view of the droplet and the other a perpendicular view of the flame. The backlight is five LEDs (620 to 670 nm) which reflect off a mirrored lens in the bottom of the experiment module. The video camera for the droplet view is attached to the Glovebox microscope. A filter on the microscope objective transmits only the LED wavelength range, blocking most of the flame radiation. The second video camera, with a view essentially orthogonal to the microscope (and equipped with a filter to block LED wavelengths), records the droplet, the fiber, and the flame. Some of these experiments were run while video downlink was unavailable, and the data were recorded on board. Such "LOS" (loss-of-signal) data were available later and are not analyzed here.

Forced flow is produced by a small DC fan, seen in the front of figure 1, that induces air flow through a honeycomb (10-to-1 cell aspect ratio) inlet section and the experiment module. Uniform forced air speeds from 30 mm/sec to 250 mm/sec can be produced. The combustion occurred at pressures (0.996 to 1.107 bar), oxygen mole fractions (0.204 to 0.222), and relative humidity (39 to 46 percent) of the Spacelab environment.

3. METHANOL

Previous computational and theoretical work^{6, 7, 8} has established that, consistent with earlier experimental observations,^{8, 9, 10} water absorption by the fuel is significant during the combustion of methanol droplets. If liquid fluid motion is excluded from the theories (no liquid flow), so that only molecular diffusion and heat conduction occur in the liquid phase, then a water-rich layer is predicted to build up rapidly at the liquid surface, quickly reducing the rate of water absorption so that the total amount of water that is calculated to accumulate within the droplet is much less than the amount measured experimentally.^{10, 11} This water deficiency also produces disagreement with experimentally observed burning-rate variations and extinction diameters, the theory predicting higher burning rates with less variation and much smaller extinction diameters. One must, therefore, conclude that mixing is occurring in the experiments, but its precise character, including how the motion develops, remains an outstanding research problem.^{6, 7} However, analyses of Marangoni instability indicate that gasifying methanol droplets can be expected to be unstable hydrodynamically if water is absorbed into the droplet from the gas phase or is initially present in the liquid phase.^{12, 13} Complete liquid phase mixing is a much better approximation for the experiments than no liquid phase motion. Comparisons are made here between the new experimental results from Spacelab and the predictions based on complete mixing for both full numerical integrations⁶ and an approximate analysis.⁷

The complete-mixing analysis predicts that extinction of the burning occurs at a droplet diameter that increases with the initial droplet diameter because the amount of water accumulated in the droplet at a given diameter increases with increasing initial diameter. Until now, data for three initial droplet sizes have been available to test this prediction. Figure 2 shows the predicted extinction diameter as a function of the initial diameter, the previous experimental results (for small diameters), and the new experimental results for the much larger droplets, obtained in the present experiments. While one of the drop tower results¹⁴ was in air, the other two ground-based results^{8, 10} were not and therefore are shown in parentheses in the figure. Their atmospheres produced somewhat higher burning rates, resulting in slightly smaller extinction diameters. In addition, none of the ground-based tests were fiber supported.

The droplets are larger in the longitudinal fiber direction than in the transverse direction normal to it, as the inset indicates. The data points in figure 2 were obtained from the area of the video image, the reported diameter being that of a circle having the same area. Data were also obtained as the cube root of the product of the longitudinal diameter with the square of the transverse diameter and as the diameter of a sphere having a volume inferred from the image by assuming symmetry about the fiber. These results all agreed within 3 percent. The error bars shown in figure 2 take the longitudinal diameter as the maximum and the transverse diameter as the minimum, augmented by the preceding 3 percent uncertainty where that is larger. The measurement uncertainty, one or two pixels with about 50 pixels/mm resolution, is about 2 percent less than the exhibited error bars.

The solid line in figure 2 is obtained from numerical integrations,⁶ while one of the dashed lines comes from the approximate analysis,⁷ which took Lewis numbers to be unity. The latter analysis is being modified^{15, 16} by introducing a Lewis number (*Le*) for water, the ratio of the thermal diffusivity to the diffusion coefficient for water, which is reported¹⁷ to be 0.83. Figure 2 shows a preliminary heuristic result, suggesting that extinction diameters increase with decreasing Lewis numbers. Although this heuristic analysis with the correct¹⁷ water Lewis number is seen to correlate the data, this is entirely fortuitous because numerical integrations indicate a much weaker sensitivity to Lewis numbers. The numerical computations take detailed thermochemistry, vapor-liquid equilibria, chemical kinetics, and transport coefficients from the literature in producing the solid line in figure 2 in the absence of radiation. Among the theoretical approximations that need further investigation for these experiments is the neglect of radiant energy loss from the flame in both the analytical and numerical computations. The importance of this effect increases with increasing droplet diameter and is quite likely to produce the rise of the three highest data points seen in figure 2. In general, the main conclusion to be drawn is that, while further theoretical work now is clearly needed, experiments and theories agree in that they show an approximate linearity between extinction and initial diameters, possibly unique for methanol, since predicted extinction diameters for other fuels, such as alkanes, are nearly independent of the initial diameter for droplets small enough for radiation to be neglected. The needed new theoretical studies are in progress.^{16, 18, 19}

4. METHANOL-WATER MIXTURES

Experiments were performed for methanol-water mixtures having methanol mass fractions of $Y = 0.8$ and $Y = 0.9$. Since the best data for $Y = 0.8$ were obtained during LOS, results are discussed here only for $Y = 0.9$. Figure 3 shows experimental and computational^{6, 20} results for the square of the droplet diameter as a function of time for both pure methanol and methanol-10 percent water mixtures. The addition of water to methanol is observed to reduce the burning rate, increase the nonlinearity of the variation of the square of the droplet diameter with time and increase the extinction diameter. The numerical model qualitatively reproduces each of these phenomena, although the predicted burning rates are somewhat larger and the extinction diameters less than observed. Reasons for differences between modeling and experiment include influences of radiant energy transfer which are neglected in the comparisons presented here. Radiant energy loss is known theoretically²¹ to produce extinction for sufficiently large droplets. Continuing numerical modeling, including spectral radiation effects, reproduces this result.^{18, 19, 22} It also decreases the slopes of the theoretical curves in figure 3, improving the agreement between numerical modeling and experiment, and it more closely predicts the experimental data in figure 2, including the apparent rise of the three data points at the largest initial diameter.

5. METHANOL-DODECANOL MIXTURES

Methanol-dodecanol mixtures are known to experience staged combustion in which methanol predominantly burns first, then becomes largely depleted in a surface layer of the liquid. After this, the flame contracts and the surface temperature increases towards the boiling point of dodecanol, resulting finally in the combustion of a fuel vapor mixture having approximately the original droplet composition. It becomes more enriched in decanol towards the end of the burning.^{14, 23} It has also been found that, for many such mixtures, the extent of surface-temperature increase following flame contraction is sufficient to cause internal nucleation leading to disruption.^{14, 23, 24, 25} Disruption has been observed for initial mass fractions Y of methanol between about 0.7 and 0.9. In the present experiments, mixtures with $Y = 0.6$ and $Y = 0.8$ were tested, but present comments are restricted to $Y = 0.6$ because the good data for $Y = 0.8$ were obtained during LOS.

Initial droplet sizes in the test results currently available for methanol-dodecanol mixtures were about 5 mm. A number of the droplets initially had bubbles inside them, and disruption was observed for all such droplets, as might be expected. One droplet at $Y = 0.6$, initially 5.5 mm in diameter, did not initially have bubbles; it experienced flame contraction after burning for about 15 sec, with a decrease in diameter by about 10 percent, followed a few seconds later by internal nucleation that propelled the droplet off the fiber. This type of disruption is consistent with earlier data if the presence of the fiber enhanced the nucleation.

6. HEPTANE-HEXADECANE MIXTURES

Like methanol-dodecanol mixtures, heptane-hexadecane mixtures are known to exhibit staged combustion and disruption.^{26, 27} In the present experiments, the initial mass fraction Y of heptane in the mixtures was 0.6 and 0.9. Because the data for $Y = 0.9$ were obtained during LOS, only data for $Y = 0.6$ are discussed here.

Figure 4 shows the time dependence of the square of the droplet diameter for two different droplet experiments (3.5 mm and 5.2 mm initial diameter). The data for the smaller droplet clearly display staged combustion, with burning-rate constants K_1 and K_3 of the first and third stages, separated by the plateau region, having values of about $0.43 \text{ mm}^2/\text{sec}$ and $0.45 \text{ mm}^2/\text{sec}$, respectively. The onset of the plateau has been observed in ground-based experiments to coincide with flame contractions associated with rapid droplet heating when the liquid surface mass fraction of hexadecane closely approaches unity. Although this is expected in the present experiment as well, it could not be verified from the downlink video because, unlike the alcohol droplet discussed in the preceding section—for which flame locations could be inferred from the location of maximum brightness of the glowing of the support fiber—no fiber glow was detectable for burning alkane droplets. This suggests that flame temperatures were very low for these mixtures.

The larger droplet in figure 4 does not display staged combustion. Instead, the burning rate of this droplet gradually decreases from the maximum value, $K = 0.38 \text{ mm}^2/\text{sec}$, becoming very small at about 25 sec into its burn. Initially it was thought that the flame had extinguished, and reignition was attempted

at 52 sec into the burn, but the burning-rate constant remained at the very small value of about $0.05 \text{ mm}^2/\text{sec}$. Combustion was accompanied by what appeared to be very heavy sooting, gradually obscuring the backlit view. The reignition attempt temporarily reduced the obscuration, enabling further data to be obtained. It seems possible that chemistry continued to occur in this experiment, but currently there is uncertainty concerning its character and whether a flame persisted.

The larger droplet in figure 4 was observed to soot much more heavily than the smaller droplet, which, in turn, sooted more heavily than even smaller droplets burnt in ground-based experiments. Yet, unlike these drop tower results,^{13, 28} no soot shells were observed in the present experiments. Another difference from ground-based observations is that blue flames were detectable visually in these initially sooty flames; for smaller droplets, any blue had been totally obscured by brighter yellow soot radiation. Further study of all of these observations is needed.

7. CONVECTION EFFECTS

To study the effects of forced convection on droplet burning characteristics, several experimental runs were made varying the initial droplet diameter and the free-stream velocity using methanol as the test fuel. Figure 5 shows the results for one of these tests, for which data (droplet view and flame view) were downlinked during the mission and recorded on the ground. During this test, the droplet was first deployed on a $150 \mu\text{m}$ fiber, ignited, and then the fan was turned on to generate the imposed air flow of 50 mm/sec parallel to the fiber. From the data for the square of the droplet diameter and the flame positions H_1 and H_3 as functions of time, it is clear that the combustion initially takes place in a quiescent environment and then undergoes a transition to a forced-flow burning configuration. The upstream flame position retreats closer to the droplet surface, while the downstream position recedes farther from the droplet. The burning rate increases as a consequence of the increased supply of oxygen to the flame through convection. As the droplet continues to burn, both the upstream and downstream flame positions shrink toward the droplet surface.

Since combustion occurs over several seconds in both quiescent and forced-flow environments, it can be assumed that quasi-steady conditions prevail during each stage. From figure 5, the burning rate constant for the quiescent period is calculated to be $0.54 \text{ mm}^2/\text{sec}$ and for the forced-convective period $0.74 \text{ mm}^2/\text{sec}$. Traditionally, the effect of forced convection on burning rates is correlated using a Frossling-type of formula.^{29, 30, 31} That is,

$$K/K_0 = 1 + C Re^{1/2}, \quad (1)$$

where K_0 is the burning-rate constant without convection, and C is a constant. For the present case, with a Reynolds number of 0.7 calculated on the basis of a diameter of 2.3 mm at the beginning of convection and a kinematic viscosity of about $180 \text{ mm}^2/\text{sec}$ for air at the arithmetic mean (1280 K) of the vaporization and flame temperatures, the value of C is 0.4. This value is higher than the previous results obtained for n-heptane droplets with smaller initial diameters ($< 1.5 \text{ mm}$),³¹ but similar to the observations of Gokalp et al.³⁰ for pure vaporization.

Earlier approximate theories³² describing the flame shapes during droplet burning in a natural-convective environment predict that the ratio H_1/H_2 is a constant, and the ratio H_3/H_1 is proportional to

$D^{1/2}$, where D is the instantaneous droplet diameter. These predictions have been verified by experiments conducted under normal gravity conditions. Unlike natural convection, for the present forced-convective burning ratio H_3/H_1 , measured here by locating the maximum radiant intensity from the droplet-support fiber, is a constant (≈ 1.6). Corresponding data of Okajima and Kumagai³¹ for n-heptane droplets with diameters around 1 mm exhibit a larger constant ratio at a higher convective velocity (~ 300 mm/sec), consistent with estimated increases in H_3/H_1 with increasing air velocity.

8. DISCUSSION AND CONCLUSIONS

The results reported here demonstrate that data on the combustion of fuel droplets as large as 5 mm in diameter are helpful for testing droplet burning theory. These large droplets burn in ways that, in many respects, are to be expected from theory and from extrapolations of observations made for smaller droplets, but that differ in other respects. There is qualitative agreement concerning extinction diameters and their dependences on droplet size for methanol and methanol-water mixtures, for example. There is also qualitative agreement with theory concerning staged burning and disruption of fuel mixtures and concerning convective effects. The observations on the largest alkane-mixture droplet, however, suggest a possible significant lack of knowledge, and radiation effects appear to become important for larger droplets. Thus, there is much more to be done in the theory of droplet combustion. Work is continuing to improve the interpretations of the data that have been obtained.

REFERENCES

1. Godsave, G.A.E.: *Fourth Symposium (International) on Combustion*, Williams and Wilkins Co., Baltimore, Maryland, 818–830, 1953.
2. Spalding, D.B.: *Fourth Symposium (International) on Combustion*, Williams and Wilkins Co., Baltimore, Maryland, 847–864, 1953.
3. Kumagai, S.: *Jet Propulsion*, 26, 786, 1956.
4. Choi, M.Y.; Cho, S.Y.; Dryer, F.L.; and Haggard, J.B.: *Microgravity Fluid Mechanics*, H.J. Rath, ed., Springer-Verlag, Berlin, 337–353, 1992.
5. Dietrich, D.L.; Haggard, J.B., Jr.; Dryer, F.L.; Nayagam, V.; Shaw, B.D.; and Williams, F.A.: *Twenty-Sixth (International) Symposium on Combustion*, The Combustion Institute, Pittsburgh, Pennsylvania, 1201–1208, 1997.
6. Marchese, A.J.; and Dryer, F.L.: *Combust. Flame*, 105, 104–122, 1996.
7. Zhang, B.L.; Card, J.M.; and Williams, F.A.: *Combust. Flame*, 105, 267–290, 1996.
8. Cho, S.Y.; Choi, M.Y.; and Dryer, F.L.: *Twenty-Third Symposium (International) on Combustion*, The Combustion Institute, Pittsburgh, Pennsylvania, 1611–1617, 1991.
9. Choi, M.Y.; Dryer, F.L.; Haggard, J.B.; and Brace, M.H.: *Third International Colloquium on Drops and Bubbles*, AIP Conf. Proc. 197 (T.G. Wang, ed.), American Institute of Physics, New York, 338–361, 1989.
10. Lee, A.; and Law, C.K.: *Combust. Sci. Tech.*, 86, 253–265, 1992.
11. Choi, M.Y.: “Droplet Combustion Characteristics Under Microgravity and Normal-Gravity Conditions,” Ph.D. Thesis, Department of Mechanical and Aerospace Engineering, Princeton University, Princeton, New Jersey, 1993.
12. Aharon, I.; and Shaw, B.D.: *Phys. Fluids*, 8, 1820–1827, 1996.
13. Aharon, I.: “Theoretical and Experimental Studies on Evaporation and Combustion of Multicomponent Droplets in Reduced Gravity,” Ph.D. Thesis, Department of Mechanical and Aeronautical Engineering, University of California-Davis, Davis, California, 1996.
14. Yang, J.C.; Jackson, G.S.; and Avedisian, C.T.: *Twenty-Third Symposium (International) on Combustion*, The Combustion Institute, Pittsburgh, Pennsylvania, 1619–1625, 1991.
15. Zhang, B.L.; and Williams, F.A.: “The Effects of the Lewis Number of Water Vapor on the Combustion and Extinction of Methanol Drops,” *Combust. Flame*, submitted, 1996.
16. Zhang, B.L.; and Williams, F.A.: “Theoretical Studies of Methanol Droplet Combustion Based on Results from the Shuttle Spacelab During the USML-2 Mission,” *Acta Astronautica*, submitted, 1996.

17. Smooke, M.D., ed.: *Reduced Kinetic Mechanisms and Asymptotic Approximations for Methane-Air Flames*, Springer-Verlag, Berlin, 21, 1991.
18. Marchese, A.J.; and Dryer, F.L.: "The Effect of Nonluminous Thermal Radiation in Microgravity Droplet Combustion," *Combust. Sci. Tech.*, accepted, 1996.
19. Marchese, A.J.; and Dryer, F.L.: "Radiation Effects in Space-Based Methanol/Water Droplet Combustion Experiments," Eastern States Section Meeting of the Combustion Institute, Hilton Head, South Carolina, Dec. 9-11, 1996.
20. Marchese, A.J.; Dryer, F.L.; Colantonio, R.C.; and Nayagam, V.: *Twenty-Sixth Symposium (International) on Combustion*, The Combustion Institute, Pittsburgh, Pennsylvania, 1209-1219, 1997.
21. Chao, B.H.; Law, C.K.; and T'ien, J.S.: *Twenty-Third Symposium (International) on Combustion*, The Combustion Institute, Pittsburgh, Pennsylvania, 523-531, 1991.
22. Marchese, A.J.: "Single- and Multi-Component Liquid Droplet Combustion: Detailed Kinetic Modeling and Microgravity Experiments," Ph.D. Thesis, Department of Mechanical and Aerospace Engineering, Princeton University, Princeton, New Jersey, 1996; also MAE Report No. 2081-T.
23. Wang, C.H.; and Law, C.K.: *Combust. Flame*, 59, 53-62, 1985.
24. Lasheras, J.C.; Yap, L.T.; and Dryer, F.L.: *Twentieth Symposium (International) on Combustion*, The Combustion Institute, Pittsburgh, Pennsylvania, 1761-1772, 1984.
25. Yap, L.T.; Kennedy, I.M.; and Dryer, F.L.: *Combust. Sci. Tech.*, 41, 291-313, 1984.
26. Lasheras, J.C.; Kennedy, I.M.; and Dryer, F.L.: *Combust. Sci. Tech.*, 26, 161-169, 1981.
27. Niioka, T.; and Sato, J.: *Twenty-First Symposium (International) on Combustion*, The Combustion Institute, Pittsburgh, Pennsylvania, 625-631, 1986.
28. Aharon, I.; and Shaw, B.D.: "Marangoni Instability in Bi-Component Droplet Gasification in Reduced Gravity," paper WSS 95F-226, Western States Section Meeting of the Combustion Institute, Stanford, California, Oct. 30-31, 1995.
29. Law, C.K.; and Williams, F.A.: *Combust. Flame*, 19, 393-405, 1972.
30. Gokalp, I.; Chauveau, C.; Richard, J.R.; Kramer, M.; and Leuckel, W.: *Twenty-Second Symposium (International) on Combustion*, The Combustion Institute, Pittsburgh, Pennsylvania, 2027-2035, 1988.
31. Okajima, S.; and Kumagai, S.: *Nineteenth Symposium (International) on Combustion*, The Combustion Institute, Pittsburgh, Pennsylvania, 1021-1027, 1982.
32. Isoda, H.; and Kumagai, S.: *Seventh Symposium (International) on Combustion*, The Combustion Institute, Pittsburgh, Pennsylvania, 523-531, 1959.

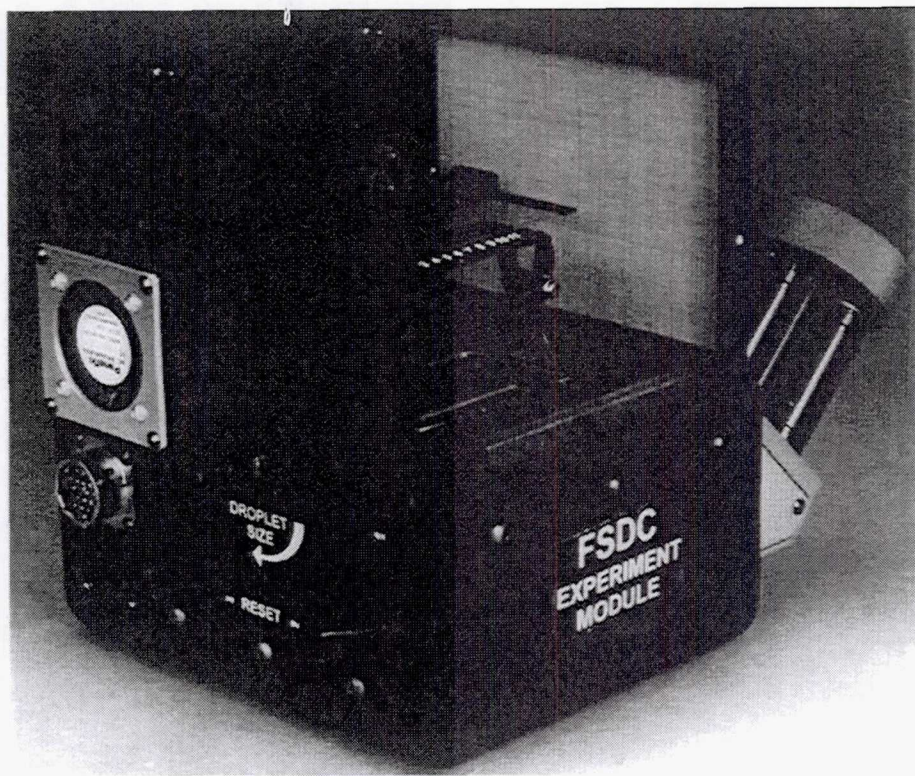


Figure 1. Photograph of the experimental apparatus.

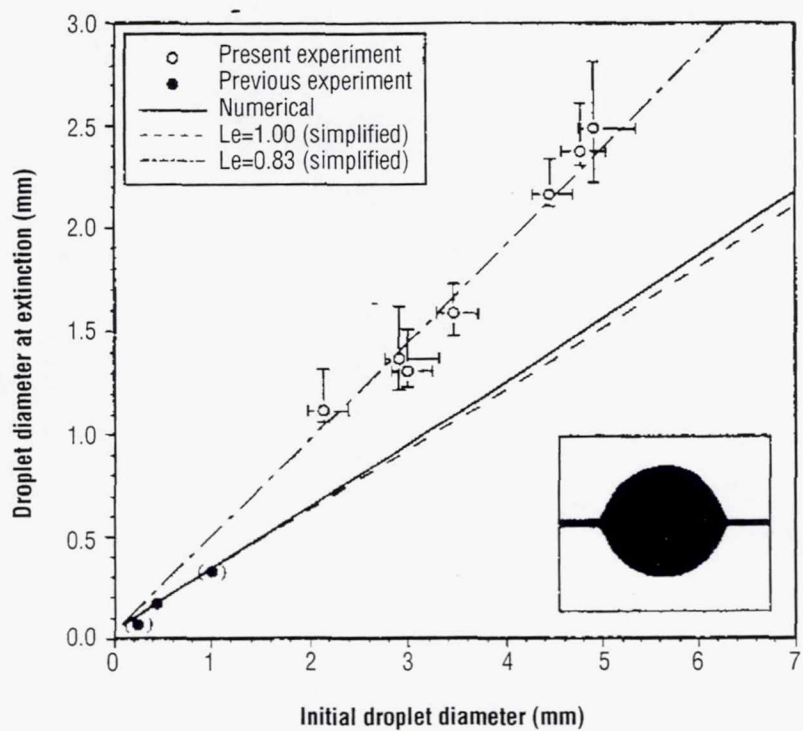


Figure 2. Dependence of the droplet diameter at extinction on the initial droplet diameter for initially pure methanol droplets; the inset is an illustration of the shape of the droplet on the fiber.

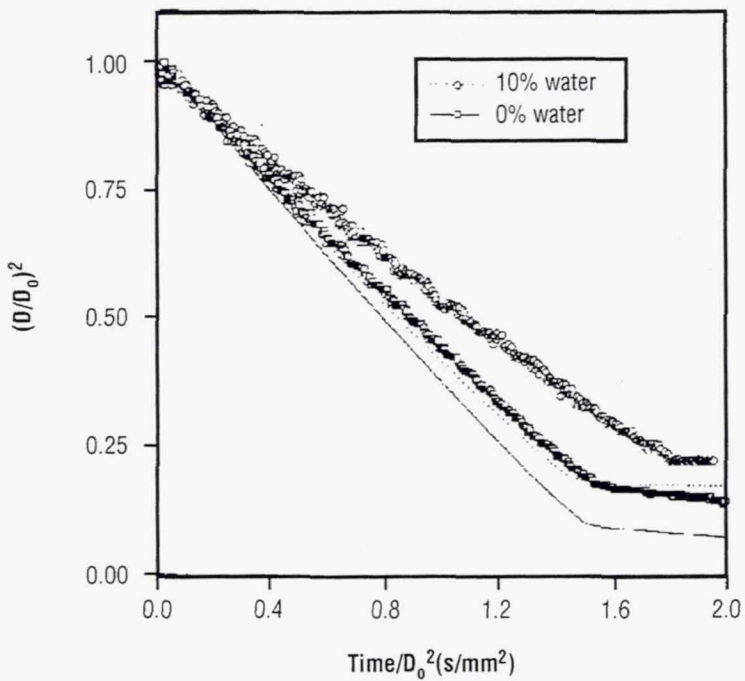


Figure 3. The square of the droplet diameter D as a function of time, for an initial droplet diameter $D_0 = 3$ mm, for initially pure methanol and methanol-water mixtures having an initial water mass fraction of 10 percent.

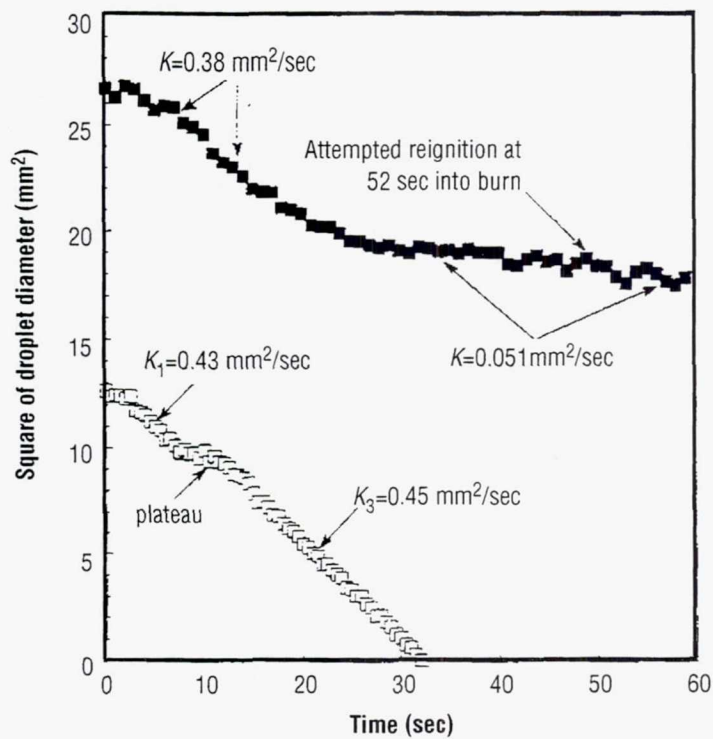


Figure 4. The square of the droplet diameter as a function of time for two heptane-hexadecane droplets with initial heptane mass fraction $Y = 0.6$.

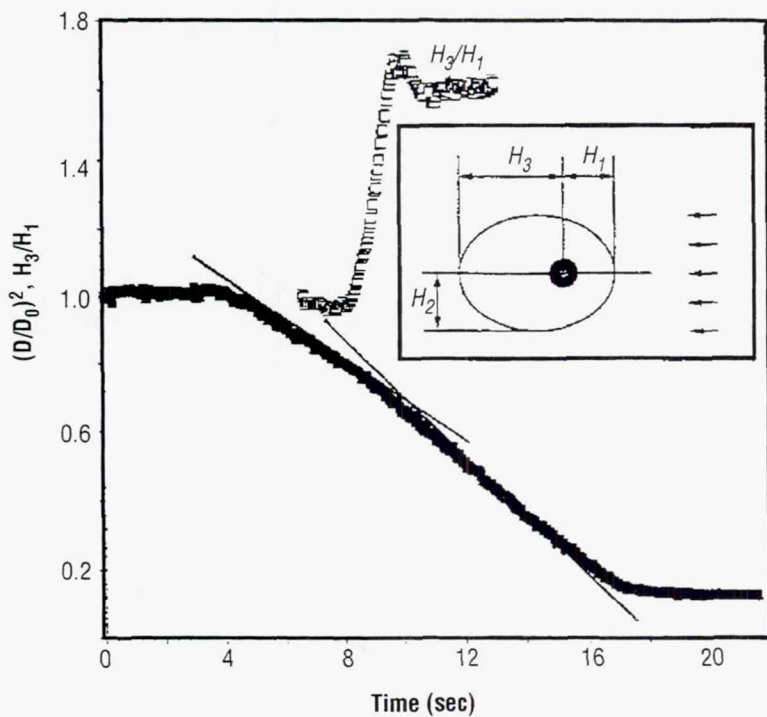


Figure 5. The square of the droplet diameter D as a function of time and the ratio of the upstream H_1 to downstream H_3 flame radius as a function of time, for a methanol droplet of initial diameter $D_0 = 3.1$ mm, in an experiment in which the forced-flow velocity is increased slowly from zero to 50 mm/sec.

EXPERIMENT XXXIII.

**CRYSTALLIZATION OF HARD SPHERE COLLOIDS IN MICROGRAVITY: RESULTS OF
THE COLLOIDAL DISORDER-ORDER TRANSITION, CDOT ON USML-2**

ACKNOWLEDGMENTS

We would like to acknowledge useful discussions with B.J. Ackerson and support from the NASA microgravity program.

c

CRYSTALLIZATION OF HARD SPHERE COLLOIDS IN MICROGRAVITY: RESULTS OF THE COLLOIDAL DISORDER-ORDER TRANSITION, CDOT ON USML-2

Jixiang Zhu

P.M. Chaikin

Department of Physics

Princeton University

Princeton, NJ 08544

Phone: 609-258-4338

Fax: 609-258-6360

E-mail: chaikin@pupgg.princeton.edu

Min Li

W.B. Russel

Dept. of Chemical Engineering

Princeton University

Princeton, NJ 08544

R.H. Ottewill

School of Chemistry

University of Bristol

Bristol, United Kingdom

R. Rogers

W.V. Meyer

NASA Lewis Research Center

Cleveland, OH

STS-73 Space Shuttle Crew

NASA Johnson Space Center

Houston, TX

ABSTRACT

Classical hard spheres have long served as a paradigm for our understanding of the structure of liquids, crystals, and glasses and the transitions between these phases.¹ Ground-based experiments have demonstrated that suspensions of uniform polymer colloids are near-ideal physical realizations of hard spheres.² However, gravity appears to play a significant and unexpected role in the formation and structure of these colloidal crystals. In the microgravity environment of the Space Shuttle, crystals grow purely via random stacking of hexagonal close-packed planes, lacking any of the face-centered cubic (FCC) component evident in crystals grown in 1 g beyond melting and allowed some time to settle.³ Gravity also masks

the natural growth instabilities of the hard sphere crystals which exhibit striking dendritic arms when grown in microgravity. Finally, high volume fraction "glass" samples which fail to crystallize after more than a year in 1 g begin nucleation after several days and fully crystallize in less than 2 weeks on the Space Shuttle.

1. CRYSTAL STRUCTURE, OBSERVATION OF DENDRITES, AND THE ABSENCE OF THE GLASS PHASE IN MICROGRAVITY

The thermodynamic phase diagram for hard spheres as obtained by computer simulations is: $\phi_{\text{liquid}} < \phi_{\text{freeze}} = 0.494 < \phi_{\text{coexist}} < \phi_{\text{melt}} = 0.545 < \phi_{\text{crystal}} < 0.74$,¹ where ϕ is the volume fraction. The simulations also find reduced diffusion and a metastable glass phase for $\phi > 0.58$. Ground-based experiments on both polymer and silica particles in colloidal suspension have substantially confirmed this phase diagram including liquid, crystal, and glass phases,²⁻⁵ but experiments in gravity are intrinsically not in equilibrium. The competition between thermal motion and gravity is best expressed in terms of the gravitation length h , $mgh = kT$, with m the buoyant mass of a particle. Thus, the height h to which kT of thermal energy can raise a particle must be much greater than the scale of the experiment for gravity to be neglected. For typical hard-sphere colloidal systems studied, $h = 1-30$ microns, is below crystallite sizes, and is much less than the sample sizes (\sim cm). Then it is not clear what effects sedimentation and gravitational stresses have on the kinetics and thermodynamics of the crystals.

These experiments were performed on the Space Shuttle *Columbia* on mission STS-73. The particles consist of uniform PMMA spheres 508 or 518 nm in diameter, polydispersity \sim 5 percent, with a thin (10 nm) grafted layer of poly (hydroxystearic acid) to prevent aggregation.⁶ The particles are suspended in an index of refraction (1.51) matching mixture of decalin and tetralin. Using a stir bar in the sample cell, the samples are mixed (shear melted) by the astronauts on Day 2 of the flight. The static light scattering results reported here were obtained by sending a 10-mW, 50- μ beam from a 791 nm laser diode through the cylindrical sample. The scattered light is focused through a thick cylinder so that parallel beams from throughout the sample align to a point on a translucent cylindrical screen. The image is then recorded with a video camera. The sample is translated to obtain data from many independent crystallites.

In figure 1, we show photographs of a sample from the coexistence region of the phase diagram. On the left is the preflight photo in 1 g. After several months of settling, the denser crystal phase lies below the liquid phase. On the right, the same sample is shown after mix-melting and 3.6 days of crystallization in microgravity. Aside from the larger size of the microgravity crystals, one surprise was the dendritic arms clearly seen in the enlarged insert, and previously undetected and unpreserved from ground-based studies. (Dendrites have been reported for charged colloids near a surface.⁷) With an interparticle spacing of 0.6 μ m, single crystals with different Bragg peaks will scatter visible white light with different colors diffracted in the same direction. This produces the red and green aspects of the crystals in figure 1.

Should we expect dendrites? Ackerson and Schatzel⁸ explored the nucleation and growth of hard sphere crystals experimentally and theoretically. Their model includes dynamics and kinetics particular to colloidal crystals. However, our linear stability analysis of their equations indicates the same instabilities toward dendritic growth as found in molecular systems.⁹

The effects of gravity on limiting the size of crystals and preventing dendritic growth are easily understood. As a crystallite grows, its mass increases and it sediments faster. The viscous stresses applied

to the crystallite surfaces support its buoyant mass and induce internal stresses on the crystallite of order $Mg/4\pi R^2$. When these stresses exceed the yield stress of the crystal, the crystal breaks. Dendritic arms are sheared off even more readily. For a crystalline solid the yield stress, $\sigma_{crit} \sim \beta G$, where G is the shear modulus and typically $\beta=10^{-1}$ to 10^{-4} . Taking $M=(4\pi/3) R^3 \Delta\phi \rho$, $G \sim \chi kT/a_0^3$, $\Delta\phi=0.05$ and $a_0=0.25\mu$ we have $R_{crit} \sim \alpha \beta kT / ((4\pi/3)a_0^3 g \Delta\phi \Delta r) \sim 80\pi \chi \beta h$, $\leq 3h$ where h is the gravitational length $\sim 30\mu$ for our samples, $\chi \sim 1$, ρ is the buoyant density of the particles and $\Delta\phi$ is the difference in volume fractions between the two phases. Thus, whatever natural growth occurs is cut short at a length scale $\sim 100\mu$ by sedimentation in 1 g. There is also a more subtle effect of sedimentation. In most growth models, particles in the liquid diffuse to the growing surface. Sedimentation sets up a flow which can alter the diffusion field. The relative importance of flow to diffusion can be characterized by the Peclet number, $Pe_0 = U_0 D$, the time to diffuse a distance compared to the time to convect the same distance. For a single particle $L=a_0$, U is the Stokes settling velocity, D is the Stokes-Einstein diffusion coefficient, and $Pe_0 = a_0/h$. For a crystallite of size R , there are many different length scales. Comparing convection to diffusion for $L=a_0$ gives $Pe_{cryst} = Pe_0 R^3/a_0^3$, for $L=R$, $Pe_{cryst} = Pe_0 R^4/a_0^4$. In either case, convection dominates diffusion once R is several a_0 , and this may alter the growth mechanism.

Crystal close packing can be obtained by stacking hexagonal planes of spheres. With a first layer as A , there are two equivalent placements B and C of the second layer above the interstitial sites of the first. If the stacking continues, the FCC lattice is the arrangement $ABCABC\dots$, Hexagonal Close Packed (HCP) is $ABABAB\dots$, but any arrangement has the same volume fraction, $\phi=0.74$. The random arrangement $ABACBACBCA\dots$ with no repeating layers is known as Random Hexagonal Close Packed (RHCP). Simulations indicate that the FCC structure is most stable for ϕ near 0.7404. But just above melting $\phi \sim 0.545$, the energy difference between FCC and HCP is less than 0.002 kT, and the suggested structure is RHCP.¹⁰ Experiments on hard sphere colloidal crystals at 1 g find a mixture of RHCP/FCC with more RHCP.³

In figure 2b, we show a CCD image recorded from the laser-Bragg screen. Very similar Bragg scattering patterns are seen for all of the crystalline samples. The unusual and characteristic feature of all of these diffraction patterns is the dominance of Bragg streaks rather than Bragg spots. Bragg scattering from three-dimensional crystals produces spots, while a two-dimensional crystal generates rods. Projected on a screen in real space (or an Ewald sphere in k space), the rods become streaks. The streaks therefore indicate immediately a large component of scattering from two-dimensional ordered sheets which are incoherently stacked, as one might expect for the RHCP structure. In order to describe the scattering from close packed hexagonal planes, Wilson¹¹ introduced a parameter, α , as the probability of every third layer being different. Then $\alpha=1$ corresponds to $ABCABC\dots \Rightarrow$ FCC, $\alpha=0$ is $ABABAB\dots \Rightarrow$ HCP and $\alpha=0.5$ is RHCP. In figures 2c and 2d, we show the images calculated for our Bragg screen for $\alpha=1$ and $\alpha=0.5$. The match with our data is clearly consistent with RHCP. To test for the presence of FCC, we digitized the CCD images from many translations of the sample cell and computed the intensity as a function of scattering wavenumber. In figure 3, we show $I(q)$ (unnormalized by the particle form factor) for the identical sample in the identical apparatus taken the same time after mix-melt in microgravity and 1 g. The bump at 80° in the 1 g data is the (200) FCC Bragg peak completely absent in the microgravity data. Growth in microgravity yields almost pure RHCP crystals.

The “glass” sample that we studied was $2a_0=508\text{ nm}$, $\phi=0.619$, well into the glassy region observed in other ground-based systems.¹² After mix-melt in 1 g, the sample was allowed to sit undisturbed for a period of more than 1 year and never crystallized. The sample was mix-melted in microgravity and to our

surprise began nucleation within 3.6 days. By the last experimental day of the Shuttle flight, the astronauts remarked on the centimeter-sized crystals that had formed and filled the cell. This sample survived reentry and sat in its fully crystalline state in our lab for 6 months. We then used the stir bar in the sample cell to mix-melt the bottom half of the sample. For 1 month the crystalline region slowly grew into the disordered region and then essentially stopped. Figure 4 shows this sample 2 months after the bottom half was mix-melted. The glass region not in contact with the crystal has shown no evidence of nucleation. We therefore conclude that, at $\phi > 0.58$, the nucleation and growth of the crystals are greatly hindered in a gravitational field. This may result from the geometry of random packings realized with and without applied stresses (e.g., random close packing is $\phi = 0.64$, random loose packing, for systems under shear or gravity, is less well defined but is found as $\phi \sim 0.58^{13}$).

Our observations of the crystallization of 0.5μ PMMA spheres lead to the following scenarios: In microgravity, crystals nucleate at a radius of $\sim 2 \mu$. They grow spherically and diffusion-controlled to $\sim 14 \mu$ at which scale dendrites start to form. Dendritic growth proceeds and yields crystallites of 1 mm or larger. In 1 g, nucleation again occurs at $\sim 2 \mu$, spherical, diffusion-controlled growth proceeds to $\sim 14 \mu$, dendritic growth follows and crystallites grow to $\sim 100 \mu$ where sedimentation shears off the dendritic arms. Alternatively, in 1 g following nucleation the sedimentation may lead to convection-controlled growth above $\sim 10 \mu$, the absence of dendritic instabilities and a size of $\sim 100 \mu$ still limited by sedimentation. In all cases, the growth is not the slow, quasi-equilibrium process that we would want to assure an equilibrium crystal structure. The RHCP structure may be the equilibrium structure, but it may also result from the kinetics and dynamics of nonequilibrium crystal growth. The fact that FCC was not found in microgravity but on crystalline samples brought back to 1 g or grown in 1 g suggests that stress may convert RHCP to FCC. One way to avoid these problems is to use a temperature gradient to control the liquid-crystal interface (by controlling osmotic pressure) and to "zone refine" the samples in a microgravity environment.

REFERENCES

1. Adler, B.J.; and Wainwright, T.E.: *J. Chem. Phys.*, 27, 1207, 1957; Hoover, W.G.; and Ree, F.H.: *J. Chem. Phys.*, 49, 3609, 1968; Adler, B.J.; Hoover, W.B.; and Young, D.A.: *J. Chem. Phys.*, 49, 3688, 1968.
2. Pusey, P.N.; and van Megen, W.: *Nature*, 320, 340, 1986.
3. Pusey, P.N.; van Megen, W.; Bartlett, P.; and Ackerson, B.J.: *Phys. Rev. Lett.*, 63, 2753, 1989.
4. Pusey, P.N.: Chapter 10 in "Liquids, Freezing and the Glass Transition," J.P. Hansen, D. Levesque and J. Zinn-Justin, eds., Elsevier, Amsterdam, 1991.
5. de Kruif, C.G.; Jansen, J.W.; and Vrij, A.: "Physics of Complex and Supramolecular Fluids," S.A. Safran and N.A. Clark, eds., Wiley-Interscience, 315-343, 1987; Smits, C.; Briels, W.J.; Dhont, J.K.G.; and Lekkerkerker, H.N.W.: *Prog. Colloid Polym. Sci.*, 78, 287, 1989.
6. Phan, S.E.; Russel, W.B.; Cheng, Z.; Chaikin, P.M.; Dunsmuir, J.H.; and Ottewill, R.H.: *Phys. Rev.*, E54, 6633, 1996.
7. Gast, A.P.; and Monovoukas, Y.: *Nature*, 351, 553, 1991.
8. Schatzel, K.; and Ackerson, B.J.: *Phys. Rev. Lett.*, 68, 337, 1992; Ackerson, B.J.; and Schatzel, K.: *Phys. Rev.*, B52, 1995.
9. Langer, J.S.: *Rev. Mod. Phys.*, 52, 1, 1980.
10. Frenkel, D.; and Ladd, A.J.C.: *J. Chem. Phys.*, 81, 3188, 1984.
11. Wilson, A.J.C.: *Proc. R. Soc. Lond.*, A180, 277, 1942.
12. van Megen, W.; and Underwood, S.M.: *Phys. Rev. Lett.*, 70, 2766, 1993; *Phys. Rev.*, E49, 4206, 1994.
13. Ononda, G.Y.; and Liniger, E.G.: *Phys. Rev. Lett.*, 64, 2727, 1990.

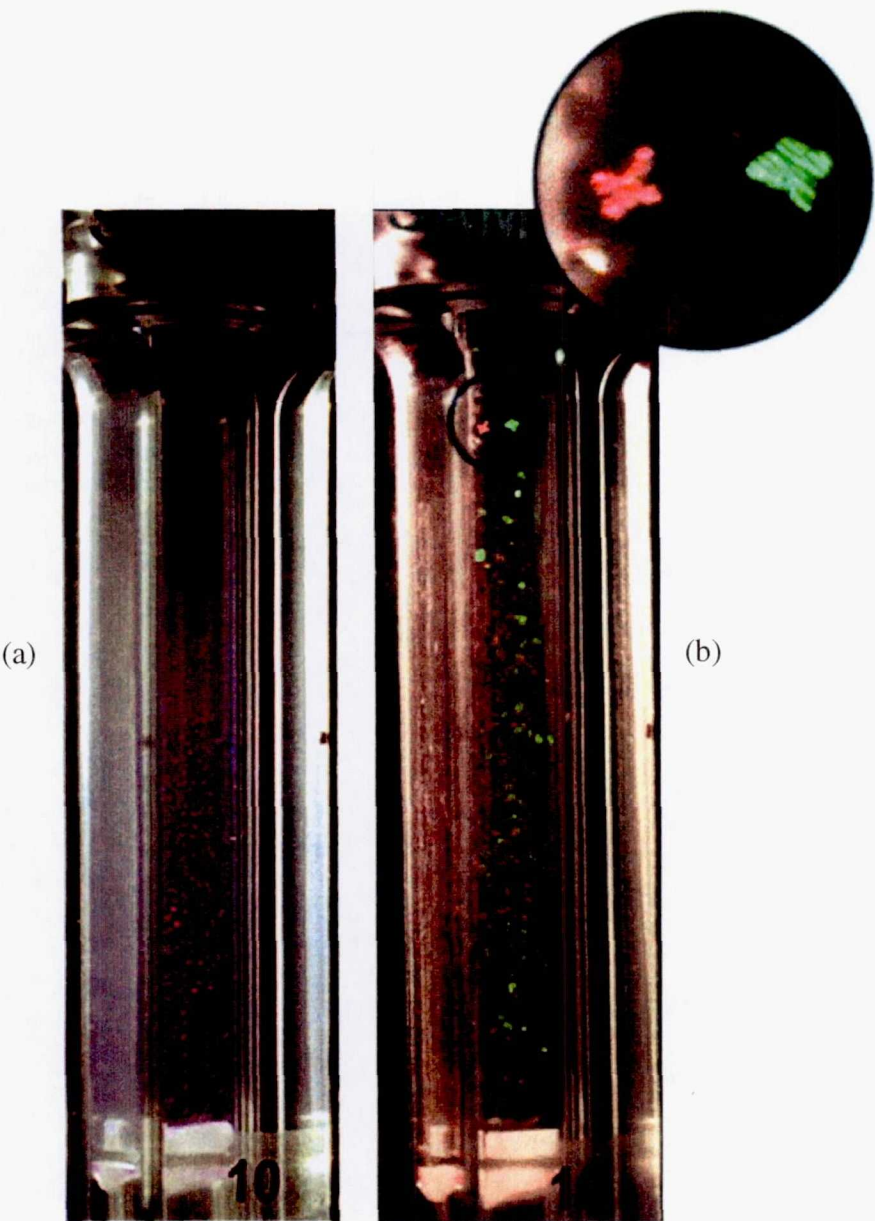


Figure 1. (a). Photo of a sample of 508 nm PMMA spheres in index matching suspension at volume fraction $\phi=0.504$, in the coexistence region of the phase diagram. In this preflight ground-based photo, the sample is phase separated with 0.1 mm crystallites in the bottom half of the tube. (b). The same sample after recrystallization on the Shuttle in microgravity. Millimeter-size crystals are dispersed in the liquid phase. The insert shows the dendritic arms on several of the crystallites grown in microgravity.

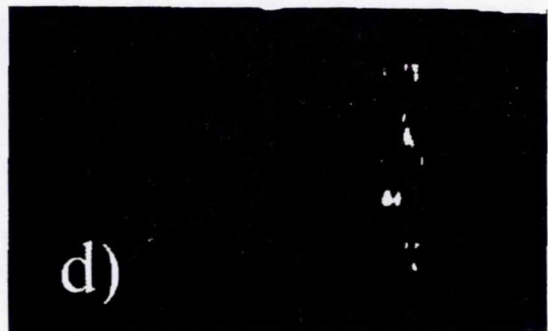
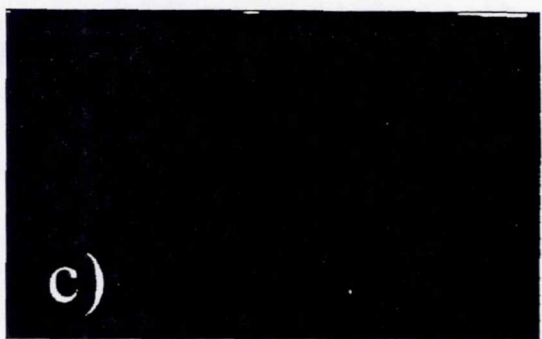
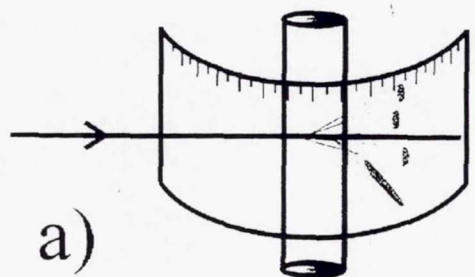


Figure 2. (a). Bragg scattering geometry. Laser beam incident on a cylindrical sample scatters onto a cylindrical screen. (b). Bragg scattering from a $d=518$ nm sample with $\phi=0.537$. Note the dominance of streaks rather than spots, indicating Bragg rods and a 2-dimensional structure as might be expected for a random hexagonal close-packed structure. (c). Computer-generated scattering pattern for FCC. (d). RHCP structures.

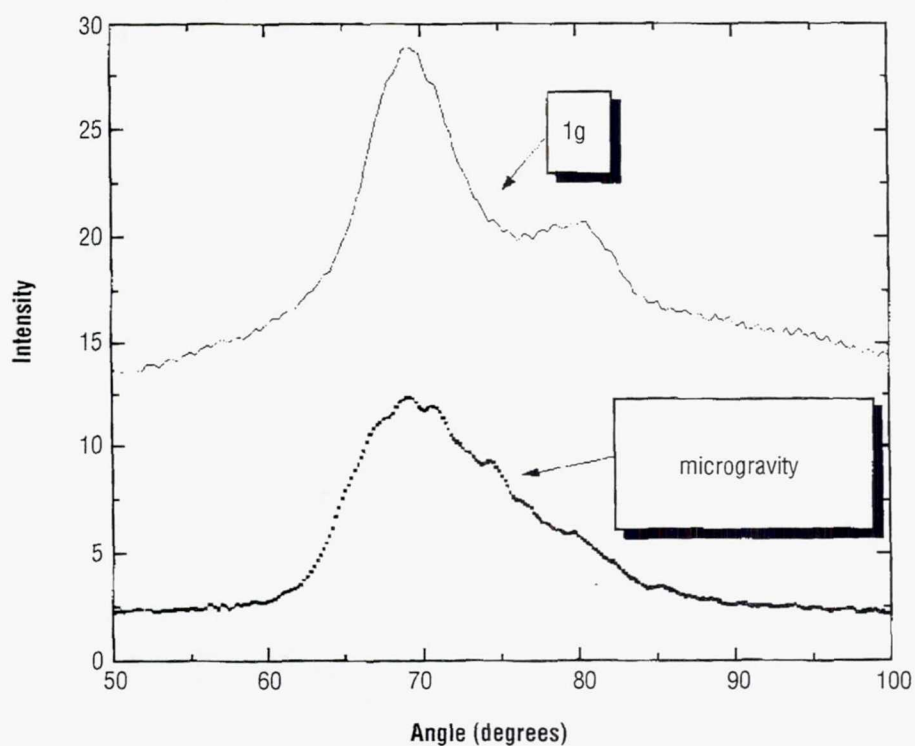


Figure 3. Scattering intensity as a function of the angle obtained by averaging many scattering images as in figure 2b for a sample with $\phi=0.537$. The peak in ground-based experiments at 80° is the (2 0 0) FCC Bragg peak and shows that samples grown in 1g have some fraction of FCC structure. Note the complete absence of any such FCC structure in the microgravity data.

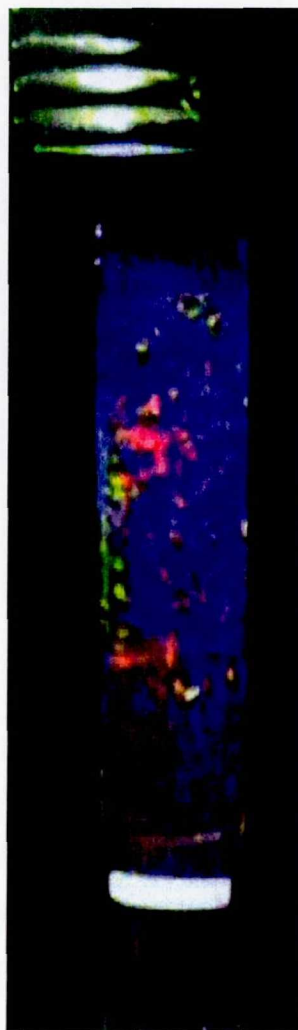


Figure 4. This sample, with $\phi=0.619$ (deep in the “glass” phase) completely crystallized in microgravity after failing to crystallize in 1g. The sample remained crystalline on return to ground. After 6 months, the bottom part of the sample was remelted using the stirbar seen suspended in the glassy region. Two months later, the bottom part of the sample remained glassy with neither nucleation nor growth in 1g.

Page intentionally left blank

EXPERIMENT XXXIV.

DENDRITIC GROWTH OF HARD-SPHERE CRYSTALS

ACKNOWLEDGMENTS

This research was supported by the NASA Microgravity Sciences Program through grant No. NAG31762. The authors thank Professor R. H. Ottewill for synthesis, initial characterization, and advice on the PMMA spheres; Walt Turner for technical support of the experiment and the flight; and the crew of Space Shuttle *Columbia*, particularly Albert Sacco, Catherine Coleman, and Fred Leslie, for the photography during STS-73.

DENDRITIC GROWTH OF HARD-SPHERE CRYSTALS

W.B. Russel

Department of Chemical Engineering
Princeton University
Princeton, NJ 08544

P.M. Chaikin

J. Zhu

Departments of Physics
Princeton University
Princeton, NJ 08544

W.V. Meyer

R. Rogers

NASA Lewis Research Center
Cleveland, OH 44135

ABSTRACT

Recent observations of the disorder-order transition for colloidal hard spheres under microgravity revealed dendritic crystallites roughly 1–2 mm in size for samples in the coexistence region of the phase diagram. Order-of-magnitude estimates rationalize the absence of large or dendritic crystals under normal gravity and their stability to annealing in microgravity. A linear stability analysis of the Ackerson and Schätzel model for crystallization of hard spheres establishes the domain of instability for diffusion-limited growth at small supersaturations. The relationship between hard-sphere and molecular crystal growth is established and exploited to relate the predicted linear instability to the well-developed dendrites observed.

1. INTRODUCTION

The entropy driven disorder-order transition for hard spheres was first discovered via computer simulations about 40 years ago. Following Kirkwood's speculation in 1939¹ that repulsive particles would become ordered at densities below close packing, he and Alder predicted the transition for hard spheres at $\phi = 0.5$. Direct observation of the first-order freezing transition for hard spheres awaited molecular dynamics calculations by Alder and Wainwright² and Monte Carlo simulations by Wood and Jacobson³ in 1957. Not until 11 years later, however, did Hoover and Ree⁴ and Alder, Hoover, and Young⁵ accurately locate coexistence at $\phi = 0.494$ and 0.545 . This Kirkwood-Alder transition, associated with greater configurational entropy for spheres in ordered hexagonal packings relative to a disordered phase, is now the cornerstone of our understanding of disorder-order transitions.

The colloidal hard-sphere disorder-order transition, first realized by Hachisu and Kobayashi⁶ with aqueous polymer lattices, has been studied extensively now for more than two decades. In recent years, nonaqueous, polymerically stabilized dispersions consisting of polymer (methyl methacrylate) cores with grafted chains of polymer (hydroxy stearic acid) (PMMA/PHSA) have enabled detailed light scattering analyses of the structure and dynamics of the crystalline and glassy phases⁷ and yielded significant data on nucleation and growth of the crystallites.⁸ The picture that emerges is reasonably consistent with expectations for the volume fractions at freezing and melting, the hexagonal symmetry for the crystalline phase,⁹ and apparent rates of nucleation and growth that are strong functions of the supersaturation.¹⁰ These same studies also identify significant open questions as to whether the face-centered-cubic structure is preferred over hexagonal close packing and whether the simple Wilson-Frenkel model¹¹ suffices to describe crystal growth.

Ground-based experiments by Pusey, et al.¹² characterize the structure of hard-sphere crystals under gravity as stacking of hexagonal planes, indicating a preference for a structure with the maximum volume fraction at close packing ($\phi = 0.7405$). However, a second plane can stack in two ways on a reference hexagonal plane *A* with crystal axes *a* and *b* shifted by either $(a+2b)/3$, denoted by *B*, or by $(2a+b)/3$, denoted by *C*. The face-centered-cubic structure corresponds to *ABCABC...* and hexagonal close packing to *ABABAB...* (Pusey, et al.), found random hexagonal packing, with equal probability of the third layer repeating the first or differing from the first two, as the most common for hard sphere crystals reforming after shear melting. Of course, under normal gravity the (heavier) particles settle increasingly rapidly as crystallites grow, leaving little time to observe crystal growth and the evolution of the equilibrium structure before the crystallites are quenched into a close packed sediment. Strategies such as “time-averaged zero gravity”¹³ and fluidized beds¹⁴ maintain dispersions for extended periods but introduce viscous flow, which can perturb the structure from equilibrium. Our objective was to observe crystalline phases grown without the influence of gravity to determine whether either the convection or the viscous stresses of settling affect the process significantly.

Studies of nucleation and growth of hard sphere crystals under normal gravity via low-angle light scattering by Schätzel and Ackerson^{10, 15} yielded intensity profiles with a maximum that suggests a depletion zone surrounding the growing crystallite and a time dependence at low supersaturations associated with diffusion-limited growth. The complex dependence on supersaturation of the growth curves, parameterized in terms of the intensity maximum and the associated wavenumber, is difficult to interpret. This prompted the authors to develop a more complete model¹⁶ accounting for the gradients in volume fraction necessary to supply particles to a growing crystallite and the dynamic adjustment of the density of the growing crystallite to balance pressures between the two phases. The predictions suggest diffusion-limited growth at small supersaturations, i.e., near freezing, and rapid growth at constant rate for initial volume fractions at, or beyond, melting. These are, of course, limits well known for the growth of molecular crystals, which raises the question of whether growth instabilities, long known for molecular crystals,¹⁷ and occasionally observed for colloidal crystals,¹⁸ should prevail for hard-sphere crystals as well.

The studies noted above of both equilibrium structure¹² and the dynamics of crystallization^{10, 15} are affected either directly or indirectly by gravity. In the former, the structure was observed to evolve as crystallites settled into a denser sediment. In the latter, sedimentation may well have limited the size of crystallites at low supersaturation where coexistence between dispersed crystallites and fluid cannot be sustained. Consequently, we are examining the structure and dynamics of the colloidal hard sphere disorder-order transition in microgravity via optical photography and light scattering. This paper reports obser-

vations of large dendritic crystallites from the first experiment of a series, which was conducted in the Glovebox of the second United States Microgravity Laboratory (USML-2) flying aboard Space Shuttle *Columbia* from October 20 to November 5, 1995. We offer an interpretation based on a linear stability of pseudosteady diffusion-limited growth extracted from the Ackerson and Schatzel theory.¹⁶ This represents a followup on a previous paper¹⁹ that briefly mentioned this observation along with a number of others.

2. FLIGHT EXPERIMENT

The Colloidal Disorder-Order Transition (CDOT) experiment consisted of two parts: (1) photographic investigation of the phase diagram (liquid, crystal, glassy regimes) and crystallite morphology and (2) light scattering and shear modulus measurements of the monodispersed samples in the CDOT hardware operated in the Shuttle Glovebox. The photography employed both a digital camera (Kodak DCS460 with 12-bit pixel depth per color and an effective pixel array of 3072×2048) and a 35 mm camera (Nikon F4 with 60 mm lens at F8 and Kodak Pro400 film). Astronauts took either digital or 35 mm photos of samples that were enclosed in a rectangular Lucite holder containing four sealed cells which provided double containment. The sample holder sat on a turntable with one cell on the axis, allowing 360° of rotation. A roughly collimated beam of white light illuminated a single cell from a 35° angle above the horizontal plane and at about 45–65° in the horizontal plane relative to the unit normal from the face of the sample holder. The axis of the camera lens was perpendicular to the vertical axis of the sample cell and formed a 35° angle in the horizontal plane with the normal to the holder. These angles are such that light scattered into the camera lens represented diffraction at 56–60° from the crystalline samples.

A day after orbit was achieved, the USML-2 crew unstowed and mixed the samples which had crystallized and/or settled slightly under normal gravity prior to launch. For mixing, the astronauts moved a neodymium-iron-boron horseshoe magnet, positioned around a single cell, axially to drag a cylindrical magnetic bar, about 7 mm long and 1 mm in diameter, through the sample in a prearranged series of translations and rotations. This homogenized samples with volume fractions beyond the disorder-order transition into a metastable fluid state. The astronauts then inspected each visually to assure homogeneity and the absence of any remnant crystals before stowing them to crystallize in microgravity. Digital photos were taken of half of the samples on the 4th day after melting and of all of them on the sixth day. The digital pictures were transmitted to the ground in near real time for analysis. In addition, 35 mm photos were taken on the 4th, 6th, and 12th days and closeups of selected samples on the 12th and 13th days.

3. SAMPLES

Professor R.H. Ottewill and his group at Bristol University synthesized the PMMA/PHSA particles and determined through transmission electron microscopy (TEM) average core diameters of $2a = 508$ and $2a = 518$. We dispersed the PMMA particles (refractive index 1.49) in a mixture of *cis/trans*-decahydronaphthalene (decalin, refractive index 1.475) and 1,2,3,4-tetrahydronaphthalene (tetralin, refractive index 1.5410) that nearly matches the refractive index of the PMMA. Since tetralin is a good solvent for PMMA and swells the particles, significantly increasing the size and raising the refractive index, matching is a dynamic process. We hastened the equilibration by heating for 2 hours at 80 °C and adjusting the composition until the cooled dispersion scattered minimally at a refractive index of 1.5094, which corresponds to 55 wt-percent tetralin. Since the particles experience similar conditions during synthesis,^{20, 21} their structure and physical properties should be unaffected aside from the swelling. Index matching prevents multiple scattering, suppresses van der Waals forces, and results in a purplish transparent suspension.

To estimate the layer thickness and confirm the degree of swelling, we constructed the phase diagram by observing the sedimentation of PMMA dispersions at various core volume fractions²² in glass vials sealed with a Teflon®-lined cap and Teflon® tape at room temperature (21 ± 1 °C). The phase diagrams determine the scale factor between the core and hard-sphere volume fractions such that the latter coincides with the theoretical value for freezing. With a stabilizing layer thickness of 12.0 ± 0.5 nm, as measured in decalin without swelling, the freezing transition indicates that tetralin swells the 518 nm spheres by 53 ± 1 nm. The melting transition occurs at $\phi_m=0.545\pm0.007$, consistent with expectations.

Further confirmation of the hard-sphere behavior is provided by x-ray profiles of equilibrium sediments of the 518-nm particles, from which we extract the equation of state.²² The phase transition is clearly apparent in the density profiles and the pressure in the fluid phase closely matches the Carnahan-Starling equation. The pressure in the crystal exceeds significantly that predicted by the Hall equation, apparently diverging at $\phi_{max}\sim0.72$ instead of 0.74. This appears to reflect either imperfect packing in the polycrystalline sediment, which exhibits visible crystallite sizes of 50–100 μm, or the modest polydispersity of the dispersion.

Fourteen samples, at volume fractions spanning from the fluid just below freezing to the glass (table 1), were mixed each day prior to liftoff to prevent sedimentation. The sample cells are quartz tubes (10 mm outer dimensions (OD), 8-mm inner dimensions (ID), 109-mm length) filled completely with the dispersion and securely sealed with a teflon-faced silicon rubber septum crimped to the flat top of the cell with an aluminum cap. For the volume fractions and particle sizes of our samples, the photographic setup, i.e., the angles of the illumination, cell holder, and camera, would orient the diffraction of red and green light from the first and second peaks for the face-centered-cubic structure, into the camera. In the image both would appear in the same region of the cell, i.e., at the same scattering angle, for such crystallites.

Table 1. Data on CDOT samples (het.xtal \geq heterogeneously crystallized).

Sample [508 nm]	Core Volume Fraction	Effective Volume Fraction	Equilibrium Phase	Sample [518 nm]	Core Volume Fraction	Effective Volume Fraction	Equilibrium Phase
1	0.40	0.488	liquid	9	0.335	0.482	liquid
2	0.42	0.512	coexistence	10	0.35	0.504	coexistence
3	0.44	0.537	crystal	11	0.38	0.547	crystal
4	0.46	0.561	crystal	12	0.43	0.619	glass
5	0.41	0.500	coexistence	13	0.345	0.497	coexistence
6	0.43	0.524	coexistence	14	0.36	0.518	coexistence
7	0.45	0.549	crystal	15	0.41	0.591	het.xtal/glass
8	0.52	0.634	het.xtal/glass	16	calibration sample		

4. OBSERVATIONS OF DENDRITIC GROWTH

Figure 1 shows a photo of a sample in the coexistence region with $\phi = 0.504$.¹⁹ In the laboratory under normal gravity (on left), the liquid-solid phase separation was accompanied by settling with the denser crystalline phase occupying the lower portion of the tube and the fluid phase above. The crystallites were rather small with a morphology that appeared to be isotropic. In microgravity (on the right), the crystallites remain suspended in the fluid phase. In addition to the larger size, an enlargement of part of the photo (insert) reveals branched or dendritic crystals with dimensions of ~ 2 mm and characteristic structure

on the scale of 100 μm . The shape observed after 12 days is indistinguishable from that after 5 days. All of the samples in the coexistence region displayed evidence of dendritic growth. Figure 2 demonstrates a similar, but somewhat larger, dendritic crystallite for $\phi = 0.512$. The significance of differences in size and morphology is difficult to ascertain from this limited sampling. The main point is that dendritic crystallites abound for samples in the coexistence region of the phase diagram. Although the literature contains observations of dendritic growth of crystals from a surface with charged (soft) spheres,¹⁸ this is the first clear evidence that the dominant growth mode for hard-sphere colloids is dendritic.

The coincidence of green and red diffracted light indicates Bragg scattering suggestive of face-centered-cubic crystallites. However, extensive analysis of associated static scattering patterns also recorded during the flight supports an alternative explanation¹⁹ in terms of Bragg streaks from random stacking of hexagonal planes. These 2-dimensional crystals produce rods of diffracted light from a single wavelength that project onto a screen or camera as intense scattering at angles spanning the first two peaks for the face-centered-cubic crystal. For our geometry, a single random hexagonal close-packed crystal will produce a rather monochromatic scattering of white light by the Bragg rod. Unlike Bragg spots, however, different orientations of a single crystal will scatter different colors with the same source-observer (camera) geometry, such as the green and red seen in figure 1.

In comparing the effects of gravity to thermal processes, whether equilibrium or kinetic, the gravitational length and the Peclet number are telling quantities. The former, $h = 3kT/4\pi a^3 \Delta \rho g$ with $\Delta \rho$ the density difference between the particles and liquid, measures the height over which thermal energy can support a particle and is $\sim 40 \mu\text{m}$ or $160 a$ on Earth and about 1 m on the Shuttle. If the solid phase is energetically favored, then fluctuations can produce a crystallite in the fluid phase that will grow if the size exceeds that of the critical nucleus. However, the crystallite has a higher density than its surroundings and will begin to settle. Stokes drag due to viscous stresses in the fluid phase then generates stress within the crystallite proportional to the buoyant mass and inversely proportional to the surface area. When this stress exceeds the yield stress σ_y of the crystalline solid, then fragments (particularly dendrites) will be sheared off, suggesting that the maximum crystallite radius R_{\max} should satisfy:

$$\frac{4\pi R_{\max}^3}{3} \Delta \phi \Delta \rho g = 4\pi R_{\max}^2 \sigma_y$$

with $\Delta \phi$ the volume fraction difference between the solid and fluid phases. Data for charged colloidal crystals in the literature^{23, 24} suggest $\sigma_y \sim nkT$ and $\sigma_y/G_o \sim 0.015$ in the vicinity of the disorder-order transition, with n the number density of spheres. Our own preliminary measurements of the modulus for the hard spheres indicate a static shear modulus of $G_o \sim 50nkT$, which would respond to $\sigma_y \sim 0.75nkT$. With this value the force balance yields the largest radius that spherical crystallites should reach as $R_{\max} \sim 22h$ or $890 \mu\text{m}$. More tenuous dendritic crystallites would break much sooner and never reach this size. Though rough, this estimate supports our observation of small nondendritic crystallites under normal gravity, in contrast to the large dendrites observed in microgravity (fig. 1). Indeed, when we recovered the samples at Kennedy Space Center immediately after the Shuttle landed, the dendrites were gone and the crystalline phase appeared exactly as in the laboratory.

The other notable observation was the persistence of the dendritic structures. As noted above photographs of the coexisting fluid and crystalline phases at 5¹⁹ and 12 days (fig. 1) into the flight produced indistinguishable dendritic crystallites. Thus, annealing of the dendrites to reduce the interfacial energy takes longer than 9 days or 8×10^5 sec. This process requires diffusion over distances comparable to the radius of curvature S . The driving force is the difference in chemical potential between flat and curved surfaces, approximately $\mu_i \sim 4\pi a^3 \gamma / 3S$, due to the interfacial tension $\gamma \sim 0.15 kT/a^2$ associated with a fluid-solid interface in the vicinity of freezing.¹³ The effective force on a colloidal particle for differences in curvature of $O(S)$ over distances of $O(S)$ is then $\partial\mu_i/\partial S \sim -4\pi a^3 \gamma / 3S^2$, which suggests a flux of the form:

$$J = \text{number density} \times \text{mobility} \times \text{force}$$

$$\approx n \times \frac{D}{kT} \times \frac{4\pi a^3 \gamma}{3S^2} \approx 0.15 \frac{D\phi}{(aS)^2}$$

The time scale for affecting the morphology follows as:

$$t = \frac{\text{number density} \times \text{volume}}{\text{area} \times \text{flux}} = \frac{nS^3}{S^2 J} = \frac{5S^3}{\pi a D}$$

The gradient diffusion coefficient approximates the Stokes-Einstein value, $D_o \sim kT/6\pi\mu a$, (4.4×10^{-13} m²/sec with $\eta = 2 \times 10^{-3}$ Pa-sec), since the thermodynamic enhancement is roughly cancelled by the hindrance from hydrodynamic interactions for hard spheres even at high volume fractions. Thus, with $t \sim 14$ days = 1.2×10^6 s, we find $S \sim 44$ μm . This rationalizes the fact that larger features, such as those visible in the photos, persisted to the end of the flight.

5. THEORY OF CRYSTAL GROWTH

We now wish to establish the mechanistic basis for the dendritic growth of hard-sphere crystals by connecting models for the growth process,¹⁶ based on knowledge of the thermodynamics and dynamics of dispersions of hard spheres, with the literature on the instability and nonlinear growth of molecular crystals.¹⁷ The only explicit difference between the molecular and colloidal situations is the role of hydrodynamics in the diffusion processes, which introduces an additional concentration dependence into the growth law. This is a potentially important difference, since the rate of growth may decrease with increasing supersaturation above a certain value, but its actual role in the phenomena remains unclear. So the primary purpose of this, and the following sections, is to link explicitly the detailed knowledge of thermodynamic and transport coefficients for hard spheres to parameters thought to control dendritic growth.

Ackerson and Schätzel¹⁶ formulated a theory for the growth of hard-sphere crystals that incorporates the known thermodynamics and dynamics into a framework that accounts for volume fraction gradients within the fluid and crystalline phases and the simplest kinetic model for propagation of the microscopic front. The treatment is classical, assuming compact spherical crystallites with uniform density in mechanical equilibrium with the adjacent fluid and lumping equilibrium variations in density near the interface into a surface tension taken from density functional theories. From this model, they extracted numerical solutions for the unsteady growth of a spherical crystallite in an effectively infinite reservoir of

disordered fluid, demonstrating the effect of supersaturation on the growth kinetics through the time exponent. At long times they observed the growth to become diffusion limited with a $t^{1/2}$ dependence at small supersaturations and pseudosteady with a constant rate at large supersaturations. Here, we extract analytical solutions for those limiting cases and then explore the stability of the former, which is most relevant to our experiment. This endeavor is fully analogous to treatments of the molecular situation by Langer and others but differs in the volume fraction dependence of the transport and thermodynamic coefficients.

Ackerson and Schätzel first calculate the critical nucleus size $R_c = 8\pi a^3 \gamma / 3\phi_{eq}(\mu_f - \mu_s)$, with $\mu_f - \mu_s > 0$ the difference between the chemical potentials of particles in the bulk fluid and solid phases, and ϕ_{eq} the volume fraction of solid in mechanical equilibrium with the bulk fluid in the absence of interfacial tension, i.e., such that the osmotic pressures of the two phases are equal. Note that R_c diverges at the phase transition, since $\mu_f - \mu_s = 0$, and decays monotonically with volume fraction for $\phi > \phi_{fr}$. They then render the equations dimensionless by scaling the crystal radius R and the radial position on R_c and time on the associated diffusion time, R_c^2/D_o . The dependent variable is the volume fraction ϕ distinguished by subscripts s and f for the solid and fluid phases, respectively. The osmotic pressure Π for each phase is scaled with the thermal energy kT divided by the particle volume. These scalings result in a dimensionless interfacial tension $K = 4\pi a^3 \gamma / 3R_c kT$. Scaling the Wilson-Frenkel form for the interfacial velocity defines a prefactor $\delta = R_c D_s / 2aD_o$ with D_s the short-time self-diffusion coefficient, which decreases with increasing volume fraction. The mutual diffusion coefficients in both phases are set equal to D_o , primarily for mathematical convenience but with the hope that the thermodynamic enhancement and hydrodynamic retardation roughly cancel (as in the fluid phase below the disorder-order transition).

The resulting conservation equations for the individual phases have the form:

$$\begin{aligned} \frac{\partial \phi_s}{\partial \tau} &= \nabla^2 \phi_s && \text{solid phase } \rho < X \\ \frac{\partial \phi_f}{\partial \tau} &= \nabla^2 \phi_f && \text{fluid phase } \rho > X \end{aligned} \quad (1)$$

with the interfacial conditions at $\rho = X = R/R_c$

$$\begin{aligned} \Pi_s &= \Pi_f + \frac{2K}{X} && \text{pressure balance} \\ \frac{dX}{d\tau} &= \delta[1 - \exp \Delta\mu] && \text{growth kinetics, [Wilson-Frenkel Law]} \\ &= \frac{\mathbf{n} \cdot (\nabla \phi_f - \nabla \phi_s)}{\phi_s - \phi_f} && \text{flux balance} \end{aligned} \quad (2)$$

and the initial and boundary conditions $X(0) = 1$ $\phi_f(\rho, 0) = \phi_o$

$$\phi_f(\infty, \tau) = \phi_o \quad \frac{\partial \phi_s}{\partial \rho}(0, \tau) = 0 \quad (3)$$

This formulation represents an early time limit, in the sense that the crystallite is assumed to grow in an infinite reservoir of fluid phase at the initial volume fraction. Several quantities depend on the volume fractions of the fluid and solid phases at the interface and thereby ultimately require constitutive relations, i.e.,

$$\begin{aligned} \Pi_f(\phi_f) \quad \Delta\mu(\phi_f, \phi_s) &= [\mu_s(\phi_s) - \mu_f(\phi_f)]/kT \\ \Pi_s(\phi_s) \quad \delta(\phi_f) \end{aligned}$$

The numerical solutions of Ackerson and Schätzel exhibit an interesting long-time behavior in which the growth rate attains one of two limits:

- (i) $\dot{X} \approx \text{constant}$ for rapid growth with $\Delta > 1$ and
- (ii) $\dot{X} \approx \tau^{1/2}$ for slow growth with $\Delta \ll 1$

where $\dot{X} = dX/d\tau$ and $\Delta = (\phi_o - \phi_{f_i})/(\phi_m - \phi_{f_i})$ is the dimensionless supersaturation. The latter limit is more appropriate for our present purposes, since dendritic crystals were evident only for samples in the coexistence region for which $\Delta < 1$. Below, we extract both limits analytically and examine the stability of diffusion limited growth to small perturbations of the interface. Growth at $\Delta > 1$ is also unstable but will not be discussed here.

5.1 Slow Growth

Growth is diffusion limited if the interfacial velocity associated with the volume fraction of the bulk fluid exceeds the characteristic rate of diffusion, i.e., $\delta(1 - \exp \Delta\mu(\phi_o, \phi_s^{eq})) > 1/X$, and pseudosteady if the actual rate of growth is slow relative to the same characteristic rate of diffusion. Both are true at small or modest undercoolings $\Delta \ll 1$, for which the numerical solutions reach a long-time asymptote in which the crystallite radius increases as the square root of time. Then, in the fluid phase:

$$\frac{\partial \phi_f}{\partial \tau} = \frac{1}{\rho^2} \frac{\partial}{\partial \rho} \rho^2 \frac{\partial \phi_f}{\partial \rho} \approx 0 \quad \text{with} \quad \begin{aligned} \phi_f(X, \tau) &= \phi_{f_i} \\ \phi_f(\infty, \tau) &= \phi_o \end{aligned} \quad (4)$$

which leads to $\phi_f = \phi_o + (\phi_{f_i} - \phi_o)X/\rho$. In the solid, the analogous equation with a symmetry boundary condition at the origin leads to the pseudosteady solution $\phi_s = \phi_{s_i}$. Substitution into the flux and pressure balances at the interface then yields:

$$\phi_{fi} = \phi_{fr} + \frac{\frac{\Delta}{X} + \frac{\delta}{\phi_m} \frac{2K}{X}}{\delta \Pi'_f \left(\frac{1}{\phi_{fr}} - \frac{1}{\phi_m} \right) + \frac{1}{X \Delta \phi}} \quad \phi_{si} = \phi_m + \frac{2K}{\Pi'_s X} + \frac{\Pi'_f}{\Pi'_s} (\phi_{fi} - \phi_{fr}) \quad (5)$$

$$\dot{X} \approx \frac{1}{X} \frac{\Delta - \frac{\phi_{fr}}{\Pi'_f (\Delta \phi)^2} \frac{2K}{X}}{1 + \frac{\phi_m \phi_{fr}}{\delta \Pi'_f (\Delta \phi)^2 X}} \quad (6)$$

and

with Π'_f and Π'_s representing the derivatives with respect to volume fraction evaluated at freezing and melting, respectively. For sufficiently large X , the second term in the numerator and denominator in each fraction becomes negligible, leading to the normal diffusion controlled limit with $X^2=2\Delta\tau$. Since $(\mu_f - \mu_s)/kT \approx (\Delta \phi)^2 \Pi'_f \Delta / \phi_{fr} \phi_m$ for $\Delta \ll 1$, the corresponding prediction for the critical nucleus size leads to $K = \Pi'_f (\Delta \phi)^2 \Delta / 2 \phi_{fr}$. Thus, the growth rate can be written as:

$$\dot{X} \approx \frac{\frac{\Delta}{X} \left(1 - \frac{1}{X} \right)}{1 + \frac{\phi_m \phi_{fr}}{\delta \Pi'_f (\Delta \phi)^2 X}} \quad (7)$$

emphasizing that the initial size must exceed that of the critical nucleus ($X=1$) for the crystallite to grow. The validity of this limit requires only that the time derivative be small relative to the spatial derivative in (4), which is satisfied if $\Delta \ll 1$.

Figure 3a illustrates the volume fraction profile through the crystallite and surrounding fluid for $X = 20$ and $\phi_0 = 0.515$ and figure 3c depicts the variation in the volume fractions at the interface (5) as functions of X for four different ϕ_0 . For $X > 15-20$ the effect of interfacial tension, which compresses the crystallite and slows the rate, becomes negligible, allowing the volume fractions to relax to the values at coexistence, ϕ_{fr} and ϕ_m . The rate of growth from (7) rises from zero to a maximum and then turns over and follows the diffusion-limited asymptote $\dot{X} \approx \Delta/X$ as shown in figure 4a. Figure 4b compares the rate of growth as a function of ϕ_0 for several X with the interfacial velocity in the absence of gradients from the Wilson-Frenkel law (2). This means evaluating the dimensionless mobility δ at the volume fraction ϕ_0 of the bulk fluid and the chemical potential difference as $\Delta\mu(\phi_0, \phi_s^{eq})$.

5.2 Rapid Growth

One should expect pseudosteady growth with a self-similar volume fraction profile and constant velocity if the actual rate of growth considerably exceeds the characteristic rate of diffusion. In addition, an overall mass balance requires the volume fraction of the solid to equal that of the bulk fluid, which is

clearly only possible for $\Delta > 1$. Indeed, the numerical solutions exhibit such a long-time asymptote. We can understand this by transforming the radial coordinate as $s = \rho - X \ll X$, which yields for the fluid phase:

$$\frac{\partial \phi_f}{\partial \tau} - \dot{X} \frac{\partial \phi_f}{\partial s} = \frac{\partial^2 \phi_f}{\partial s^2} + O\left(\frac{1}{X}\right) \quad (9)$$

with $\phi_f(0, \tau) = \phi_{fi}$ and $\phi_f(\infty, \tau) = \phi_o$. If the volume fraction at the interface remains constant, the pseudosteady solution:

$$\phi_f \approx \phi_o - (\phi_o - \phi_{fi}) \exp(-\dot{X}s) \quad (10)$$

should suffice. The corresponding balance in the solid phase has exactly the same form as (9) but with $\phi_s(0, \tau) = \phi_{si}$ and $\partial \phi_s(-\infty, \tau) = 0$, which also yields a pseudosteady solution $\phi_s \approx \phi_{si}$. At the interface $\rho = X$

$$\begin{aligned} \dot{X} &= \delta(\phi_{fi}) \left[1 - \exp(\Delta \mu(\phi_{fi}, \phi_{si})) \right] \\ &= \frac{(\phi_o - \phi_{fi})}{\phi_{si} - \phi_{fi}} \dot{X} \quad \Pi_s(\phi_{si}) = \Pi_f(\phi_{fi}) + O\left(\frac{1}{X}\right) \end{aligned} \quad (11)$$

which for $X \gg 1$ dictate that $\phi_{si} \approx \phi_o$, as expected from the overall balance. Thus, the solution conforms to the classical treatment of directional solidification with the fluid transforming into solid at the initial volume fraction and a constant growth rate dictated, in this case, by the volume fractions at the interface set through the balance of pressures. Figure 3b illustrates the volume fraction profile in the crystallite and surrounding fluid from (10) for $\phi_o = 0.575$ and $X = 25$. Note that the volume fraction relaxes to the bulk value on a length scale $\dot{X}^{-1} \ll X$, due to the compression of contours of volume fraction by the advancing interface. Figure 4c compares the growth rate from (11), which is independent of X , with the interfacial velocity from (2) evaluated as described above.

The validity of this solution depends on the time derivatives of the volume fractions being small relative to the spatial second derivative and the surface tension being negligible in the normal force balance and the growth equation, i.e., $X = \dot{X}^2 t \gg 1$ and $\Pi_s(\phi_o) \approx \Pi_f(\phi_{fi}) \gg K/X$. Clearly, these imply long times and large undercoolings or a large prefactor in the growth equation. The last, i.e., $\delta \gg 1$, is less likely since $D_{so}/D_o \ll 1$ and R/a is not substantially greater than unity at large undercoolings. This result is valid for any $\Delta > 1$, since the compressibility of the solid phase allows adjustment to the bulk fluid density provided $\phi_o > \phi_{fr}$.

6. LINEAR STABILITY ANALYSIS

Comparison of the asymptotic results for slow growth with the intrinsic rate in figure 4b indicates the cost of the volume fraction gradients required to transport particles to the growing crystallite. This difference presents the possibility that a perturbation in the interface, generating a surface with a shorter length scale and, therefore, a larger gradient, will be unstable, leading to a nonspherical mode of growth.

To examine this, we follow Langer¹⁷ and assume a small amplitude periodic perturbation of the interface between fluid and solid. Substitution of the corresponding perturbations to the volume fraction profiles into the governing equations yields a linear, pseudosteady problem that determines whether the perturbation grows or decays with time. Langer's results for the same base states with analogous boundary conditions suggest that both the rapidly and slowly growing crystallites should be unstable to sufficiently long wavelength disturbances. Here, we verify the diffusion-controlled limit in detail, revealing the parametric dependence peculiar to hard-sphere colloids.

The general form for the perturbation in spherical coordinates:

$$\rho = X + \varepsilon Y_{j,m} \exp(\omega_j \tau) \quad (12)$$

has amplitude ε and the symmetry of $Y_{j,m}$, the surface harmonic of order j,m that satisfies $\nabla_s^2 Y_{j,m} = -j(j+1)Y_{j,m}/X^2$ with ∇_s indicating the gradient in the plane of the surface. The associated unit normal and curvature are:

$$\mathbf{n} = \frac{\rho}{\rho} - \varepsilon e^{\omega_j \tau} \nabla_s Y_{j,m} \quad \kappa = \frac{2}{X} + \frac{\varepsilon}{X^2} Y_{j,m} (j-1)(j+2) e^{\omega_j \tau} \quad (13)$$

Figure 5 illustrates the shapes of the lowest four modes for different amplitudes ε , indicating that the $j=1$ mode changes the shape only slightly, while distinct lobes appear for $j > 1$. The density profiles take the corresponding form:

$$\phi = \phi^o(\rho, \tau) + \varepsilon \phi^j(\rho, \tau) Y_{j,m} \exp(\omega_j \tau) \quad (14)$$

where the first term represents the spherically symmetric pseudosteady solution. The radial perturbation ϕ^j must satisfy an ordinary differential equation that follows from separating variables in the 3-dimensional version of the conservation equation determining the base profiles.

The perturbation of the boundary generates an $O(\varepsilon)$ change from the base volume fraction profiles, requiring the perturbation in the volume fractions to restore the balance. These equations, therefore, take the following forms at $O(\varepsilon)$:

$$\begin{aligned} \left(\phi_s^j - \frac{d\phi_f^o}{d\rho} - \phi_f^j \right) \dot{X} + (\phi_s^o - \phi_f^o) \omega_j &= \frac{d\phi_f^j}{d\rho} + \frac{d^2 \phi_f^o}{d\rho^2} - \frac{d\phi_f^j}{d\rho} \quad \text{flux balance} \\ \omega_j &= \phi_s^j \frac{\partial \dot{X}}{\partial \phi_s^o} + \left(\frac{d\phi_f^o}{d\rho} + \phi_f^j \right) \frac{\partial \dot{X}}{\partial \phi_f^o} \quad \text{kinetics} \end{aligned} \quad (15)$$

$$\phi_s^j \frac{d\Pi_s}{d\phi_s^o} = \left[\frac{d\phi_f^o}{d\rho} + \phi_f^j \right] \frac{d\Pi_f}{d\phi_f^o} + \frac{K}{X^2} (j-1)(j+2) \quad \text{pressure balance}$$

with all terms evaluated at $\rho=X$. Note that the chemical potential is related to the osmotic pressure through

$$\mu = \int^\phi \Pi \frac{d\phi}{\phi^2} + \frac{\Pi}{\phi} \quad (16)$$

which with Wilson-Frenkel form for the interfacial velocity leads to

$$\begin{aligned} \frac{\partial \dot{X}}{\partial \phi_s} &= -\delta \exp \Delta \mu \frac{\partial \Delta \mu}{\partial \phi_s} = (\dot{X} - \delta) \frac{1}{\phi_s} \frac{d\Pi_s}{d\phi_s} \\ \frac{\partial \dot{X}}{\partial \phi_f} &= \dot{X} \frac{d \ln \delta}{d \phi_f} - (\dot{X} - \delta) \frac{1}{\phi_f} \frac{d\Pi_f}{d\phi_f} \end{aligned} \quad (17)$$

These balances and the equations governing the perturbed volume fraction profiles comprise the stability analysis for determining the growth exponent ω_j .

The equation governing the concentration perturbations is again pseudosteady, such that:

$$0 \approx \frac{1}{\rho^2} \frac{\partial}{\partial \rho} \rho^2 \frac{\partial \phi_f^j}{\partial \rho} - j(j+1) \frac{\phi_f^j}{\rho^2} \quad \text{with} \quad \phi_f^j(\infty) = \frac{\partial \phi_f^j}{\partial \rho}(0) = 0 \quad (18)$$

The solutions, $\phi_f^j = c_f^j (X/\rho)^{j+1}$ and $\phi_s^j = c_s^j (\rho/X)^j$, must satisfy the interfacial conditions (15), providing a set of equations that determine the constants of integration c^j and the growth constant ω_j :

$$\begin{aligned} \left(\dot{X} + \frac{j}{X} \right) c_s^j & - \left(\dot{X} - \frac{j+1}{X} \right) c_f^j + \Delta \phi \omega_j = \frac{\phi_o - \phi_f}{X} \left(\dot{X} - \frac{2}{X} \right) \dot{X} \\ \Delta \dot{X} \frac{\Pi_s'}{\phi_s} c_s^j & - \left(\Delta \dot{X} \frac{\Pi_f'}{\phi_f} - \dot{X} \delta' \right) c_f^j + \omega_j = \frac{\phi_o - \phi_f}{X} \left(\Delta \dot{X} \frac{\Pi_f'}{\phi_f} - \dot{X} \delta' \right) \\ \Pi_s' c_s^j & - \Pi_f' c_f^j = \frac{\phi_o - \phi_f}{X} \Pi_f' + \frac{K}{X^2} (j-1)(j+2) \end{aligned} \quad (19)$$

where ϕ_f and the parameters:

$$\begin{aligned} \Delta \phi &= \phi_s - \phi_f > 0 & \dot{X} &> 0 \\ \Delta \dot{X} &= \delta - \dot{X} > 0 & \Pi' &= \frac{d\Pi}{d\phi} > 0 & \delta' &= -\frac{d \ln \delta}{d \phi_f} > 0 \end{aligned} \quad (20)$$

are evaluated with the unperturbed solution at the interface. Solution of this set, with the limiting form in the line before (7) for K , determines the growth constant for $\Delta \ll 1$ as:

$$\begin{aligned}\omega_j \approx (j-1)\Delta\phi \frac{\dot{X}}{X} & \left\{ \Pi'_s \left[\Delta\dot{X}\Pi'_f \left(\frac{1}{\phi_f} - \frac{1}{\phi_s} \right) - \dot{X}\delta' \right] \right. \\ & - \frac{1}{2}(j+2) \frac{\Delta\phi\Pi'_f}{\phi_f} \left[\Delta\dot{X} \left(\left(\dot{X} + \frac{j}{X} \right) \frac{\Pi'_f}{\phi_f} - \left(\dot{X} - \frac{j+1}{X} \right) \frac{\Pi'_s}{\phi_s} \right) - \left(\dot{X} + \frac{j}{X} \right) \dot{X}\delta' \right] \left. \right\} \\ & + \left\{ \Delta\phi\Pi'_s \left[\Delta\dot{X}\Pi'_f \left(\frac{1}{\phi_f} - \frac{1}{\phi_s} \right) - \dot{X}\delta' \right] + \left(\dot{X} + \frac{j}{X} \right) \Pi'_f - \left(\dot{X} - \frac{j+1}{X} \right) \Pi'_s \right\} \end{aligned} \quad (21)$$

Although the dimensionless surface tension K does not appear explicitly, the numerator reflects a competition between enhanced diffusion in the first term, which is destabilizing, and the consequences of interfacial tension, which suppress the perturbation.

The physics is more obvious if, as assumed by Langer, $\Pi'_s \gg j/X \gg \dot{X} = \Delta/X$, then:

$$\omega_j = (j-1) \frac{\dot{X}}{X} \left\{ 1 - (j+2) \frac{\Delta\phi\Pi'_f}{2\phi_f\Pi'_s X} \frac{\Delta\dot{X} \left(j \frac{\Pi'_f}{\phi_f} + (j+1) \frac{\Pi'_s}{\phi_s} \right) - j\dot{X}\delta'}{\Delta\dot{X}\Pi'_f \left(\frac{1}{\phi_f} - \frac{1}{\phi_s} \right) - \dot{X}\delta'} \right\} \quad (22)$$

which has the same form as his (3.26). Thus,

- (i) the $j=1$ mode is neutrally stable since it hardly affects the shape (fig. 5),
- (ii) the $j=2$ mode is unstable only when the radius exceeds a critical value:

$$X > 4 \frac{\Delta\phi\Pi'_f}{\phi_f\Pi'_s} \frac{\Delta\dot{X} \left(\frac{\Pi'_f}{\phi_f} + \frac{3}{2} \frac{\Pi'_s}{\phi_s} \right) - \dot{X}\delta'}{\Delta\dot{X}\Pi'_f \left(\frac{1}{\phi_f} - \frac{1}{\phi_s} \right) - \dot{X}\delta'} \quad (23)$$

- (iii) the most unstable mode appears for $j > 2$ when X is sufficiently large.

If we ignore the volume fraction dependence of the self-diffusion coefficient such that $\delta=0$, the growth rate reduces to:

$$\omega_j = (j-1) \frac{\dot{X}}{X} \left\{ 1 - \frac{(j+2)}{2\phi_s^2 X} \left[j \left(\frac{\phi_s \Pi_f'}{\phi_f \Pi_s'} + 1 \right) + 1 \right] \right\} \quad (24)$$

The correspondence:

$$\beta = \frac{\Pi_f' / \phi_f}{\Pi_s' / \phi_s} \quad \frac{vR_c}{D_o} = \dot{X} \quad \frac{3}{4\pi a^3 kT} \frac{\partial \mu}{\partial n} = \frac{\Pi_f'}{\phi_f} \quad (25)$$

with the terms in Langer's chemical model and the limiting form $R_c \approx 2\gamma/\Delta(\Delta n)^2 \partial \mu / \partial n$ for the size of the critical nucleus at small supersaturations yields the dimensional growth rate as:

$$\begin{aligned} \hat{\omega}_j &= (j-1) \frac{v}{R} \left\{ 1 - \frac{((1+\beta)j+1)(j+2)}{R^2} \frac{D_o \gamma}{v(\Delta n)^2 \partial \mu / \partial n} \right\} \\ &= (j-1) \frac{v}{R} \left\{ 1 - ((1+\beta)j+1)(j+2) \frac{\ell}{2R} \right\} \end{aligned} \quad (26)$$

The first form is identical to his (3.26) and clarifies the effect of surface tension in suppressing the instability. The second indicates the $j=2$ mode to be unstable only when $R > 2R_c[2(1+\beta)+1]$. So the critical radius depends on the ratio of the compressibilities of the fluid and solid phases.

A fuller appreciation of the dependence on ϕ_o and X for hard spheres follows from numerical evaluation of the complete result (21) in the next section.

7. DISCUSSION

As noted by Ackerson and Schätzel, all the requisite thermodynamic and transport quantities are known within a reasonable degree of approximation for hard spheres. Thus, we evaluate the growth exponent for the diffusion-limited case as a function of the supersaturation Δ , the instantaneous radius X , and the wavenumber j with the following expressions suggested by Ackerson and Schatzel (A&S):

$$\begin{array}{llll} \Pi_f(\phi_f) & \text{A\&S (7)} & \Pi_s(\phi_s) & \text{A\&S (8)} \\ \Delta\mu & \text{A\&S (15)} & D_s^0(\phi_f)/D_o & \text{A\&S (11)} \end{array}$$

The osmotic pressures diverge at maximum packing for the appropriate phases and the short-time self-diffusion coefficient goes to zero at random close packing. The chemical potential difference vanishes for coexistence and diverges at close packing.

The intrinsic growth rate or interfacial velocity given by the Wilson-Frenkel law (2) is zero for $\phi \leq \phi_{fr}$, since the driving force is zero, and vanishes at close packing along with D_s^o . Consequently, a maximum exists in the vicinity of melting.²⁵ Scaling with the critical nucleus size and the diffusion time, however, produces a dimensionless rate that decays monotonically from a finite value at freezing (fig. 4b).

The normalized rate of diffusion-limited growth produces a maximum in \dot{X} at $X > 1$, due to the effect of interfacial tension (fig. 4a). The asymptotic rates of growth in both regimes generally lie below the intrinsic rate (fig. 4b and 4c) because gradient diffusion lowers the thermodynamic driving force at the interface below the bulk value. However, a crossover appears at large supersaturations (fig. 4c) where microscopic diffusion limits the intrinsic rate due to hindrance of self-diffusion by hydrodynamic interactions ($D_s^o < D_o^o$) as captured in the prefactor of the growth law ($\delta < 0$). Then a macroscopic gradient, which reduces the volume fraction at the interface, enhances self-diffusion and the overall rate of crystallization. For $\dot{X}(\phi_o, \phi_s^{eq}) > \dot{X}(\phi_{fi}, \phi_{si})$, a perturbation that exposes the interface to fluid at a higher volume fraction will grow, unless sufficiently retarded by the thermodynamic consequences of the additional curvature or the kinetic consequences of additional hydrodynamic interactions. Thus, the vertical distance $\dot{X}(\phi_o, \phi_s^{eq}) - \dot{X}(\phi_{fi}, \phi_{si})$, the difference between the rate from the Wilson-Frenkel law in the absence of gradients and the actual rate, in figures 4b and 4c identifies the potential for an instability.

Figure 6 presents the growth exponent ω_j from (21) for diffusion-limited growth, which scales linearly on Δ . Note that $j=2$ is initially the most unstable mode with the onset of instability at $X_{min} \approx 13$ and a maximum at $X_{max} \approx 20$. Reference to figures 3b and 4a indicates that instability only appears well into the diffusion-limited regime, where interfacial tension is negligible and the interfacial concentrations are approaching the equilibrium values. As the crystallite grows even larger, the fastest growing instability shifts to higher modes, while maintaining $X_{max}/(j+2)(2j+1)$ of order unity and roughly constant in accord with (21). This reflects the curvature at which the detrimental effect of interfacial tension balances the enhanced rate of diffusion. Thus, interfacial tension both stabilizes the initial crystallite and promotes the development of higher order modes.

Both the growth rate and the growth exponent for the instability are rather small and fall monotonically beyond the maximum in ω_j , maintaining $X\omega_2/\dot{X} = 0.3-0.8$ for the range of parameters shown. The disturbance grows exponentially, while the underlying growth is diffusion limited and, therefore, considerably less than linear in time. Thus, the potential exists for the perturbation to become comparable to the radius. However, straightforward integration of the equation, assuming the linear theory to hold and the growth rate to adjust to the instantaneous X , indicates otherwise for each individual mode. For example, approximating the exponent for $j=2$ as:

$$\omega_2 = \frac{\Delta}{X^2} \left(1 - \frac{X_{min}}{X} \right) \quad (27)$$

permits the growth equations:

$$\frac{d\epsilon}{dt} = \omega_2 \epsilon \quad \frac{dX}{dt} = \frac{\Delta}{X} \quad \text{with } \epsilon = 1 \text{ and } X = X_{min} \text{ at } t = 0 \quad (28)$$

to be combined into:

$$\frac{d\varepsilon}{dX} = \frac{\varepsilon}{X} \left(1 - \frac{X_{min}}{X}\right) \quad (29)$$

and integrated to obtain:

$$\varepsilon = \frac{X}{X_{min}} \exp\left(\frac{X_{min}}{X} - 1\right) \quad (30)$$

Thus, the ratio of the perturbation to the radius of the crystallite falls from the initial value of $1/X_{min}$ to $0.37/X_{min}$. Clearly, a perturbation at a particular j does not outpace the underlying growth, primarily because the actual wavelength grows as $X/(j+1)$. However, the amplitude does keep pace with the overall growth, leaving open the possibility of nonlinearities triggering faster growth.

Further evolution of the instability could involve nonlinearities due to the finite size of the perturbations or the shifting wavelength of the fastest growing disturbance as the overall size increases. In addition, the instability may not await the attainment of a pseudosteady state for the underlying growth, since a sharper transient profile might be even more unstable. The primary value of this analysis is to indicate that spherical growth is linearly unstable to the formation of a modulated surface early in the process. Presumably, these modulations grow into the dendritic arms that we observe, which appear to correspond to $j = 4$.

However, as in most cases of dendritic growth, the characteristic size of the dendrites is determined by the interfacial velocity, which itself depends on the tip radius. The typical form for diffusion-limited growth at low supersaturations with the effect of curvature from (7):

$$\dot{X} \approx \frac{\Delta}{X} \left(1 - \frac{1}{X}\right) \left(1 + \frac{X_o}{X}\right)^{-1} \quad (31)$$

with $X_o = \phi_m \phi_{fr} / \delta \Pi_f (\Delta\phi)^2$, should apply to dendrites as well and allows for a variety of tip radii and growth rates up to the maximum:

$$\dot{X}_{max} = \frac{\Delta}{X_{max}^2} \text{ at } X_{max} = 1 + (1 + X_o)^{1/2} \quad (32)$$

The observation of Glicksman that dendrites grow at a rate $\dot{X}_{cri} = 0.02 \dot{X}_{max}$ agrees fairly well with the prediction from the marginal stability hypothesis for $\Delta = 0.05$. For hard spheres at $\phi_o = 0.504$ or $\Delta = 0.20$ with $X_o = 0.476$, this corresponds to a radius of curvature of $X = 245$. If one takes $X_o = 0$, which better corresponds to the molecular situation, then $X = 200$. Converting back to dimensional form yields a tip radius of $S = 5468a = 1389 \mu\text{m}$ with $X_o = 0.476$ or $4464a = 1134 \mu\text{m}$ for $X_o = 0$. Both are rather larger than observed, suggesting that the dendrites have not yet reached this growth regime. Likewise, the shape of the dendritic crystallites, resembling $j = 4$, suggests a state of development intermediate between the early

linear growth and the self-similar growth of dendritic arms at long times. Thus, we might expect the scale of the dendrites to conform to the wavelength, $2\pi X/j$, of the fastest growing linear mode. For the lowest three modes, $2\pi X/j = 63, 70, 77$, which corresponds to 360–450 μm . Thus, the tip radius for self-similar growth is greater than observed and the wavelength for the fastest growing linear modes is less than the spacing of the dendritic arms, consistent with an intermediate stage of development.

8. SUMMARY

- Microgravity experiments produce millimeter-size dendritic crystallites for all samples in the coexistence region, whereas observations under normal gravity consistently yield small, apparently nondendritic, crystallites that settle to the bottom of the cell.
- A linear stability analysis for diffusion-limited growth of hard-sphere crystallites identifies unstable modes for crystallites sizes greater than a critical value. Also, the spherical harmonic associated with the fastest growing mode increases with crystallite size, while the wavenumber remains roughly constant.
- Pseudosteady growth of the instability on top of the diffusion-limited growth of the crystallite itself leads to a constant ratio of the amplitude of the perturbation of a particular mode to the crystallite radius.
- The tip radius controlling self-similar growth and the wavelength associated with the fastest growing linear modes lie on either side of the characteristics of the dendrites observed, suggesting an intermediate regime for the growth.

NOMENCLATURE

a	sphere radius [m]
c^j	constant of integration for j th mode
D, D_o	diffusion coefficient, Stokes-Einstein value [m^2/s]
D_s^o	short-time self-diffusion coefficient [m^2/s]
g	gravitational acceleration [m^2/s]
G_o	static shear modulus [N/m^2]
h	gravitational length [m]
j	mode of surface harmonic
J	flux of particles [#/ $\text{m}^2\text{-s}$]
K	$4\pi a^3 \gamma / 3R_c kT$ dimensionless interfacial tension
kT	thermal energy [J]
n	number density [#/ m^3]
\mathbf{n}	unit normal to surface
R	crystallite radius [m]
R_c	critical nucleus size [m]
s	$\rho - R$ dimensionless distance from surface
S	radius of curvature [m]
t	time [s]
v	dimensional interfacial velocity [m/s]
X	R/R_c dimensionless crystallite radius
\dot{X}	$dX/d\tau$ dimensionless growth rate of crystallite
$\Delta\dot{X}$	$\delta - \dot{X}$ (20)
$Y_{j,m}$	surface harmonic

Greek

β	$\Pi_f' \phi / \Pi_s' \phi_f$ ratio of “mobilities” or compressibilities (25)
δ	$R_c D_s^o / 2a D_o$ dimensionless diffusion coefficient
δ'	$-d\ln \delta / d\phi_f$ (20)
Δ	$(\phi_o - \phi_{fr}) / (\phi_m - \phi_{fr})$ dimensionless supersaturation
ε	dimensionless amplitude of perturbation
ϕ, ϕ^{eq}	volume fraction, value with equal osmotic pressures
ϕ^o, ϕ^j	spherically symmetric solution, radial dependence of j th mode
$\Delta\phi$	$\phi_s - \phi_f$ (20)
∇	gradient normalized on R_c
γ	fluid-solid interfacial tension [N/m]
η	solvent viscosity [$\text{Pa}\cdot\text{s}$]
κ	curvature normalized on R_c
μ	chemical potential [J]
$\Delta\mu$	$(\mu_f - \mu_s) / kT$ (20)
Π	osmotic pressure normalized with $3kT/4\pi a^3$

Π	$d\Pi/d\phi$
ρ	radial position normalized on R_c
ρ	radial vector normalized on R_c
$\Delta\rho$	density difference between particle and fluid [kg/m ³]
σ_y	yield stress [N/m ²]
τ	$D_o t/R_c^2$ dimensionless time
ω_j	$R_c^2 \hat{\omega}_j/D_o$ dimensionless growth exponent for j th mode
$\hat{\omega}_j$	growth exponent for j th mode [s ⁻¹]

Subscripts

f	fluid
fr	freezing
i	interface
m	melting
max	maximum
min	value at onset of instability
o	initial value
s	solid, surface

REFERENCES

1. Kirkwood, J.G.: *J. Chem. Phys.*, 7, 611, 1939.
2. Alder, B.J.; and Wainwright, T.E.: *J. Chem. Phys.*, 27, 1208, 1957.
3. Wood, W.W.; and Jacobsen, J.D.: *J. Chem. Phys.*, 27, 1207, 1957.
4. Hoover, W.G.; and Ree, F.H.: *J. Chem. Phys.*, 47, 4873, 1967.
5. Alder, B.J.; Hoover, W.G.; and Young, D.A.: *J. Chem. Phys.*, 49, 3688, 1968.
6. Hachisu, S.; and Kobayashi, Y.: *J. Colloid Interface Sci.*, 46, 470, 1974.
7. Pusey, P.N.; and van Megan, W.: *Physics of Complex and Supramolecular Fluids*, S.A. Safran and N.A. Clark, eds., Wiley-Interscience, New York, 673, 1987.
8. Paulin, S.E.; and Ackerson, B.J.: *Phys. Rev. Lett.*, 64, 2663, 1990.
9. Pusey, P.N.: *Liquids, Freezing, and the Glass Transition* J.P. Hansen, D. Levesque, and J. Zinn-Justin, eds., Elsevier, Amsterdam, 673, 1991.
10. Schätzel, K.; and Ackerson, B.J.: *Phys. Rev. Lett.*, 68, 337, 1992; *Phys. Rev. E.*, 48, 3766, 1993.
11. Wilson, H.A.: *Phil. Mag.*, 50, 238, 1990.
12. Pusey, P.N.; van Megan, W.; Bartlett, P.; Ackerson, B.J.; Rarity, J.G.; and Underwood, S.M.: *Phys. Rev. Lett.*, 63, 2753, 1989.
13. Bartlett, P.; Ottewill, R.H.; and Pusey, P.N.: *J. Chem. Phys.*, 93, 1299, 1990.
14. Rutgers, M.A.; Xue, J.-Z., Herbolzheimer, E.; Russel, W.B.; and Chaikin, P.M.: *Phys. Rev. E.*, 51, 4674, 1995.
15. He, Y.; Ackerson, B.J.; van Megan, W.; Underwood, S.M.; and Schätzel, K.: *Phys. Rev. E.*, to appear.
16. Ackerson, B.J.; and Schätzel, K.: *Phys. Rev. E.*, 52, 6448, 1995.
17. Langer, J.S.: *Rev. Mod. Phys.*, 52, 1, 1980.
18. Gast, A.P.; and Monovoukas, Y.: *Nature*, 351, 553, 1991.
19. Zhu, J.; Li, M.; Rogers, R.; Meyer, W.; Ottewill, R.H.; Crew of STS-73; Russel, W.B.; and Chaikin, P.M.: *Nature*, accepted.
20. Cairns, R.J.R.; Ottewill, R.H.; Osmond, D.W.J.; and Wagstaff, I.: *J. Colloid Interface Sci.*, 54, 45, 1992.
21. Antl, L.; Goodwin, J.W.; Hill, R.D.; Ottewill, R.H.; Owens, S.M.; and Papworth, S.: *Colloids Surf.*, 7, 67, 1986.

22. Phan, S.-E.; Russel, W.B.; Cheng, Z.; Zhu, J.; Chaikin, P.M.; Dunsmuir, J.H.; and Ottewill, R.H.: *Phys. Rev. E*. 1996, 54, 6633. (Note that our earlier detailed characterization of the samples accounted for the effect of the 5-percent polydispersity of the PMMA samples on the freezing and melting transitions in order to compare with measurements on other hard sphere dispersions. In the current work we retained the familiar values for monodisperse hard spheres for simplicity. Conversion of the hard sphere volume fractions reported here to those reported in Phan, *et al.* simply multiply by 1.022.)
23. Lindsay, H.M.; and Chaikin, P.M.: *J. Phys. (Paris) C3*, 46, 269, 1985.
24. Chow, M.K.; and Zukoski, C.F.: *J. Rheol.*, 39, 33, 1995.
25. Russel, W.B.: *Phase Trans.*, 21, 127, 1990.

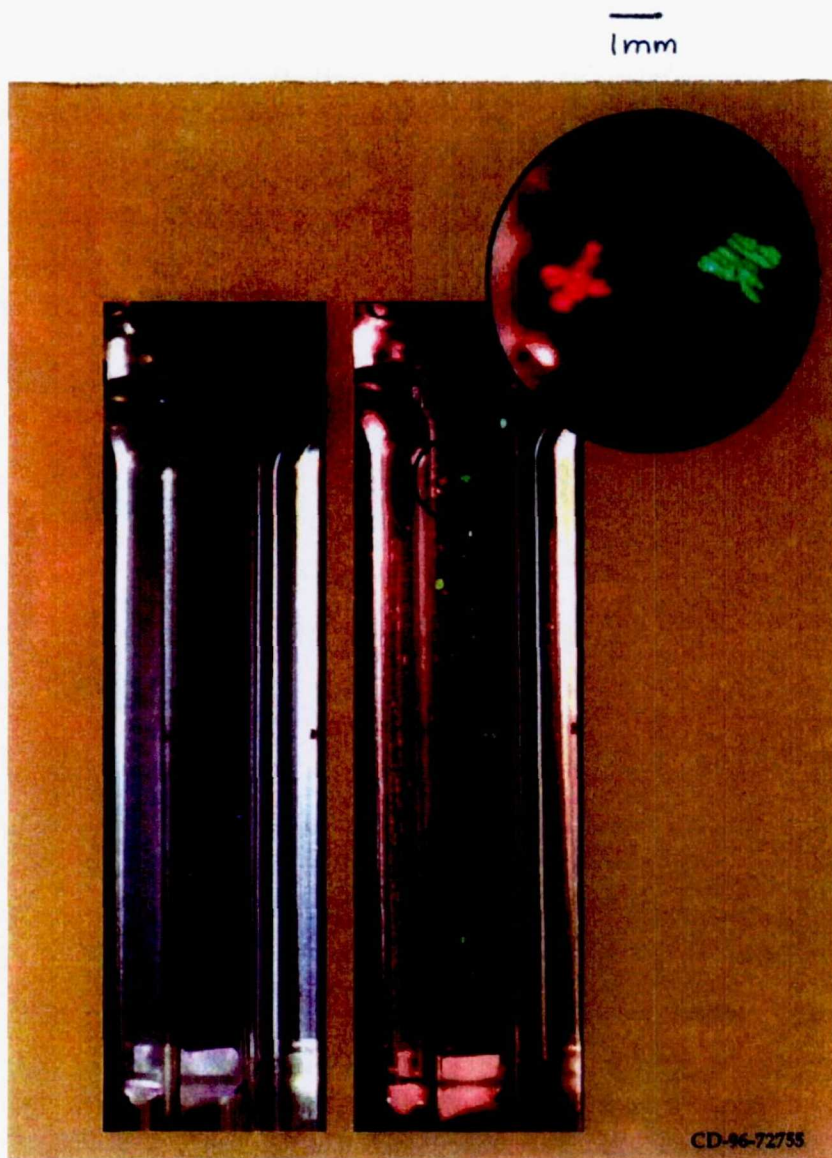


Figure 1. A 35 mm photograph 12 days after mixing of a 10 mm diameter sample cell containing PMMA spheres with $2a = 508$ nm at $\phi = 0.504$ in index matching mixture of decalin and tetralin illustrating large dendritic crystallites surrounded by disordered fluid, which form within 5 days under microgravity in the Space Shuttle.¹⁹ The figure 1 insert is a closeup of the dendritic crystallites demonstrating the detailed structure, which persisted for the duration of the flight. [Reproduced with permission from Zhu, et al. *Nature*, to appear, 1997].

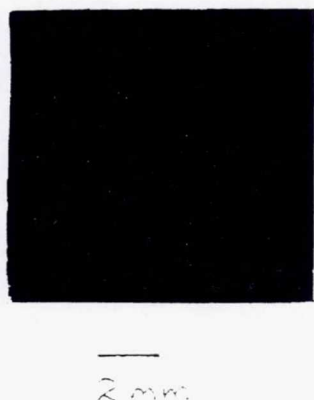


Figure 2. Digital photograph of a dendritic crystallite in a 10 mm diameter sample cell containing PMMA spheres with $2a = 518$ nm at $\phi = 0.512$ in index matching mixture of decalin and tetralin in the Space Shuttle after 5 days (subsequent to mixing) under microgravity.

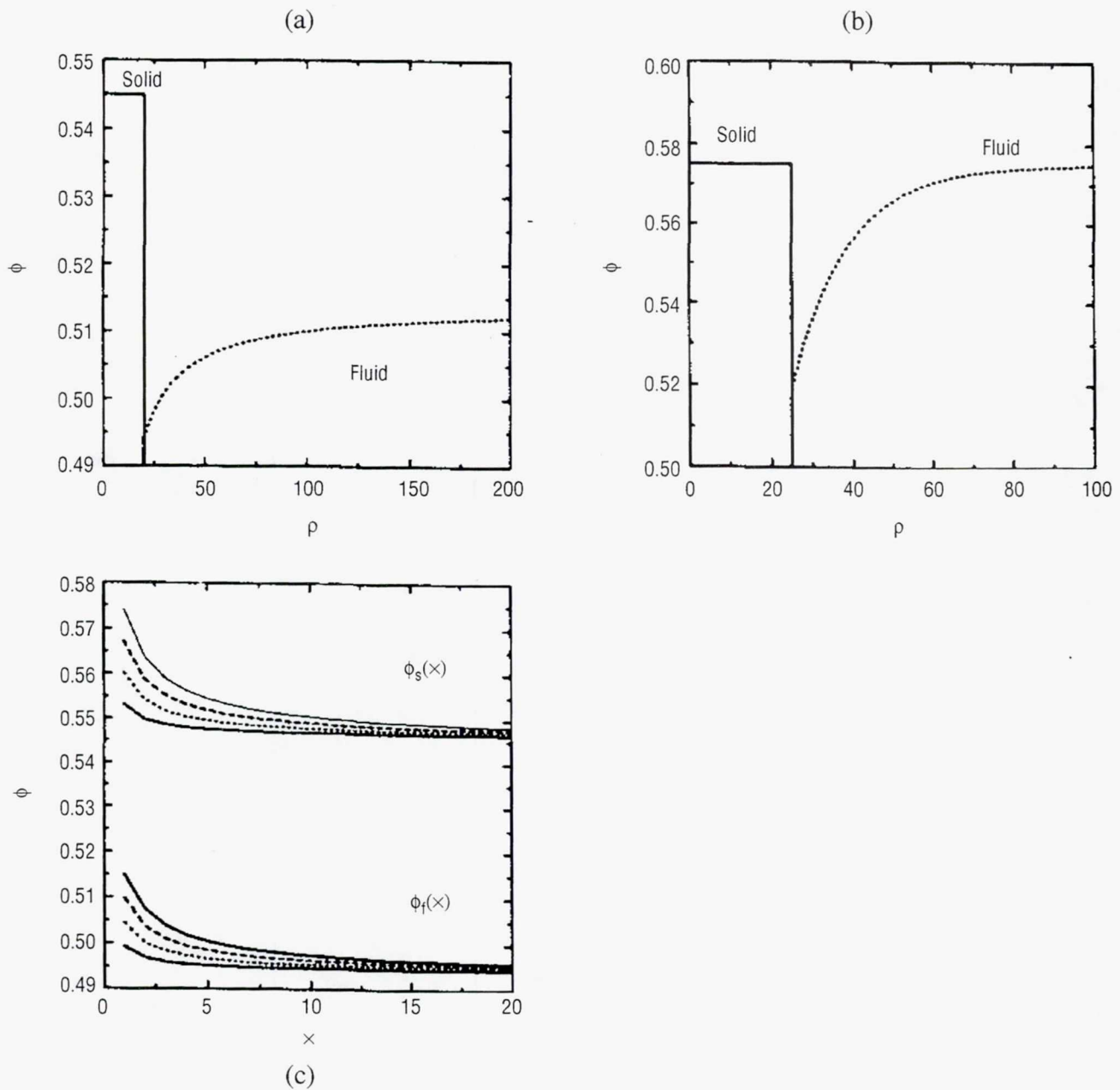


Figure 3. (a) Volume fraction profiles within a growing crystallite ($\rho < X$) and the surrounding metastable fluid ($\rho > X$) for (left) slow, diffusion limited growth with $\phi_o = 0.514$ and $X = 20$ and (right) rapid growth with $\phi_o = 0.575$ and $X = 25$. (b) Volume fractions on the fluid, ϕ_f , and solid, ϕ_s , sides of the interface as functions of the crystallite size X for diffusion-limited growth at $\phi_o = 0.499, 0.504, 0.509, 0.514$. (c) Variation in the volume fractions at the interface as functions of X for four different ϕ_o .

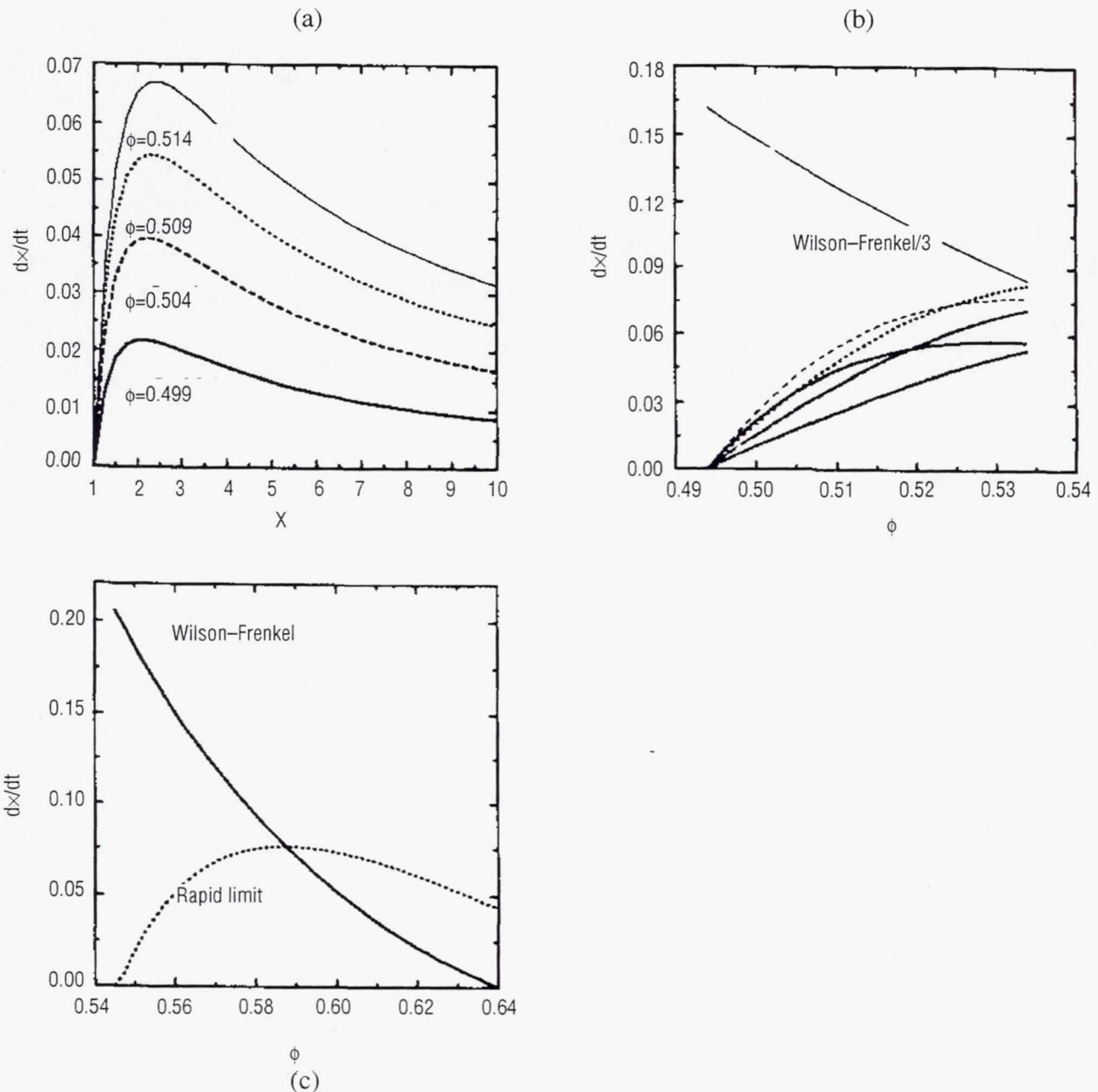


Figure 4. Rates of diffusion limited growth as a function of (a) the crystallite size X for $\phi_o = 0.499$, 0.504 , 0.509 , 0.514 , and (b) the overall volume fraction ϕ_o for $X = 2$ (···), 4 (····), 8 (··), 12 (—), 16 (····), and (c) rapid growth for $X \gg 1$ as a function of ϕ_o compared with the interfacial velocity from the Wilson-Frenkel law.

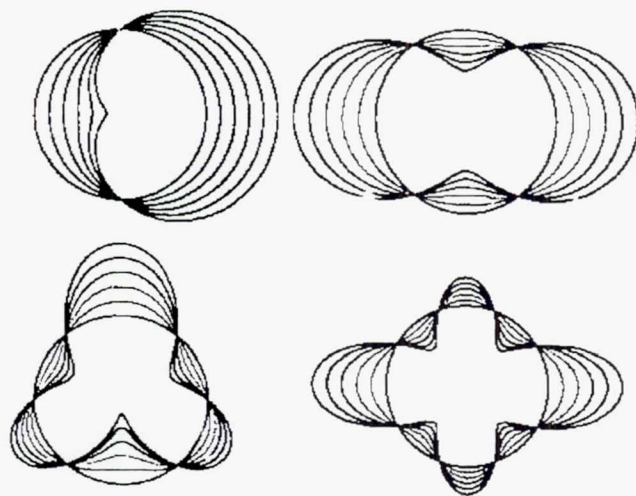


Figure 5. Cross sections of perturbed crystallites with $j = 1, 2, 3, 4$ for $\varepsilon = 0, 0.2, 0.4, 0.6, 0.8$, and 1.0.

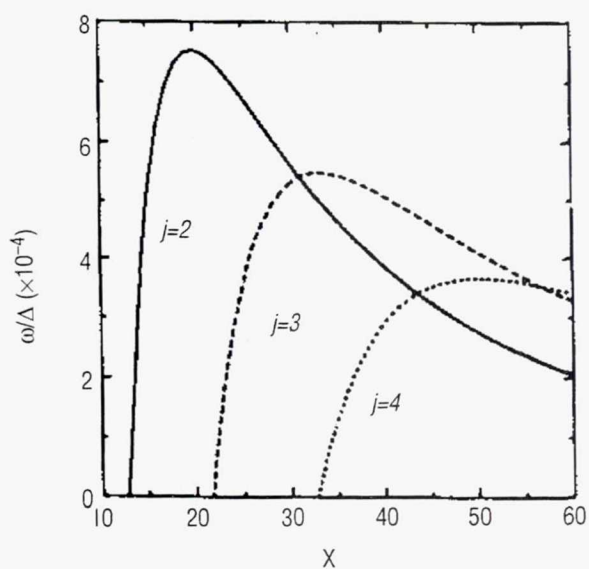


Figure 6. Growth exponent for the three lowest unstable modes normalized by the fractional supersaturation Δ as functions of the crystallite size X .

EXPERIMENT XXXV.

**CATASTROPHIC COLLAPSE OF PARTICULATE CLOUDS: IMPLICATIONS FROM
AGGREGATION EXPERIMENTS IN THE USML-1 AND USML-2 GLOVEBOX**

Page intentionally left blank

CATASTROPHIC COLLAPSE OF PARTICULATE CLOUDS: IMPLICATIONS FROM AGGREGATION EXPERIMENTS IN THE USML-1 AND USML-2 GLOVEBOX

John Marshall, Friedemann Freund, Todd Sauke, and Minoru Freund

SETI Institute, MS 239-12
NASA Ames Research Center
Moffett Field, CA 94035-1000
Phone: 415-604-4983
Fax: 415-604-0092
E-mail: jmarshall@mail.arc.nasa.gov

ABSTRACT

Experiments with electrostatic aggregation of well-dispersed (nominally, mono-dispersed), freely suspended particles in the United States Microgravity Laboratory (USML) Glovebox have determined that filamentary aggregates are a universal product of grain interactions in relatively dense particulate clouds. Aggregate growth from the experimental particle clouds primarily involves dipole-dipole interactions for nonconducting materials; dipole interactions account for both attraction between grains as well as the cohesive force that maintains the integrity of the filamentary structures. When a cloud undergoes a turbulent-to-quiescent transition after damping of fluid and ballistic grain motions, aggregation occurs almost instantaneously and the cloud is transformed into a population of "heavier" clusters of material with organized electrical structures. This abrupt transformation could initiate catastrophic gravitational collapse of certain regions of particulate clouds, thus controlling the longevity and fate of cloud systems as diverse as protoplanetary dust disks and volcanic eruption plumes.

1. INTRODUCTION

In 1989, NASA published plans for the Gas-Grain Simulation Facility (GGSF), an experimental facility for the *International Space Station (ISS)* that would enable long-term suspension studies of aerosols and grain clouds.^{1,2} Creating uniformly dispersed aerosols and particulates as the starting point for aggregation experiments would be a technological challenge. The studies reported here were conducted in the first and second United States Microgravity Laboratories (USML-1 and USML-2) flown on Space Shuttle *Columbia* in 1992 and 1995 respectively, as precursor tests of grain dispersion methods. The experimental apparatus employed for both flights was referred to as the "Particle Dispersion Experiment" or "PDE," so titled in view of the original (USML-1) experiment objectives; for the results described herein, it would have been more appropriately named the "Particle Aggregation Experiment." Although the experiments had a strong technological component, we were interested scientifically in the electrostatic aggregation of particles in dust and debris clouds injected into planetary atmospheres by meteorite impact, volcanism, and aeolian activity.

Additionally, it may be possible to extend the implications of these investigations, albeit tenuously, to other natural particulate clouds, such as those occurring in protoplanetary dust disks, in planetary ring systems such as those of the Jovian planets, and in the dense protostellar and interstellar dust nebulae. Because the two flights had an integrated approach, we have combined the results from USML-1 and USML-2 into this one report. Scientific results from the missions are described; technological aspects of the missions have been reported previously.³

The USML studies were prompted many years ago by a small but revealing experiment conducted in the laboratory. Using air pulses to generate dense suspensions of electrostatically-charged basaltic dust,⁴ we found that after cessation of air turbulence, the dust clouds would suddenly clear with the appearance of rapidly-precipitating filamentary aggregates of >1 cm length. Could this behavior lead to abrupt sedimentation within dense natural cloud systems? How did the static forces produce filaments? Were the observations a function of cloud density? What role did grain size, shape, and composition (dielectric properties) play in the aggregation process? Microgravity experiments on USML-1 and USML-2 would help us answer these questions by delaying sedimentation and by preventing gravitational forces from masking Coulombic effects.

2. CLOUDS AND AGGREGATION

When sufficiently dense particulate clouds are generated, whether on an astrophysical scale or on a planetary scale, there will be forces tending to cause coalescence of the material. Grain-to-grain forces involved in aggregation include the long-range but relatively weak force of gravity, long-range strong forces of electrostatics and magnetism, and short-range sticking forces such as van der Waals attractions, and covalent, ionic and other matter-bonding forces. Electrical fields often associated with dust and debris clouds create static charges on grains through dielectric induction, but there are many other electrochemical, triboelectrical, and radiation-related processes in particulate clouds that can lead to electrostatic charging.^{5,6}

Particulate aggregation influences the way in which stars are born from collapsing nebulae, the formation of planets through accretionary processes, and the behavior of planetary ring systems.^{2,5,7} In dense dust clouds prominent in the constellation Cygnus, in the massive debris disks around stars such as Vega and its neighbors, in the Herbig-Haro (HH) objects (dense spheroidal interstellar clouds) near T-Tauri stars, and in the Bok globules of dense dust, grain-number densities may be sufficiently high for interactions of the grain population. These clouds are either the birthplace of stars, or they constitute the remnants of stellar formation (protoplanetary disks). We postulate that aggregation has the potential to contribute to, or even cause, collapse of these clouds, and the collapse may occur at a dramatic rate owing to self-reinforcing mechanisms of electrostatic attraction as noted below. Electrostatic charges on grains are expected from photoelectric and thermionic effects caused by radiation bombardment, transient heating pulses, and shock-wave phenomena emanating from proximal nova explosions. In particular, in the case of T-Tauri stars, the very dense solar winds and high UV flux should both induce static charges.^{8,9} It is noted, however, that radiation bombardment can lead to a population of grains with like charges that tend to cause grains to repel one another, rather than leading to aggregation.

On a scale more intimately related to this planet, we consider the impact of a K-T type bolide—an impact ejecta curtain and subsequent atmospheric dust pall results from the comminution of debris in the

explosion and from the incineration of organic matter.^{10,12} Immediate effects on the biosphere, and the longer-term climatic effects of sunlight occlusion, will both depend on how fast the atmosphere is cleansed. This, in turn, depends on cloud density and the level of electrostatic charging of both the dust grains and the cloud. Ironically, the denser cloud regions should clear more rapidly because grain collisions are more frequent and charge levels are higher. The importance of impacts on planetary surfaces in terms of devastation to a biosphere is usually assessed in terms of bolide energy. However, we feel justified in proposing that since the major biological/ecological effects might result from the global dust pall, the propensity for aggregation of dust may be at least as important as the initial bolide energy as a factor in determining the consequences for life.

Clouds in planetary atmospheres that are the product of violent rock comminution have extremely high electrical charge levels during the initial minutes;^{13,14} lightning frequently accompanies volcanic eruptions, for example. Aggregation in the super dense dust and debris palls of volcanic eruptions could generate aggregate population that gravitationally downsurge in a way not dissimilar from that occurring with hail in thunderstorms. Could this lead to the observed collapse of eruption plumes and the commensurate production of devastating pyroclastic surges and flows that spread for many kilometers from the eruption site?

3. EXPERIMENTAL METHOD

The apparatus flown on USML-1 and USML-2 (fig. 1) consisted of eight experiment modules or miniature cloud chambers (of 125 cm³ internal volume) which were individually plugged into a pump base. Each module was a self-contained experiment, "loaded" prior to Shuttle launch with several grams of some selected granular material (table 1). The pump unit consisted of a hand-cranked piston device for generating 100 cm³ of 12 psig compressed air which was released as a jet through the base of the attached module. This forcefully dispersed grains around the inside of the module chamber with the air escaping (without the grains) through chamber-wall screens. Air motion typically damped out after ~30 seconds, and the dispersed grains were then allowed to aggregate for up to 30 minutes while being videotaped through the module windows. In some experiments, the astronaut mechanically dispersed the grains by shaking the modules. All experiments were conducted at the ambient conditions of the USML Glovebox facility.

Table 1. Grain type, size, and quantity in USML experiments.

	Module	Material	Grain Size (mm)*	Weight (gm)
USML-1	01	q	0.8	3
	02	q	0.1	3
	03	q	0.4	3
	04	q	0.8	2
	05	q	0.4	2
	06	q	0.8	2
	07	q	0.1	2
	08	q	0.1	2
USML-2	01	v	0.4	6
	02	v	0.4	2
	03	q	0.4	6
	04	q	0.4	2
	05	aq	0.4	3
	06	v+p	0.4+5.0	3 (excl. pebbles)
	07	c	0.4	10
	08	c+q	0.4	5 + 1.5

* approximate mean diameter

q = quartz (natural, rounded alluvial sand), v = volcanics (Mt. Shasta pyroclastics), v+p = volcanic grains with four pebbles of 5 mm diameter mixed with the sand, aq = angular quartz (produced by crushing quartz crystals), c = copper (elongate filings from pure copper block, grain diameter nominal).

The effect of grain size on aggregation was tested in USML-1 with three diameters of rounded quartz grains. The effect of material type was tested in USML-2 with homogeneous, nonconducting material (quartz), with a heterogeneous nonconductor (pyroclastics), and with an electrical conductor (copper grains) that would act as a control for observations made of the mineral materials. The copper-quartz combination in module 08 of USML-2 would determine if there were any special effects of mixing conductors with insulators. The copper particles employed as an experimental control provided enlightening results, but the emphasis of this paper will be on the nonconducting materials because, with the possible exception of some astrophysical settings, the natural particulate clouds that we are chiefly concerned with (those in planetary atmospheres) are composed of nonmetallic grains. Unless otherwise stated, reference is always to the nonconducting materials.

Module 05 of USML-2 had angular quartz grains for shape-effect comparisons with the rounded quartz in other modules. Module 06 of USML-2 had four large (5 mm) volcanic pebbles added to the volcanic sand to determine if they would act as platforms for aggregate growth; results from this module were relatively inconclusive and will not be included in this report. The role of initial cloud density was tested in USML-1 with two different grain loads for quartz, and in USML-2 with three different grain loads for both quartz and volcanics. As an experimental control, the interior walls were changed from insulating anodized aluminum in USML-1 to conductive alodined surfaces in USML-2. This had no apparent effect upon observed processes, leading to the conclusion that electrostatic interactions between grains were not an artifact of the chamber properties.

Grains were "naturally" charged; they were not treated in any way to either enhance or reduce static electricity—the effects of the Shuttle's internal environment notwithstanding. The choice of sand-size material was made for convenience of grain dispersion and video imaging, but sand is an important component of some debris clouds, and the electrostatic behavior of sand can be extrapolated, within limits, to dust-size grains and to larger millimeter sizes. A weightless environment enables static forces to be decoupled from gravity. Large grains enable static forces to be decoupled from short-range sticking forces because the latter can only act very weakly on large masses with small contact points.

4. SUMMARY OF USML-1 AND USML-2 RESULTS

4.1 Grains of All Types Produced Aggregates

Both quartz and pyroclastic material (volcanic ash) immediately produced aggregates after cessation of air turbulence in the experiment modules. There were no observable differences between the behavior of rounded and angular quartz grains. Quartz and pyroclastics are mineralogically quite distinct materials (the ash itself containing several mineral phases and glass), and we feel confident in predicting that probably all nonconducting geological materials (with similar triboelectrical histories) will aggregate. There is certainly no experimental evidence to suggest otherwise. Even conductive copper grains produced aggregates despite our expectations that aggregation might be difficult for such material, although grain-to-grain cohesion was considerably weaker than that for the mineral aggregates. The production of aggregates for both insulating and conducting materials was a direct consequence of grain-to-grain attraction—grain interactions were always attractive. We did not observe any general trend for grains to repel one another, although repulsive interactions would have been unnoticed in the sense that they would have led to increased grain motion that would ultimately match the repelling grains with other partners. There was no observational evidence that grain-to-grain repulsions played any role in determining the overall behavior of the grain clouds.

4.2 Aggregates Always Formed Filamentary Structures

This was not to the total exclusion of any other type of clustering, but the filamentary form was the predominant form, and provided the fundamental building block for both simple and complex aggregate structures (fig. 2). Filaments appeared to be constructed as generally straight strands of single-grain width; variability within this general picture included kinked, wavy, bifurcating forms, and filaments with knots or clusters. In some uncommon cases, strands appeared to be greater than one grain in width. In general, however, the single strand of grains, typically 5 to 20 grains in length was the "standard" aggregate morphology. The conductive copper grains also produced similar filamentary forms.

Experiments were inconclusive in determining the role of particle size in the aggregation process, but it was determined that grains of all sizes tested (0.8 mm to 0.1 mm, but also including 0.01 mm in ground experiments referred to earlier) have a tendency to form filamentary structures. There is no *a priori* reason to suspect that grains larger than those tested will not also aggregate in the same way. However, as grains become larger, their mass increases more rapidly than their surface area, so that interactions that depend upon a constant value of charge-per-unit surface area will become progressively weaker for larger grains. The experiments showed quite conclusively that initial cloud density (grain number density per unit

chamber volume) played an important role in determining the length of filaments. There appeared to be a close correlation between initial density and aggregate length. Aggregates up to 30 grains per chain were observed in the dense quartz cloud experiments. However, cloud density did not affect the morphology of the aggregates—higher densities produced longer filaments—although the interaction of these longer and more closely-spaced filaments also produced complex web-like networks with interspersed clusters or knots of material.

Filamentary structures imply electrical field alignment, or polarization effects. In the case of nonconductors, the electrostatic attraction was due to both fixed static dipoles as well as induced dielectric effects; the attraction does not necessarily depend upon a net charge, nor is it negated by net charge unless all grains carry charges of like sign in sufficient numbers to overcome any dipole interactions. For conductors, the formation of filaments results from electrical field gradient effects and from transient dipoles that become superseded by short-range forces once contact has been made between grains. These attraction and cohesion mechanisms, although quite different between conductors and nonconductors, can lead to the same aggregate morphology. We have successfully duplicated experimental results using computational simulations of our electrostatic model of grain interactions. The present description of interaction mechanics has been limited (including reference to the computational model) because it is currently being submitted for publication elsewhere.

4.3 Aggregate Formation Was Virtually Instantaneous

As figure 3 shows, during the first 30 seconds or so while air turbulence damps out, there are transient populations of aggregates attempting to establish themselves against the disruptive turbulent drag forces. But as soon as turbulence falls below some critical level of intensity, the aggregate population appears instantly. At least for clouds of the density tested in USML (generally > 10 grains/cm³), there is no gradual growth in the size and number of aggregates, rather, the process of formation is immediate, for all practical purposes. For both dilute and dense clouds tested, the result was the same, and in both cases, there was no further significant development of aggregates after the first few tens of seconds. (Again, we limit discussion at this point regarding the mechanisms responsible for creating a “Coulombic stasis” in undisturbed granular systems, because it forms the subject of another manuscript.) Thus, for cloud systems that rapidly transition from turbulent to quiescent, there is virtually no time period when the cloud can be considered as a dispersion of single grains if electrostatic forces are present. The cloud instantly becomes, and remains, a population of aggregates. This rapidity of transition is, of course, only applicable to very dense clouds. Many natural clouds with orders-of-magnitude lower density will exhibit appreciable time scales for the aggregation growth phase, providing that the grains are not so dispersed as to be “unaware” of one another. Of course, particulate cloud systems in planetary atmospheres are never likely to become totally quiescent, so there will always be a tendency to create grain-to-grain encounters as both grains and their associated electrical structures become continually rearranged. Nevertheless, the experimental results serve to illustrate the potency of the forces driving aggregation, and this must be accounted for in models of natural cloud systems (also recalling the transition rapidity in the ground tests with basalt noted earlier).

4.4 Poorly-Dispersed Grain Masses Can Evolve “Giant” Self-Sustaining Aggregates

In several instances where manipulation of the modules by the astronaut had caused local concentrations of material, “giant” 3-dimensional, loosely-bound aggregate clods of grains were formed with

diameters of several centimeters (fig. 4). These were composed of thousands of grains and, in many cases, they were observed to induce dramatic infall of particles from several centimeters distance at velocities of $0.5\text{--}1.0\text{ cm sec}^{-1}$, clearly indicating the presence of strong electrical fields surrounding the aggregates. The infall produced "fractal" surface morphologies constructed from numerous filamentary, tentacle-like protrusions. The electrical fields around such aggregates are probably enhanced by this organized stacking of grains whereby the (electrically-polarized) attractive ends of the filaments become arranged in directional unison. The variable behavior of these large clusters (sometimes attractive, sometimes not) was not a function of grain composition, nor did it appear to depend on the electrical properties of the walls. Notably, no grains were ever repelled by these large aggregates.

5. IMPLICATIONS AND CONCLUSIONS

The fact that particulate clouds can electrostatically transform themselves more or less instantly into populations of aggregates must have important implications for natural particulate clouds where there are turbulent/quiescent transitions, and the presence of electrostatic forces between the grains. It almost goes without saying that a cloud that is suddenly transformed from one type of structure to another within such a short time frame will undergo significant changes in physical properties such as gravitational buoyancy, temperature, electrical conductivity, radiation permeability, fluidization resistance to drag forces, etc. Additionally, there will be discharge and redistribution of electrical, acoustic, and thermal energy directly caused by the formation of the aggregates themselves. The following implications about natural clouds are based largely upon the fact that materials aggregate with persistent regularity and do so with extreme rapidity. The extrapolations are based less upon the other findings regarding the shape of the aggregates as either filaments or (under special circumstances) giant clod-like structures. The morphological trends observed in aggregating materials (despite their remarkable universality) are more important scientifically in providing clues to the Coulombic mechanisms that underlie aggregation; it is the elucidation of these aggregation mechanics that enables predictions about the real world to be made with a greater degree of confidence.

Extrapolations to astrophysical settings are inherently difficult because so little is known about the conditions in nebulae clouds in terms of physical proximity of materials, or in terms of the processes that might create or destroy electrostatic forces between grains. Considering only the static forces in our discussion, it is possible, nevertheless, to make some assertions about potential processes occurring in interstellar clouds or in the dense protoplanetary dust and debris disks that give birth to planetary systems such as our own. Intense ionizing radiation from a solar source may cause grains to acquire such high charge levels of the same sign that they repel one another. Additionally, the repulsive monopole interaction is stronger at greater distances than the attractive dipole interaction. Thus, a dilute interstellar cloud could conceivably acquire a charged state that causes perpetual expansion and dispersal of the material.

On the other hand, there are situations in dense protoplanetary dust disks where the core of the disk is gravitationally condensed to the point where the center of the disk volume becomes shielded from solar radiation. Electrostatic forces (from triboelectrification or other processes) might then lead to enhanced and rapid condensation or coalescence of the disk core as a result of the processes described above (sudden aggregate growth or the formation of giant aggregates with voracious appetites for adjacent material). Once initiated, this collapse could trigger accretionary processes that ultimately lead toward the formation

of planetesimals, leaving a residual, dispersed umbra of ionized and dilutely-dispersed particulates that may play a later role in planetary development. The aggregation would become a “runaway” phenomenon once initiated because the cloud collapses into an ever-increasing density in which electrical forces increase much more rapidly than the linear distance between individual pieces of matter. At this point, we add a note regarding more traditional modeling of accretion and coalescence in astrophysical environments; models that depend on encounters between grains based on random motion or gravitational forces between grains will underestimate the encounter potential by orders of magnitude. Firstly, when a grain is electrostatically charged or possesses a dipole moment its effective cross-section visible to another grain is enlarged by many orders of magnitude. Secondly, electrostatic forces between grains (even due to a single excess electron) are again many orders of magnitude greater than gravitational forces between the grains.

Although electrical forces and particle aggregation have been discussed for volcanic,¹⁵⁻¹⁷ aeolian,¹⁸⁻²⁰ and nuclear/firestorm events,^{21,22} the full potential has not been theoretically or experimentally explored for the more generic role that electrostatic aggregation might play in inducing the collapse of clouds subject to gravitational forces in an atmospheric environment. Our experiments strongly suggest that materials produced violently during volcanism or impact will almost certainly attempt to form great numbers of filamentary structures during their residence time in the atmosphere. Consider, for example, the extremely dense particulate clouds in volcanic eruptions. Close to the eruption source the clouds are extremely violent, preventing the formation of any aggregates other than transient structures. Electrostatic charging in volcanic clouds reaches extremely high levels as evidenced by the frequently observed discharge of lightning from eruption plumes. We note at this point that electrical models of eruption plumes^{13, 14, 23} often involve regions of strongly separated charges in the clouds—hence the potential that gives rise to the lightning—but this represents bulk charge of the plume and does not necessarily mean that all grains within these regions will be charged in the same way. Thus, dipole attractions between grains are not necessarily inhibited (nor enhanced) as a consequence of this charge separation in the cloud as a bulk unit.

In the higher altitude regions of a volcanic plume distant from the eruptive source, there is much-reduced turbulence and the presence of thermally-buoyant masses of hot gases keep large numbers of grains in suspension. Under localized circumstances within volcanic clouds, filamentary aggregates may thus be levitated for some time in updrafts. The jostling, entanglement, and distortion of countless numbers of filaments within updrafts might produce amalgamated clusters of filaments that become aerodynamically compacted into “fluffy” aggregates. Their open structure will trap colliding particles from the grain-saturated flows that loft them in suspension. They might also scavenge material by electrically emulating the large “fractal” structures observed in the USML experiments (fig. 4). It is not difficult to imagine that the vertical buoyancy of an eruption plume may be at least as effective in lofting granular aggregates as a thunderstorm is at lofting giant (>1 kg mass) hail stones. (Uniquely large, baseball size, loosely bound “volcanic hail” composed of ash grains have been encountered on the ground and by aircraft²⁴ during the Mount St. Helens’ eruption.) As with thunderstorms the hail eventually precipitates suddenly, and in great numbers, to the ground. Were such a similar process to occur within a volcanic eruption cloud, the gravitational downsurging of millions of tons of aggregated “volcanic hail” could conceivably trigger the collapse of an eruption plume. Plume collapse has been regarded by some researchers^{25, 26} as the cause of the catastrophic pyroclastic flows and surges that spread outwards from an eruption with devastating effects for tens or even hundreds of kilometers. Accelerated dissipation of volcanic clouds by aggregation has been proposed by several workers.²⁷⁻³⁰ As we have noted earlier, both USML results, and results from laboratory experiments,⁴ suggest that aggregation will be virtually instantaneous when cloud density, charge state, and waning turbulence levels combine into some optimal condition.

A meteorite impact (on this or any other terrestrial body) will generate, if of sufficient energy, an ejecta curtain that can inject vast quantities of debris into both the atmosphere and into orbital and suborbital trajectories. The amount and distribution of fine particulate material injected depends upon the initial energy and location of the impact (those in water obviously generate less, if any, solid debris), the effects of subsequent aerodynamic sorting as the curtain travels outwards and upwards, and subsequent grain interactions such as electrostatic aggregation. Comminuted debris in an ejecta curtain will be highly charged owing to the violent triboelectrical interactions, particularly in the immediate vicinity of the impact site. Ballistic sedimentation can give rise to ground surging of the curtain in the outward radial direction, but we propose that this is probably driven primarily by the larger, longer-trajectory debris. Aerodynamic sorting during curtain expansion will actually leave great quantities of fine debris behind the main curtain front and, as a result of self-reinforcing aggregation (of the type we have just described), the result may be sudden downsurging of bolidiclastic material directed inwards to the crater site. Rapid sedimentation from the denser parts of an impact-generated cloud might abate the solar occlusion and concomitant climatic effects hypothesized for bolide or nuclear events.³¹⁻³³

In conclusion, we believe that electrostatic aggregation might play a significant, albeit unrecognized, role in triggering the collapse of particulate clouds. Charging of natural materials is ubiquitous, and charge levels in natural clouds are significantly higher than those in the USML experiments as a result of the intense electrification processes associated with cloud formation. Understanding the driving forces behind grain interactions in particulate clouds is important for hazard assessment in volcanic areas where aggregation can control eruption behavior and the corresponding threat to life. It is also important as a step towards being able to assess the role of impacts in Earth history, and perhaps even the role that it might play in driving processes on vast scales in astrophysical settings.

REFERENCES

1. Fogelman, G., et al.: *NASA CP 10026*, 1989.
2. Squyres, S.W.; McKay, C.P.; and Schwartz, D.E. (eds.): *NASA CP 2496*, 1987. (See in particular, Experiment No. 13 by F. Freund and M.M. Freund).
3. Marshall, J.R.: *NASA CP 3272 (II)*, eds., N. Ramachandran, et al., 717–732, 1994.
4. Marshall, J.R., et al.: *NASA TM 84211*, 208–210, 1981.
5. Lewis, J.S.: *Physics and Chemistry of the Solar System*, Academic Press, 1995.
6. Krupp, H.: *Static Electrification, Conf. Ser. No. 11*, Instit. Phys. Bristol, 1971.
7. Encrenaz, T., et al.: *The Solar System*, Springer, 1987.
8. Churchwell, E.: *Interstellar Dust*, *NASA CP 3036*, 195, 1988.
9. Evans, A.: *The Dusty Universe*, Ellis Horwood, 1993.
10. Alvarez, L.W., et al.: *Science*, 208, 1095, 1980.
11. Covey, C., et al.: *GSA Spec. Pap.*, 247, 263, 1990.
12. Schultz, P. H.; and Gault, D.: *GSA Spec. Pap.*, 247, 239, 1990.
13. Anderson, R., et al.: *Science*, 148, 3674, 1179, 1965.
14. Brook, M.; and Moore, C.B.: *J. Geophys. Res.*, 79 (3), 472, 1974.
15. Sorem, R.K.: *J. Volc. Geotherm. Res.*, 13, 63–71, 1982.
16. Gilbert, J.S.; and Lane, S.J.: *U.S. Geol. Survey Bull.*, 2047, 31–38, 1991.
17. Carey, S.N.; and Sigurdsson, H.: *J. Geophys. Res.*, 87 (B8), 7061–7072, 1982.
18. Krinsley, D.H., et al.: *NASA Tech. Memo.* 81776, 244–245, 1980.
19. Pye, K.: *Aeolian Dust and Dust Deposits*, Academic Press, London, Chapter 3, 1987.
20. Stow, C.D.: *Weather*, 24, 134–140, 1969.

21. Porche, W.M., et al.: *Atmos. Environ.*, 20 (5), 919–929, 1986.
22. Turco, R.P., et al.: *Science*, 247, 166–176, 1990.
23. Ishikawa, G., et al.: *Geomag. Geoelectr.*, 3, 9–17, 1951.
24. Hobbs, P.V., et al.: *Science*, 211, 816, 1981.
25. Sparks, R.S.J.; and Wilson, L.: *J. Geol. Soc. Lond.*, 132, 441–451, 1976.
26. Sparks, R.S.J., et al.: *J. Geophys. Res.*, 83, B4, 1727–1739, 1978.
27. Gilbert, J.S., et al.: *Nature*, 349, 598–600, 1991.
28. Self, S.; and Sparks, R.S.J.: *Bull. Volcanol.*, 41 (3), 196–212, 1978.
29. Carey, S.N.; and Sigurdsson, H.: *J. Geophys. Res.*, 87 (B8), 7061–7072, 1982.
30. Rose, W.I.; and Hoffman, M.F.: *NASA CP 2240*, ed., A. Deepak, 1–14, 1982.
31. Alvarez, L.W., et al.: *Science*, 208, 1095–1108, 1980.
32. Covey, C., et al.: *Global Catastrophes in Earth History*, V. Sharpton and P. Ward, eds, *Geol. Soc. Am. Spec. Pap.*, 247, 263–270, 1990.
33. Turco, R.P., et al.: *Annu. Rev. Earth Planet. Sci.*, 19, 383–422, 1991.



Figure 1. Experimental apparatus flown in USML-1. Pump base unit and the eight modular experiment chambers are shown. For scale, the windows of the modules are 5 by 5 cm. Each self-contained module is plugged into the base to provide a pulse of compressed air that disperses the grains inside the experiment volume. The volume is not pressurized by this action because the air escapes (without the grains) through chamber-wall screens. The compressed air (~12 psig) is held in a small reservoir in the pump and is derived by operation of the crank handle at right which actuates a small compressor piston. Pressure is released into the chambers by an externally operated shutter mechanism built into the base of each module. Magnified ($\times 4$) video images were obtained of all the experiments; grains were imaged as silhouettes against a diffuse backlight panel placed behind the rear window of each module.

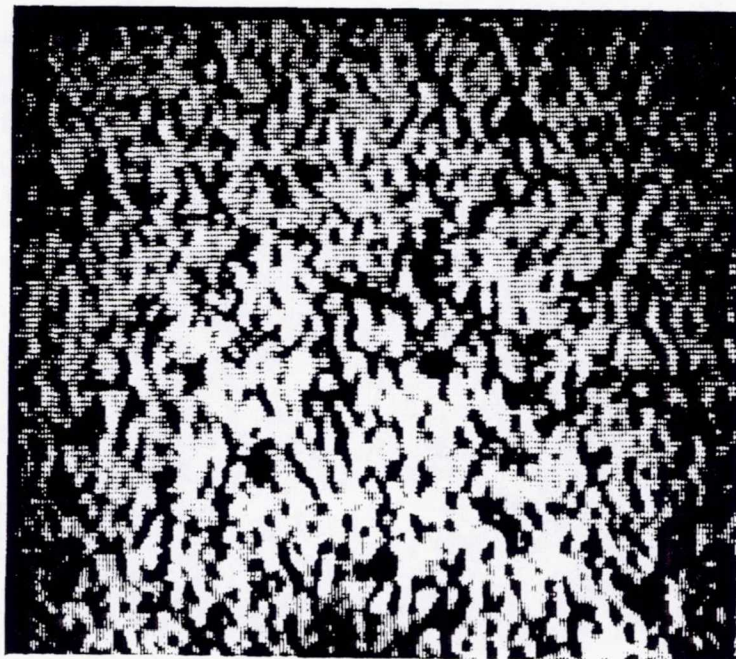
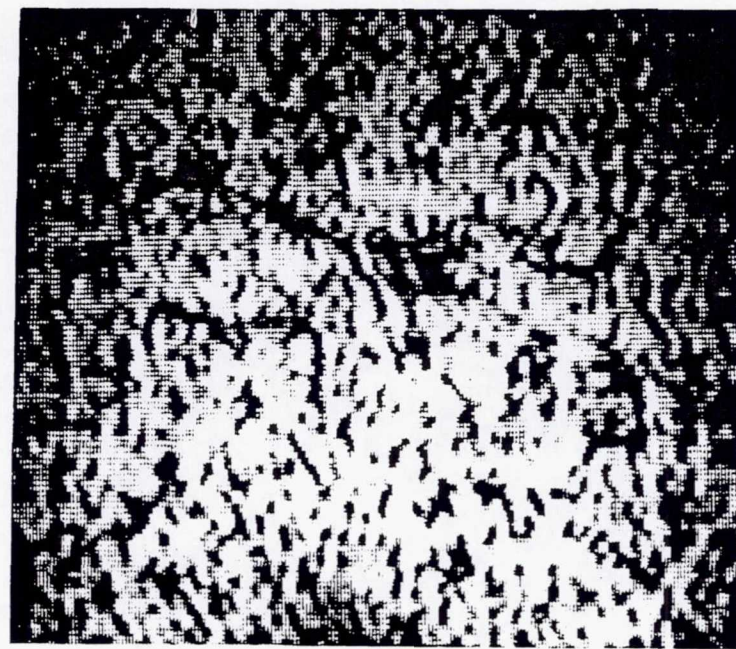


Figure 2. Two views of aggregates formed from a dense dispersion of 0.4 mm quartz grains. The various aggregate shapes are essentially all expressions of the basic filamentary "building block" aggregate structure. Note also the complex network-like structure formed by the filaments. These aggregate populations were formed within the first 30–60 seconds of the experiment and experienced virtually no subsequent changes with time. Field of view in both cases is approximately 2.5 cm across.

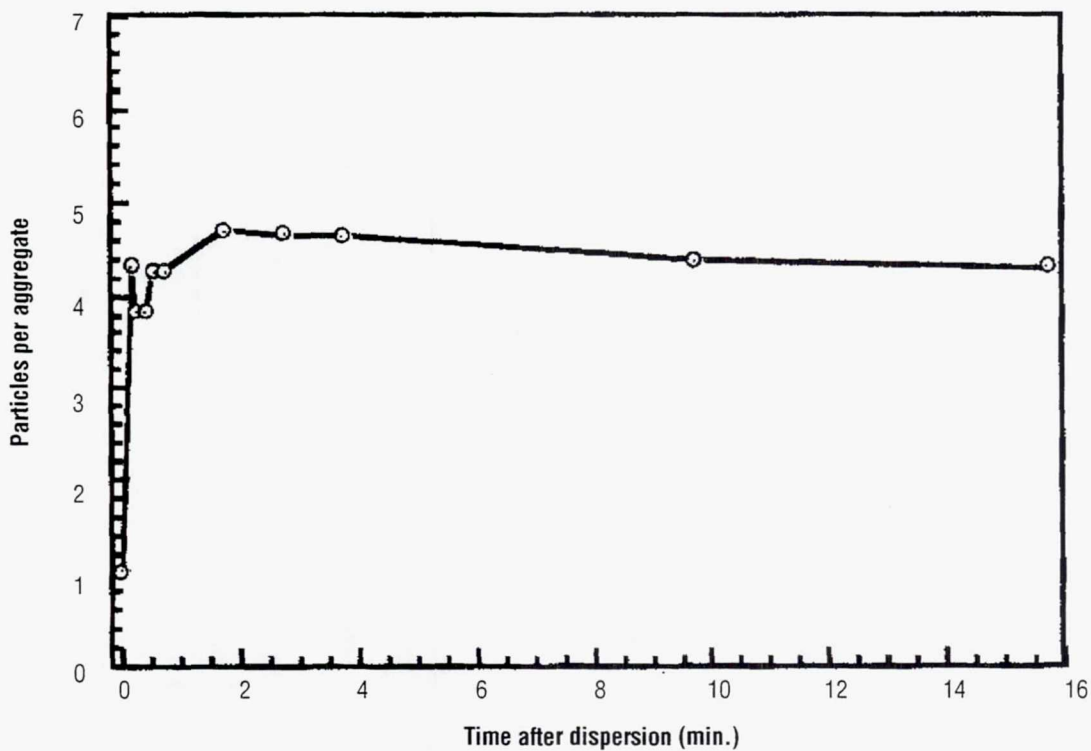


Figure 3. Length of aggregates versus time for 0.4 mm quartz grains (USML-1 data). Note the rapid rise in length from the monodispersed state to "full aggregation" within the first few tens of seconds (corresponding to the period of turbulent damping). The data points represents average aggregate lengths determined from 100–200 aggregates for each still frame taken from the video. The number of grains per aggregate takes into account the foreshortening effect of the 3-dimensional structures as seen on 2-dimensional video images.

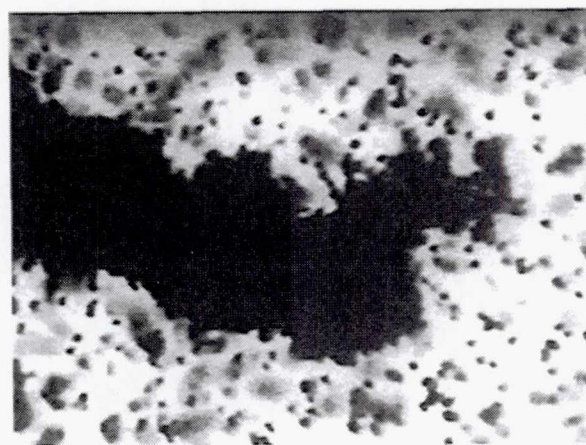


Figure 4. Giant "clod-like" aggregate formed in microgravity during manipulation of experiment chamber by the astronaut. Note filamentary, tentacle-like growths from surface. The aggregate is composed of several thousand 0.4 mm quartz grains. All of the remaining free grains within the field of view are being drawn towards the aggregate at speeds up to 1 cm/sec as a result of the strong electrostatic field produced by the aggregate itself. Field of view \approx 3 cm across.

EXPERIMENT XXXVI.

ONE YEAR REPORT FOR SAMS AND OARE ON STS-73/USML-2

Page intentionally left blank

ONE YEAR REPORT FOR SAMS AND OARE ON STS-73/USML-2

Roshanak Hakimzadeh
NASA Lewis Research Center
Cleveland, OH 44135
Phone: 216-433-8738
E-mail: roshanak@lerc.nasa.gov

1. INTRODUCTION

The Second United States Microgravity Laboratory (USML-2) payload flew on the orbiter *Columbia* on mission STS-73 from October 20 to November 5, 1995. The USML-2 payload on STS-73 was dedicated to microgravity experiments. Two accelerometer systems managed by the NASA Lewis Research Center (LeRC) flew to support these experiments, namely the Orbital Acceleration Research Experiment (OARE) and the Space Acceleration Measurements System (SAMS). OARE downlinked real-time quasi-steady acceleration data, which were provided to the investigators. The SAMS recorded higher frequency data onboard for post-mission analysis.

The Principal Investigator Microgravity Services (PIMS) project at NASA LeRC supports principal investigators of microgravity experiments as they evaluate the effects of varying acceleration levels on their experiments. A summary report¹ was prepared by PIMS to furnish interested experiment investigators with a guide to evaluate the acceleration environment during STS-73, and as a means of identifying areas which require further study. The summary report provides an overview of the STS-73 mission, describes the accelerometer systems flown on this mission, discusses some specific analyses of the accelerometer data in relation to the various activities which occurred during the mission, and presents plots resulting from these analyses as a snapshot of the environment during the mission.

Numerous activities occurred during the STS-73 mission that are of interest to the low-gravity community. Specific activities of interest during this mission were crew exercise, payload bay door motion, Glovebox fan operations, water dumps, Ku band antenna activity, orbital maneuvering system, and primary reaction control system firings, and attitude changes. The low-gravity environment related to these activities is discussed in the summary report.

2. ACCELEROMETER SYSTEMS

Two NASA LeRC accelerometer systems, OARE and SAMS, measured the low-gravity environment of the Space Shuttle *Columbia* during the STS-73 mission. The OARE was designed to measure quasi-steady accelerations from below 1×10^{-8} g up to 2.5×10^{-3} g. It is mounted near the center of gravity of the Space Shuttle vehicle. On STS-73, the SAMS unit was located in the Spacelab module in support of USML-2 experiments. Three SAMS triaxial sensor heads (TSH) were located remotely at experiment sites

(table 1). The signals from these sensor heads were filtered by low-pass filters with cutoff frequencies listed in table 1. These signals were then sampled, and the data were recorded on optical disks.

Table 1. SAMS configuration for USML-2.

Sensor Head	Cutoff Frequency	Sampling Rate (samples/sec)	Sensor Location
TSH A	5 Hz	25	Mounted to surface tension driven experiment package waffle plate (Rack 3)
TSH B	2.5 Hz	12.5	Mounted to Rack 9 support structure baseplate (crystal growth furnace IFEA)
TSH C	25 Hz	125	Mounted (on orbit) under the Glovebox (Rack 12)

3. COORDINATE SYSTEMS

The OARE data are typically presented in the orbiter body coordinate system (X_b , Y_b , Z_b). In this coordinate system, the direction from tail to nose of the orbiter is $+X_b$. The direction from port wing (left wing) to starboard wing (right wing) is $+Y_b$, and the direction from the top of the fuselage to the orbiter belly is $+Z_b$. This coordinate system is centered at the center of gravity (CG) of the orbiter (fig. 1).

The SAMS data are typically presented in the orbiter structural coordinate system (X_o , Y_o , Z_o). In this coordinate system the direction from nose to tail of the orbiter is $+X_o$. The direction from port wing to starboard wing is $+Y_o$, and the direction from the orbiter belly to the top of the orbiter fuselage is $+Z_o$. This coordinate system is centered at the tip of the orbiter external fuel tank (fig. 2).

4. COLUMBIA MICROGRAVITY ENVIRONMENT: STS-73

The microgravity environment measured by an accelerometer system on the orbiter has many components. The quasi-steady microgravity environment is related to orbital phenomena such as aerodynamic drag and rotational motion and to gravity gradient (GG) effects based on the distance from the orbiter center of gravity. In addition to these quasi-steady accelerations, all ongoing operations of crew life support systems and activities and operations of the orbiter, crew, carrier, and experiments tend to have transient and vibratory components that contribute to the background acceleration environment. The following subsections describe some of the most interesting events which contributed to the microgravity environment during the mission.

4.1 Orbiter Attitude

The orbiter attitudes for missions are typically defined in advance of launch. Several factors drive the determination of attitude. These are, for example, orbiter thermal conditions, maximizing continuous communications, and experiment operations requirements.

The attitude timeline for the STS-73 mission included a solar inertial attitude for thermal conditioning, a nominal USML-2 GG attitude, and specific attitudes designed for the Geophysical Fluid Flow Cell (GFFC) and Crystal Growth Furnace (CGF) experiments. These attitudes are shown in figure 3. The acceleration environment differences related to the different attitudes are not particularly apparent in the whole mission OARE data plot (fig. 4).

The solar inertial attitude was used to point the orbiter belly at the Sun to increase the temperature of the tires. The effect on the quasi-steady microgravity environment is shown in figure 5.

The CGF attitude was used in support of the CGF experiments. This attitude is of interest to the CGF principal investigators (PI's) as it aligns the furnace with the velocity vector. A typical plot of the OARE data while the orbiter was flown in this attitude is shown in figure 6.

Plots of the quasi-steady microgravity environment obtained when the orbiter was in the GG and GFFC attitudes are shown in figures 7 and 8, respectively.

4.2 Crew Activity

The seven-member crew of STS-73 worked on a dual shift schedule. Figure 4 shows the OARE data for the extent of the STS-73 mission. Note that, unlike single-shift missions, the quasi-steady environment represented by these data is relatively constant throughout the mission. Daily cycles in the acceleration levels may be seen in the X_b axis, especially for the first 250 hours of the mission. These are due to the daily mission activities of experiment operation and crew cycles.

Figure 9 shows an example of the vibration environment of the Spacelab module as recorded by SAMS during a period when the working crew voiced down that they were being quiet. The data plots in column (a) of figure 9 are 20-minute time histories of the three axes of SAMS TSH A data starting at approximately MET 005/07:09. The data plots in column (b) of figure 9 show PSD representations of the column (a) data. These plots represent the microgravity and vibration environment in the Spacelab during STS-73 that resulted, in part, from various equipment and life support systems that were operational at the time. Therefore, figure 9 can be used as a basis of comparison for other activities discussed.

4.3 Attitude Control

Acceleration levels caused by thruster firings are of concern to investigators. Orbiter attitudes for microgravity payloads are therefore often designed to minimize the number of firings of the vernier reaction control system (VRCS) jets used for attitude control. Figure 10 shows the microgravity environment caused by VRCS and primary reaction control system (PRCS) jet firings. This plot is the vector magnitude of the three axes of SAMS TSH B data collected over 5 hours when the orbiter was cycling among VRCS attitude control, PRCS attitude control, and free drift. This figure shows the acceleration magnitude difference between PRCS and VRCS activity. The acceleration magnitudes related to a single PRCS jet firing are in the 0.01- to 0.025-g range, compared to VRCS jet acceleration magnitudes of about 3×10^{-4} to $7 \times 10^{-4}\text{ g}$.

4.4 Payload Bay Door Motion

The port payload bay door was kept partially closed during the STS-73 mission to help limit the number of debris hits to the cargo bay. The port payload bay door had to be fully opened once during the mission so that a Spacelab condensate could be performed. The port payload bay door began to open for the dump at about 004/23:49. The condensate dump occurred at MET 005/00:19 and lasted for 2 minutes. Motion to return the door to its partial closed position began at about 005/00:26. Figure 11 shows SAMS TSH A data collected during the door opening operations. The impact of the door motion is seen most clearly on the Y_o and Z_o axes.

4.5 Glovebox Fan Operations

The Glovebox cooling fan and the air circulation fan contributed vibratory components to the microgravity environment on USML-2. Figure 12 shows SAMS TSH C data for the time period when the two fans were shut off. A slight decrease in acceleration levels can be seen in the time history data about 2.5 min into the time history plot. Note that the PSD's are displayed out to the highest frequency possible to show the frequency components at approximately 38, 43, 48 and 53 Hz which may be related to the fans. The effects of these two fans can be seen more clearly using a color spectrogram.¹

4.6 Water Dump Operations

Supply and waste water dumps are performed using nozzles on the port side of the orbiter. About 16 water dumps can be clearly seen in the figure 4 plot of the OARE data for the entire mission. These dumps each lasted for about 1 hour, and the apparent acceleration in the Y_b -axis is on the order of -1×10^{-6} g. Two larger excursions in the OARE data at about MET 90 hours and 190 hours were caused by simultaneous waste and supply water dump operations. A more detailed plot of the OARE data obtained during two water dumps is shown in figure 13. This figure is a plot of the acceleration environment for a 24-hour period.

5. CONCLUSIONS

The microgravity environment of the Space Shuttle *Columbia* was measured during the STS-73 mission using two LeRC accelerometers, namely the OARE and the SAMS. The microgravity environment related to several different orbiter, crew, and experiment operations was presented.

The OARE provided investigators with real-time quasi-steady acceleration measurements. SAMS recorded higher frequency data on board, which was analyzed postmission. The OARE data were compared in real time to the predicted quasi-steady environment provided by the Microgravity Analysis Workstation (MAWS) and developed by Teledyne Brown Engineering (TBE). These agreed very well throughout the mission. The MAWS quasi-steady environment calculation and a comparison of this calculation with OARE data were used to assess how appropriate the planned CGF attitude was for one CGF experiment run.

REFERENCES

1. Rogers, M.J.B.; and DeLombard, R.: "Summary Report of Mission Acceleration Measurements for STS-73," *NASA TM 107269*.

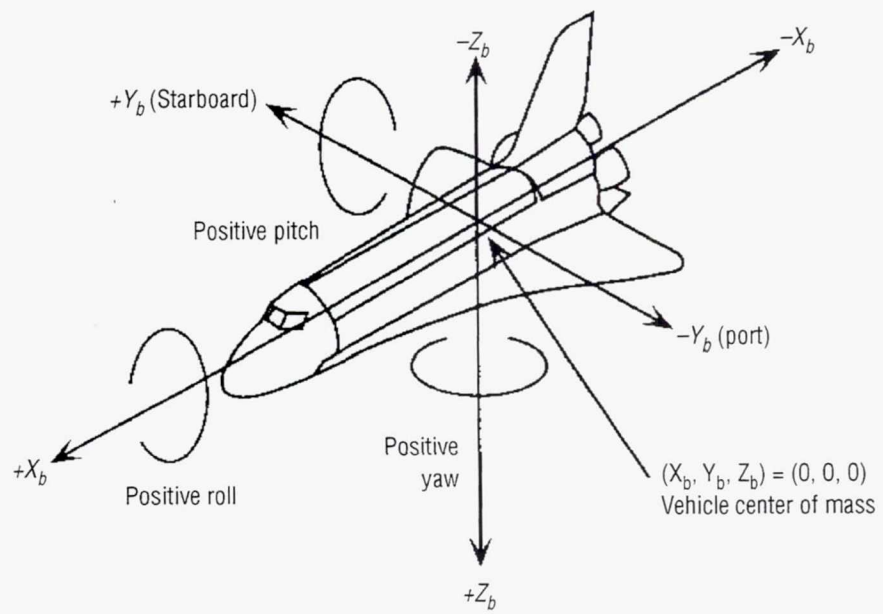


Figure 1. Orbiter body coordinate system.

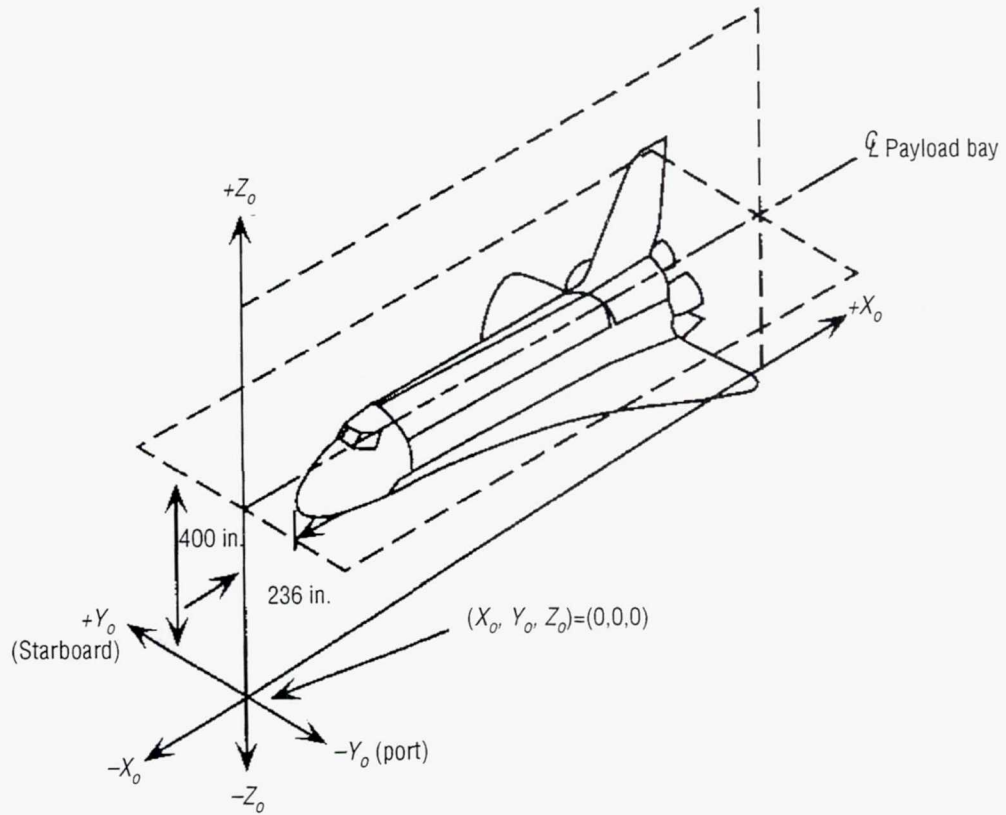


Figure 2. Orbiter structural coordinate system.

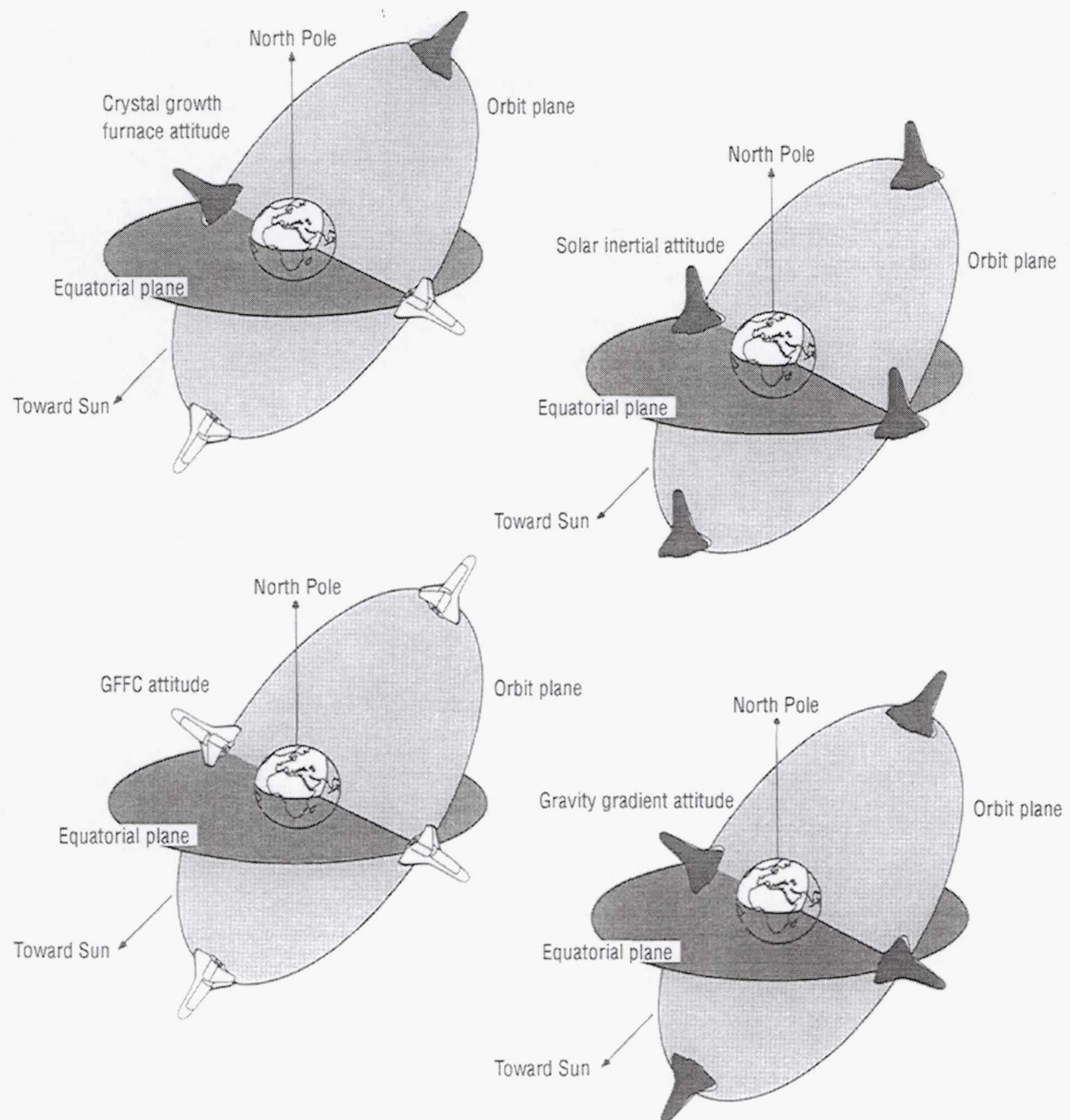


Figure 3. USML-2 major attitudes.

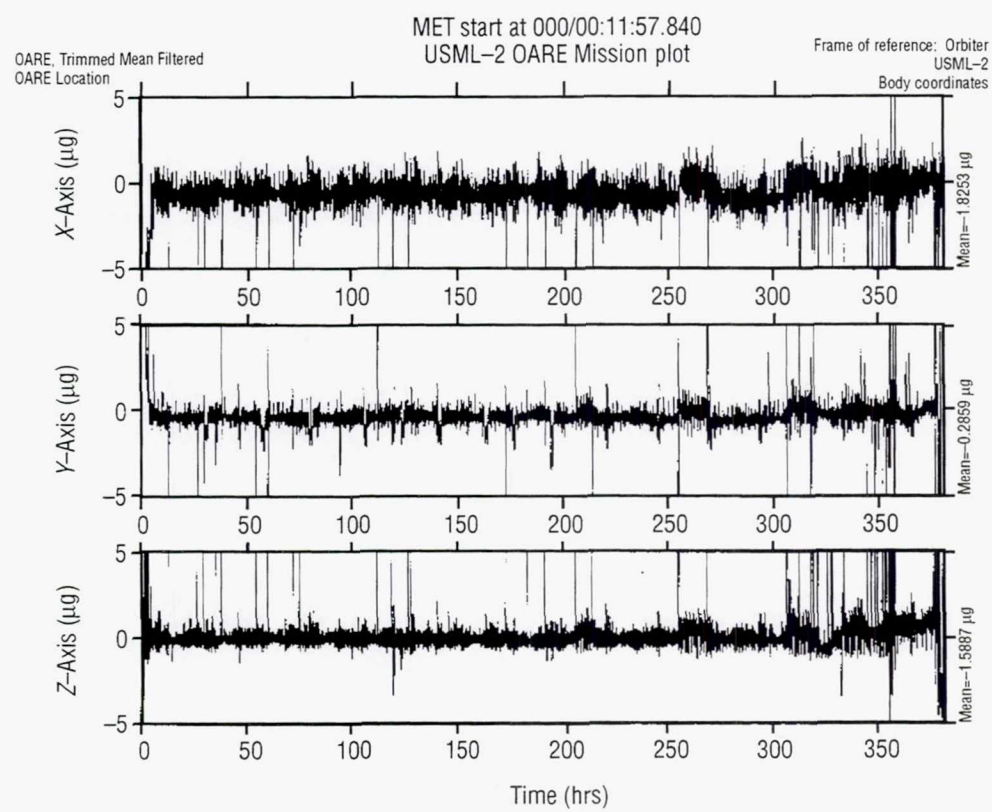


Figure 4. Trimmean filter OARE data for entire STS-73 mission.

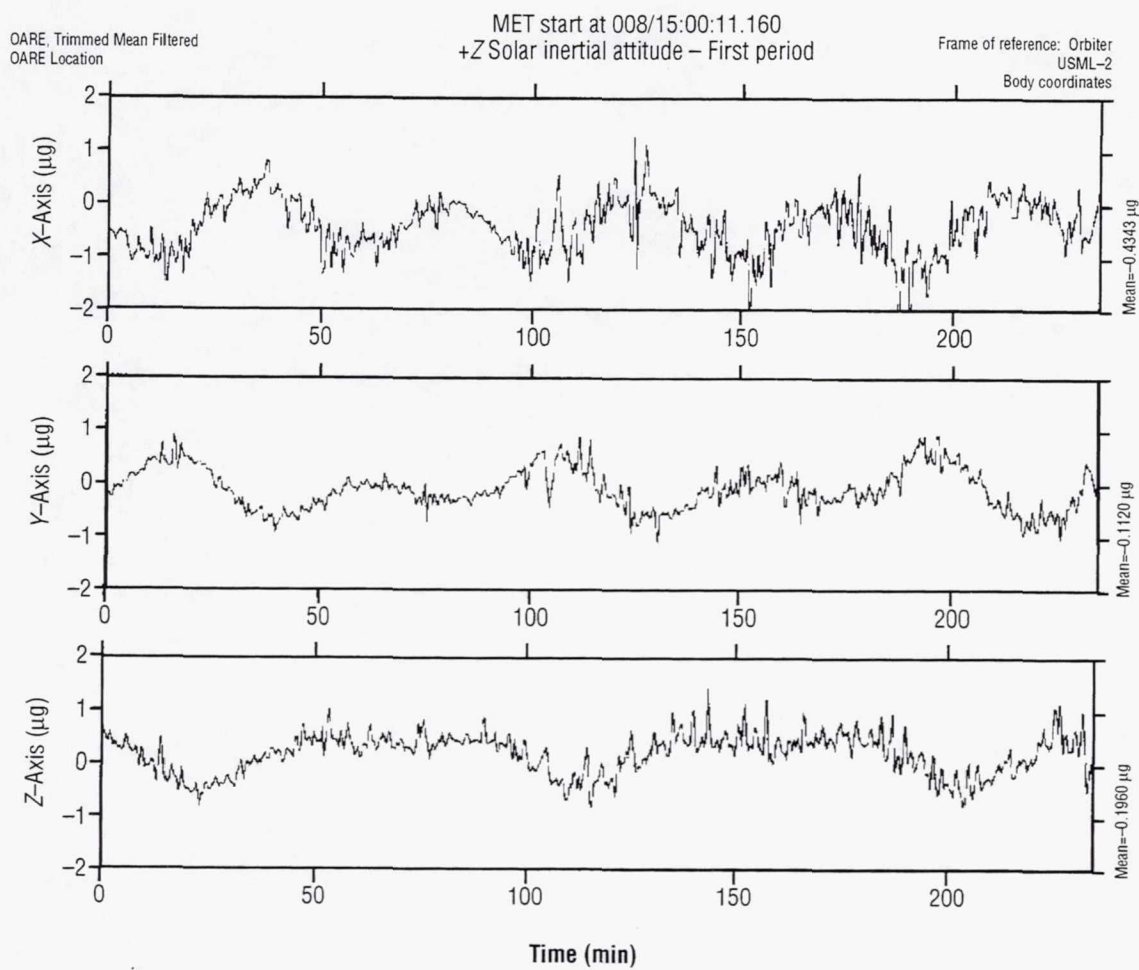


Figure 5. Trimmean filter OARE data for period when *Columbia* was in the solar inertial attitude for tire warming.

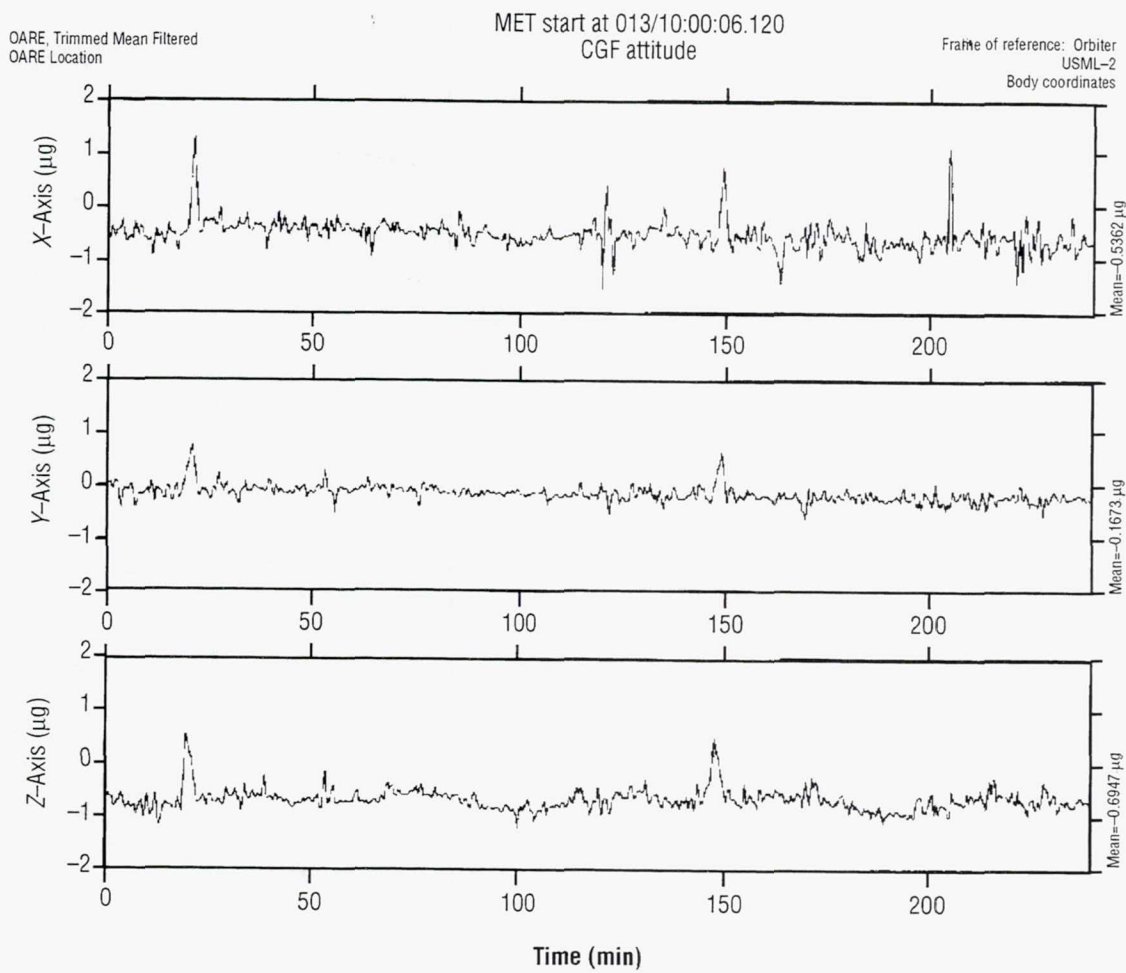


Figure 6. Trimmean filter OARE data for period when *Columbia* was in the CGF attitude in support of one CGF experiment.

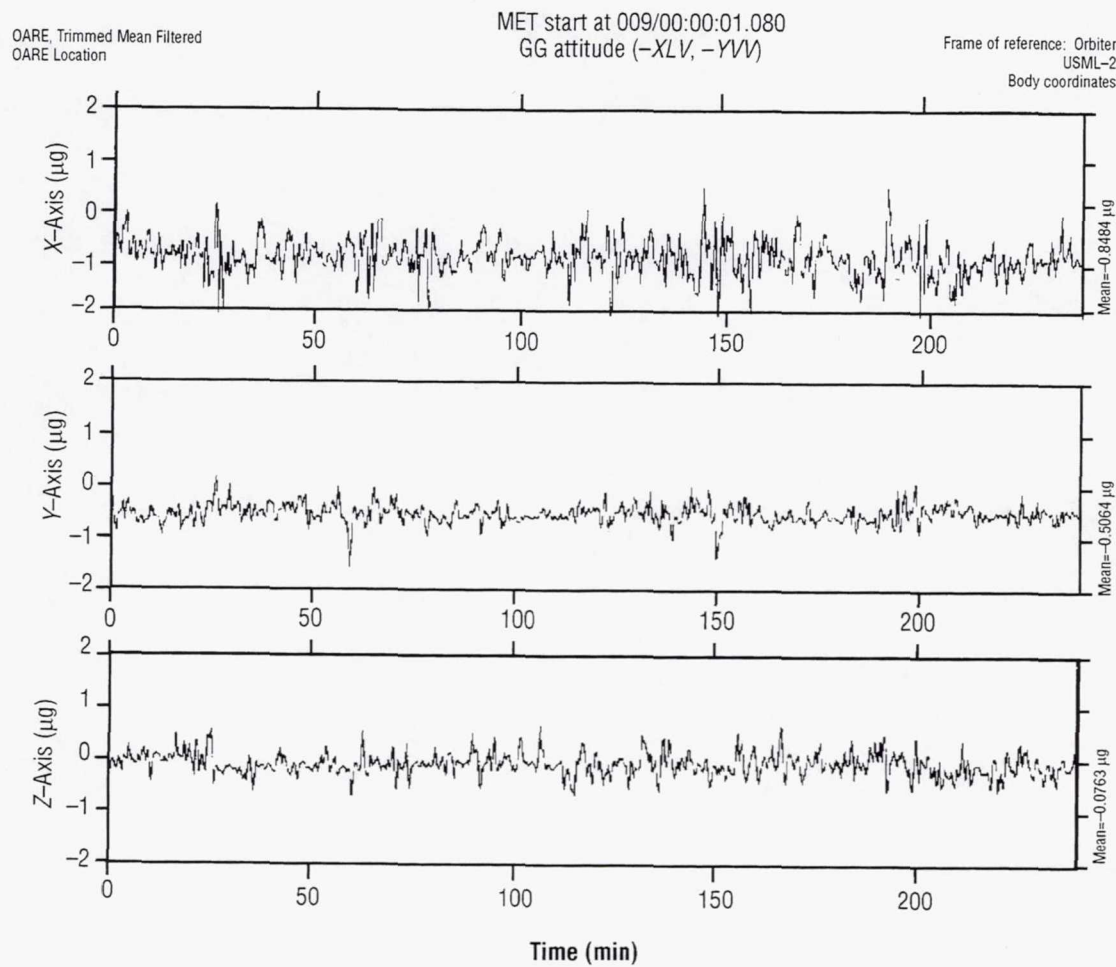


Figure 7. Trimmean filter OARE data for period when *Columbia* was in the GG attitude.

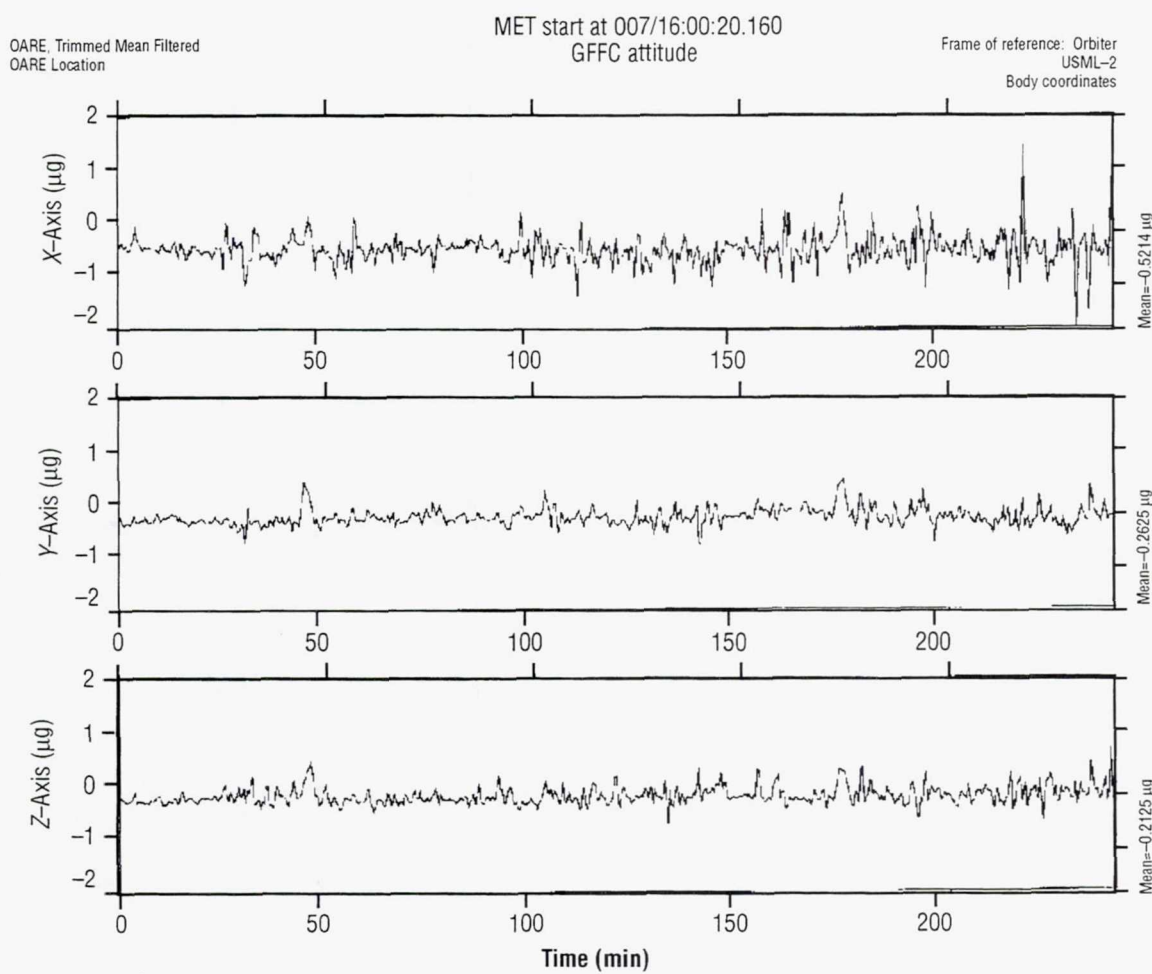


Figure 8. Trimmean filter OARE data for period when *Columbia* was in the GFFC attitude.

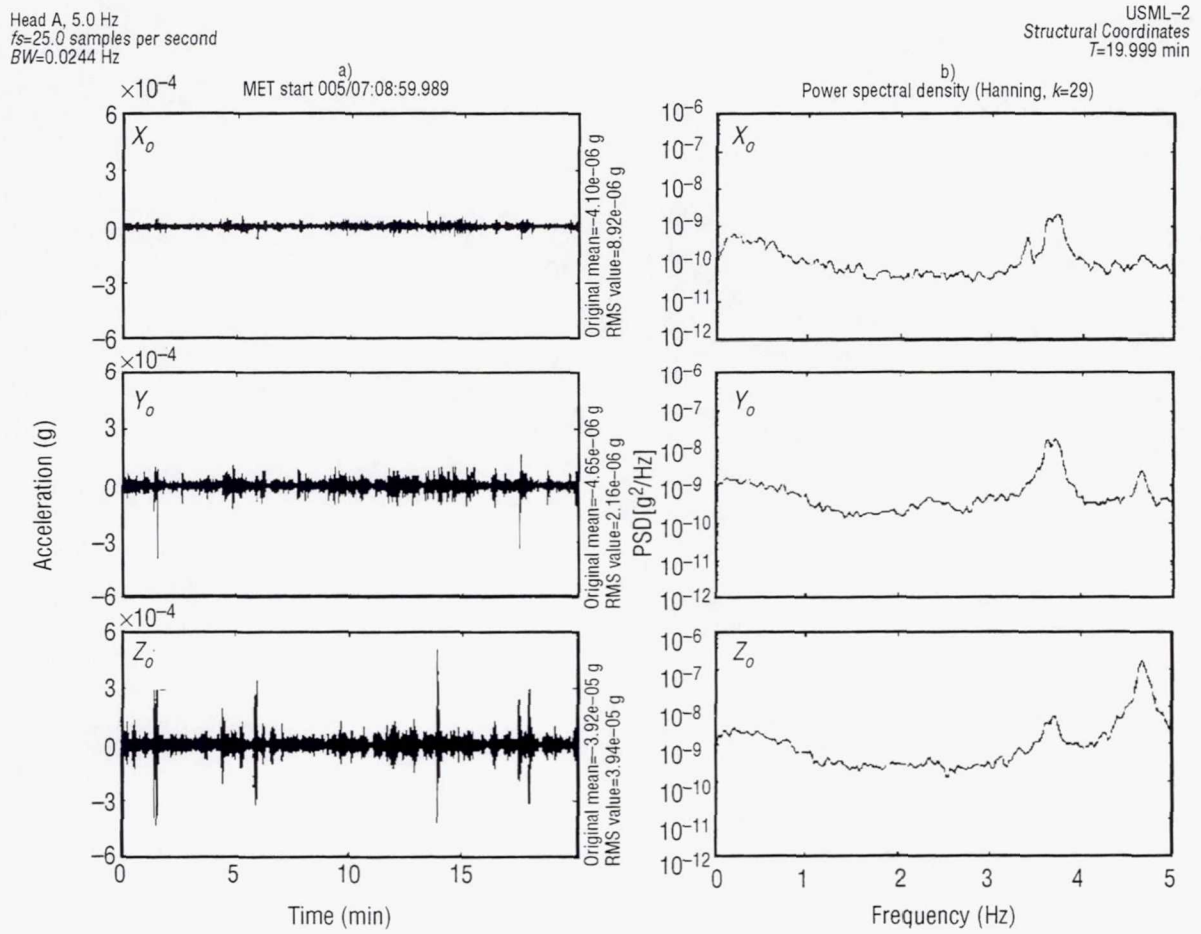


Figure 9. SAMS TSH A data for crew quiet period. (a) Time history; (b) PSD.

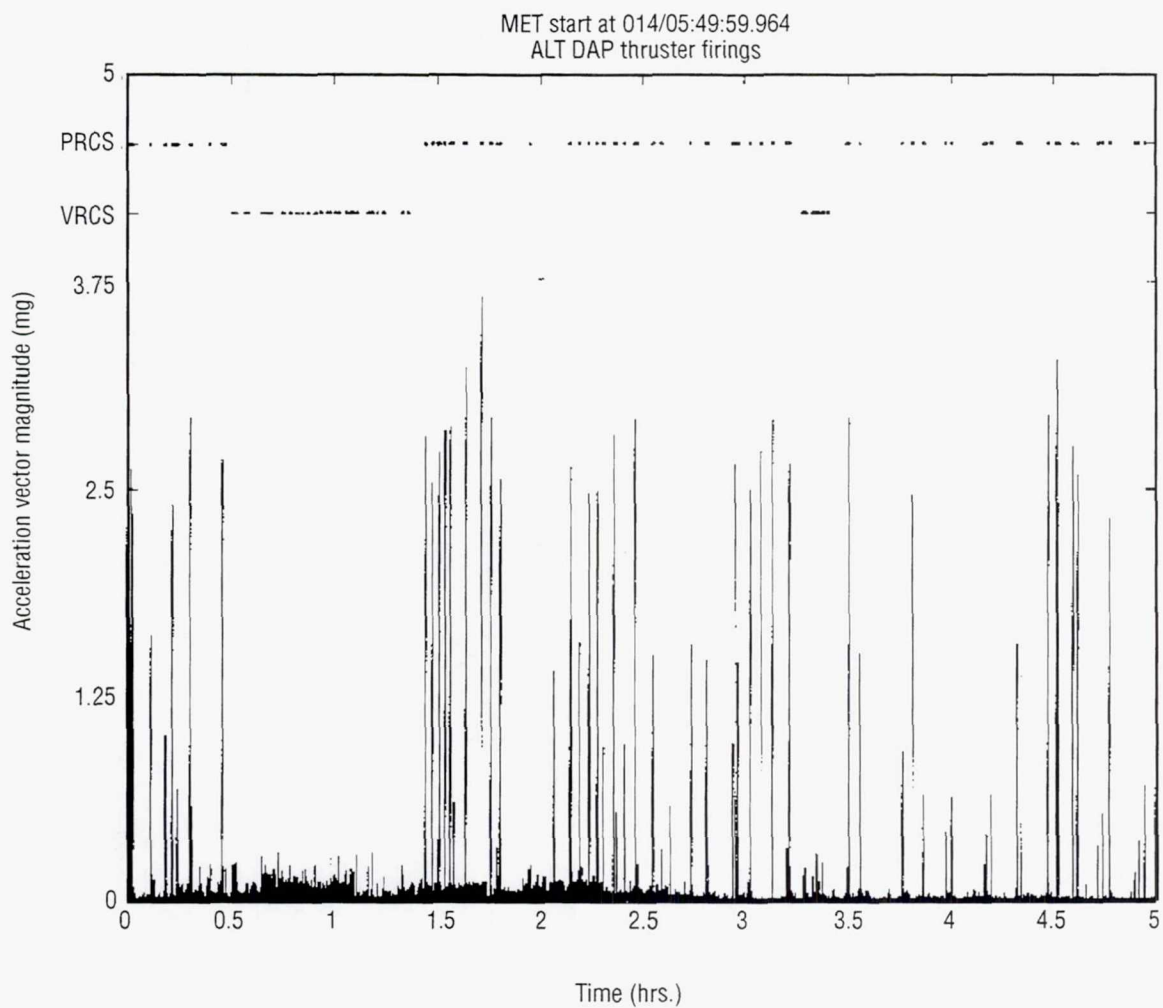


Figure 10. SAMS TSH B data vector magnitude for 5-hour period. PRCS and VRCS jet firings are indicated across top of plot.

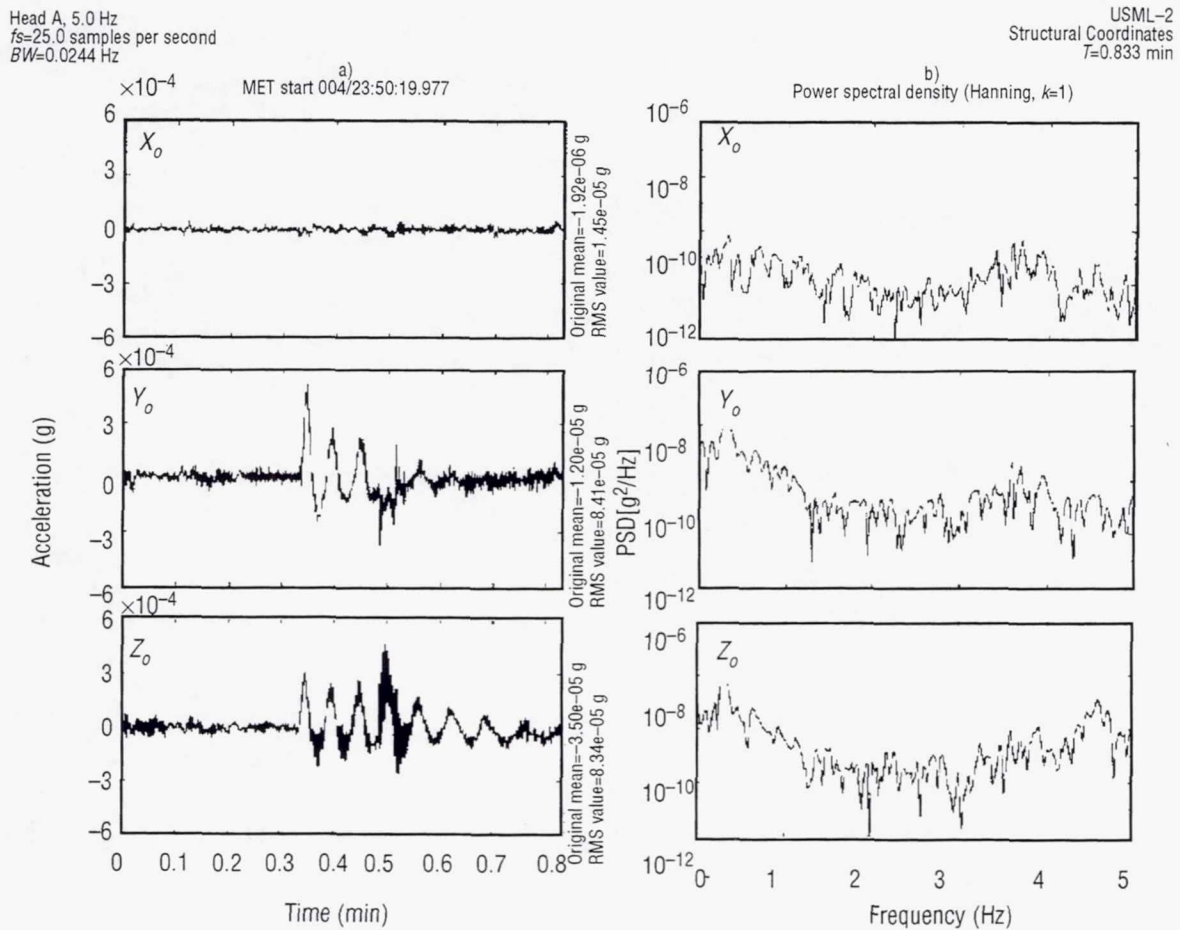


Figure 11. SAMS TSH A data during payload bay door opening motion. (a) Time history; (b) PSD.

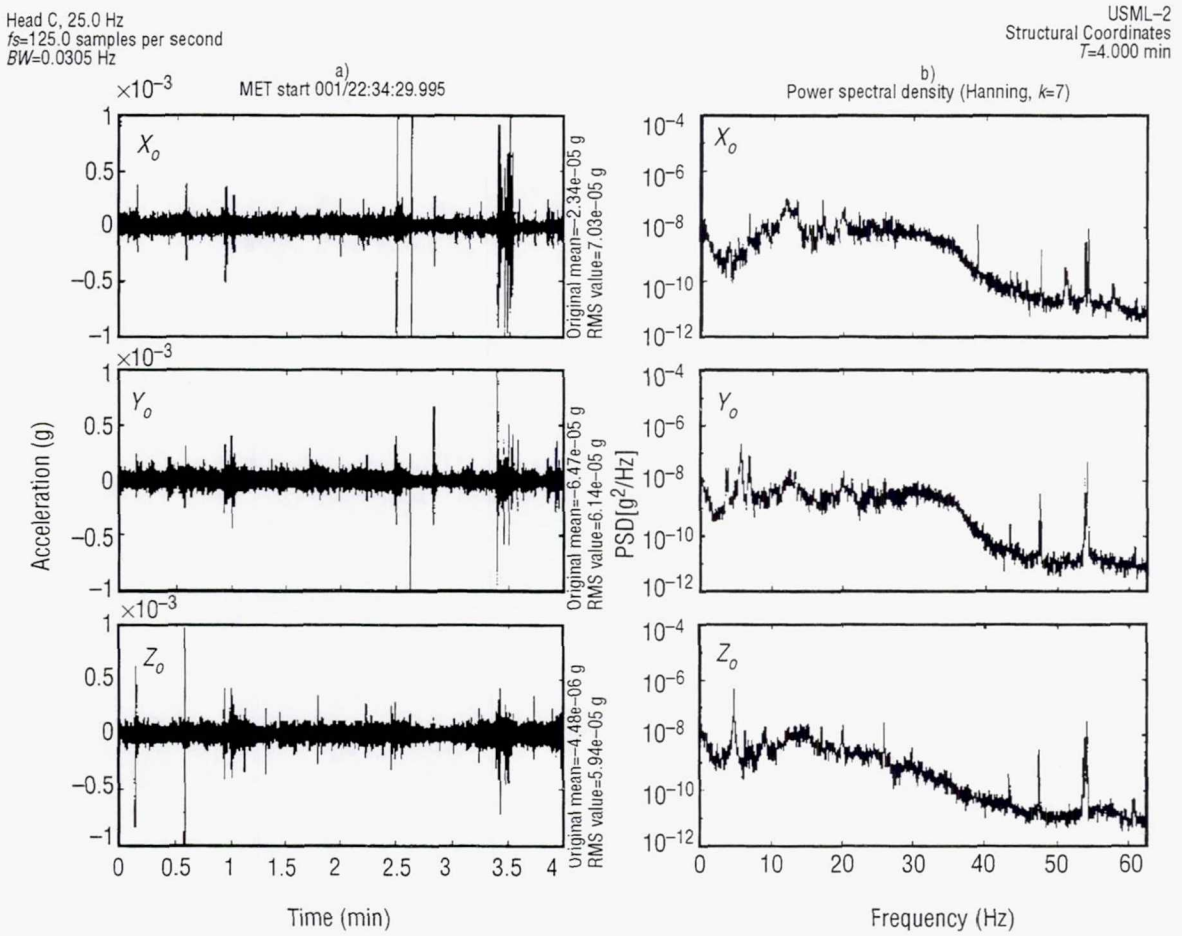


Figure 12. SAMS TSH C data during Glovebox fan operations. (a) Time history; (b) PSD.

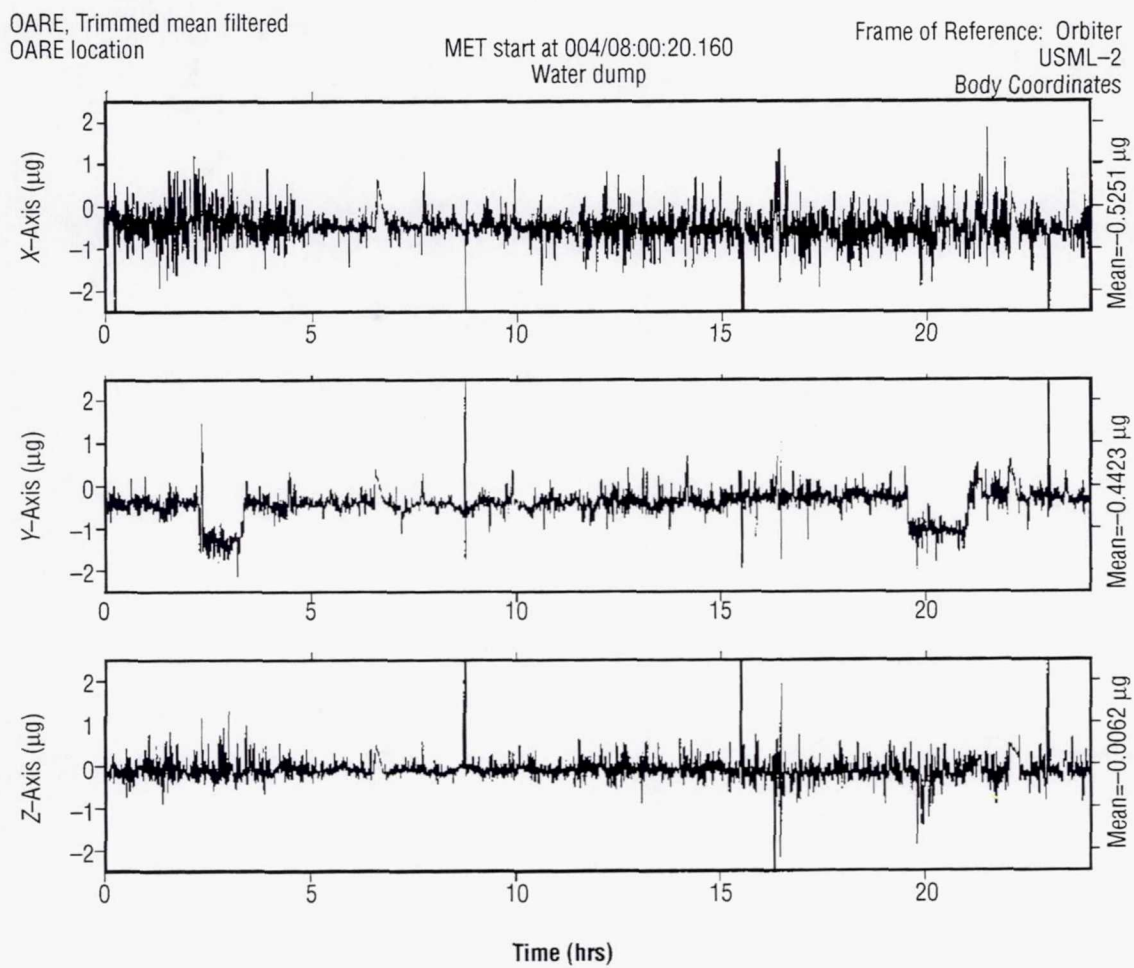


Figure 13. Trimmean filter OARE data showing the effects of two water dump operations.

Page intentionally left blank

EXPERIMENT XXXVII.

**3-DMA ACCELERATION MEASUREMENT
ON USML-2/STS-73**

Page intentionally left blank

3-DMA ACCELERATION MEASUREMENT ON USML-2/STS-73

Jan A. Bijvoet

Philip D. Nerren

Consortium for Materials Development in Space
University of Alabama in Huntsville
Huntsville, AL 35899

Phone: 205-890-6620

Fax: 202-890-6791

E-mail: bijvoetj@email.uah.edu

ABSTRACT

A model of the Consortium for Materials Development in Space (CMDS) Three-Dimensional Microgravity Accelerometer (3-DMA) was flown to further validate new system designs and to support the USML-2 mission. The design comprised, among others, the following: downlinking of all microgravity data in true real-time; distribution of the real-time data in the Payload Operations Control Center (POCC); simultaneous and continuous acceleration data in three frequency ranges from all accelerometers at all locations; real-time frequency spectra; use of hard disk drives; recording of automatic data for the full mission, not demanding crew actions; new invertible accelerometers design for measurement of quasi-stationary disturbances; panoramic data display; and low-cost marketable system.

The above designs have been validated. It has also been acknowledged that a true real-time down-link of acceleration data is very valuable to PI's, if not mandatory. The system performed as designed for 5 days after which the automatic switchover to drive No. 2 failed to take place due to a software transfer error. This error existed premission and has been corrected. However, the automatic switchover had been performed correctly at two previous STS/SpaceHab missions.

A few examples are given of the data recorded and the frequency spectra derived. Analysis of the invertible accelerometer data will be published separately.

1. INTRODUCTION

Material processing at very low levels of gravity requires knowledge of the microgravity environment of the materials for the following reasons:

- Determining which levels of low acceleration are actually needed, and
- Reproducing and maintaining the correct environments in flight for materials manufacturing.

The CMDS, one of the NASA- and Industry-sponsored Commercial Space Centers (CSC) which is administered by the University of Alabama in Huntsville (UAH), developed the 3-DMA in support of the two following objectives:

- Provision of a low-cost marketable system. To be commercially successful, processing and manufacturing of materials in space needs to be cost-effective; therefore, low-cost instrumentation is required.
- Validating a novel, low-cost mapping system for space station for the quasi-stationary microgravity disturbances. Under the "IN-STEP" technology program, directed by the NASA Langley Research Center, a development program had been undertaken earlier by UAH aimed at providing a small number of fixed acceleration sensors at widely separated locations in a space station and deriving by computer calculations the acceleration environment at any of the experiment locations without the need to mount a large number of accelerometers.

In the past, the CMDS has flown different versions of the 3-DMA on three SpaceHab missions and six sounding rocket flights.

The USML-2 mission is the second flight of U.S. microgravity experiments in the Spacelab onboard the Space Shuttle.

2. 3-DMA TEAM

The following were the 3-DMA team members:

- Jan A. Bijvoet-Principal Investigator (PI)
- Philip D. Nerren-system integration and data display
- Gregory Tyler and Stephen B. Collins-machining
- John R. Blakely-novel data display software

The following were the 3-DMA team consultants:

- Jeffrey A. Randorf, TSD Consultants-invertible accelerometer
- Lauritz D. Larsen, Applied Astronautics-software
- John Weber, Orbital Sciences-signal conditioning-and telemetry-electronics
- Lyle B. Jalbert-software systems

3. 3-DMA MISSION OBJECTIVES

The specific objectives of the mission of the 3-DMA on the second USML-2 were threefold:

- 1) Providing and validating a full-performance, low-cost, marketable 3-DMA system consistent with the goals of the CSC.

2) Further validating the following new designs—

- Downlink in true real-time of acceleration data from all onboard locations to the ground and distribution in the POCC to PI's and mission scientists.
- The simultaneous and continuous measurement, provision and recording of acceleration data in three frequency ranges from all accelerometers.
- Fully automatic data recording on board for the duration of the mission; no routine crew actions required.
- Using hard-disk drives for data recording onboard.
- A novel, low-cost "Invertible Accelerometer System" for the continuous measurement of absolute acceleration by the continuous elimination of the bias errors inherent to all accelerometers. Continuous elimination of the bias errors is required for the correct measurement of constant and very low-frequency quasi-stationary disturbances.
- Presentation of all multilocation and multifrequency data on a novel panoramic data display, permitting full mission scanning in a short time.
- Provision of expanded scale presentations and frequency spectra by electronic mail upon request.

3) Support to the mission and the PI's by—

- Providing on-the-ground true real-time acceleration data enabling PI's to schedule experiment runs after the dying out of the effects of transients or to schedule a sample rerun.
- Providing simultaneously from each 3-D head three frequency ranges for each accelerometer, thereby obviating the limitation and need to select a specific frequency range per experiment before flight.
- Provision of a novel panoramic data display and dissemination by a single 8 mm DAT tape or on the Internet, permitting full mission scanning in a short time.
- Provision of frequency spectra of the real-time data as requested.

4. THE 3-DMA SYSTEM IN SPACELAB

3-DMA systems are flown in different configurations of larger or smaller extent depending on needs, platform facilities, and space. Since the USML-2 mission, significant further extensions have been made on the 3-DMA complement. The configuration flown on the USML-2 mission comprised three 3-D Remote Units, three single-axis invertible accelerometers, three hard-disk drives, and a real-time data downlink.

The elements of the 3-DMA system and their integration with Spacelab are shown in figure 1. The main elements were located as follows:

- A Central Unit (CU), located in the central aisle and comprising:
 - Three single-axis invertible accelerometers
 - A data processor
 - Three hard-disk drives for data storage
 - Data downlink electronics
 - Power conditioning electronics
- Three Remote Units (RU), each comprising three accelerometers in an orthogonal mounting arrangement, signal conditioning electronics, and power distribution circuits. The RU's were located as follows:
 - RU-1: on starboard side, in Rack 8 on the inside of the 45-degree slanted rack top-backside.
 - RU-2: on port side, in Rack 5 on the inside of the 45-degree slanted rack top-backside.
 - RU-3: under the Spacelab subfloor in the center backside of the laboratory.

Detailed pictures of the CU and the RU as mounted are shown in figures 2 through 5.

5. 3-DMA CHARACTERISTICS

The functions of the 3-DMA elements as flown on the USML-2 mission are:

- Measurement of microvibrations and transients with three 3-Dimensional Remote Units.
- Measurement of absolute acceleration and quasi-stationary disturbances with three single-axis invertible accelerometers.
- All measurement units use Allied Signal type QA-3000-10 accelerometers.
- The signal conditioning electronics for each accelerometer generate at each location and for each measurement-axis, simultaneously and continuously, three information channels with frequency bands and measurement sensitivities corresponding to the spectrum and levels of disturbances nominally encountered on Space Shuttle missions.

On the USML-2 mission the channel characteristics for each accelerometer were as follows:

Table 1. Channel Characteristics

Channel	Frequency Band	Estimated Noise Level	Maximum Range
Fine	0 to 13 Hz*	0.6 μ g	1 milli-g
Medium	0 to 24 Hz*	1.1 μ g	10 milli-g
Coarse	0 to 80 Hz*	4.0 μ g	-12 g to +8 g (for ascent)
	*/Double pole		

- Sampling rate: 45 samples per second, all channels.
- Total number of analog acceleration, temperature, and status channels: 58.
- Automatic onboard data recording on three Seagate hard-disk drives of all analog channels. Recording capacity: 3×4.3 GB.
- Automatic switchover between drives. No crew actions needed. No interruption of operation during module close down for extravehicular activities.
- Telemetry to the ground of all acceleration, temperature, and 3-DMA system status channels. Available downlink bandwidth: 150 kHz.

During periods of loss-of-signal (LOS), all channels were recorded on the Spacelab High Data Rate Recorder and delayed-transmitted to the ground. All data received on the ground were recorded by the POCC systems at NASA MSFC and by the 3-DMA ground computer.

- Upon PI request, up to three selected acceleration channels could be displayed on the ground and broadcast to PI's using the POCC video matrix. Alternatively, frequency spectra could be generated, displayed, and broadcast.
- Power requirements: Central Unit: 46 W average
Remote Units: 5 W each; total 3 for RU's: 15 W average

Total 3-DMA: 61 W average
- Cooling: Forced air cooling only.

6. MISSION OPERATIONS

The Space Shuttle *Columbia* was launched on October 20, 1995, at 8:52:57 a.m. CDT (or GMT 293 days, 13 hours, 52 minutes, 53 seconds) from the NASA Kennedy Space Center for Shuttle Mission STS-73. *Columbia* carried the Spacelab laboratory for a second mission of a U.S. microgravity payload (USML-2). This space mission lasted nearly 16 days. Landing took place at the Kennedy Space Center on November 5, 1995, at 5:45 a.m. (MET 15/21:52).

Orbiter crew of STS-73:	Commander: Kenneth D. Bowersox
	Pilot: Kent V. Rominger
	Mission Specialist: Catherine G. Coleman
	Mission Specialist: Michael E. Lopez-Alegria
	Payload Commander: Kathryn C. Thornton
	Payload Specialist: Fred W. Leslie
	Payload Specialist: Albert Sacco, Jr.
	Alternate Payload Specialist: David H. Matthieson
	Alternate Payload Specialist: R. Glynn Holt

3-DMA was turned on by the crew on MET 00/06:55. No other actions by the crew were needed until switch off prior to termination of Spacelab operations and orbiter return. 3-DMA system design included automatic switchover of the data recording from a full hard-disk drive to the next hard disk drive.

To ensure minimal eventual loss of 3-DMA data on this mission, the crew was asked to perform a "monitor" action approximately every 12 hours (i.e., once per crew shift). The monitor action essentially recycled the processor and also effectuated a status check. During testing on the ground, there had been an occasional problem with retrieving data files. After the mission, it was found that no such data files were lost.

In parallel to recording on board, all acceleration data were transmitted in real time to the ground and routed to the POCC at the NASA Marshall Space Flight Center. These data were recorded on the ground by 3-DMA Ground Support Equipment and also by the POCC systems. Three selected channels were broadcast by the 3-DMA ground system to USML-2 PI'S and the mission scientist via the video matrix of the POCC.

The 3-DMA ground system allowed the generation of concurrent frequency spectra from the real-time data and transmission on the video matrix.

During the periods of LOS, the 3-DMA microgravity acceleration data were recorded onboard by the Spacelab High Data Rate Recorder (HDDR). After reacquisition of the orbiter signal, the recorded data from the HDDR were transmitted to the ground in parallel with the current real-time data. This second stream of data was recorded by the POCC systems and could be called up by the 3-DMA ground support systems.

Microgravity data were received on the ground immediately following activation. For the first three days, the ground data were frequently interrupted and/or showed large spikes. The problem was traced to faulty cabling in the POCC. After that, the data received were of excellent quality. Data analysis after the mission showed that the onboard data were uninterrupted and had no spikes from data errors.

Data reception on the ground was interrupted after 5 days. The telemetry link to the ground was suspected, and the crew was asked to reseat connectors. Investigation after the mission showed that the 3-DMA telemetry link had worked correctly. The data interruption was caused by a software error which prevented the data recording system from selecting the next drive for continued recording and reinitiation of the operation software. However, the automatic switchover between drives had been validated before at two previous Space Shuttle/SpaceHab missions.

Invertible accelerometer data were also received on the ground for the first 5 days. Due to the frequent data interruptions and voltage spikes at the HOSC, no absolute g levels could be obtained the first 3 days. After that, the absolute g levels, as derived by the 3-DMA ground systems from the acceleration data received, converged to low-g values. The low levels obtainable were limited by the LOS periods. Further analysis requires further processing of the onboard recorded data. The results of this analysis for the invertible accelerometers will be published separately.

7. RESULTS, EXAMPLES OF DATA, AND ANALYSIS

7.1 Validation of New Technologies

One of the primary objectives of the 3-DMA mission on STS-73 was the validation of several new designs. The data obtained validated the following:

- Telemetry in real time (the transmission delay from orbiter to the ground and from HOSC data buffering is displayed by the 3-DMA together with the acceleration data) of the data from all accelerometers to the ground and dissemination of a selectable set of channels to the PI's and the mission scientist via the video matrix of the HOSC. All 64 channels of data were received; 36 of these contained acceleration data from three remote units each with three accelerometers and from three invertible accelerometers, each with one accelerometer. Each of the accelerometer signal conditioning circuits generated three different acceleration data channels. The other channels carried accelerometer temperature information, invertible accelerometer orientation indications and central unit housekeeping data.
- Generation of three different acceleration information channels from each accelerometer and providing these channels continuously and simultaneously. The three channels per accelerometer have different bandwidths and corresponding increases in measurement sensitivities. The bandwidths and sensitivities are matched to the spectrum and level of microgravity disturbances usually encountered on STS missions.
- Display upon request of the frequency spectrum of any of the real-time data channels received (dubbed "a flying FFT") and forwarding on the video matrix.
- Novel panoramic display, permitting an overview of all data simultaneously from four locations: Rack 5, Rack 8, Subfloor, and Central aisle, including display of the different frequency bands and for the orbiter X-, Y-, and Z-axes.
- Operation of a prototype invertible accelerometer. Data were obtained and recorded on board. A report on the analysis of the invertible accelerometer data will be issued separately.
- Full acceleration measurement performance with a low-cost system.

Note: Automatic transfer of data recording after 5 days from the first hard-disk drive to the second did not take place due to a preflight existing software error. However this automatic operation has been successfully performed on two previous Shuttle/SpaceHab missions and has since been corrected.

7.2 Nominal Disturbance Levels

A typical panoramic display of microgravity disturbances is shown in figure 6. Each of the subplots shows a 10-minute recording period. Separate plots are shown for the X -, Y -, and Z -axes for each of the RU's. The start and stop times are shown for GMT and MET. The three frequency channels are shown simultaneously: fine channel = green; medium channel = blue; coarse channel = red (see the section on 3-DMA characteristics). The vertical scale for the acceleration level is in volts because three levels of sensitivity are displayed simultaneously. The correspondence is as follows:

Fine Channel: $5 \text{ V} = 1 \text{ mg}$

Medium Channel: $5 \text{ V} = 10 \text{ mg}$

Coarse Channel: 2 g/V and a zero offset of -1 V .

Expanded plots, together with the Fast Fourier Transform for the corresponding frequency content of the disturbances for a typical period for remote unit (RU) -1, X -, Y - and Z -axes and similarly for RU-2 and RU-3, are shown in figures 7 through 15. All plots are for the medium channel so that the frequency content in the range of 0 to 22 Hz can be derived reliably without aliasing. The frequency content can be filtered if desired. Filtering applied is shown in the top, right-hand corner of the plot. The filtering, if any, is applied to the time plot. Also shown is the root-mean-square (rms) value of the acceleration signal in g. The vertical scale is in g. As a verification, the plots show the usually detected disturbance from the Ku-band antenna jitter at 17 Hz.

A comparison of typical nominal rms values for the different locations and different axes is given in the table below:

Table 2. Nominal rms values acceleration, medium channel (all values in g).

	X -axis	Y -axis	Z -axis
RU-1/Rack 8	$4.3 \text{ E-}5$	$5.9 \text{ E-}5$	$7.0 \text{ E-}5$
RU-2/Rack 5	$4.1 \text{ E-}5$	$8.6 \text{ E-}5$	$8.2 \text{ E-}5$
RU-3/Subfloor	$1.8 \text{ E-}5$	$1.8 \text{ E-}5$	$1.2 \text{ E-}5$

It can be noted from this table that the disturbances as detected by RU-3, which is rigidly mounted on the subfloor, are considerably smaller than those measured by RU-1 and RU-2, which are mounted on the topsides of the racks. It appears that the flexible and possibly resonant racks cause larger vibrations of elements in the racks than Spacelab subsystems mounted on the subfloor.

Transients from orbiter thruster firings of the reaction control system occur regularly and throughout the mission. These transient levels are typically about $10 \text{ E-}3 \text{ g}$ or $1000 \mu\text{g}$. Figures 7 through 15 and the expanded frequency scale plot of figure 34 show that the orbiter's natural vibration frequencies are prominent at 3.6 and 4.7 Hz.

7.3 Glovebox Fan Disturbances

At MET 01/14:50, the 3-DMA operator on watch noted a large disturbance on RU-2 in Rack 5, Y- and Z-axes, alerted the mission scientist and asked for correlation with an event. When PI's raised concerns, the crew was alerted and a crew member, Kathie Thornton, reported that the Glovebox air circulation system had been operated (fig. 29). To verify that one or both of the Glovebox fans caused the large disturbance, the Glovebox was turned off in two steps (i.e., one fan after the other). The resulting changes in disturbance levels, as shown in figures 25 and 26, confirm the source.

Comparing the frequency spectra of figures 25 and 26 with figures 7 through 15 for nominal operations (no Glovebox or door operations) shows that Glovebox fans disturbance frequencies are around 12.5 Hz, 18.6 Hz and 19 Hz as measured in the bandwidth of the medium channel. Figure 27 shows the effect of filtering out the 12.5-Hz signal. It follows that the 12.5 Hz is associated with the first fan turned off and the 18.5 and 19 Hz signals with the second fan.

A set of data for nominal Glovebox operations is shown in figures 16 through 24. A comparison of typical rms values of the disturbances as measured in the medium channel (0 to 24 Hz) for the different locations and different axes is given in the table below:

Table 3. Glovebox fans, rms values acceleration, medium channel (all values in g)

	X-axis	Y-axis	Z-axis
RU-1/Rack 8	1.75 E-4	1.28 E-4	1.95 E-4
RU-2/Rack 5	1.65 E-4	9.90 E-4	8.67 E-4
RU-3/Subfloor	8.88 E-5	9.54 E-5	2.29 E-5

The disturbance levels at the subfloor were much lower, as expected (fig. 22 through 24).

7.4 Payload Bay Door Movements

On this mission the payload bay doors were not fully opened for reasons of protection from micrometeorites. Upon request from the mission scientist, microgravity disturbances caused by movement of the payload bay doors were observed, displayed in real time to PI's and recorded. The doors would be opened fully and, after that, partially closed again to the previous position. Door opening started at MET 04/23:49:28.

The disturbances from the door opening as recorded on board, together with the frequency content, are shown in figures 33 to 42 for RU's-1, -2, and -3 and for the three orbiter axes (station coordinates). Comparing the frequency spectrum for a nominal period (without door movements or Glovebox fan operations, etc.) with that for the door movement, it is clearly seen that the door vibrations (or orbiter vibrations induced by the door movement) are a spectrum of several frequencies between 0.2 Hz and 0.8 Hz. (See expanded scale frequency plot of figure 34.)

Peak-to-peak levels of the highest deviations during the door movement are shown in the table below:

Table 4. Payload bay door movement, highest peak-to-peak acceleration levels, medium channel (all values in g)

	X-axis	Y-axis	Z-axis
RU-1/Rack 8	11.0 E-4	11.2 E-4	10.9 E-4
RU-2/Rack 5	11.0 E-4	7.4 E-4	9.6 E-4
RU-3/Subfloor	4.9 E-4	6.2 E-4	3.1 E-4

Door closing commenced at about MET 05/00:26:40 and terminated at MET 05/00:27:30. The data received on the ground showed that the disturbance levels at closing were lower than at door opening (about 4 E-4 peak-to-peak). This could correlate with the procedure whereby door opening uses two motors and closing only one.

7.5 Other Operations

Figure 43 shows disturbances seen from a not yet identified Spacelab system, Spacelab experiment, or orbiter operation with a frequency of 8.5 Hz.

6. CONCLUSION

New 3-DMA systems designs were further validated on this mission. Real-time microgravity data from four locations in Spacelab and for three frequency bands for each accelerometer were received in the POCC for 5 days and selected channels redistributed in the POCC to PI'S and the mission scientist. Also, frequency spectra were derived from the real-time data. The availability on the ground of true real-time acceleration data from several locations in the orbiter/Spacelab has been shown by the 3-DMA system to be very valuable, if not mandatory. This also applies to the frequency spectra from the real-time data. Automatic switchover of data recording on board did not take place due to a preflight existing software error but has been validated on two previous STS missions. Other new designs as listed in section 3 have also been validated. Examples of data recorded, displayed, and analyzed in section 7, show the capacity and performance of the system. Results of the invertible accelerometers operations will be published subsequently.

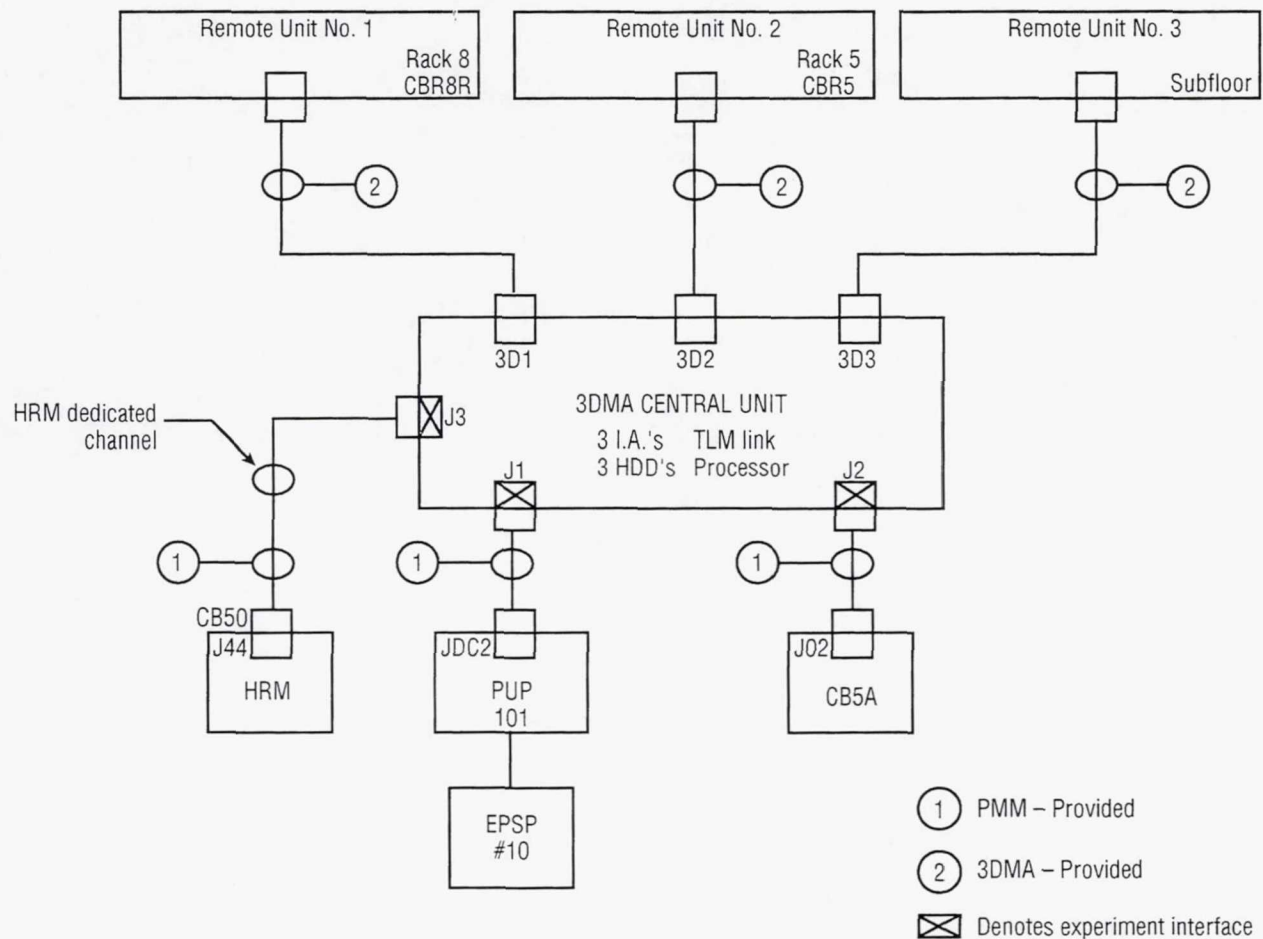


Figure 1a. 3-DMA electrical/CDMS interfaces.

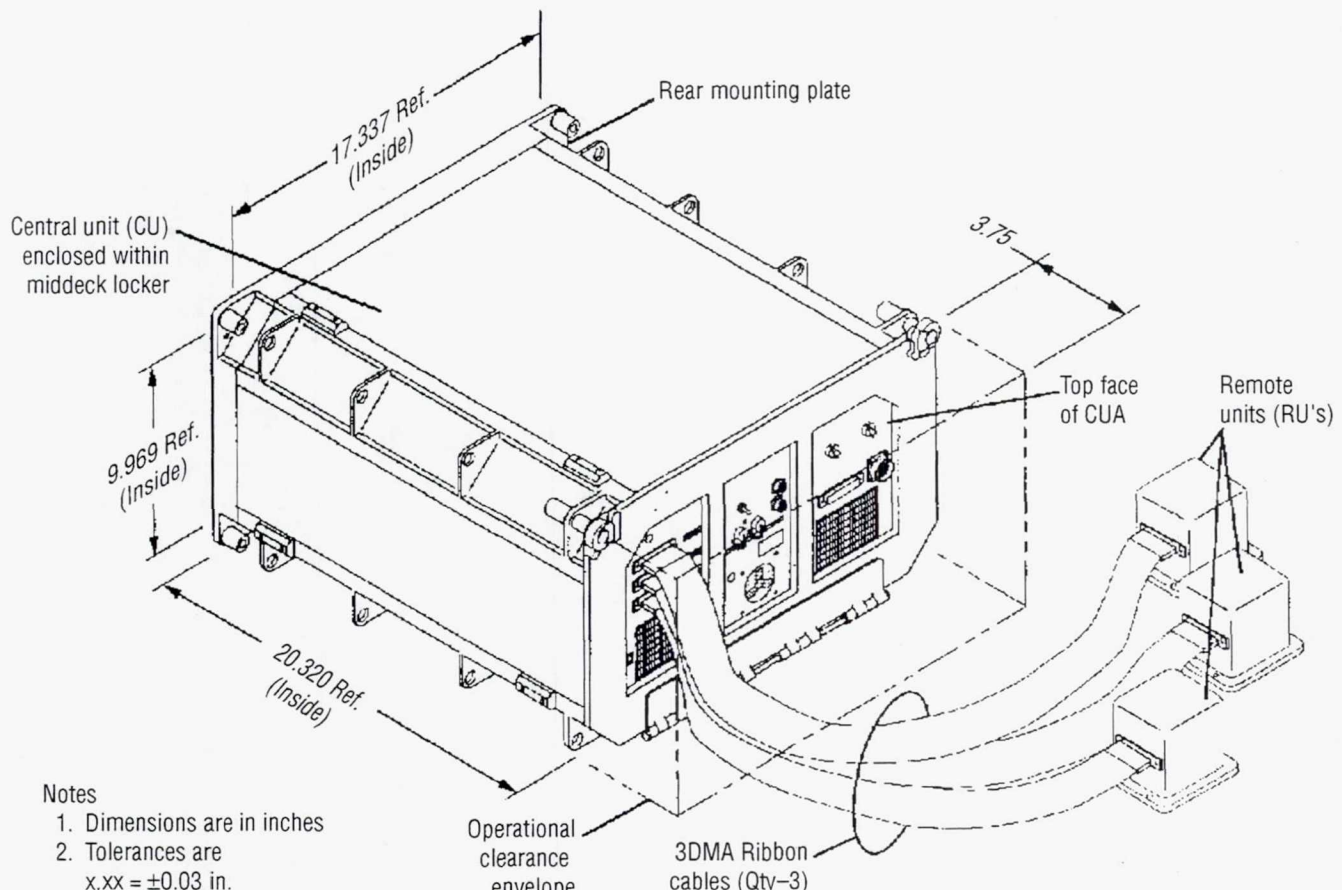


Figure 1b. 3-DMA hardware.



Figure 2. STS-73 Commander Kenneth Bowersox performs a "Monitor" operation on the Central Unit of 3-DMA.

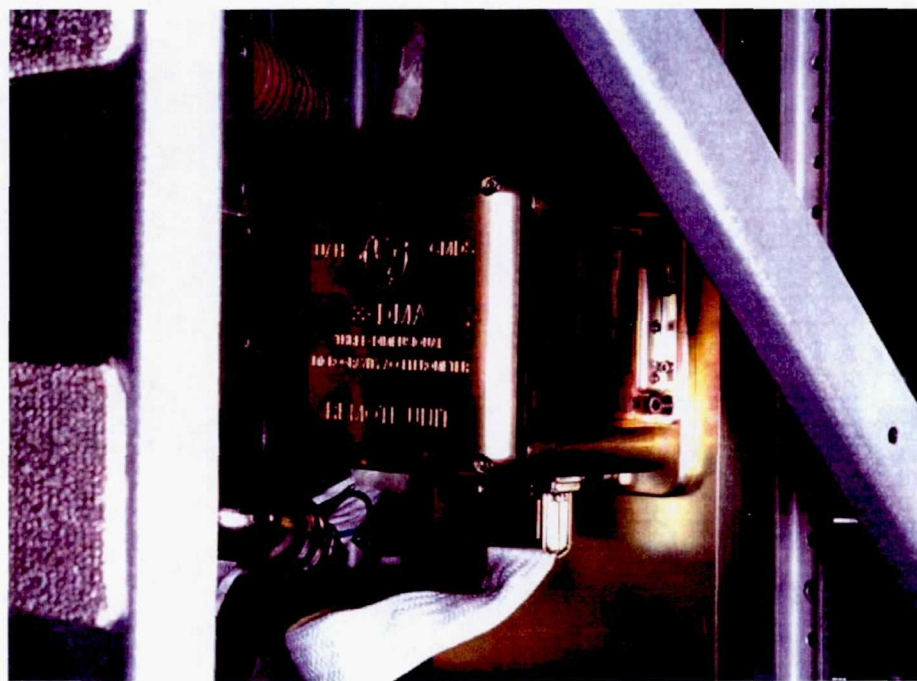


Figure 3. 3-DMA, RU-1 in rack 8, STS-73, Spacelab.



Figure 4. 3-DMA, RU-2 in rack 5, STS-73, Spacelab.

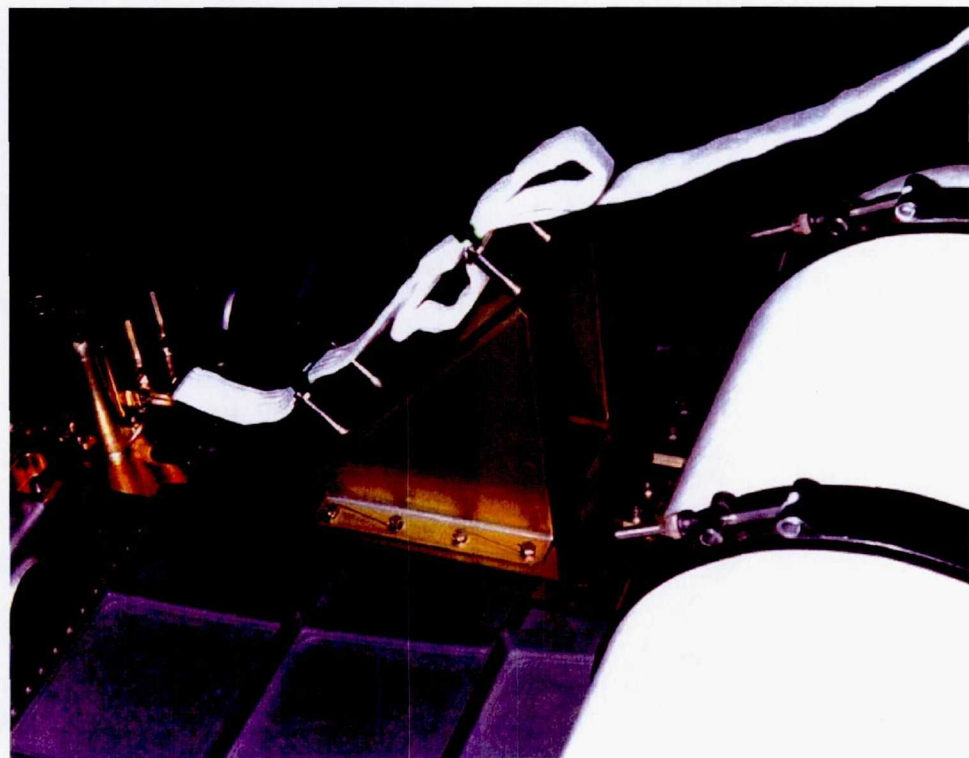


Figure 5. 3-DMA, RU-3 on subfloor, STS-73, Spacelab.

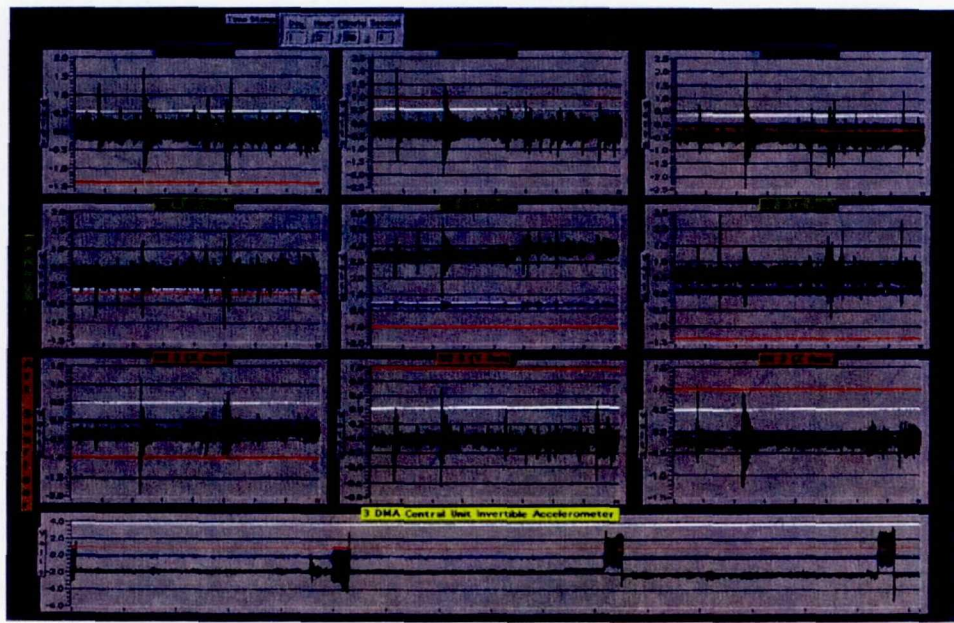


Figure 6. STS-73 mission, 3-DMA panoramic data display.

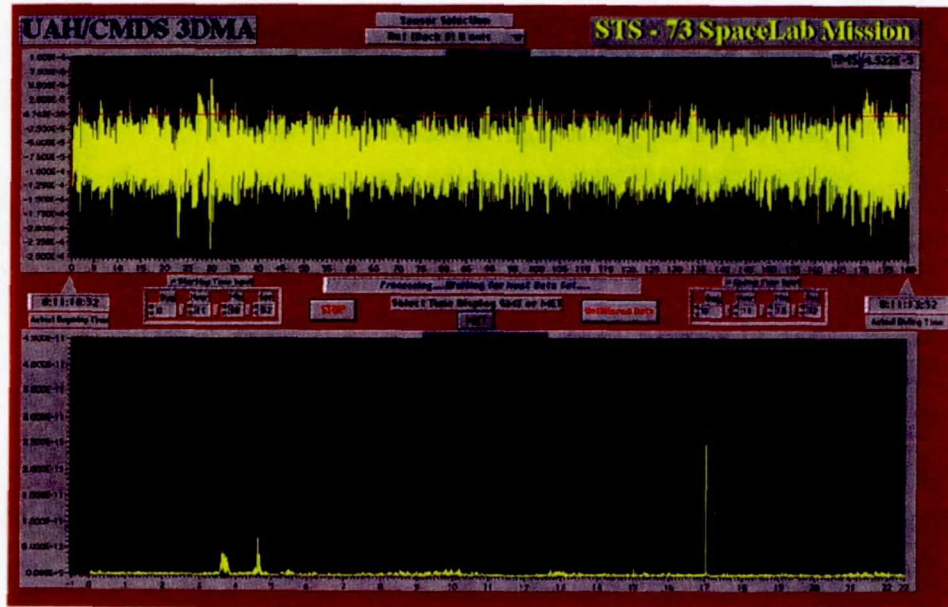


Figure 7. Nominal STS-73 disturbance levels.

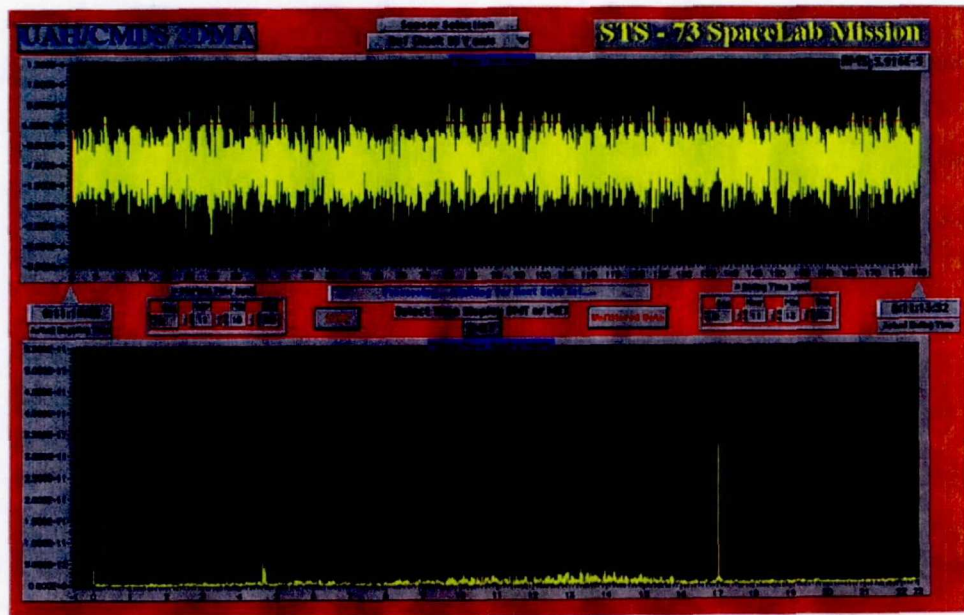


Figure 8. Nominal STS-73 disturbance levels.

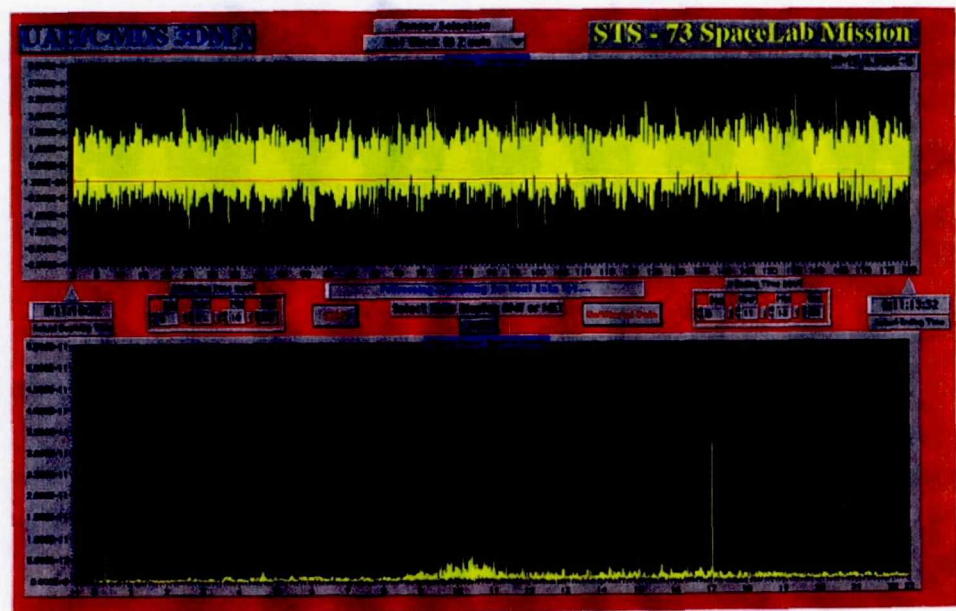


Figure 9. Nominal STS-73 disturbance levels.

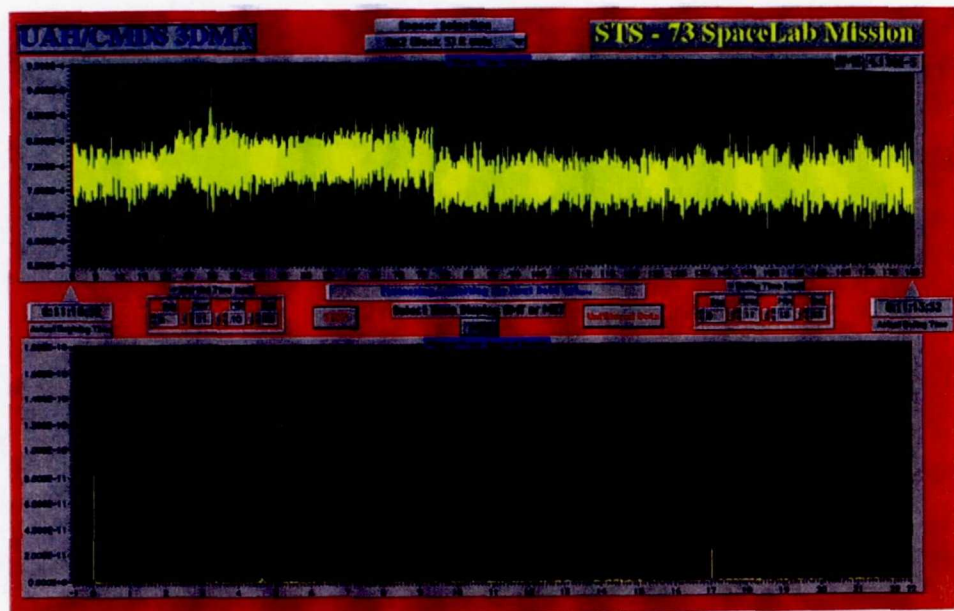


Figure 10. Nominal STS-73 disturbance levels.

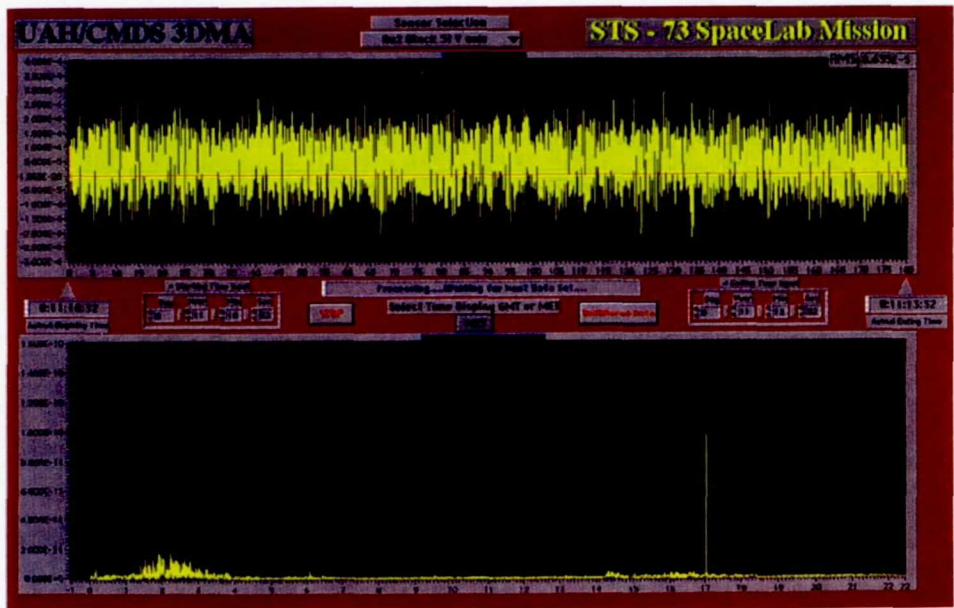


Figure 11. Nominal STS-73 disturbance levels.

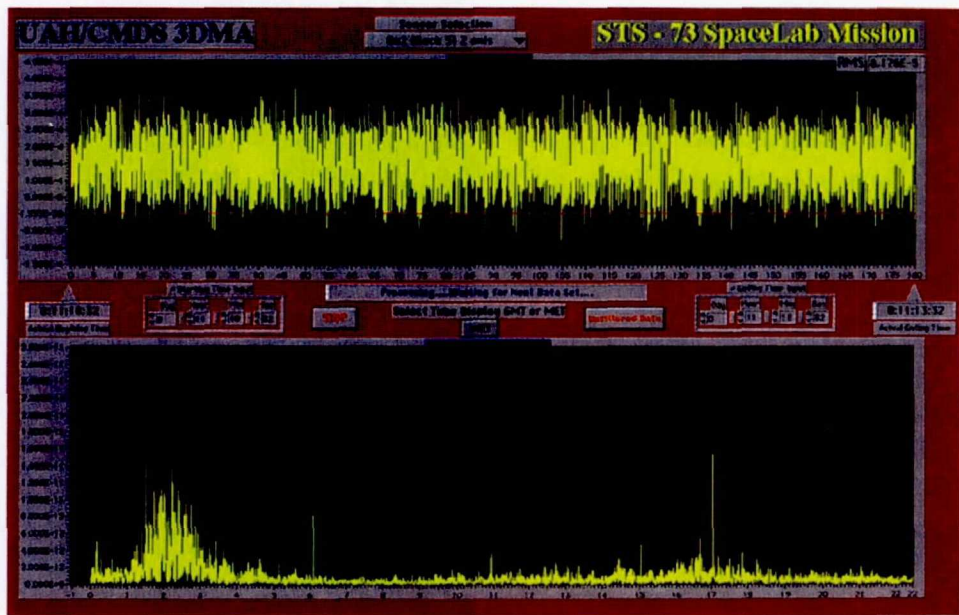


Figure 12. Nominal STS-73 disturbance levels.

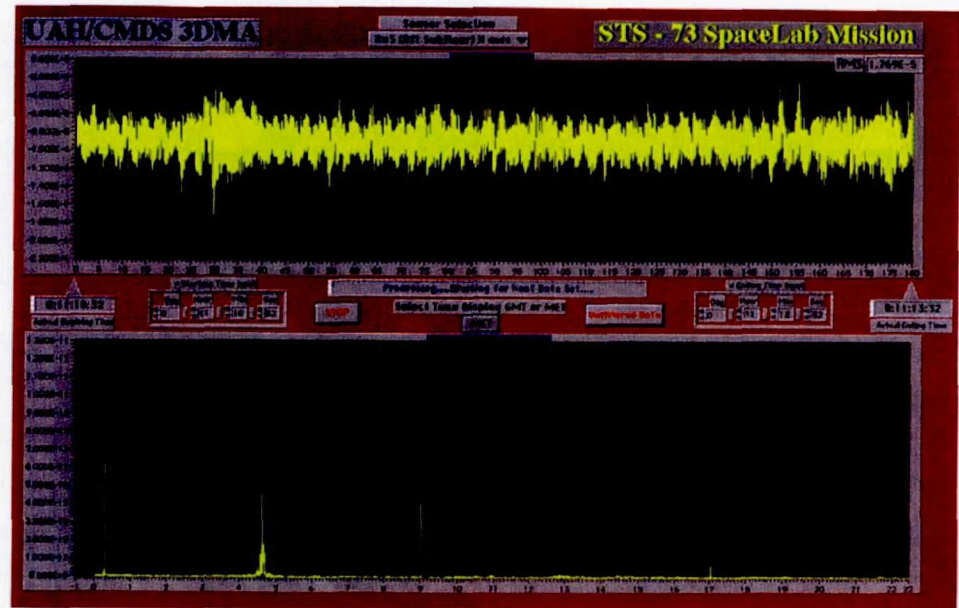


Figure 13. Nominal STS-73 disturbance levels.

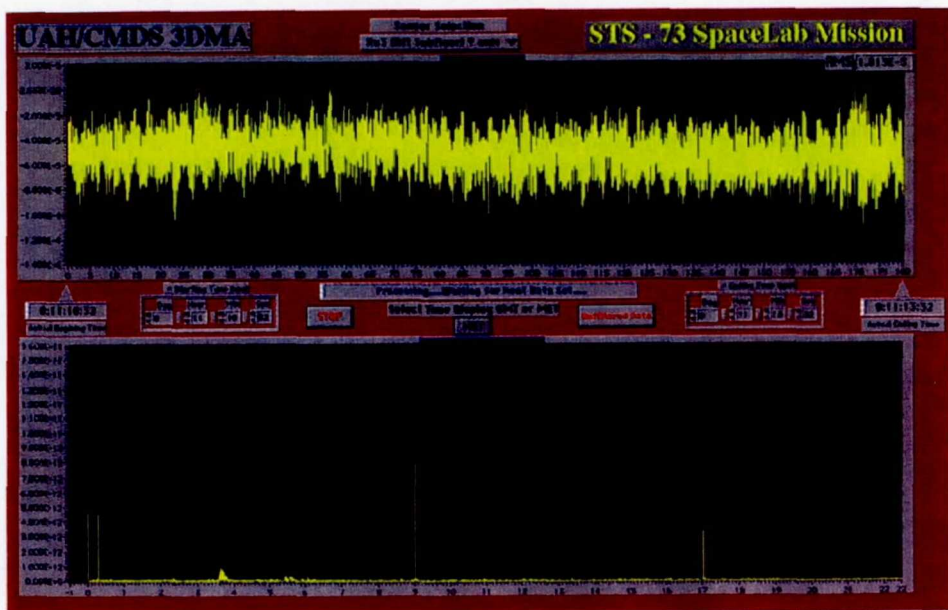


Figure 14. Nominal STS-73 disturbance levels.

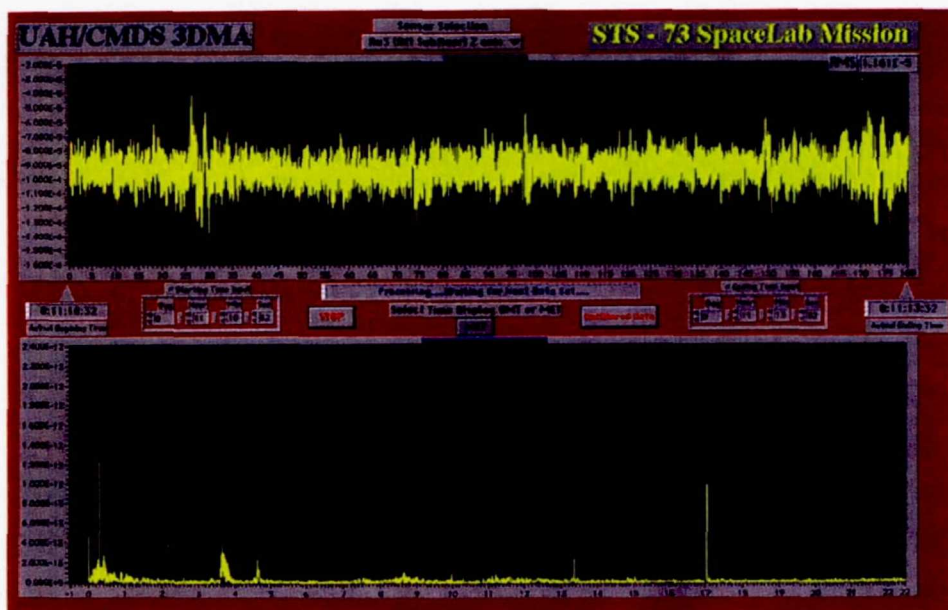


Figure 15. Nominal STS-73 disturbance levels.

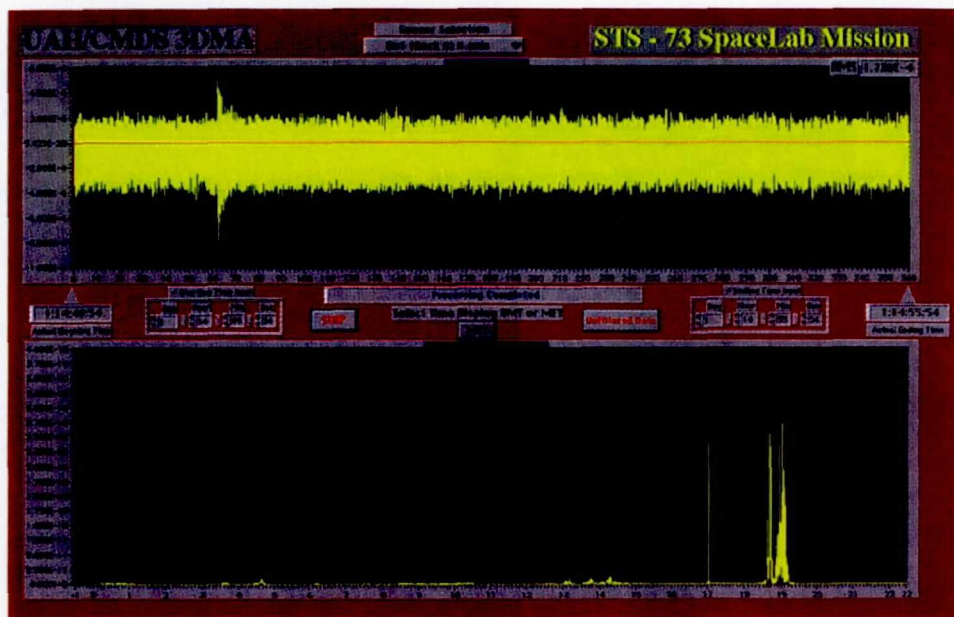


Figure 16. Glovebox nominal.

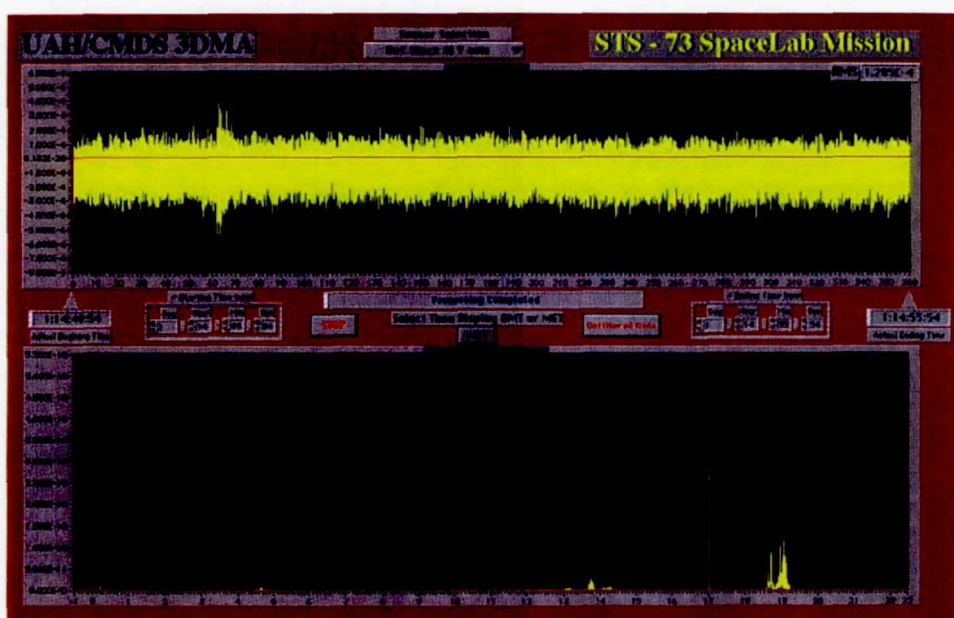


Figure 17. Glovebox nominal.

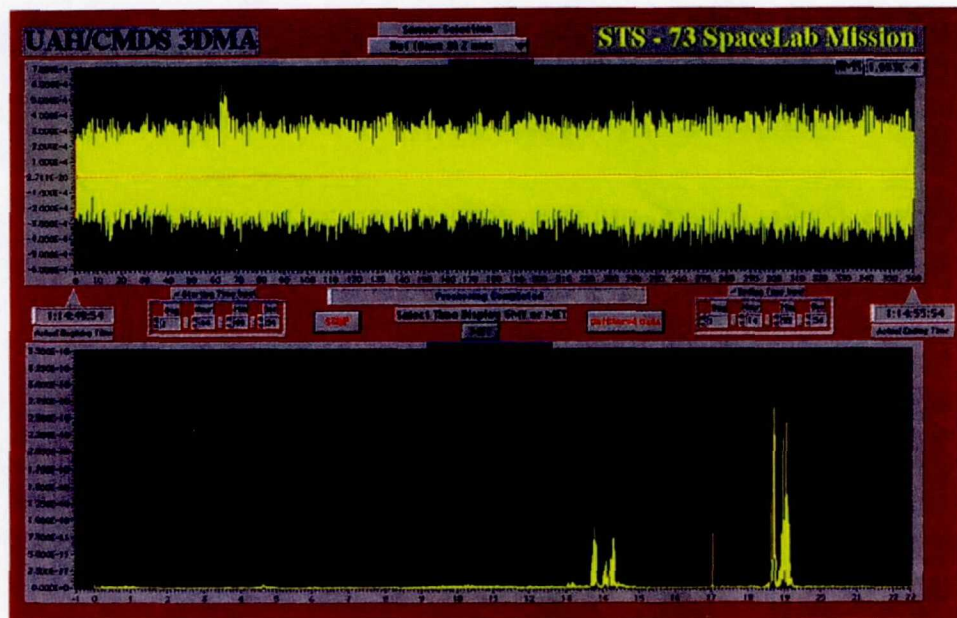


Figure 18. Glovebox nominal.

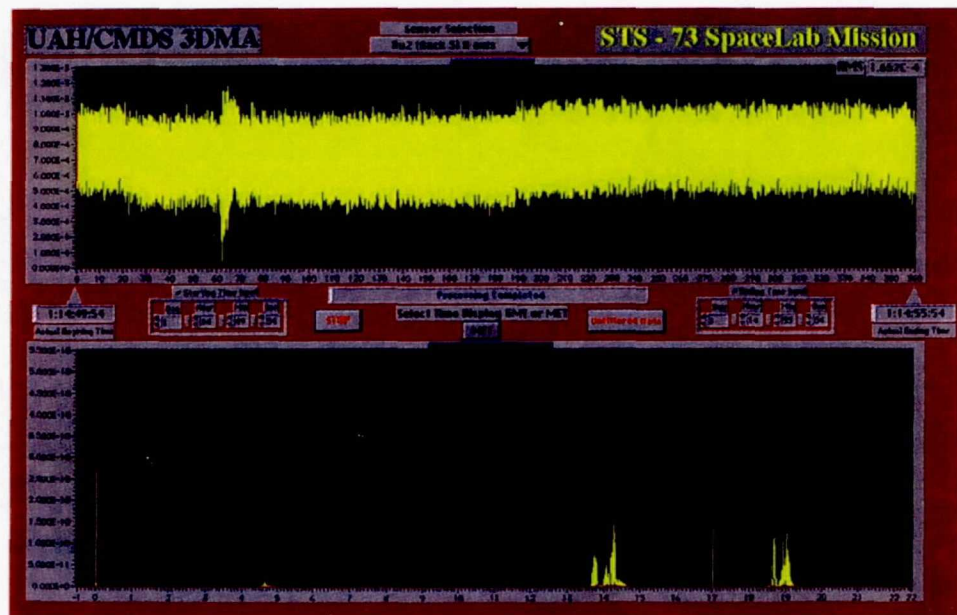


Figure 19. Glovebox nominal.

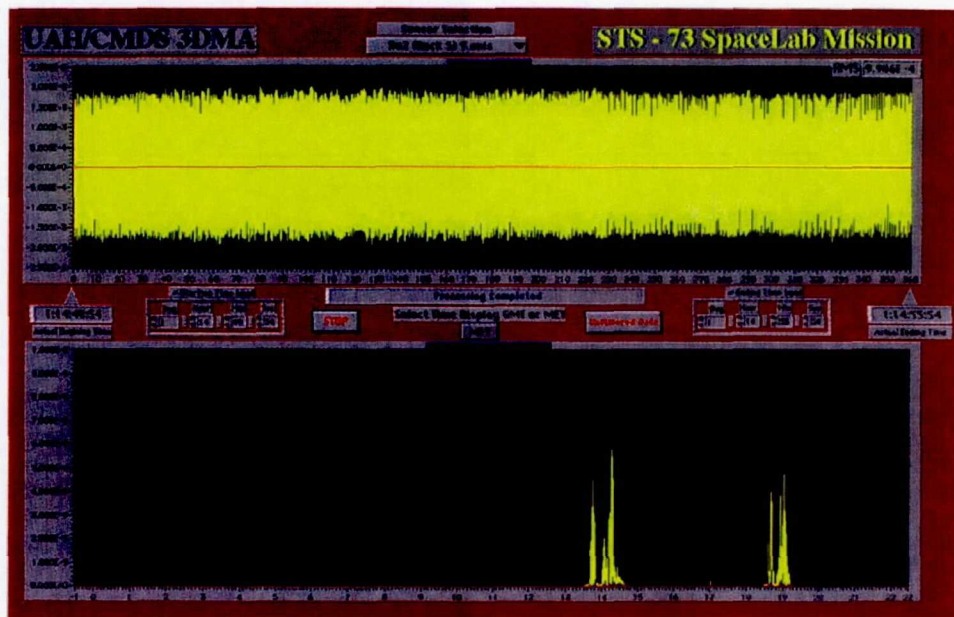


Figure 20. Glovebox nominal.

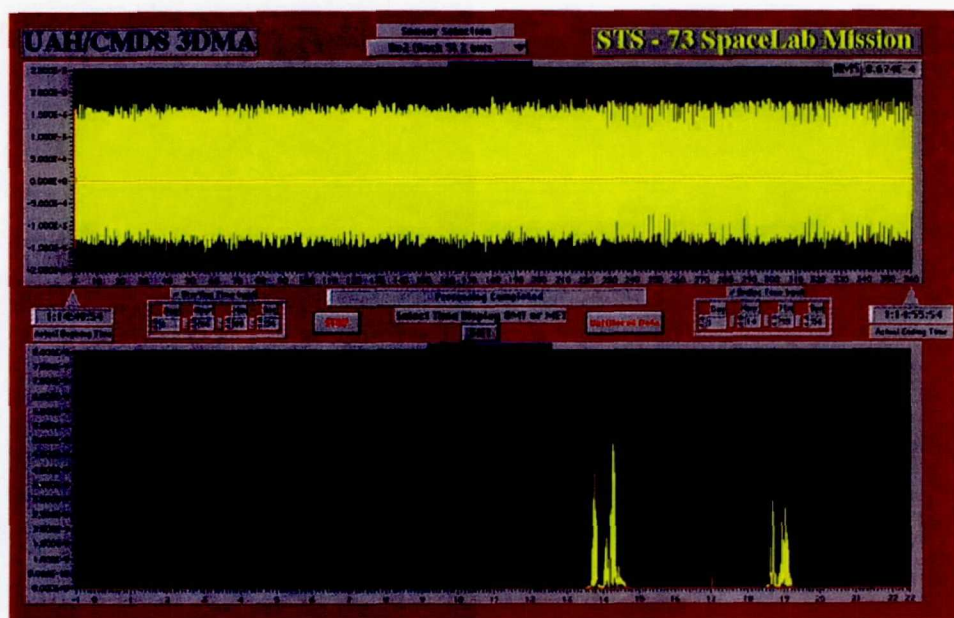


Figure 21. Glovebox nominal.

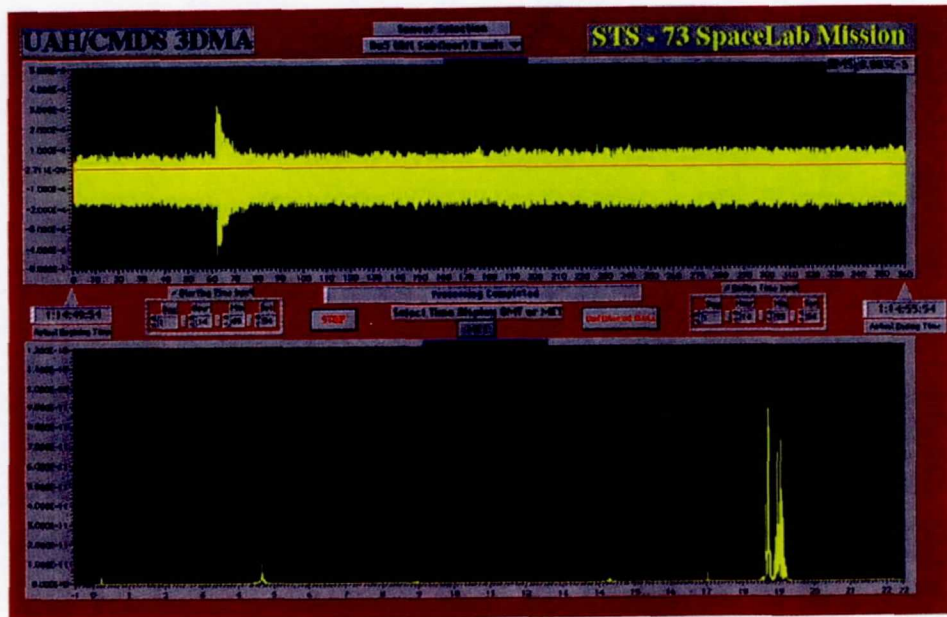


Figure 22. Glovebox nominal.

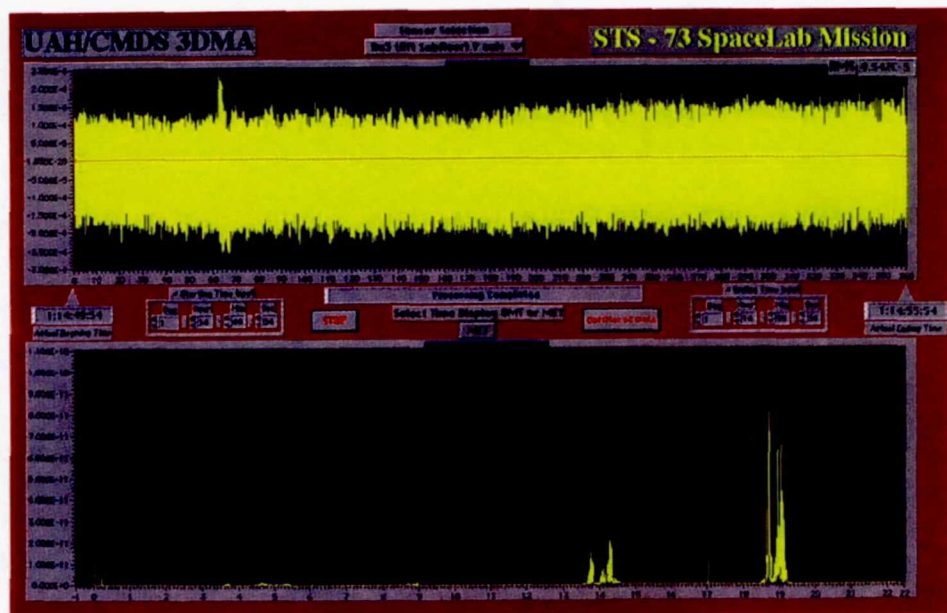


Figure 23. Glovebox nominal.

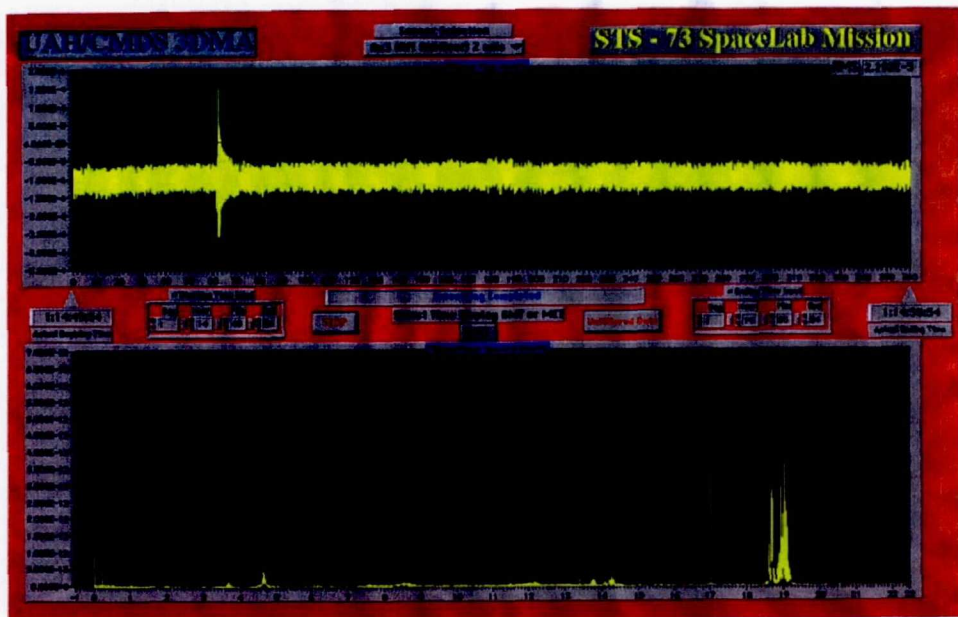


Figure 24. Glovebox nominal.

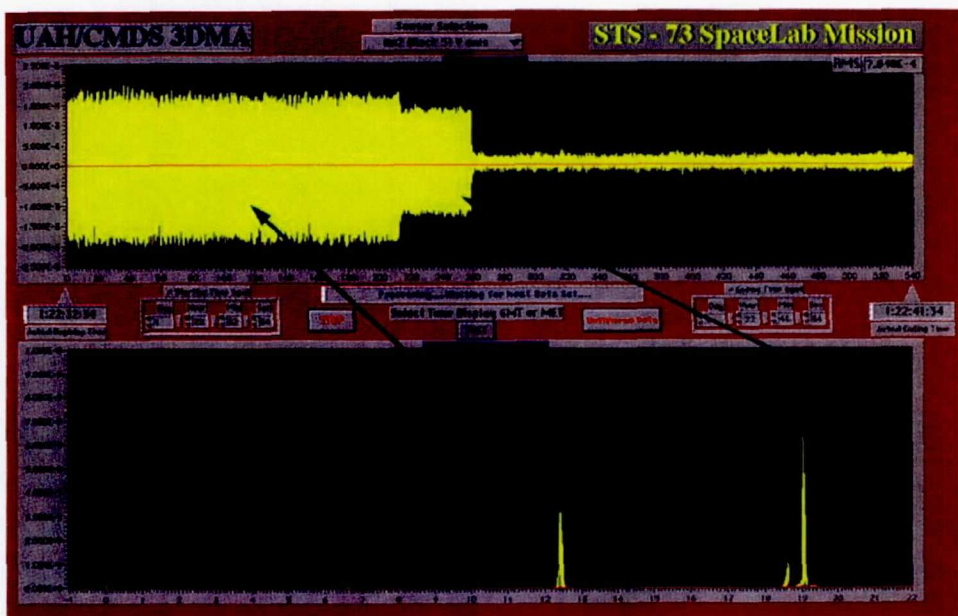


Figure 25. Glovebox fan turned off in two steps.

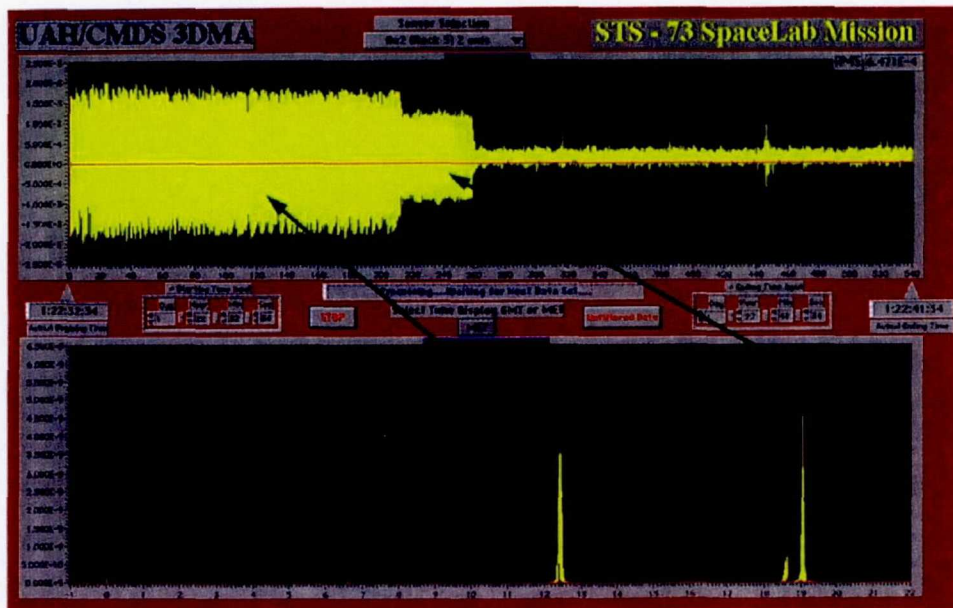


Figure 26. Glovebox fans turned off in two steps.

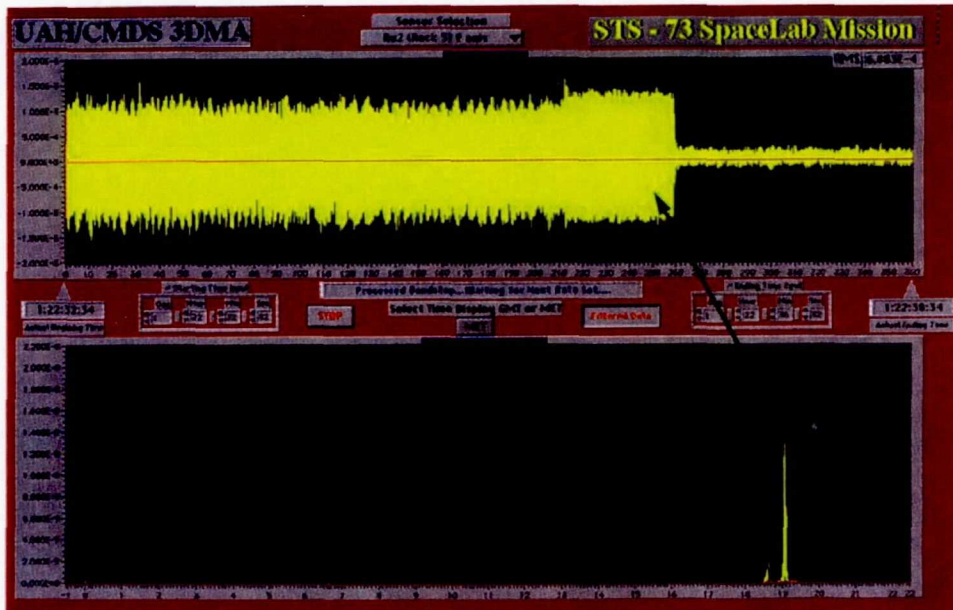


Figure 27. Glovebox fan turning off: frequencies around 12.5 Hz subtracted.

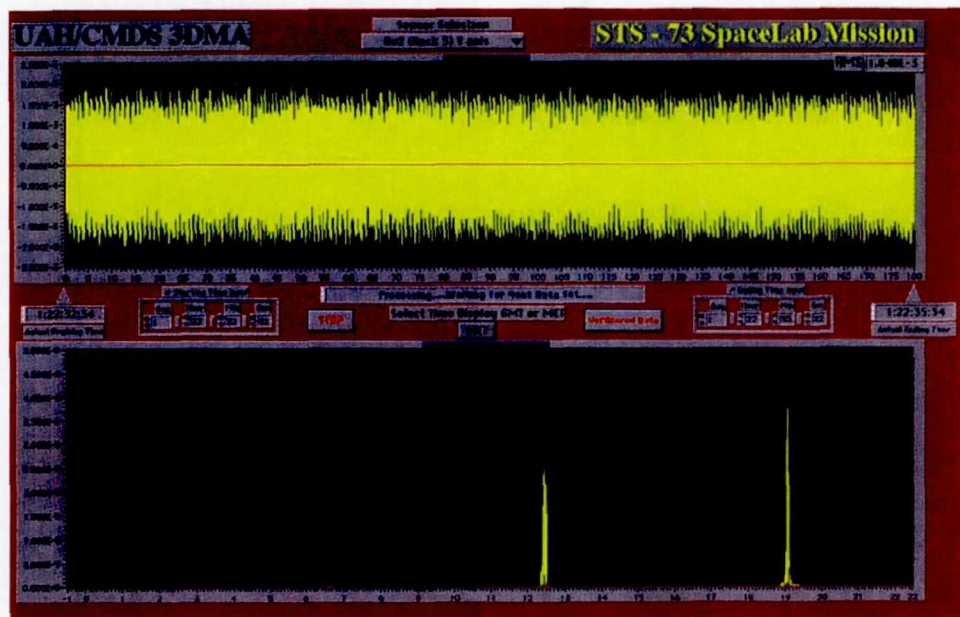


Figure 28. Worst case RMS Glovebox disturbance.

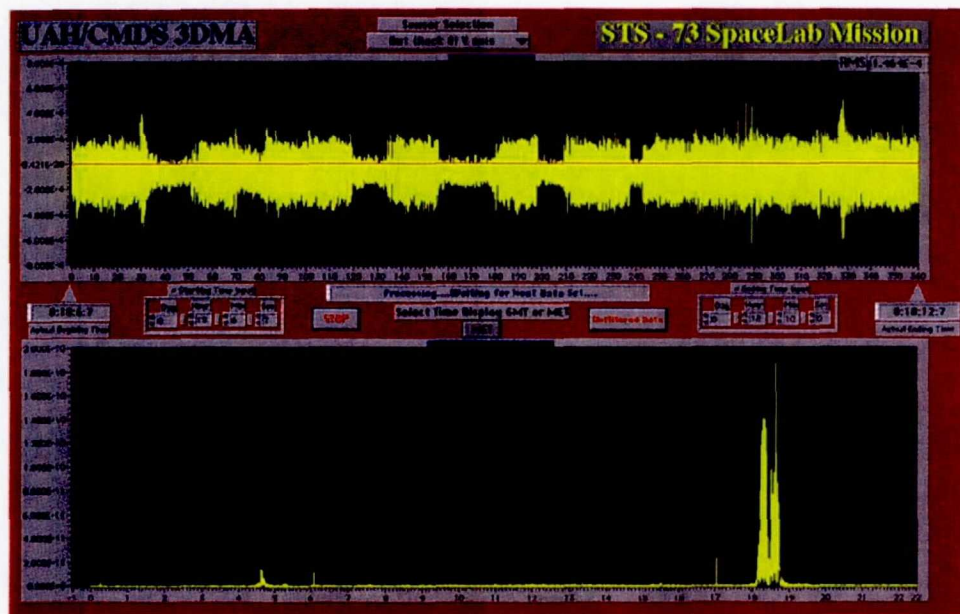


Figure 29. Other Glovebox fan activity.

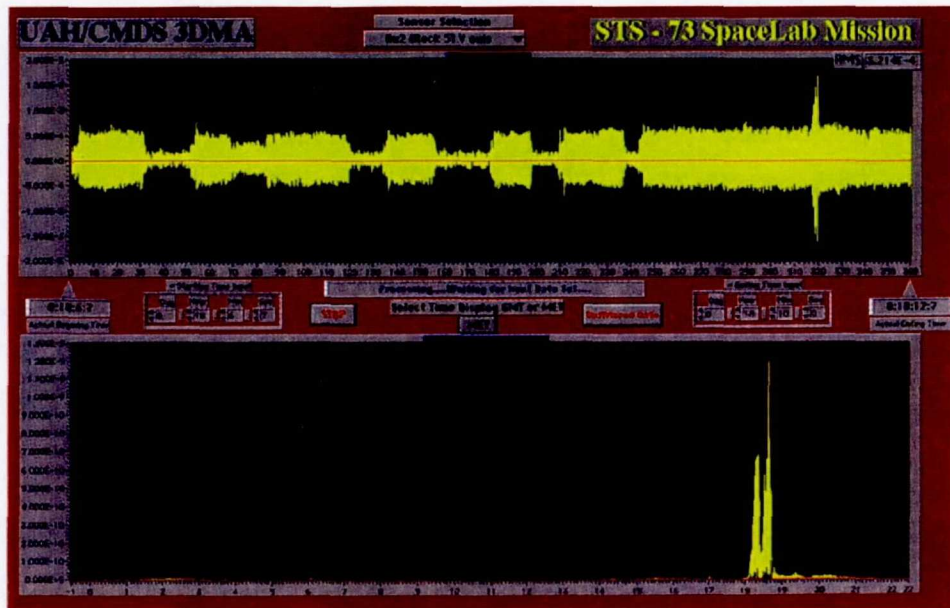


Figure 30. Other Glovebox fan activity.

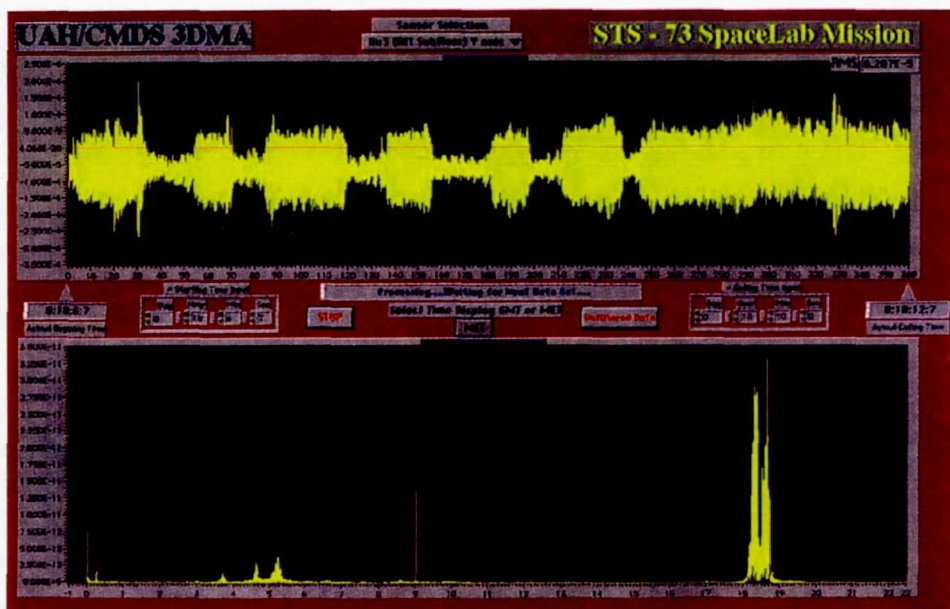


Figure 31. Other Glovebox fan activity.

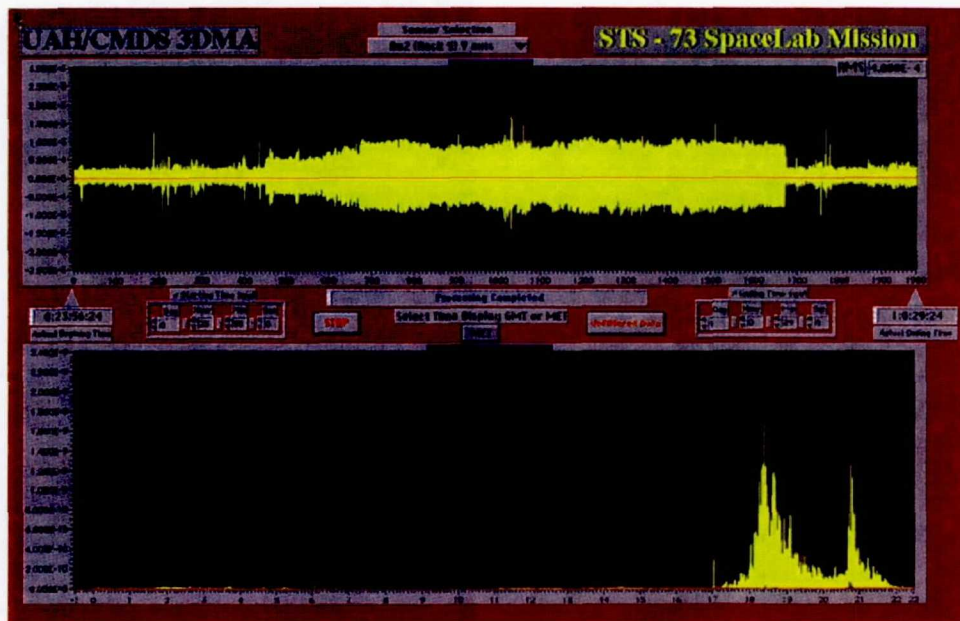


Figure 32. Other Glovebox fan activity.

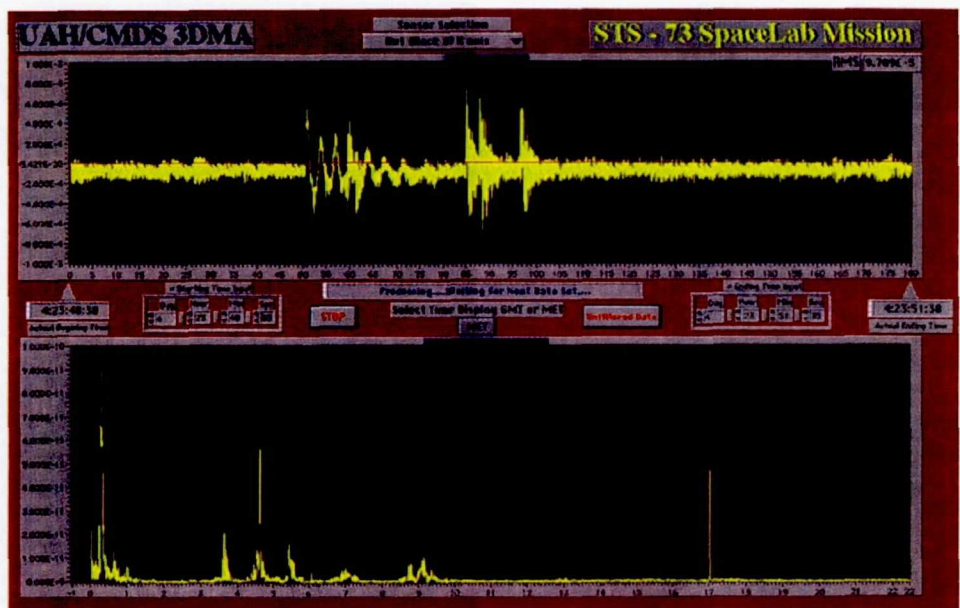


Figure 33. Payload bay door opening.

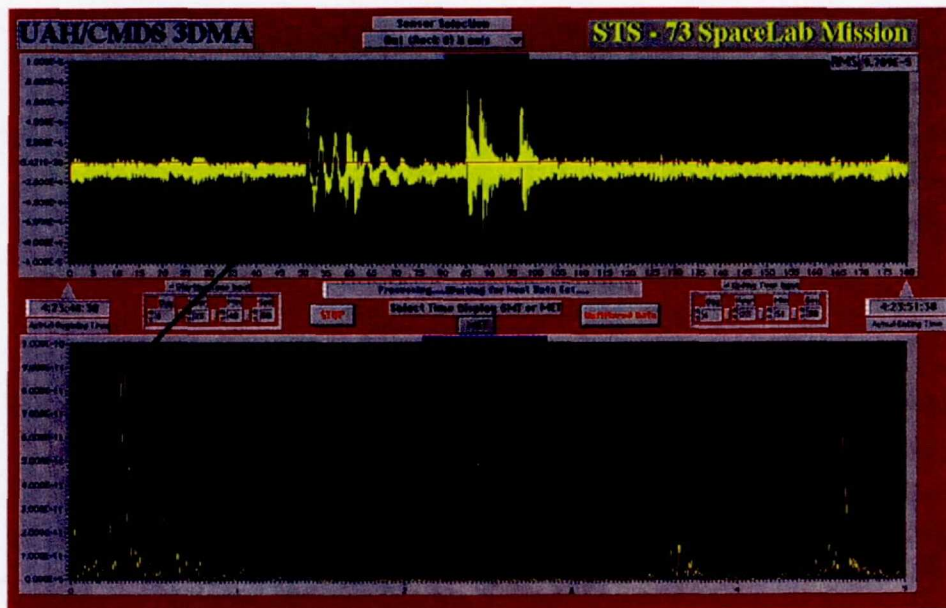


Figure 34. Payload bay door opening (0–5 Hz spectrum).

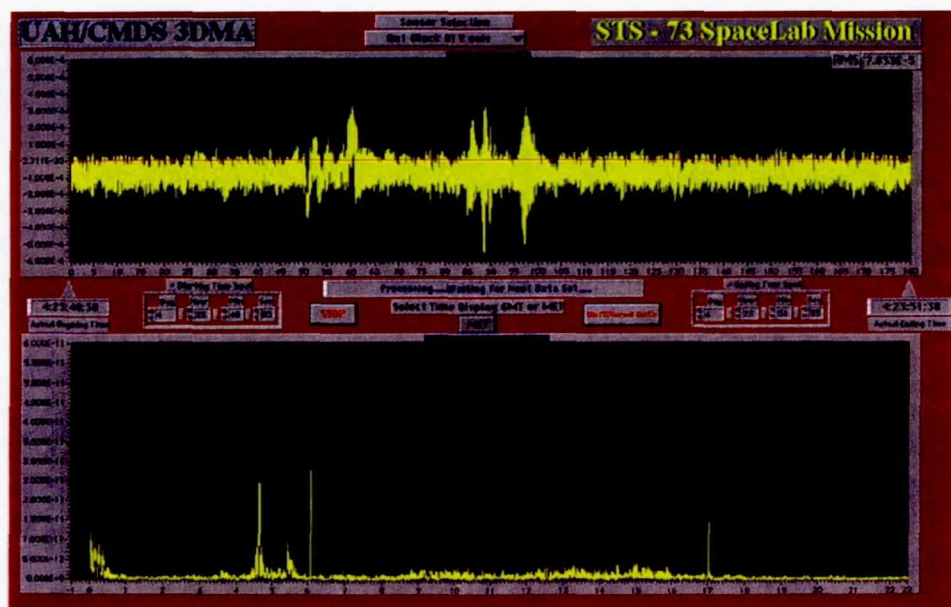


Figure 35. Payload bay door opening.

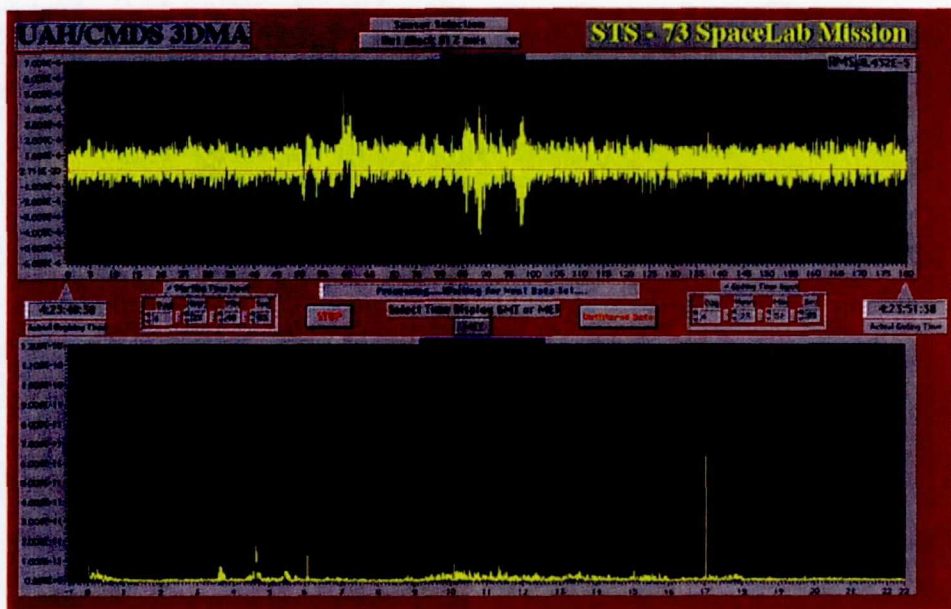


Figure 36. Payload bay door opening.

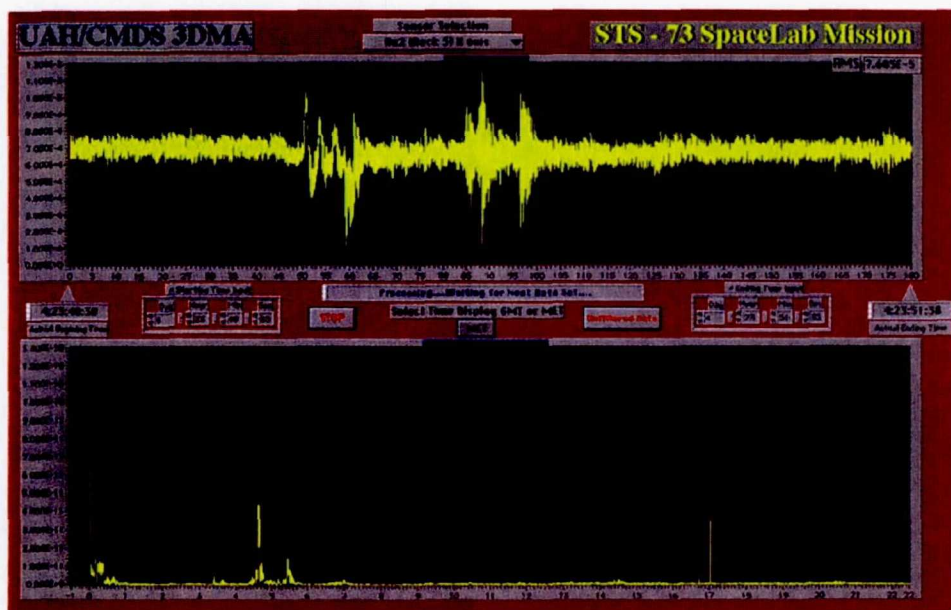


Figure 37. Payload bay door opening.

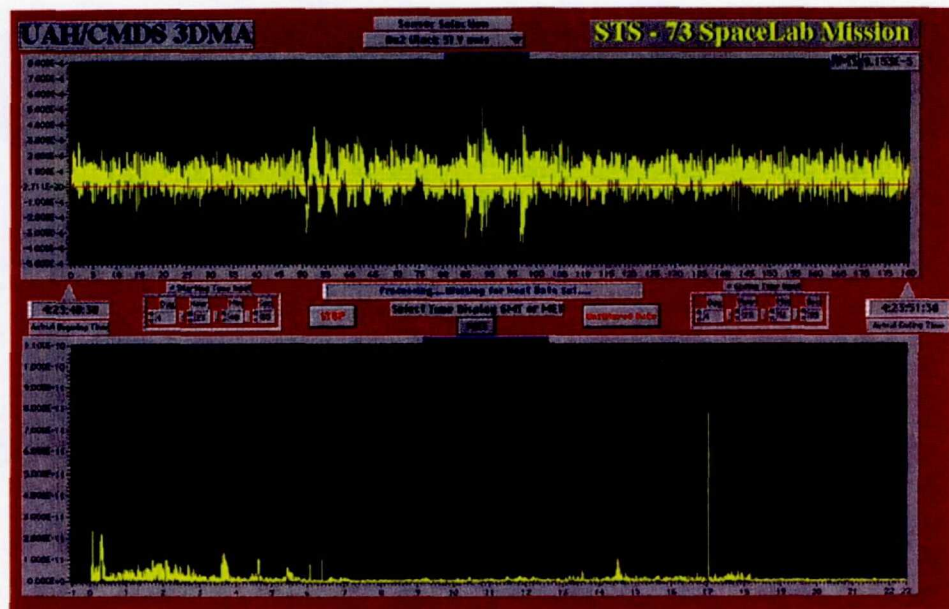


Figure 38. Payload bay door opening.

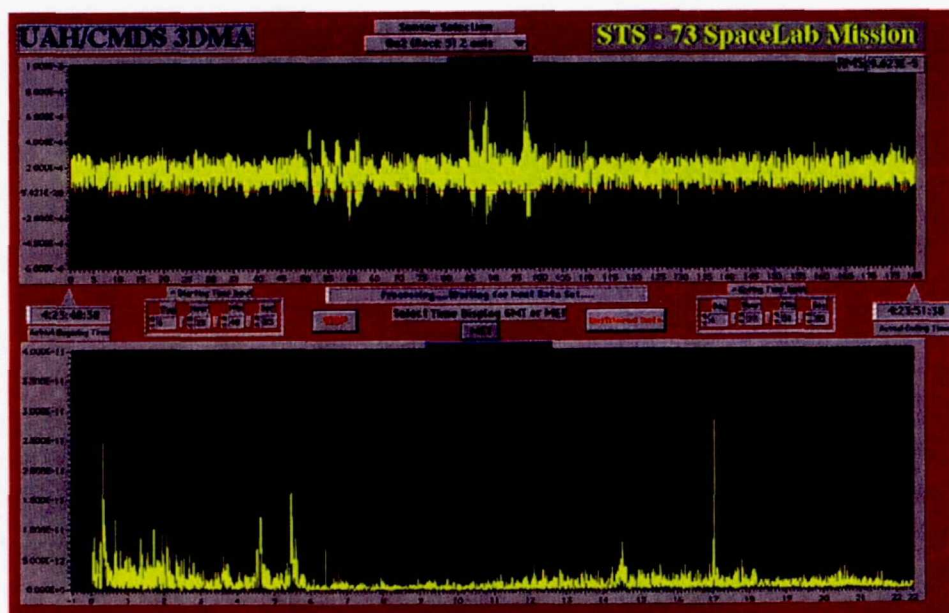


Figure 39. Payload bay door opening.

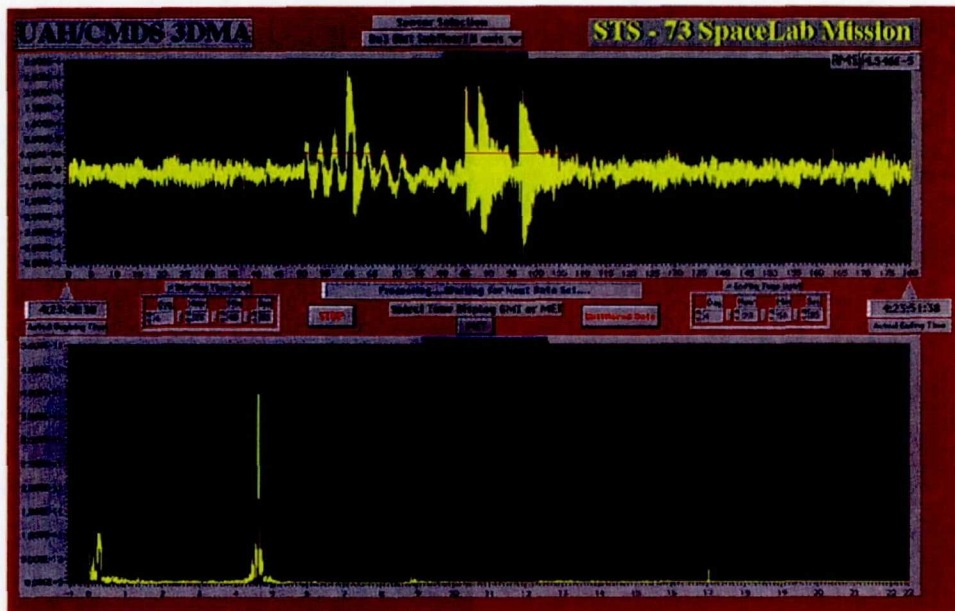


Figure 40. Payload bay door opening.

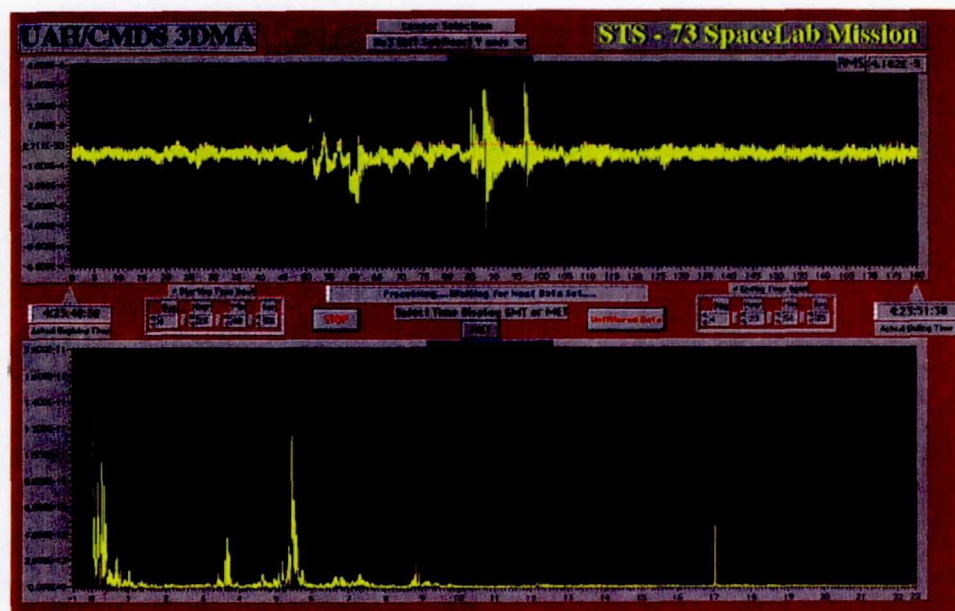


Figure 41. Payload bay door opening.

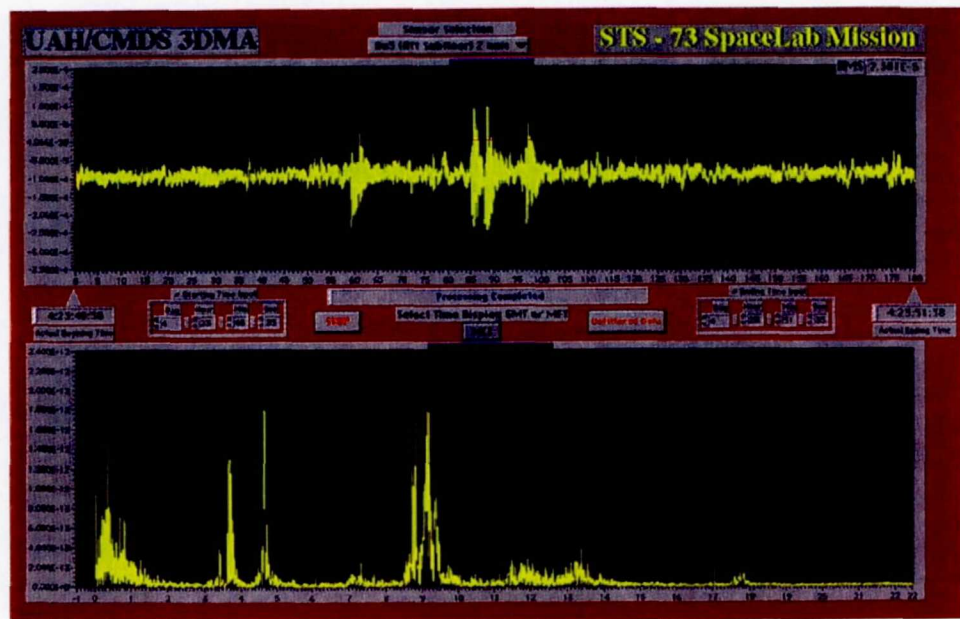


Figure 42. Payload bay door opening.

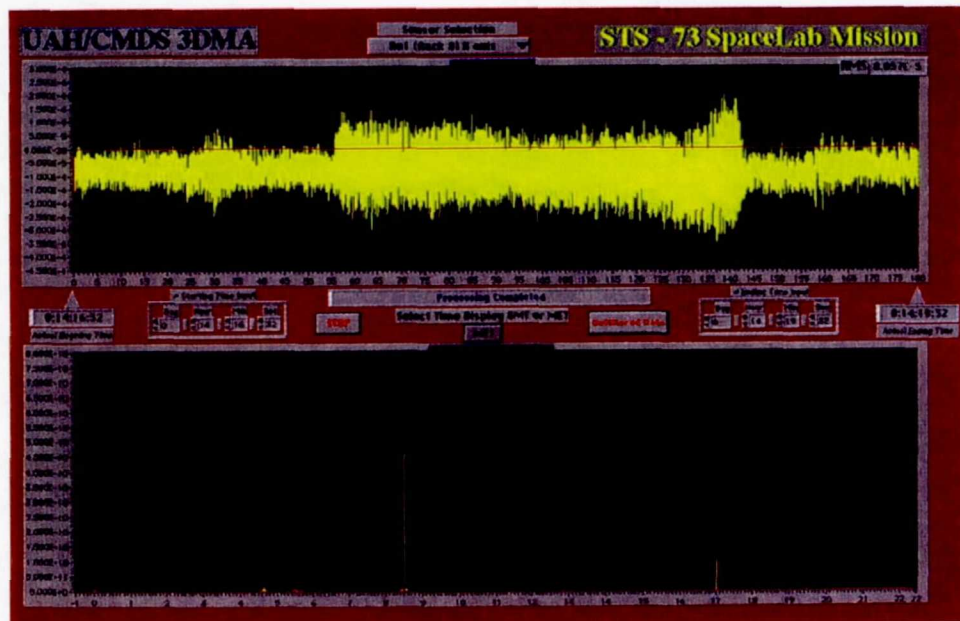


Figure 43. Disturbance of unknown origin.

Page intentionally left blank

EXPERIMENT XXXVIII.

**SUPPRESSION OF TRANSIENT EVENTS BY
LEVITATION (STABLE)—RESULTS FROM THE USML-2 MISSION**

Page intentionally left blank

SUPPRESSION OF TRANSIENT EVENTS BY LEVITATION (STABLE)—RESULTS FROM THE USML-2 MISSION

Gerald S. Nurre, PI

NASA Marshall Space Flight Center,
Huntsville, AL 35812

Donald L. Edberg, PI

McDonnell Douglas Aerospace,
Huntington Beach, CA 92647

1. INTRODUCTION

1.1 Background

Microgravity science payloads can be extremely sensitive to vibrations from machinery, acoustics, ventilation, and crew activity. Suppression of Transient Acceleration by Levitation (STABLE) is an active vibration isolation system designed to protect payloads from these disturbances.

This paper gives an account of results from the flight demonstration of the STABLE microgravity isolation system, which was developed and successfully flight tested in orbit during USML-2, with the participation of Astronaut Fred Leslie (fig. 1). Following a very brief description of the operational principles, the hardware and software design, and performance criteria, results of the analysis of measured flight data are presented to provide an evaluation of system performance parameters, including acceleration attenuation, assessment of sway space, system power consumption, and other factors critical to the performance of an isolation system. Lessons learned and potential design improvements and evolutions are discussed.

Data reduction by Robert Boucher of McDonnell Douglas Aerospace (MDA) was substantially assisted by Kenneth Hrovat of Tal-Cut, Inc., under support from National Aeronautics and Space Administration/Lewis Research Center (LeRC), Cleveland, OH.

1.2 Description

STABLE provides six-degrees-of-freedom isolation by “floating” a platform and its experiment payload on three dual-axis wide-gap electromagnetic actuators, as illustrated in figure 2.¹ These actuators apply Lorentz forces to counteract external forces that are transmitted to the platform through umbilicals,

¹ U. S. patents have been obtained by MDA for the STABLE isolation system, and international patents are pending.

and also internal forces that may be generated on some part of the isolated platform itself. The actuators are actively controlled, using feedback from appropriately placed accelerometers and position sensors. The accelerometer signals are used by a high-bandwidth feedback controller to command counteracting actuator forces and minimize the higher frequency components of the platform motion. In addition, there is a very low bandwidth position loop that tends to keep the platform centered within a ± 1 cm sway space, compensating for the extremely low-frequency disturbances for which adequate space cannot otherwise be provided. The floating platform is very gradually recentered over a period of minutes. For this purpose, signals from three dual-axis optical sensors measure the relative position and orientation of the platform.

Built under a cooperative agreement by engineers and scientists from McDonnell Douglas Aerospace (MDA), Huntington Beach, CA, and the National Aeronautics and Space Administration/Marshall Space Flight Center (MSFC), Huntsville, AL, the entire STABLE demonstration system fit inside a single SMIDEX locker (fig. 3), although it is quite readily adaptable to a variety of other device configurations. The demonstration system flew in October 1995 on USML-2, where it isolated a fluid physics experiment called CHUCK. The flight hardware was designed, fabricated, integrated, tested, and delivered for launch during a remarkably short 5-month period. More thorough descriptions of the STABLE system, and of its anticipated applications as well, may be found in references 1-3. The CHUCK experiment is described in reference 4.

1.3 Performance Criteria

Two criteria are of prime importance for characterizing the performance of a vibration isolation system—the attenuation of the ambient environmental vibration, and the acceleration floor achieved. Performance will be evaluated mainly with respect to these criteria.

2. RESULTS

2.1 Representative Flight Data

The STABLE flight demonstration recorded measurements of absolute accelerations from several positions on the isolated platform and the nonisolated base, the position of the platform relative to the base, actuator currents, accelerometer temperature, control system gain settings, and system configuration data. In addition, thermal and video data from the science payload were recorded. There were 72 total hours of flight data recorded for STABLE, including periods during which various kinds of activities, such as crew exercise, water dumps, thruster firings, a payload-bay door opening, sleep, and normal routines, occurred.

The data acquisition system recorded data from six QA-2000 accelerometers on the isolated platform and three on the nonisolated base, at a rate of 250 samples/sec. This provided data on system behavior at frequencies up to a theoretical maximum of 125 Hz, although frequency data above about 50 Hz were considered less reliable. All of these signals passed through a 130-Hz low-pass filter to reduce aliasing effects.

For the purposes of this report, representative accelerometer data have been selected for discussion, primarily from a particular 22-minute time period on October 5, 1995, starting at MET: 005/19:56:47, a period nominally identified as a "crew exercise" period. For brevity, the discussion is limited to vertical

acceleration, ignoring horizontal motion and rotations. The analog accelerometer outputs were digitized over a 12-bit range, with a least significant bit of approximately $13 \mu\text{g}$, for both the base and platform data. For much of the data reduction the (approximately) 22-minute uninterrupted recording period was subdivided into twenty 65.536-sec "ensembles," each containing 16,384 samples, so that averages over these ensembles could be calculated.

Reduced data have been generated in several forms, including:

- Acceleration time histories for 22-, 1.1-, and 0.1- minute periods
- Acceleration probability densities (histograms)
- Estimated probabilities of exceedence
- 1/3 octave acceleration spectra
- Color acceleration spectrograms
- Power spectral densities (PSDs)
- Base and platform acceleration coherence
- Attenuation
- Platform-displacement time histories
- Actuator currents
- Accelerometer temperature
- Control system gain settings.

Examples of several of these will be discussed below. In examining the acceleration data, it should be kept in mind that the lowest platform accelerations observed were probably dominated by various kinds of noise and may not reveal the actual acceleration levels achieved by STABLE.

Extensive files of reduced data of various types from many different time periods have been prepared by Robert Boucher (MDA) and Kenneth Hrovat (Tal-Cut/LeRC). The most significant of these are to be made available in a NASA Technical Paper.

2.2 Acceleration Time Histories

Isolation performance of STABLE is perhaps most directly revealed in time history plots of the accelerometer data, such as that shown in figure 4. The red (nonisolated) data are from the vertically-oriented accelerometer mounted on the backplate inside the locker where the backplate is attached to the SMIDEX rack, and the green (isolated) data are from a weighted average of the accelerometer records, an average intended to yield the vertical acceleration of the center of mass of the isolated platform. Because of the rigidity of the locker and its attachment to the rack and the rigidity of the mounting structure for the actuators, these components are assumed to move as a rigid unit, except possibly at the highest frequencies. Thus, data from the backplate accelerometers are assumed to be approximately representative of the ambient spacecraft environment.

The root mean square (rms) accelerations on the base and platform are 574 and $21.2 \mu\text{g}$, respectively, suggesting an attenuation factor of the order of 27 (as becomes more obvious in plots of these data in which the time scale has been expanded). These estimates are valid provided that it is legitimate to take the backplate acceleration as representative of general nonisolated-base vertical motion, and the above

mentioned platform average as representative of the vertical motion of the platform center of gravity. Both of these assumptions appear to be valid based on some simple consistency checks. It is, of course, also necessary that the platform acceleration measure an attenuated form of the base (environmental) motion, rather than measure unrelated motion or be dominated by noise. This latter condition does not appear to be satisfied over the full spectrum, as will be discussed further later on.

It may also be noted that during the selected 22.85-sec time period, there were 1,624 occurrences (~0.5 percent of the samples) of backplate acceleration exceeding 1,000 μg , but no occurrences this large among the platform samples. The 1,000- μg criterion is the highest transient acceleration permitted under *International Space Station (ISS)* microgravity requirements.

The peak value of the acceleration on the backplate (~4400 μg) was 43 times that on the platform (~103 μg).

2.3 Probability Densities (Histograms)

Histograms showing the fractions of samples having values within small acceleration intervals serve to estimate the probability density of finding acceleration values in those intervals. The histogram shown in figure 5 is typical.

2.4 Probabilities of Exceedence for Acceleration Levels

The probability of an observation exceeding an arbitrary acceleration level can be estimated from data such as those in figure 6, obtained by integrating the probability densities. Curves such as these may help an experimenter make an estimate of the probability of a successful experiment based on experiment sensitivity levels.

2.5 Color Spectrograms

STABLE flight data were also analyzed using color spectrograms similar to those used for the Space Acceleration Measurement System (SAMS). The extensive set of color spectrograms has been created by Kenneth Hrovat (Tal-Cut/LeRC), covering large portions of the 72-hr duration of STABLE data acquisition, including periods during which a variety of spacecraft, machinery, and crew activities occur. The frequency scale is linear and displays information roughly over the band 1 to 125 Hz (the lower bound is not precise). The data above about 60 Hz are thought to not be very reliable. This is primarily due to quantization noise introduced by A/D conversion for data recording, to aliasing introduced by A/D conversion for data recording, and to an anti-aliasing filter used for the Fast Fourier Transform (FFT) data reduction.

Figure 7 is a set of spectrograms for the three orthogonally-oriented accelerometers mounted on the base (with the third spectrogram oriented vertically), covering eight sequential 22-minute periods (nominally identified as "crew exercise"). Figure 8 is a similar set, except that the data are from accelerometers on the platform, and the three are all vertically oriented. The data comparisons made in figures 4-6, and for the other types of data to be presented later, are for data from just the fourth 22-minute time period in figures 9-10 (starting MET: 005/21:05:01). The log-scale color coding of the power spectral density (in units of g^2/Hz , where g is Earth gravity) is shown on the right.

The great difference in overall colors between figures 9 and 10 illustrates the general isolation achieved by STABLE, but in figure 10 there is some evidence of certain distinct platform vibrations that may or may not be real. For several reasons it has often been difficult to clearly identify the origins of these apparent vibrations, which may in some cases represent real platform acceleration, and in others represent artifacts due to aliasing that was introduced in the original A/D data conversion.

In order to convey a sense of the present understanding of the meaning of the data, it may be useful to mention some of the ideas that have been considered with respect to certain of its notable features. In particular, it may be noted that the relatively strong platform acceleration apparent at 60 Hz is not noticeable in the horizontal motion (not shown). It is definitely absent in both the base and platform data before an interruption occurring at an entirely different time in the data record (sometime around MET 010/06:00:00), and definitely present after. The origin of this signal may be mechanical equipment in neighboring USML-2 experiments (the CHUCK fluid physics experiment was not powered while these data were recorded), but it is not understood. Another signal, one that appears to vary around 12–15 Hz, may be noted both in some of the base data and in some of the platform data. This signal does not have an identifiable origin at present. Also, the orbiter's Ku band antenna dither is strongly visible at 17 Hz in the base data, but it is attenuated enough to be only just barely detectable in the platform data. Further speculations along these lines will be mentioned later on.

The data comparisons made elsewhere in this report are all for data from just the fourth 22-minute time period (starting MET: 005/21:05:01) shown in figures 9–10, and the comparisons are between the backplate vertical acceleration (denoted as nonisolated) and the calculated vertical acceleration of the platform center of gravity (denoted as isolated). In the color spectrograms of figures 7–10, however, the comparisons are between the backplate vertical accelerometer and only one of the platform accelerometers, the vertically-oriented accelerometer at the front of the platform. Figures 9–10 are included to allow comparisons of spectrograms on an expanded scale for these latter two accelerometers. The color scale has also been changed so that the numbers associated with the colors now represent the rms acceleration in a frequency interval equal to the $250 \text{ Hz}/16384 = 0.0153 \text{ Hz}$ frequency resolution of the FFT's and averaged over the 20 ensembles identified in section 2.1.

2.6 Acceleration Power Spectral Densities (PSDs)

Power spectral densities were calculated using standard Fast Fourier Transform (FFT) windowing and averaging techniques, transforming the $16384 = 2^{14}$ samples in each of the 20 ensembles, and then averaging over the ensembles. These plots use a logarithmic frequency scale and cover the much wider band 0.015–125 Hz, revealing spectral information below 1 Hz not available from the color spectrograms. Typical results are shown in figure 11.

Below about 0.1 Hz, the position control loop introduces extremely small accelerations to ensure that the platform does not wander too far in its sway space as the local spacecraft structure moves and not much isolation is to be expected. Over the intermediate frequency range, the vibration environment is substantially attenuated, as is evident when one considers the reductions in the values of the strong peaks at 1.15 Hz and its first three harmonics. In between these peaks, the data for the isolated platform are in the range of a few μg and probably represent more noise than actual platform acceleration. In the higher frequency range above 10 Hz, the data system noise floor is probably considerably higher than the actual values of the platform acceleration, but there appears to be no way to be sure without either substantially

improving the data acquisition to reduce measurement noise or testing in a more strongly disturbed environment than USML-2 provided. One important source of noise is the low 12-bit range of the recorded acceleration data. A simple change to 16 bits would greatly improve the measurement of platform performance. Note that the data quantization has no effect on actual platform motion because the data acquisition system is independent of the platform controller.

The sharp spikes present at 10 Hz and their harmonics are not found in the external environment and have been identified as a consequence of a compromise made in the rapid development of the STABLE centering system design. Because these spikes are so narrow, they contain relatively little power. They are associated with the 10 Hz refresh rate for the position control loop, and it is expected that their amplitude will be greatly reduced by some simple changes in the control system, changes intended to either smooth the introduction of the position control signal with an improved filter or speed up the refresh rate.

The two broad peaks near 12 and 15 Hz correspond to the wandering signal mentioned in section 2.5. This signal is not well understood at present and is still being studied. It seems unlikely that it could be generated by acoustic transmission from the fans in the nearby glovebox, but this and other possible explanations are being considered. This signal, and/or some other features that appear in the PSDs and in the color spectrograms, may actually be associated with phenomena at frequencies above the Nyquist frequency that are then aliased down to low frequencies when the accelerometer data are first digitized. Such high-frequency phenomena may include either real platform motion, or unphysical artifacts of the data acquisition process, or both.

If STABLE were to function perfectly, the only force that might tend to shake the nonisolated components, an unwanted force that could then be transferred to the locker and rack, would be the vector sum of the forces exerted by the umbilicals and the reaction force from the actuators. This net force is expected to be very small. An additional force will be present if the actuator currents include any significant control error. A brief examination of PSDs and color spectrograms like those in figure 7 was made in order to see if any evidence could be found that STABLE might be shaking the local spacecraft structure while it was operating. No such evidence has been found, but it will probably be possible to make some estimates of the shaking that would be expected based on estimates of the actuator forces as determined from actuator current measurements. Because of the relatively large mass and rigidity of the local structure, it is doubtful that disturbances generated by STABLE would be detectable above the ambient environment in the base accelerometer data.

The accelerometer data were also briefly examined to discover if they might reveal any clues to the nature of the motion and flexure of the power and data umbilicals, without success. The umbilicals had such relatively low mass and stiffness that it would have been surprising to find any distinguishable effects.

An alternative way of presenting spectral data is to calculate rms acceleration spectra averaged over one-third octave bands, as shown in figure 12. Even though the USML-2 and *ISS* environments are expected to be quite different, such plots allow a qualified comparison with the nominal *ISS* requirement, which is also shown in figure 8.

Also shown are estimates of the noise and error bars associated mainly with statistical sampling and discretization in the accelerometer data. These estimates were obtained by combining the manufacturer's

accelerometer noise specification with the sampling errors resulting from quantization and aliasing. A higher data sampling rate, 12-bit digitization, and better filter choices are expected to provide substantial improvement. Such changes could allow the results of future tests to determine how low the actual platform accelerations lie.

2.7 Correlation Between Base and Platform Acceleration

At low frequencies, the position control loop of STABLE is designed so the platform motion will follow the base motion, and the signal-to-noise ratios for the base and platform accelerations are low, so that one may expect the low-frequency components to be well correlated with each other. On the other hand, at high frequencies, the acceleration control loop is designed to suppress the high-frequency components of the platform motion, and one may expect the accelerations off and on the platform to be poorly correlated, presuming the latter to be dominated by noise. At intermediate frequencies, a gradual transition occurs with its location determined largely by the signal-to-noise ratio of the platform acceleration. This general behavior is evident in figure 13.

2.8 Vibration Attenuation Spectra

The one-third-octave band-averaged acceleration spectra from figure 12 yield the attenuation data shown in figure 14, but it must be kept in mind that, because of noise present in the measurements, the actual attenuations may be significantly better than the plots indicate. The acceleration data from the accelerometers on the platform were recorded with a low signal-to-noise ratio in some frequency ranges. This made it difficult to determine the acceleration levels actually present on the platform, except when the environment was experiencing a particularly strong disturbance and the platform responded at a level significantly above the noise. It follows that if one finds corresponding peaks in the PSDs for accelerations off and on the platform at some particular frequency, one may expect that the ratio of the peak values will provide a reasonable estimate for the attenuation. Thus, in figure 14, some of the upward peaks at middle and high frequencies that seem to suggest poor attenuation are actually misleading.

An alternative procedure for estimating the attenuation will be described next; one that is more complete and better justified. The PSD data averaged over 20 ensembles are used, without averaging over one-third octave bands, and the ratios of PSD values were calculated using only data at frequencies such that the coherence was greater than 0.5 (fig. 13). The result shown in figure 15 is a set of points that suggests a smooth curve describing the increase in attenuation with frequency.

During the course of the flight, the astronauts provided various force inputs to the Shuttle during their normal activities. Orbiter vernier thrusters were fired every few minutes, and primary thrusters were fired several times per day. Other events such as water dumps and payload bay door operation were also captured in the STABLE data. Unfortunately, STABLE was not able to access the orbiter time reference system; instead, approximate mission time was recorded by a crew member during the changeout of each STABLE hard drive. Thus, these events can be only approximately located in the data prior to processing. It is expected that special techniques such as band-pass filtering will be required to accurately identify particular events.

2.9 Platform Motion and Sway Space

Platform displacements during nominal operations were typically limited to a few millimeters as shown in figure 16. Most of the time, the floating platform is within 0.5 mm of its nominal centered position. Occasional transient events increase the displacement to about 2 mm, but the position loop of the controller restores the platform to its nominal centered position in about a minute.

The six position measurements were also converted into the translations and rotations of the floating platform about its own center of mass. Since the platform was designed for extremely high stiffness—the first structural mode is over 200 Hz—this calculation was accomplished by a simple rigid-body transformation. The platform center of mass displacements are on the order of a few millimeters, similar to the actuator displacements, and the platform rotations are typically on the order of a tenth of a degree, as shown in figure 17.

When a displacement becomes too large, and thus allows the platform to approach contact with the base, a high-gain mode is initiated in the position control loop in order to increase the centering forces and to avoid contact. Among all the data examined so far, only one event produced sufficient relative displacement to trigger the high-gain mode of the control system—a payload bar door closing operation on mission day 12. The maximum displacement seen during this event was approximately 8 mm.

2.10 System Power Measurements

The power required by STABLE's actuators was remarkably small. The average actuator power draw was on the order of 10 mW with transient events drawing several times that. Even the most energetic event yet analyzed, a Shuttle payload bay door closing, required a peak actuator power of about a tenth of a watt. The high efficiency of the STABLE actuators obviates the need for any kind of distributed active cooling system.

Electronic control system power for STABLE is estimated to have averaged about 30 W, much higher than all actuators combined. This power was consumed by the digital processor, a cooling fan, and analog and power electronics. Since the actuator power was so small, it can be concluded that umbilical stiffness and bias effects were minimized by STABLE's design.

3. CONCLUSIONS

The objective of the STABLE flight experiment was to demonstrate vibration isolation on-orbit with an operating scientific experiment, while passing power, data, and other services over a service umbilical. Based on the analysis of flight data, STABLE accomplished the objective of actively attenuating microgravity disturbances that might otherwise reach the experiment. The data suggest that the rms acceleration environment was generally reduced by at least a factor of the order of 15–20 in the 0.1–100 Hz frequency band. Although noise interfered with the possibility of obtaining reliable measurements of the residual acceleration of the isolated platform, in the 0.1–10-Hz frequency range of most interest, the mea-

sured levels (averaged over one-third octave bands) were generally of the order of a few μg , and the data provide a rough upper bound on the actual levels. STABLE's isolation performance appears to be limited by the noise in the accelerometers used to sense the isolated platform's acceleration by removable disturbances at multiples of 10 Hz and by some still-unexplained phenomena.

No evidence was found that STABLE was shaking the local rack and spacecraft structure when it was operating.

The experiment demonstrated the feasibility of a fast-track development and flight program. The challenge was to design, fabricate/procure, integrate, test, qualify, and deliver flight hardware in a 5-month period. In order to meet this challenge, it was necessary to accept limitations that reduced abilities to fully explore, measure, and evaluate the isolation capabilities of the STABLE system. Some minor improvements are expected to remove some of these limitations on any future flights. One such change will reduce or eliminate a small control-signal error introduced at multiples of 10 Hz. Other minor changes will reduce noise contamination of the acceleration data and thereby enable better evaluation of the isolation performance.

4. REFERENCES

1. Edberg, D.L.; Nurre, G.S.; Boucher, R.; and Whorton, M.S.: "Performance Assessment of the STABLE Microgravity Vibration Isolation Flight Demonstration," AIAA Paper 97-1202, to be presented at the AIAA Structures, Structural Dynamics, and Materials Conference, Orlando, FL, April 7, 1997.
2. Nurre, G.S.; and Edberg, D.L.: "Suppression of Transient Events by Levitation (STABLE)," The Second United States Microgravity Laboratory 90-Day Science Report, 101, March 1996.
3. Edberg, D.L.; Boucher, R.; Schenck, D.; Nurre, G.S.; Whorton, M.S.; Kim, Y.; and Alhorn, D.: "Results of the STABLE Microgravity Vibration Isolation Flight Experiment," McDonnell Douglas Aerospace paper MDC 96H0806A, February 1996, presented to the 19th Annual AAS Guidance and Control Conference, Breckenridge, CO, February 7-11, 1996, and published in Guidance and Control 1996, Vol. 92, Advances in the Astronautical Sciences, R.D. Culp and M.L. Odefey, Eds., Univelt, San Diego, 1996.
4. Ramachandran, N.; Baugher, C.R.; Rogers, J.; Peters, P.; Roark, W.; and Pearcy, G.: "Thermal Diffusion Experiment 'CHUCK'—Payload of STABLE," SPIE Proceedings, Vol. 2809, 367-378, July 1996.

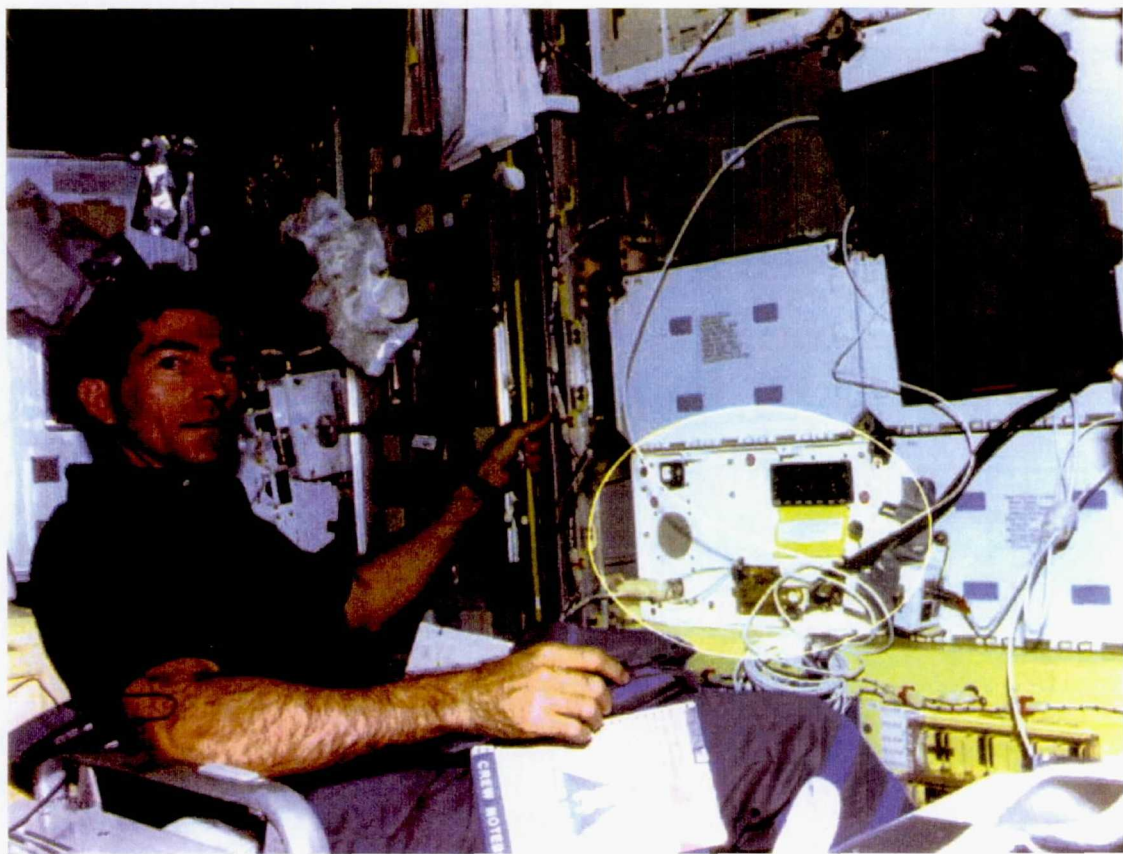


Figure 1. Astronaut Fred Leslie operating STABLE on USML-2/STS-73.

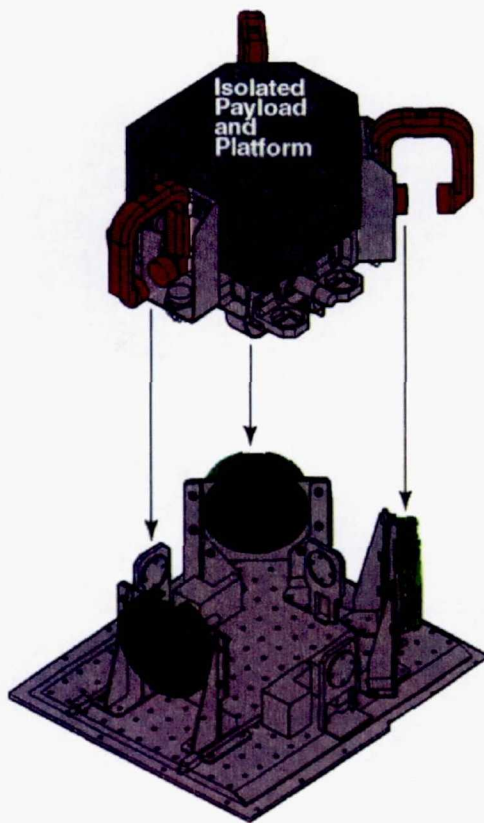


Figure 2. The isolated platform and its experiment payload float above the non-isolated base.

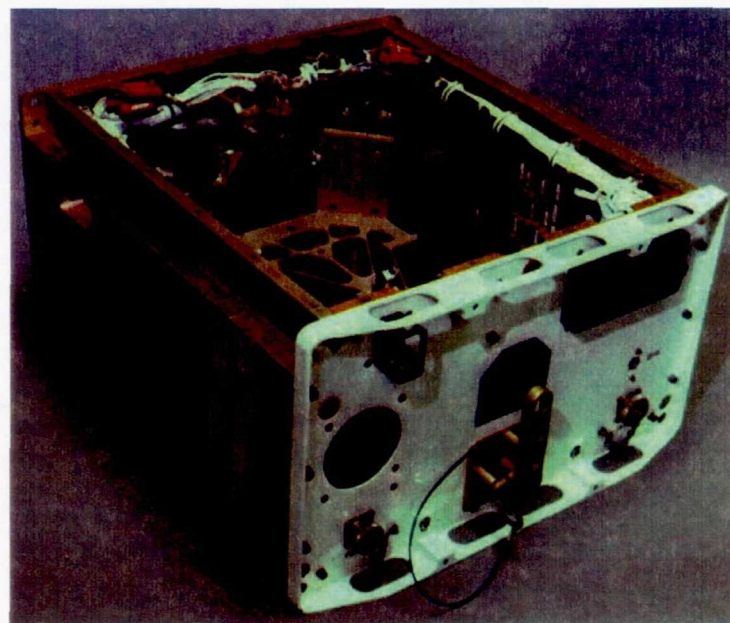


Figure 3. The SMIDEX locker for STABLE on USML-2. Inside can be seen the webbed isolated platform before installation of the science experiment CHUCK.

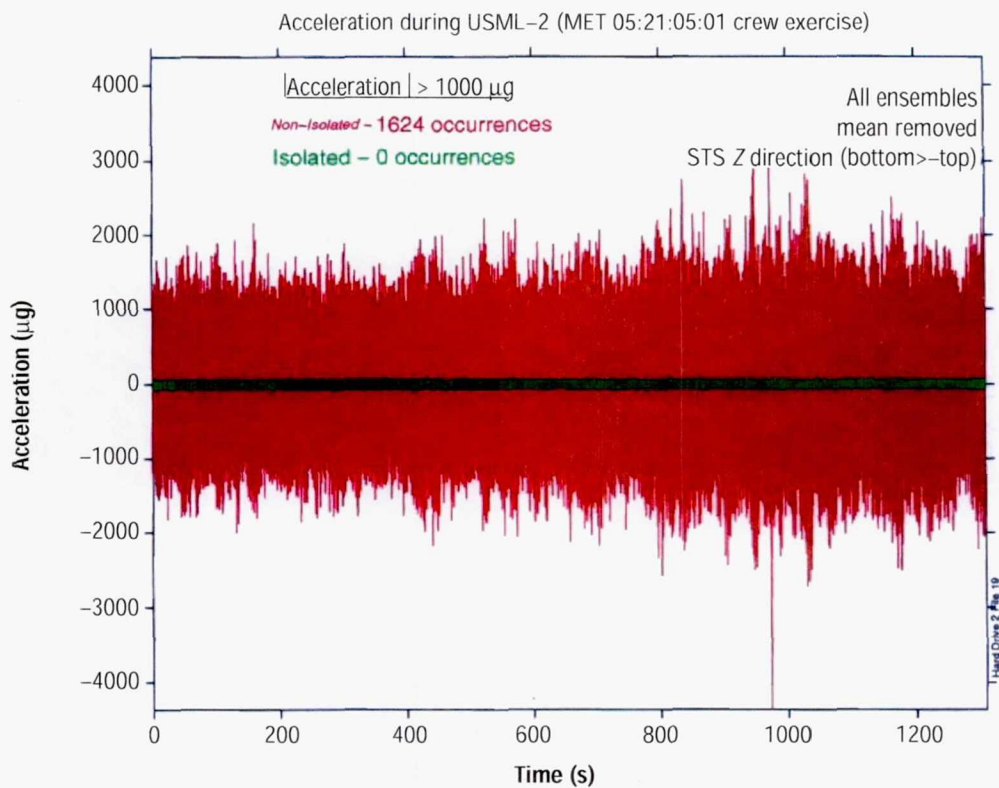


Figure 4. Comparison of acceleration time histories off and on the isolated platform.

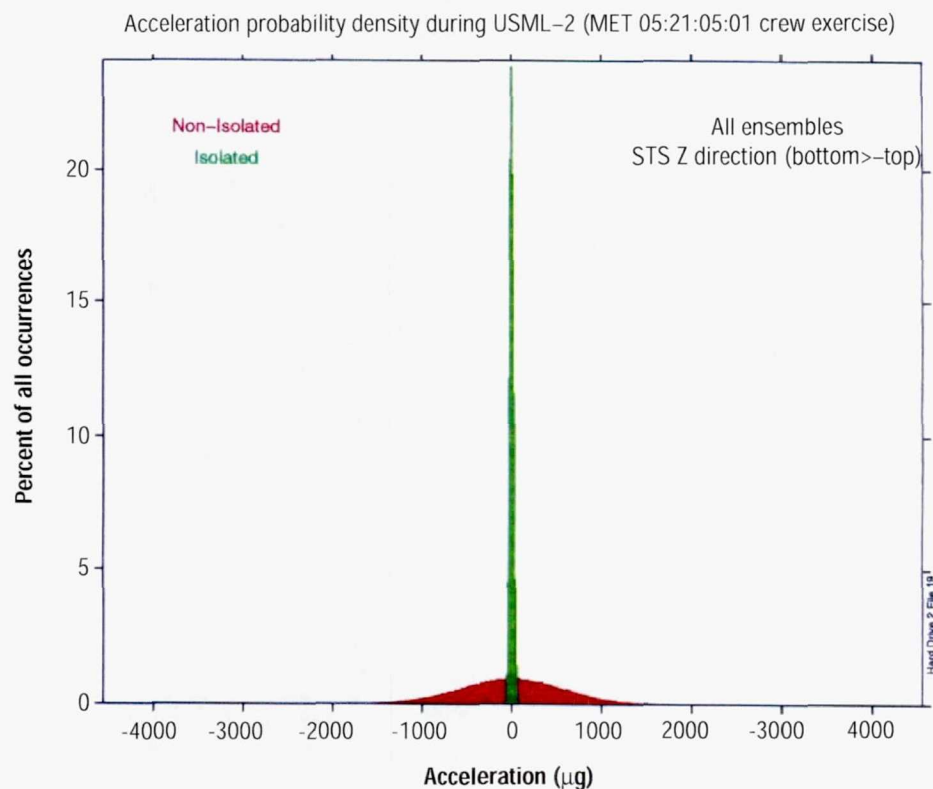


Figure 5. A comparison of acceleration probability densities (histograms) illustrates the frequencies of occurrence of different acceleration levels.

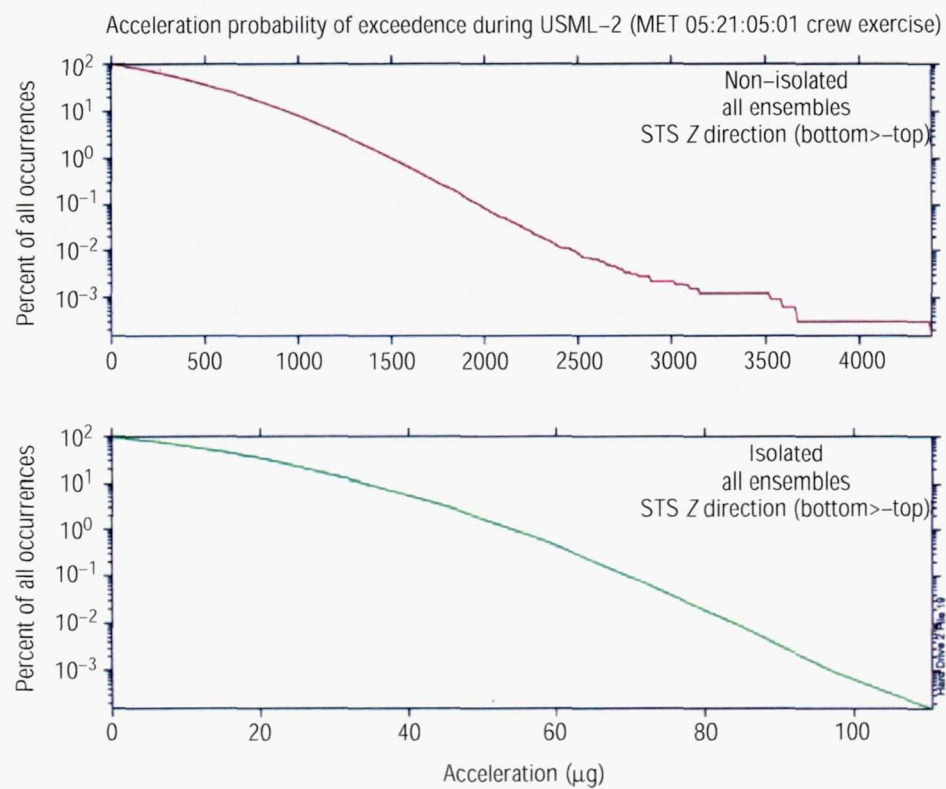


Figure 6. Comparison of probabilities of exceedence.

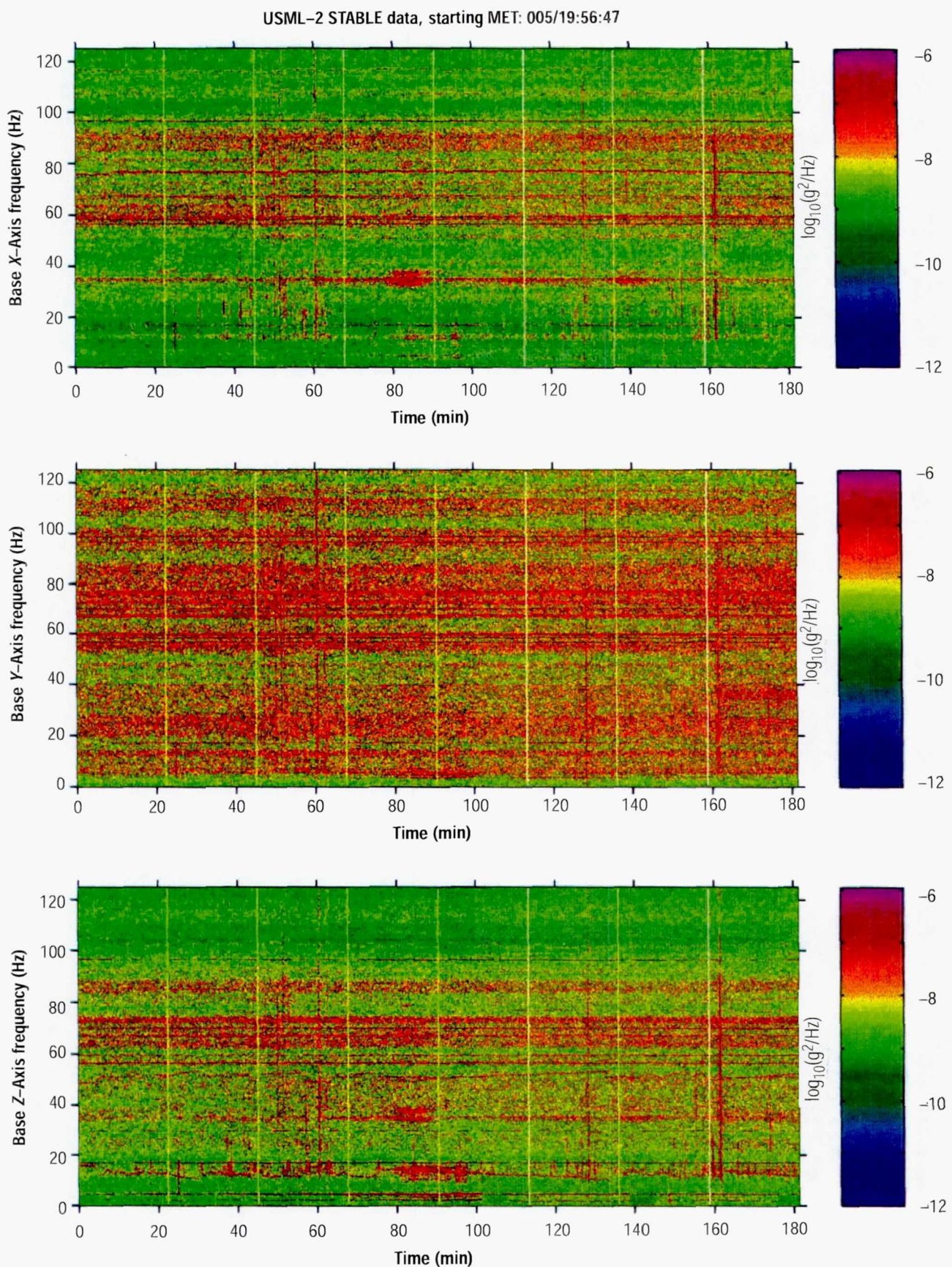


Figure 7. Color spectrograms for the three orthogonal accelerations measured on the locker backplate over a 3-hour period.

USML-2 STABLE data, starting MET: 005/19:56:47

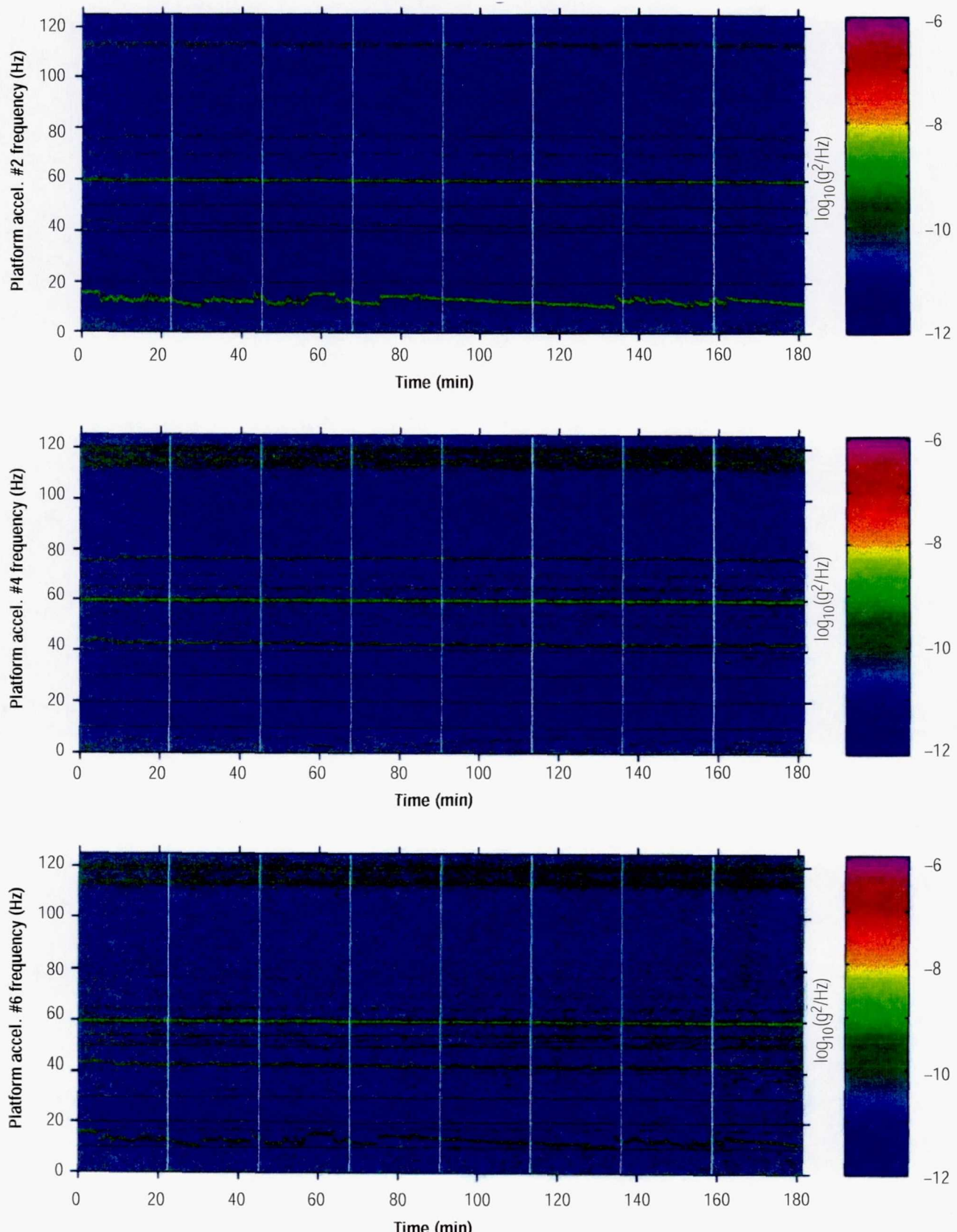


Figure 8. Color spectrograms for the three vertical accelerations measured on the platform over a 3-hour period.

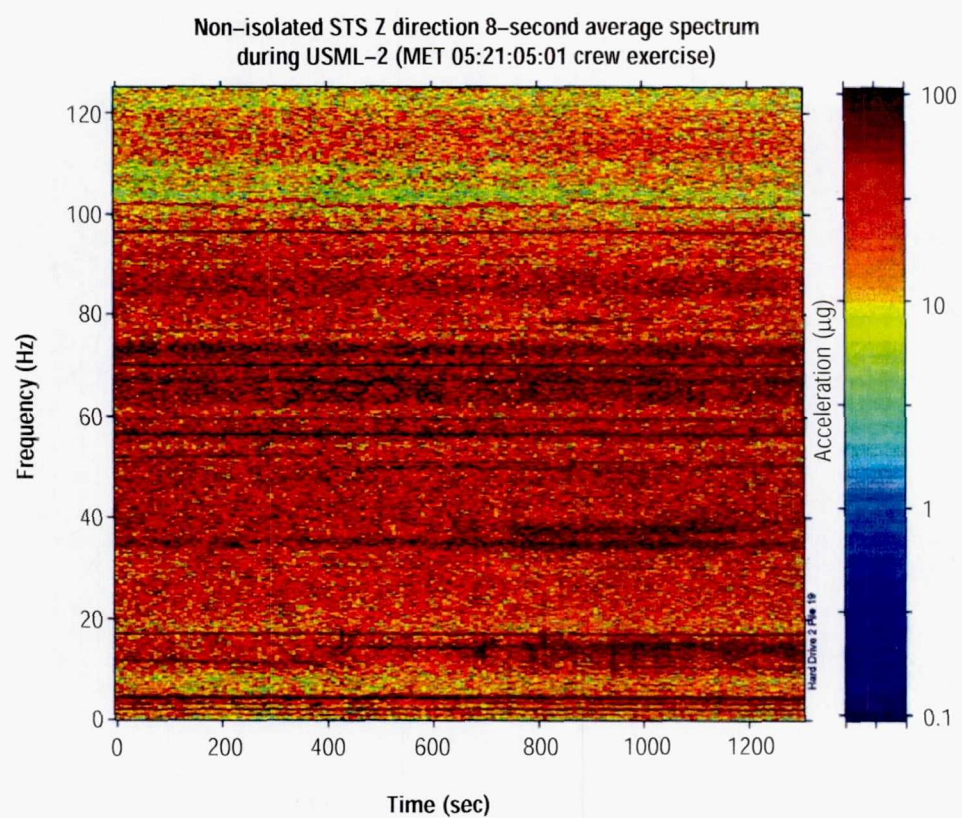


Figure 9. Color spectrogram for the vertical acceleration measured on the locker backplate over a 22-minute period.

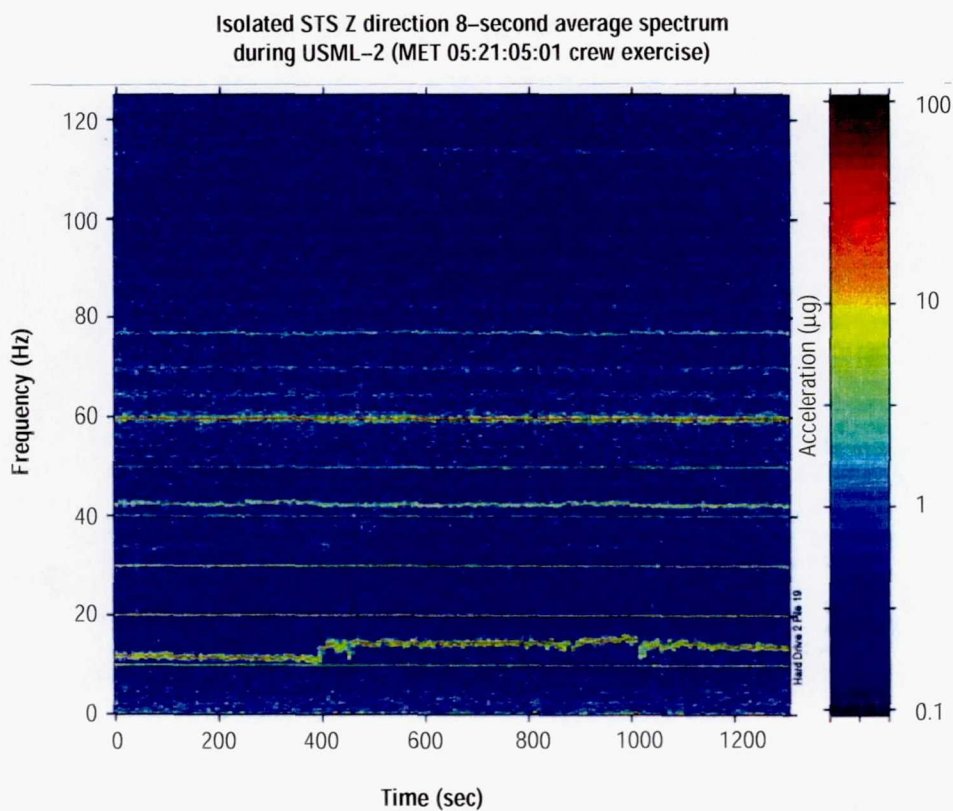


Figure 10. Color spectrogram for a vertical acceleration measured on the isolated platform over a 22-minute period.

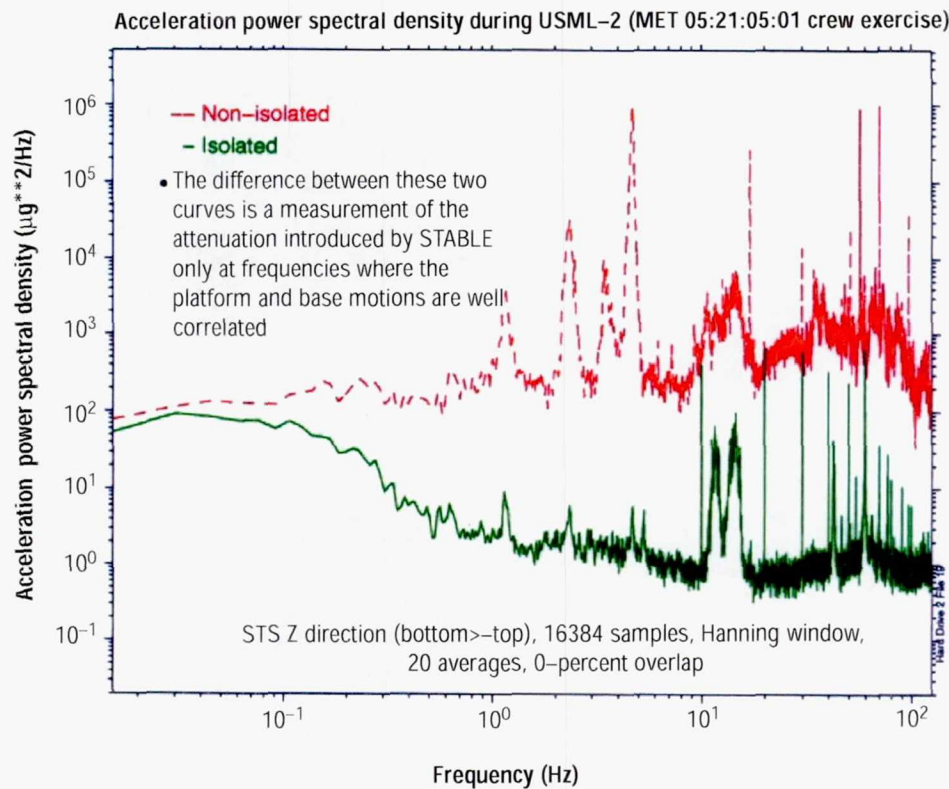


Figure 11. Representative power spectral density plot.

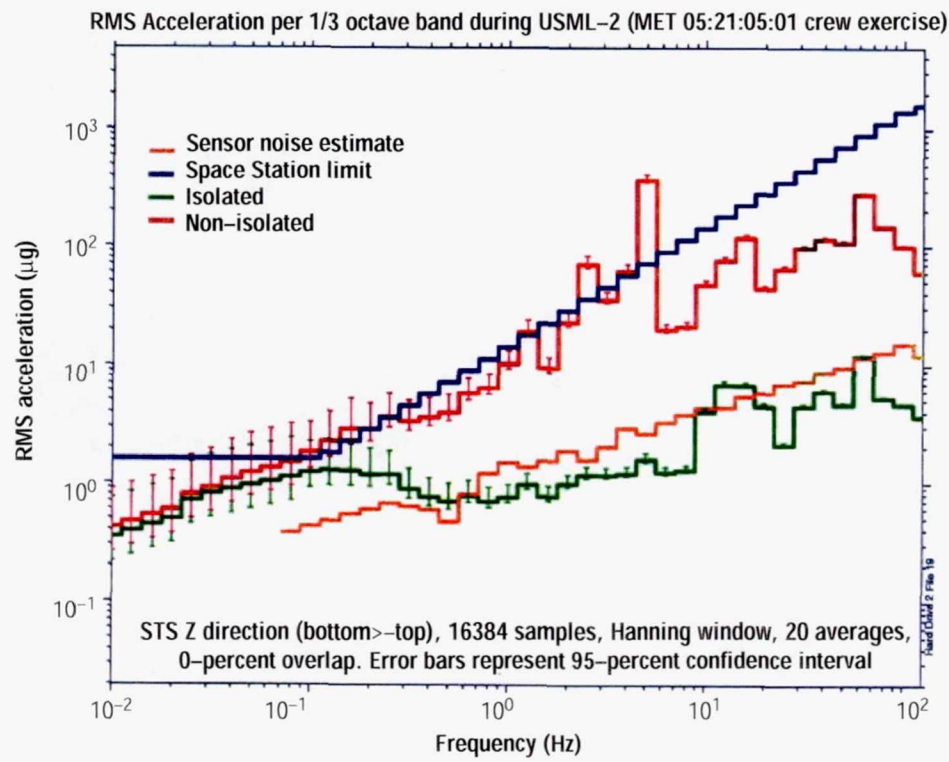


Figure 12. Comparison with ISS requirements and theoretical noise levels.

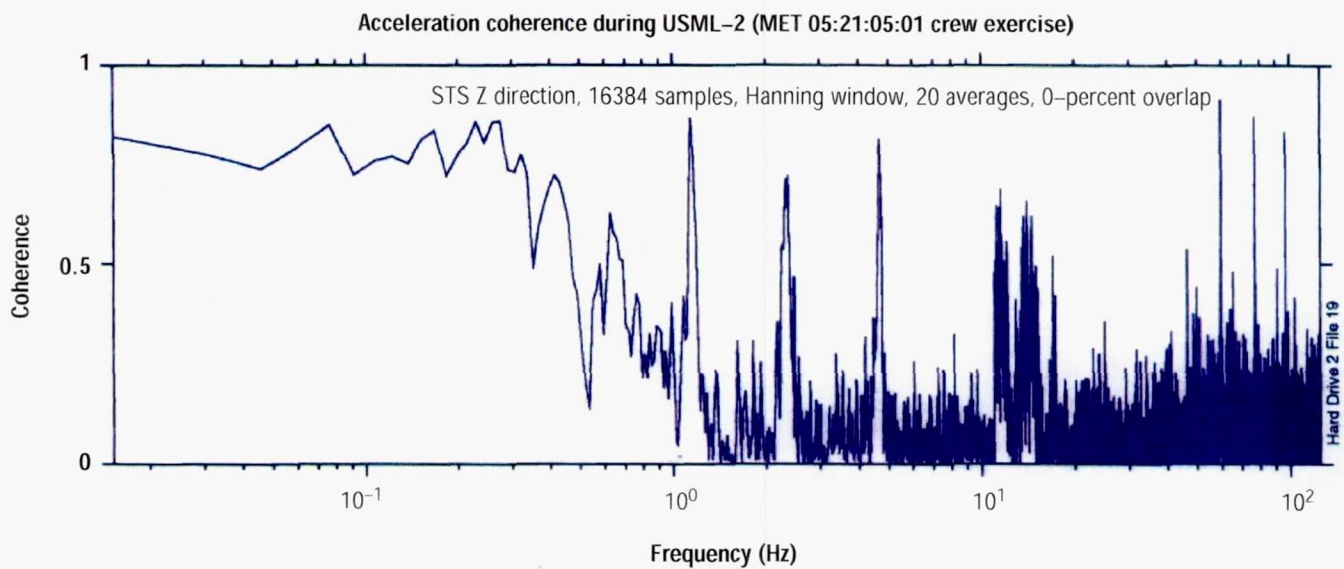


Figure 13. Degree of coherence between vertical acceleration measurements off and on the platform.

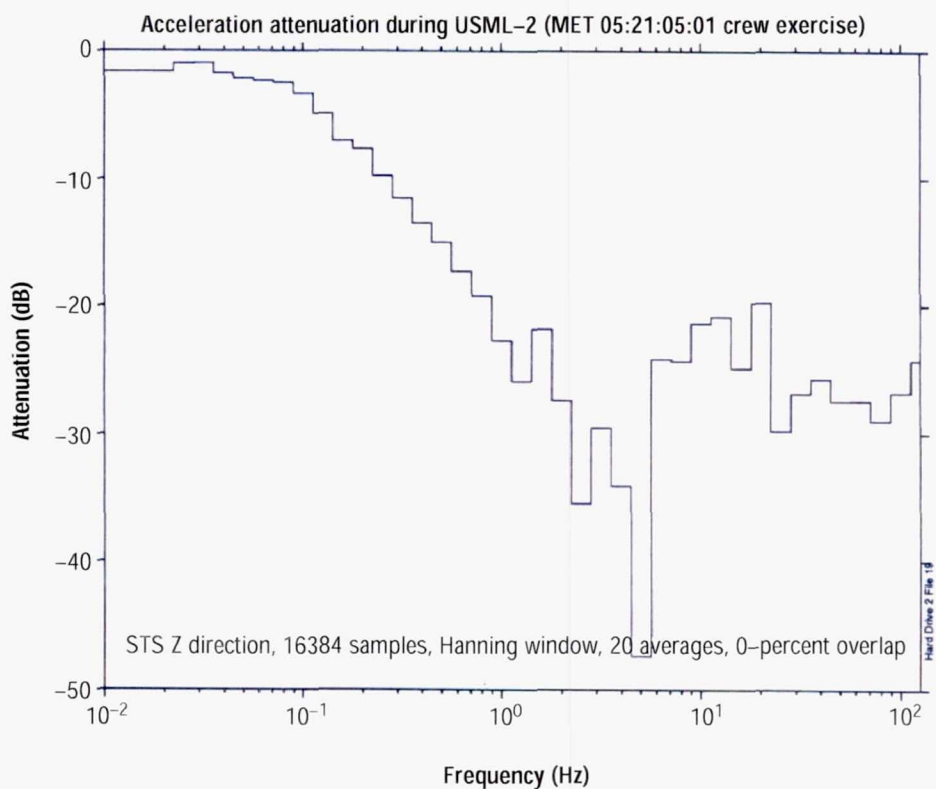


Figure 14. Preliminary estimate of attenuation.

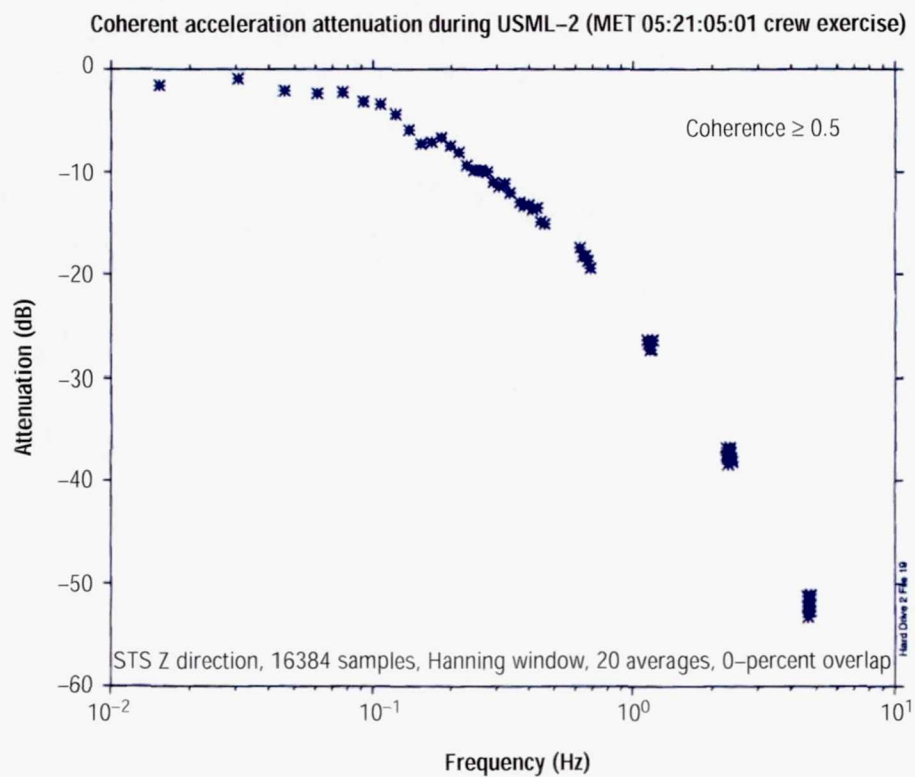


Figure 15. Better estimate of attenuation, using only well-correlated data.

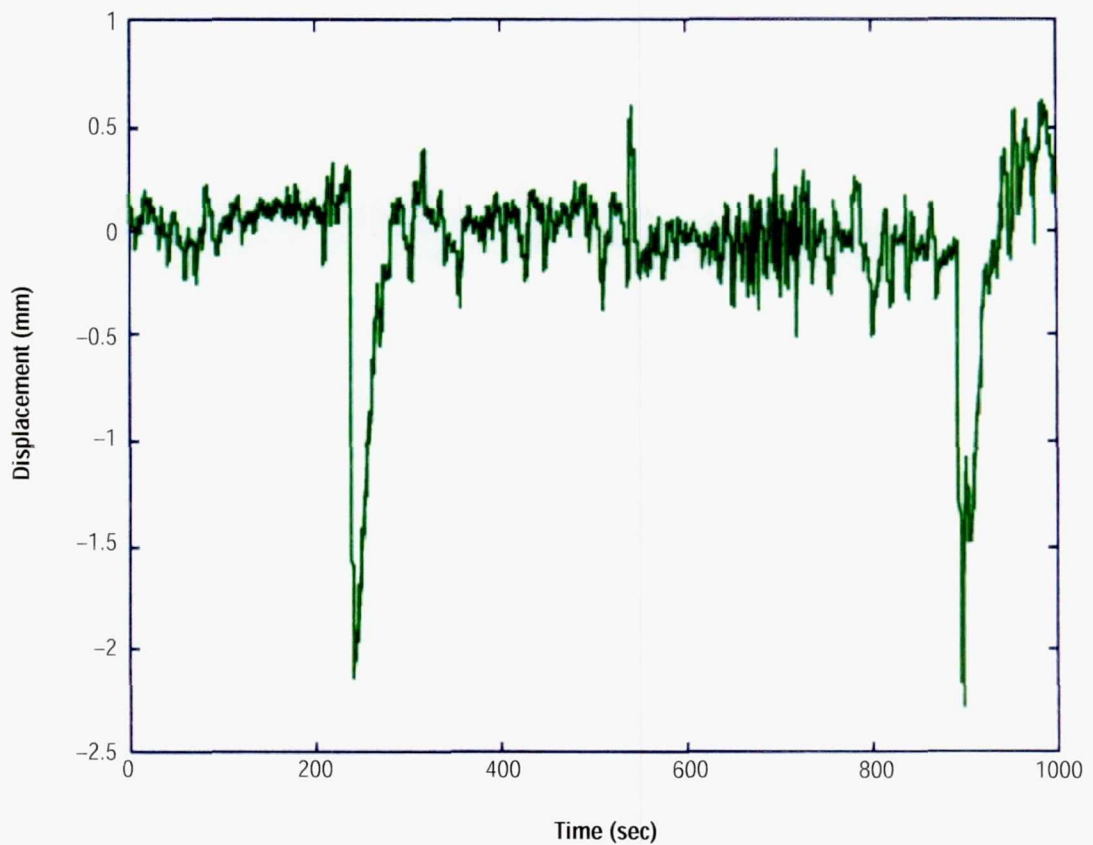


Figure 16. Typical time history of the platform displacement.

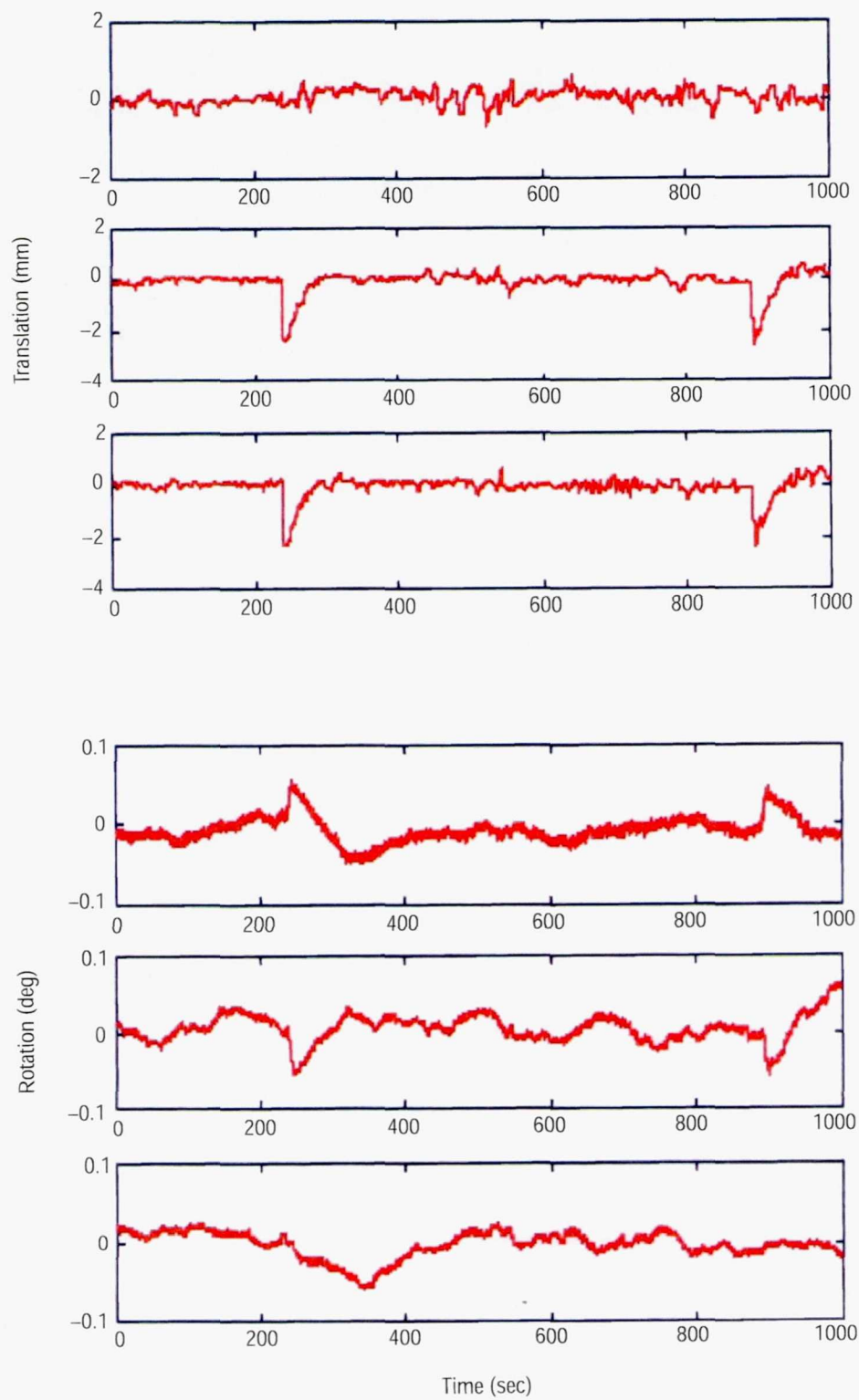


Figure 17. Typical time history of displacement and rotation at center of mass.

REPORT DOCUMENTATION PAGE

Form Approved
OMB No. 0704-0188

Public reporting burden for this collection of information is estimated to average 1 hour per response, including the time for reviewing instructions, searching existing data sources, gathering and maintaining the data needed, and completing and reviewing the collection of information. Send comments regarding this burden estimate or any other aspect of this collection of information, including suggestions for reducing this burden, to Washington Headquarters Services, Directorate for Information Operation and Reports, 1215 Jefferson Davis Highway, Suite 1204, Arlington, VA 22202-4302, and to the Office of Management and Budget, Paperwork Reduction Project (0704-0188), Washington, DC 20503

1. AGENCY USE ONLY (Leave Blank)		2. REPORT DATE August 1998	3. REPORT TYPE AND DATES COVERED Technical Memorandum
4. TITLE AND SUBTITLE Second United States Microgravity Laboratory: One Year Report, Volume 2		5. FUNDING NUMBERS	
6. AUTHORS M. Vlasse, D. McCauley,* and C. Walker,**			
7. PERFORMING ORGANIZATION NAMES(S) AND ADDRESS(ES) George C. Marshall Space Flight Center Marshall Space Flight Center, Alabama 35812		8. PERFORMING ORGANIZATION REPORT NUMBER M-893	
9. SPONSORING/MONITORING AGENCY NAME(S) AND ADDRESS(ES) National Aeronautics and Space Administration Washington, DC 20546-0001		10. SPONSORING/MONITORING AGENCY REPORT NUMBER NASA/TM-1998-208697/VOL2	
11. SUPPLEMENTARY NOTES The science reports are the culmination of research performed by the investigators in the period following the return of the 15-day USML-2 Space Shuttle mission. Prepared for Space Sciences Laboratory, Science and Engineering Directorate. * UAH ** USRA			
12a. DISTRIBUTION/AVAILABILITY STATEMENT Unclassified-Unlimited Subject Category 88 Standard Distribution		12b. DISTRIBUTION CODE	
13. ABSTRACT (Maximum 200 words) This document reports the one year science results for the important and highly successful Second United States Microgravity Laboratory (USML-2). The USML-2 mission consisted of a pressurized Spacelab module where the crew performed experiments. The mission also included a Glovebox where the crew performed additional experiments for the investigators. Together, about 36 major scientific experiments were performed, advancing the state of knowledge in fields such as fluid physics, solidification of metals, alloys, and semiconductors, combustion, and the growth of protein crystals. The results demonstrate the range of quality science that can be conducted utilizing orbital laboratories in microgravity and provide a look forward to a highly productive Space Station era.			
14. SUBJECT TERMS USML-2, Spacelab, microgravity research, materials science, protein crystal growth, fluid dynamics, drop dynamics, biotechnology, combustion		15. NUMBER OF PAGES 345	
		16. PRICE CODE A15	
17. SECURITY CLASSIFICATION OF REPORT Unclassified	18. SECURITY CLASSIFICATION OF THIS PAGE Unclassified	19. SECURITY CLASSIFICATION OF ABSTRACT Unclassified	20. LIMITATION OF ABSTRACT Unlimited